

Experimental Investigation and Lattice Modelling of 3D Printed Concrete Buildability quantification and early-age creep behaviour

Chang, Z.

DOI

[10.4233/uuid:ffa68da2-cd02-45a8-b4bc-99a289638571](https://doi.org/10.4233/uuid:ffa68da2-cd02-45a8-b4bc-99a289638571)

Publication date

2023

Document Version

Final published version

Citation (APA)

Chang, Z. (2023). *Experimental Investigation and Lattice Modelling of 3D Printed Concrete Buildability quantification and early-age creep behaviour*. [Dissertation (TU Delft), Delft University of Technology]. <https://doi.org/10.4233/uuid:ffa68da2-cd02-45a8-b4bc-99a289638571>

Important note

To cite this publication, please use the final published version (if applicable).
Please check the document version above.

Copyright

Other than for strictly personal use, it is not permitted to download, forward or distribute the text or part of it, without the consent of the author(s) and/or copyright holder(s), unless the work is under an open content license such as Creative Commons.

Takedown policy

Please contact us and provide details if you believe this document breaches copyrights.
We will remove access to the work immediately and investigate your claim.

Experimental Investigation and Lattice Modelling of 3D Printed Concrete

Buildability quantification and early-age creep behaviour

Propositions

Accompanying the dissertation

Experimental Investigation and Lattice Modelling of 3D Printed Concrete

Buildability quantification and early-age creep behaviour

By

Ze Chang

1 All models are wrong, but some are useful. (George E. P. Box)

[This proposition pertains to this dissertation]

2 So far, 3D concrete printing is still more an avant-garde concept rather than a practical construction method.

[This proposition pertains to this dissertation]

3 There is no best algorithm, only the most suited algorithm exists.

[This proposition pertains to this dissertation]

4 To learn without thinking is blindness, to think without learning is idleness (The Analects)

5 If you make a decision, acting soon rather than later is always preferable.

6 During the PhD process, "creep failure" is more likely than "fatigue failure."

7 Literature review is not the best and most efficient method for knowledge acquisition.

8 Doing a PhD is not as good as you expect or as bad as you fear. The attitudes to failure and frustration throughout the PhD process determine the level of success in the PhD.

9 Excessive pursuit of research output burns out the love for research.

10 Knowing what to give up is equally important as learning to solve problems.

These propositions are regarded as opposable and defensible, and have been approved as such by the promotor Prof.dr.ir. E. Schlangen and co-promotor Dr. B. Šavija.

Experimental Investigation and Lattice Modelling of 3D Printed Concrete

Buildability quantification and early-age creep behaviour

Dissertation

for the purpose of obtaining the degree of doctor

at Delft University of Technology

by the authority of the Rector Magnificus, Prof.dr.ir. T.H.J.J. van der Hagen

chair of the Board for Doctorates

to be defended publicly on

Thursday 23 February 2023 at 12:30 o'clock

by

Ze CHANG

Master of Engineering in Structural Engineering,

Dalian University of Technology, China,

Born in Shandong, China

This dissertation has been approved by the promotor

Composition of the doctoral committee

Rector Magnificus	chairperson
Prof.dr.ir. E. Schlangen	Delft University of Technology, promotor
Dr. B. Šavija	Delft University of Technology, copromotor

Independent members:

Prof.dr.ir. P.C. Louter	Delft University of Technology
Prof.dr.ir. J.G. Rots	Delft University of Technology
Prof.dr.ing. K. Van Tittelboom	Ghent University, Belgium
Dr. S. Qian	Nanyang Technological University, Singapore
Dr.ir. R.J.M. Wolfs	Eindhoven University of Technology



This research was financially supported by China Scholarship Council and Femris B.V..

Keywords: 3D concrete printing, buildability quantification, early-age creep, lattice

Printed by: Ipskamp Printing, The Netherlands

Cover design: Ze Chang and Yu Chen

Copy right @ 2023 by Ze Chang

ISBN: 978-94-6366-658-9

To my family

CONTENTS

CONTENTS	9
1. GENERAL INTRODUCTION	13
1.1 RESEARCH BACKGROUND	14
1.2 RESEARCH SIGNIFICANCE	15
1.3 RESEARCH OBJECTIVES	16
1.4 RESEARCH METHOD	16
1.5 THESIS OUTLINE	17
REFERENCES	19
2. LITERATURE REVIEW	21
2.1 INTRODUCTION	22
2.2 OVERVIEW OF PRINTING STAGES OF 3DCP	23
2.3 STAGES OF THE PRINTING PROCESS	23
2.4 METHODS FOR BUILDABILITY QUANTIFICATION	29
2.5 CONCLUSIONS	45
REFERENCES	46
3. A DISCRETE LATTICE MODEL FOR ASSESSMENT OF BUILDABILITY PERFORMANCE OF 3D PRINTED CONCRETE	53
3.1 INTRODUCTION	54
3.2 MODEL OVERVIEW	54
3.3 NUMERICAL ANALYSES	62
3.4 CONCLUSIONS	76
REFERENCES	78
4. EFFECT OF DEFORMED GEOMETRY AND INDUCED DAMAGE ON STRUCTURAL FAILURE OF PLASTIC COLLAPSE	81
4.1 INTRODUCTION	82
4.2 MODEL DESCRIPTION	82
4.3 RECAPITULATION OF LOAD-UNLOAD AND INCREMENTAL METHODS	83
4.4 MODEL METHODOLOGY ON 3D CONCRETE PRINTING	86

4.5	NUMERICAL ANALYSES	89
4.6	DISCUSSION	97
4.7	CONCLUSIONS	98
	REFERENCES	100
5.	MODELLING OF ELASTIC BUCKLING FAILURE IN 3DCP	101
5.1	INTRODUCTION	102
5.2	MODEL OVERVIEW	102
5.3	GEOMETRIC NONLINEARITY	103
5.4	NUMERICAL MODEL	107
5.5	DISCUSSION	114
5.6	CONCLUSIONS	116
	REFERENCES	118
6.	EARLY-AGE CREEP: EXPERIMENTS AND ANALYTICAL MODELLING	121
6.1	INTRODUCTION	122
6.2	MATERIALS AND METHODS	122
6.3	ANALYTICAL MODELLING	128
6.4	RESULTS	130
6.5	MODEL VALIDATION	135
6.6	DISCUSSION	137
6.7	CONCLUSIONS	142
	REFERENCES	144
7.	LATTICE MODELLING OF EARLY-AGE CREEP	147
7.1	INTRODUCTION	148
7.2	METHODOLOGY	148
7.3	MODEL VALIDATION	153
7.4	DISCUSSION	157
7.5	CONCLUSIONS	160
	REFERENCES	162
8.	THE IMPACT OF EARLY-AGE CREEP ON BUILDABILITY OF 3D PRINTED CONCRETE	163
8.1	INTRODUCTION	164

8.2	MODEL IMPLEMENTATION	164
8.3	NUMERICAL ANALYSIS	167
8.4	DISCUSSIONS	170
8.5	CONCLUSIONS	176
	REFERENCES	178
9.	RETROSPECTION, CONCLUSIONS AND RECOMMENDATIONS	179
9.1	RETROSPECTION	180
9.2	CONCLUSIONS	180
9.3	RECOMMENDATION FOR FUTURE RESEARCH	182
	REFERENCES	184
	SUMMARY	185
	SAMENVATTING	187
	ACKNOWLEDGMENTS	189
	LIST OF PUBLICATIONS	193
	CURRICULUM VITAE	197

1. GENERAL INTRODUCTION

This chapter presents the background of 3D printed concrete. The research significance, objectives and methods are illustrated afterwards. In the end, the thesis outline is given.

1.1 RESEARCH BACKGROUND

Over the past decades, the construction industry has been gradually moving towards digital manufacturing. Automated manufacturing technologies such as 3D concrete printing (3DCP) have generated considerable interest in academia and industry, and many groups are currently engaged in 3DCP research worldwide [1, 2]. This additive manufacturing technology can transform digital data from a computer model to a physical product [3]. Not only can 3DCP do away with the need for conventional molds, thereby reducing post-construction waste, it can also considerably accelerate the manufacturing process and yield geometrically complex, non-standard structural elements instead of rectilinear shapes [4-6], as shown in Figure 1-1.

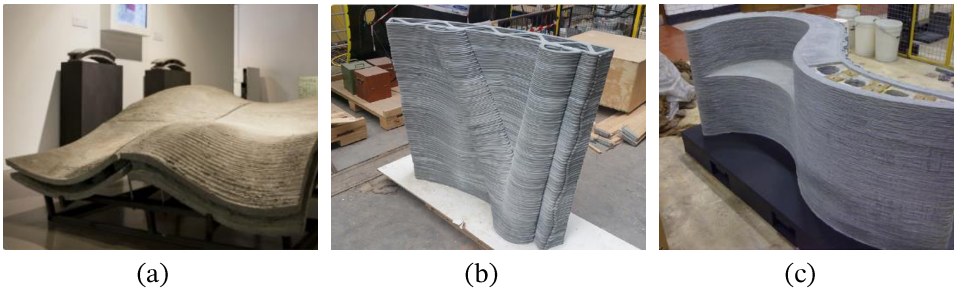


Figure 1-1 Examples of 3DCP application on geometrically complex, non-standard structural elements. (a) horizontal component manufacture from Loughborough University, UK.[1] (b) a vertically printed panel component from France.[1] (c) vertical cavities inside a printed structure from Loughborough University [7]

Based on the acknowledged feasibility of 3DCP in the construction industry, there have also been several large-scale constructions (See Figure 1-2) over the past several years. Eindhoven University of Technology has completed a bicycle bridge in Gemert for public use using the 3D printing technology [8]. Zhang et al. manufactured a bus station in situ without formwork using self-developed high-thixotropy 3D printable materials [9]. A more complex geometric cellular structure has been printed by a cooperative research group from the University of Southern Denmark and Politecnico di Milano. These projects demonstrate the application of 3DCP in the construction sector. However, full acceptance in the industry is still far from being straightforward, and several challenges related to different aspects, including material science and mechanical analysis, need to be solved.

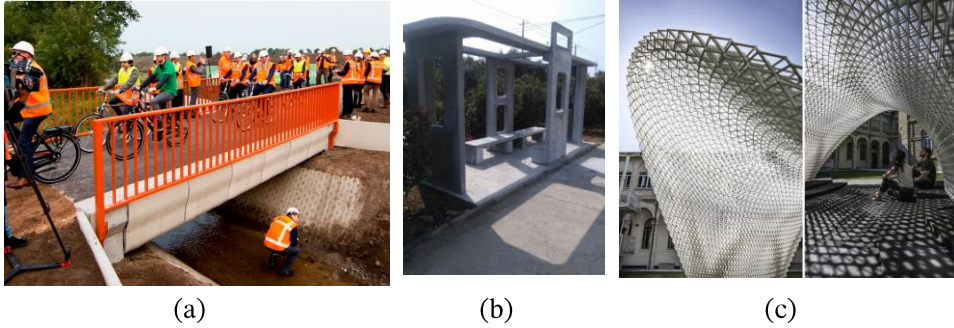


Figure 1-2 Noteworthy 3D printing applications: (a) Gemert bicycle bridge [8] (b) Bus stop [9] (c) Trabeculae pavilion [10]

1.2 RESEARCH SIGNIFICANCE

Due to the novelty of this technology, the structural properties of 3D printed concrete in the fresh state must be fully understood. Research gap still exists concerning the relationship between the material properties, mechanical properties and printing parameters.

While printing, the materials are extruded from the nozzle to build a computer-designed object using a robotic arm. After deposition, the material should be strong enough to retain its shape and avoid collapse or buckling under self-weight and the gravitational load from subsequent printing layers. This is defined as buildability performance [6, 11]. To complete the printing process and achieve good performance for structural elements or large-scale constructions, excellent buildability is required.

However, the structure buildability is co-determined by several factors, including material properties, printing geometry and printing parameters. Till now, most printing parameters have been determined through a series of trial-and-error experiments, whereby it remains unclear whether optimized parameters have been derived for the target object. Besides, experiments are time and resource-intensive, especially for large structures such as those used in real-life engineering and architectural applications. Compared with experiments, numerical modelling can provide a cheaper, faster, and more easily controlled alternative.

However, development of numerical or analytical models to simulate the printing process and assess structural buildability had not attracted much attention at the moment this project has started. To the best of the authors' knowledge, the first numerical model for buildability quantification of 3DCP is proposed based on the ABAQUS package at the starting stage of this PhD project in 2018 [12]. Until the finishing stage of this PhD project in 2022, more numerical or analytical models have been developed to study the printing process and predict the critical printing height of 3DCP [11-16]. Those models demonstrate the growing interest and feasibility of

numerical or analytical models for quantifying buildability as an alternative to the experimental method.

1.3 RESEARCH OBJECTIVES

This thesis aims to give insight into the structural behaviour of 3DCP in the fresh state. A numerical model is proposed to assess the structural buildability of 3DCP. In addition, an experimental program is presented to measure the early-age creep of 3D printable mortar. The experimentally derived early-age creep is incorporated into 3D printing model to study its impact on structural behaviour during the printing process. The main objective will be completed through the following tasks:

- To develop a numerical model for buildability quantification, which can reproduce the typical failure mode including plastic collapse, elastic buckling and combined failure modes reported in the literature;
- To study the impact of material properties, printing geometry and printing scheme on structural failure, this model should incorporate numerous influencing parameters. They must include material properties development, printing velocity, geometry of printed object, material heterogeneity and non-uniform gravitational load due to the continuous printing process;
- To develop an experimental procedure and numerical model to characterize the early-age creep behaviour and study its impact on buildability quantification;

1.4 RESEARCH METHOD

In order to complete the research objectives, this research will be conducted in the following three steps:

Step 1: Preliminary understanding of the failure modes while printing process of 3DCP

- Define the commonly observed failure modes while printing and understand the relevant failure mechanism towards them;
- Develop an underlying model to reproduce these common failure modes reported in the literature quantitatively;

Step 2: Introduce a series of factors associated with printing parameters and material properties into the developed model and study their impact on buildability quantification

- Analyze the influential factors associated with printing parameters during the printing process of 3DCP;
- Introduce these factors into the numerical model and study their impact on buildability quantification;

Step 3: Understanding the early-age material properties such as creep on buildability quantification

- Devise a method to investigate the early-age creep behaviour of 3D printable materials;
- Develop a numerical method to simulate this early-age creep behaviour;
- Incorporate this experimentally observed behaviour into the 3D printing model for buildability quantification and study its impact;

1.5 THESIS OUTLINE

As shown in Figure 1-3, this thesis is divided into four parts. The chapters are arranged as follows,

Part I: A general introduction and literature review.

Chapter 1 serves as an introduction to the research background, research objectives and thesis outline.

Chapter 2 presents a literature review on the current research process of buildability quantification of 3DCP, early-age creep behaviour of 3D printable materials, lattice numerical analysis and machine learning application on 3DCP.

Part II: Propose the underlying model to simulate the plastic collapse and elastic buckling failure modes during the printing process of 3DCP.

Chapter 3 adopts the lattice model with load-unload method to simulate the plastic collapse failure mode, which uses a new structural failure criterion and studies the impact of non-uniform gravitational load, localized damage, and material heterogeneity.

Chapter 4 incorporates the incremental algorithm into lattice model to understand the impact of deformed geometry and induced damage on critical printing height prediction of 3DCP.

Chapter 5 introduces the geometric nonlinearity into lattice model with incremental solution and simulates the buckling failure response during printing process.

Part III: Investigate the early-age creep behaviour of 3D printable material and study its impact on buildability quantification.

Chapter 6 experimentally and analytically investigate the early-age creep behaviour of 3D printable materials.

Chapter 7 proposes a numerical method to simulate the early-age creep behaviour of 3D printable materials based on the lattice model.

Chapter 8 incorporates the early-age creep into 3D printing model and studies its impact on structural behaviour during printing process.

Part IV: Gives the conclusions of the thesis and indicates an outlook for future studies.

Chapter 9 provides the main findings of this thesis and gives recommendations for future studies.

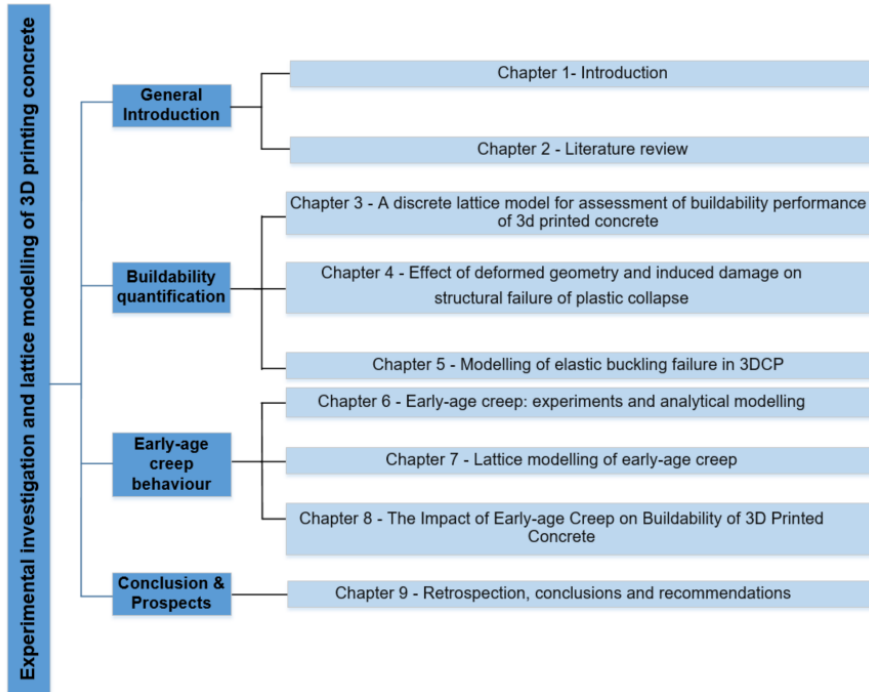


Figure 1-3 Thesis outline

REFERENCES

- [1] R.A. Buswell, W.L. de Silva, S. Jones, J. Dirrenberger, 3D printing using concrete extrusion: A roadmap for research, *Cement and Concrete Research* 112 (2018) 37-49.
- [2] Y. Chen, Z. Li, S. Chaves Figueiredo, O. Çopuroğlu, F. Veer, E. Schlangen, Limestone and Calcined Clay-Based Sustainable Cementitious Materials for 3D Concrete Printing: A Fundamental Study of Extrudability and Early-Age Strength Development, *Applied Sciences* 9(9) (2019) 1809.
- [3] C. Gosselin, R. Duballet, P. Roux, N. Gaudillière, J. Dirrenberger, P. Morel, Large-scale 3D printing of ultra-high performance concrete—a new processing route for architects and builders, *Materials Design* 100 (2016) 102-109.
- [4] S.C. Paul, Y.W.D. Tay, B. Panda, M.J. Tan, Fresh and hardened properties of 3D printable cementitious materials for building and construction, *Archives of Civil and Mechanical Engineering* 18(1) (2018) 311-319.
- [5] Y.W.D. Tay, B. Panda, S.C. Paul, N.A. Noor Mohamed, M.J. Tan, K.F. Leong, 3D printing trends in building and construction industry: a review, *Virtual and Physical Prototyping* 12(3) (2017) 261-276.
- [6] F. Bos, R. Wolfs, Z. Ahmed, T. Salet, Additive manufacturing of concrete in construction: potentials and challenges of 3D concrete printing, *Virtual and Physical Prototyping* 11(3) (2016) 209-225.
- [7] S. Lim, R.A. Buswell, T.T. Le, S.A. Austin, A.G.F. Gibb, T. Thorpe, Developments in construction-scale additive manufacturing processes, *Automation in Construction* 21 (2012) 262-268.
- [8] T.A. Salet, Z.Y. Ahmed, F.P. Bos, H.L. Laagland, Design of a 3D printed concrete bridge by testing, *Virtual and Physical Prototyping* 13(3) (2018) 222-236.
- [9] Y. Zhang, Y. Zhang, W. She, L. Yang, G. Liu, Y. Yang, Rheological and harden properties of the high-thixotropy 3D printing concrete, *Construction and Building Materials* 201 (2019) 278-285.
- [10] R. Naboni, L. Breseghello, A. Kunic, Multi-scale design and fabrication of the Trabeculae Pavilion, *Additive Manufacturing* 27 (2019) 305-317.
- [11] N. Roussel, A thixotropy model for fresh fluid concretes: theory, validation and applications, *Cement and Concrete Research* 36(10) (2006) 1797-1806.
- [12] R. Wolfs, F. Bos, T. Salet, Early age mechanical behaviour of 3D printed concrete: Numerical modelling and experimental testing, *Cement and Concrete Research* 106 (2018) 103-116.
- [13] B. Panda, N. Mohamed, N. Ahamed, S.C. Paul, G. Bhagath Singh, M.J. Tan, B. Šaviša, The effect of material fresh properties and process parameters on buildability and interlayer adhesion of 3D printed concrete, *Materials* 12(13) (2019) 2149.
- [14] A.S.J. Suiker, Mechanical performance of wall structures in 3D printing processes: Theory, design tools and experiments, *International Journal of Mechanical Sciences* 137 (2018) 145-170.
- [15] J. Kruger, S. Zeranka, G. van Zijl, 3D concrete printing: a lower bound analytical model for buildability performance quantification, *Automation in Construction* 106 (2019) 102904.
- [16] R. Jayatilakage, P. Rajeev, J. Sanjayan, Yield stress criteria to assess the buildability of 3D concrete printing, *Construction and Building Materials* 240 (2020) 117989.

2. LITERATURE REVIEW

This chapter reviews the methods for buildability quantification of 3D printable concrete, including the experimental approaches, analytical modelling and numerical simulations. First, a brief introduction of printing process is given. This provides a fundamental understanding on the material behaviors in different stages. The printability, which consists of the pumpability, extrudability and buildability, is discussed. Subsequently, this chapter presents a brief review of the experimental and analytical models for buildability quantification and discusses their limitations. An overview on the numerical tools for 3DCP is then given. These numerical models serve to predict the structural performance during printing process and optimize the printing parameters, therefore, providing a more economical solution for buildability quantification. In the end, a summary and discussion on the limitations of numerical tools for buildability quantification is provided, as well as recommendations for model improvement.

2.1 INTRODUCTION

The construction industry serves as a cornerstone of global economy, contributing 6% to GDP and bringing in close to \$10 trillion annually [1, 2]. Despite this, the construction technique remains low-tech, with the majority of construction projects being executed using manual labour [3]. Besides, the increase in number of (0.1)construction projects results in a heavy burden on the environment [4]. According to the estimation of the United Nations, the global population will rise to around 10.9 billion by 2100. The dramatic growth will result in a significant burden on living and housing [5].

Considering the great burdens of conventional construction methods on sustainability and productivity it is essential to explore high-efficiency construction strategies. An advanced technology, i.e., 3D concrete printing (3DCP), has been proposed to replace traditional construction techniques with a lower labour-and-resource cost. Buswell et al. [7] reviewed the number of implemented projects by means of additive manufacturing techniques, as shown in Figure 2-1. Clearly, this advanced manufacturing technology generates a growing interest in academic and construction sectors. The projects range from building elements to entire structures, including a cycling bridge in the Netherlands [8], houses in China [9], the USA and the Middle East [10-12]. In contrast to conventional construction methods, 3DCP can create complex geometries without formwork, thereby resulting in a reduced cost with respect to formwork materials.

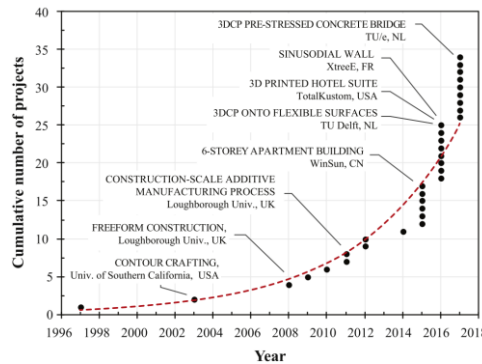


Figure 2-1 The increase in number of large-scale concrete 3D printed projects since 1997 [7]

Although 3D concrete printing shows potential, full adoption in the construction sector is still far away due to the lack of knowledge regarding material properties and structural behaviours in the fresh state. To understand the material printability, lots of studies have been conducted from different aspects, which include material mixing, pumping, extrusion, building-up, curing, and durability [13-15]. In order to provide a common platform to discuss these novel ideas and research findings, three RILEM

international conferences on the topic of 3DCP were held in Zurich in 2018 [16], Eindhoven in 2020 [17], and Loughborough in 2022 [18].

Herein, a review of structural behaviour of printable concrete in fresh state is provided. This work first summarizes the basic principles of the printing process, consisting of pumping, extrusion and build-up stages. Subsequently, strategies for buildability quantification are reviewed, including experiments, analytical and numerical models. In the end, some limitations of analytical and numerical methods are discussed, and research gaps are identified.

2.2 OVERVIEW OF PRINTING STAGES OF 3DCP

The 3DCP process contains at least three stages: a) the pumping stage from pump to nozzle (i.e., the print head) through a pipe or a hose; b) the deposition process through the nozzle; and c) the build-up stage [19, 20]. In general, three criteria, namely, pumpability [21, 22], extrudability [23, 24] and buildability [25-27], are used to describe the material printability in different stages, as described in Figure 2-2. Pumpability ensures that printable material can be transferred within pipe without blockage, which requires the material to be flowable. After that, the material will be extruded from the print head. The geometry of the nozzle may affect material properties [28, 29]. This is followed by the structural build-up stage, which requires that the extruded material has sufficient stiffness and strength to sustain its geometry under the loading from itself and subsequent printing layers. There should be a balance between pumpability and buildability [21]: the former requires the cementitious material to behave as a liquid, while the latter demands the extruded material to act as solid.

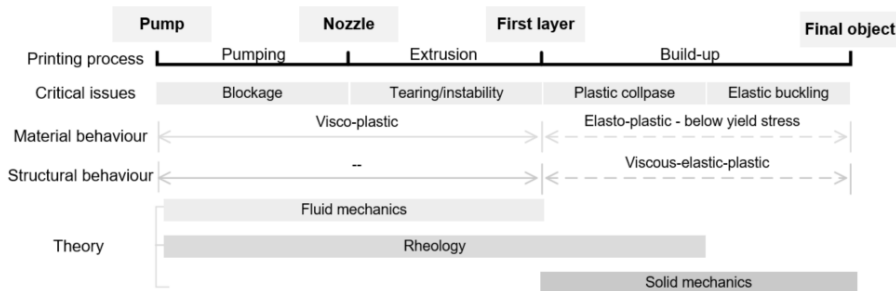


Figure 2-2 A schematic diagram of 3DCP at different stages

To assess the printability of cementitious materials, numerical and analytical methods have been proposed over the past several years as alternatives to experiments. Understanding material behaviour during printing process is crucial for mix design and printability assessment.

2.3 STAGES OF THE PRINTING PROCESS

2.3.1 Pumping stage

The pumping stage refers to the process during which the cementitious material is conveyed from pump to nozzle. In general, pumpability of cementitious materials can be measured by laboratory testing. To set the optimal parameters for pumping process, a full understanding on the relationship between material pressure and flow rate is required [30, 31].

Printable cementitious materials are often assumed to behave as Bingham liquids. The traditional Buckingham-Reiner equation is often used to compute the pumping pressure for complex suspensions. However, this equation may overestimate the pumping pressure around 2-5 times [32, 33] since it does not allow for the impact of shear-induced cement particles and segregation and water transfer. The pipe parameters (i.e., length and radius), pump pressure and particle size of printable materials are the factors that determine the pumpability through the pumping process [19]. Figure 2-3 describes the distribution of shear stress and material flow behaviour. Since the cementitious materials for 3DCP are not homogeneous, the shear stress may result in movement of large aggregate particles towards the region with a lower shear rate (namely, the centre of transmission pipe). A 'lubrication layer' (LL) with more water forms near the pipe wall, leaving the 'bulk material' in the pipe's centre [34, 35]. Compared to the bulk material, the LL is exposed to higher shear stress. Due to the migration of cement particles, the material within LL undergoes a structural breakdown process, in which shear stress breaks the connections between cement particles built by flocculation and hydration [36, 37]. Thus, LL has a lower yield stress and viscosity compared to the bulk material [34, 38]. To investigate the impact of pipe and material properties on pumping pressure Δp_{tot} , Kaplan et al. [39] presented two analytical models. These models incorporate a series of printing parameters and material properties, which include flowrate Q_p , shear yield stress τ_0 and plastic viscosity μ , as shown in Eq. 2-2 and Eq. 2-3.

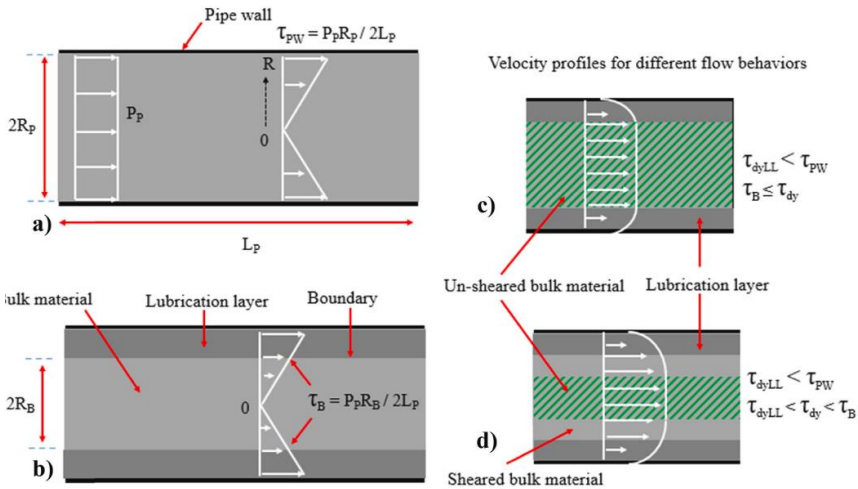


Figure 2-3 Pumping processes and flow behaviour in 3DCP [19]

$$Q_p = \pi \frac{3\Delta p_{tot}^4 R^4 + 16\tau_0^4 L^4 - 8\tau_0 LR^3 \Delta p_{tot}^3}{24\Delta p_{tot}^3 \mu L} \quad \text{Eq. 2-1}$$

$$\Delta P = \frac{2L_{pipe}}{R_{pipe}} \left[\frac{Q_p \mu_i}{\pi R_{pipe}^2 k} + \tau_{0,i} \right] \quad \text{Eq. 2-2}$$

$$\Delta P = \frac{2L_{pipe}}{R_{pipe}} \left[\frac{\frac{Q_p}{\pi R_{pipe}^2 k} - \frac{R_{pipe}}{4\mu} \tau_{0,i} + \frac{R_{pipe}}{3\mu} \tau_0}{1 + \frac{R_{pipe}}{4\mu} \mu_i} \mu_i + \tau_{0,i} \right] \quad \text{Eq. 2-3}$$

Where L_{pipe} and R_{pipe} refer to the pipe length and radius.

Besides pipe and material properties, the temperature and air content also affect the pumping pressure. The friction from the transmission pipe raises the material temperature and causes the material to rapidly dissolve or incorporate air [36, 40, 41], affecting its' rheological properties.

2.3.2 Extrusion stage

After the pumping stage, the printable material should be extruded from the nozzle. There are two commonly utilized extruders, namely, piston or screw-type [42-45], as shown in Figure 2-4. In the piston extrusion, the barrel is filled with printable material, the piston then applies pressure from the pump to push the material out of the nozzle [46, 47]. An Archimedes screw or a similar device is generally used for screw extrusion [48, 49], enabling the material to be continuously supplied to the extruder [50].

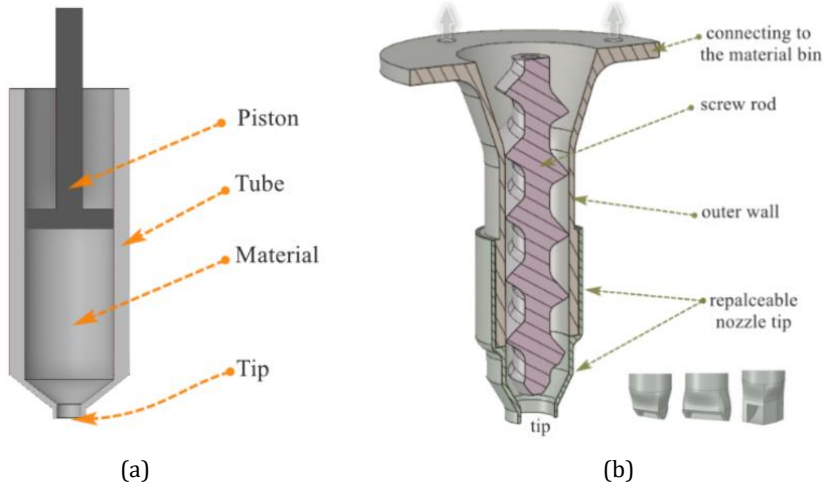


Figure 2-4 Two commonly used extruder types in 3DCP [45] (a) a piston extruder; (b) a screw-type extruder

In the piston extruder, the stress condition of extruded material depends on the nozzle configuration. According to Roussel [29], there are two cases due to the different nozzles, as shown in Figure 2-5. In a rectangular nozzle, the cementitious material is extruded in an unsheared condition. A high static yield stress can be obtained after material deposition. Consequently, the extruded material is stiff and the geometry of printed filament is close to cross-section of the nozzle [51]. The second one refers to non-laminar flow from a conical kind of nozzle, and the extruded material is subjected to shear stress because of the transition of cross-section of printhead. In this regime, the competition between gravity and yield stress determines the final shape of the extruded layer.

These two cases also introduce different additional loadings to the printed structure during the extrusion process [45]. [46]. If the thickness of the individual layer is larger than “stand-off distance” (i.e., the distance between print head and previously deposited layers), the printed filament will be locally compressed and deformed until the layer height decreases to that distance. For the rectangular nozzle, the printed filament is generally placed on previously printed structure without compression, given that the stand-off distance is larger than the layer height. In such a case, the next printed segment may ‘drop’ into the printed structure, thereby threatening its stability [52], as shown in Figure 2-6. When it comes to the buildability quantification, this additional load may affect the structural build-up capacity.

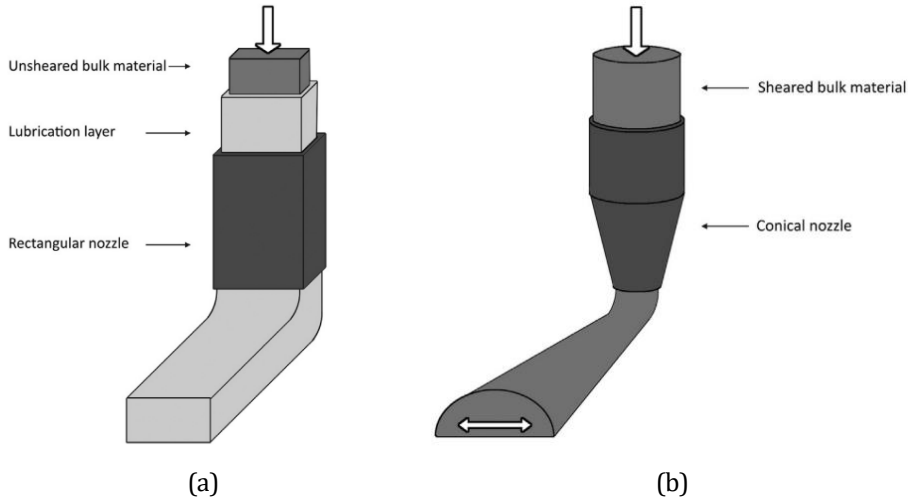


Figure 2-5 Two printing cases at the printhead and deposition zone levels zone [29] (a) laminar flow from rectangular kind of nozzle (b) non-laminar flow from conical kind of nozzle

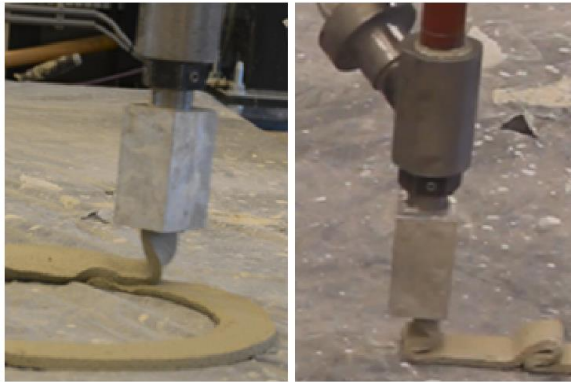


Figure 2-6 Illustration of printing process due to the excessive standoff distance [52]

In order to adjust the height between print head and previous layer, accessories can be installed into the nozzle to monitor the flatness [52-54], layer height, width and stand-off distance. The monitoring signal is sent back to the printer in order to adjust the nozzle height in a real test, as shown in Figure 2-7. In that case, the influence of dynamic loading which is detrimental to structural stability can be eliminated.

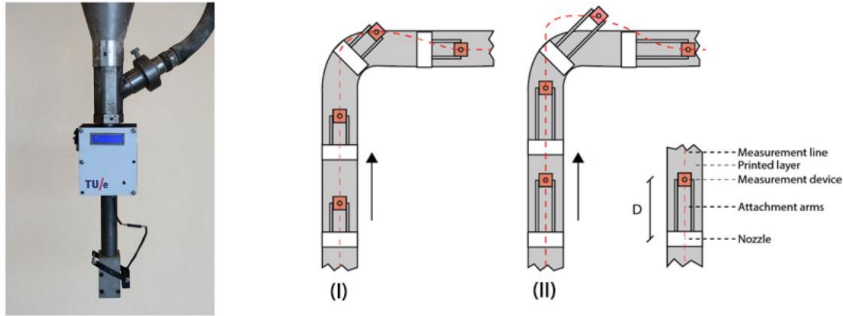


Figure 2-7 Nozzle height measuring equipment (left); the position of this device during printing process from the top view (right) [52]

Besides the installation of nozzle accessories, recently, a two-pipe printing strategy is proposed to ensure the good buildability of printable cementitious materials [55-59]. Unlike the traditional manufacturing method, in which the accelerators are added in the mixing process, in the two-pipe method the accelerator is added into the printed material in the nozzle. This advanced technique can not only ensure the material stiffness after deposition, but also avoid the high pumping pressure and blockages during the pumping process. At present, there are two commonly utilized two-pipe systems, namely, dynamic and static mixers. The dynamic mixer refers to the machine with one or more electric motor-driven shafts [60]; the static mixer is employed to continuously mix a liquid material, by means of a number of fixed baffles instead of moving components [61]. In contrast to the dynamic mixing system, no issues with dead zones occur in the two-pipe pumping system since it uses a static mixer. Besides, when employing a static mixer, a much higher pumping pressure is needed than when using a dynamic mixer [62]. In addition, it should be noted that printable materials with different properties can be mixed using various kinds of static mixers. Further research is required to assess the practicability and their influence on mix homogeneity and required pumping pressure for cementitious-based materials.

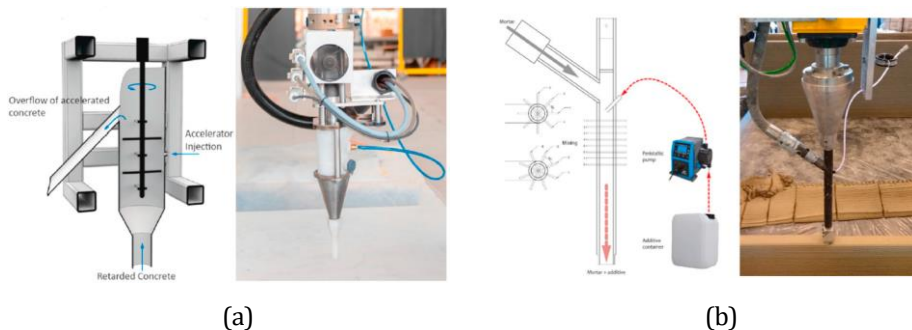


Figure 2-8 3D concrete printing using accelerators added through inline mixing process (a) a mixing reactor for smart dynamic casting that has a pin mixer type tool (left); a mixing reactor

for extrusion-based 3D printing which has a pin mixer type tool (right) [58] (b) liquid additive injection equipment. A schematic diagram for this setup (left); a general view of the accelerator injection during printing process (right), taken [59]

2.3.3 Build-up stage

Extrusion-based concrete printing can create the computer-designed geometry without external support. This can eliminate the need for formwork, thereby decreasing the amount of waste in construction. However, the absence of the formwork during the extrusion process raises the possibility of structural failure after material deposition [35, 63, 64]. During the printing process, gravitational loading from successive printing layers increases. Subject to the gradual incremental loading, the printed structure may fail due to plastic collapse determined by material yielding, structural instability dominant by elastic buckling, or a combination of the two. These typical failure modes are shown in Figure 2-9.

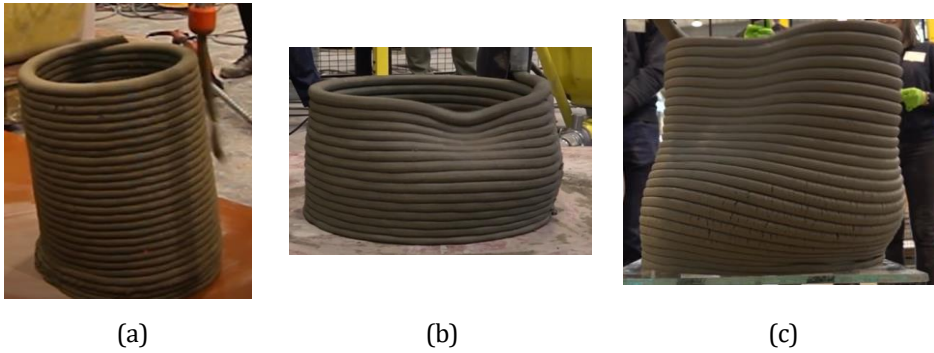


Figure 2-9 Typical failure modes during the printing process (a) plastic collapse dominant failure mode (b) elastic buckling dominant failure mode (c) failure mode between elastic buckling and plastic collapse [65]

In general, to prevent structural failure during printing process, both material strength and stiffness of the deposited materials should develop to defend the gradually increasing loading of the printed structure [66-69]. This increment of gravitational loading is codetermined by printing speed and material density.

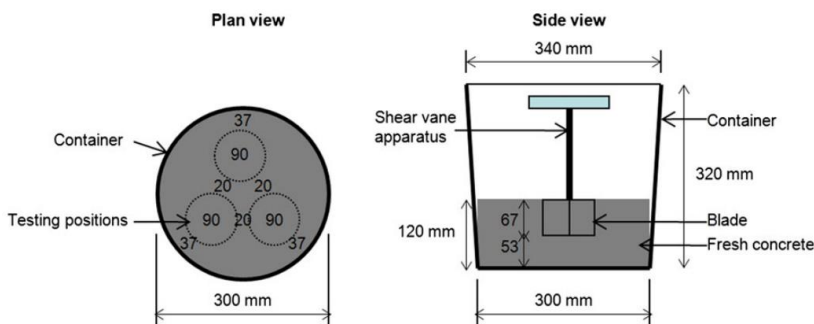
To quantify whether and when the printed structure may fail during printing process, different approaches have been proposed. These methods compare the (minimal) development of material stiffness and strength to the (maximal) printing speed of designed structure. In the following section, a detailed review of the strategies for buildability quantification of 3DCP will be given from the perspectives of experimental investigation, analytical modelling and numerical simulation.

2.4 METHODS FOR BUILDABILITY QUANTIFICATION

2.4.1 Experimental methods

Buildability is a complicated and process-specific feature that is codetermined by material composition and a series of parameters, such as printing velocity and geometry [26]. Le et al. [70] stated that the most straightforward approach to assess buildability of cementitious materials is through printing trials, in which the critical printed layers (i.e., maximum number of printed layers) can be experimentally measured given a specific printing geometry. A hollow cylinder [71], square [72-74] and wall structures [74, 75] are most frequently used for buildability quantification. Three typical failure modes mentioned above can be observed through these printing geometries. Although the printing trials can directly reflect the structural build-up capacity, these test procedures are time-and-labour consuming.

In pursuit of more convenient experimental methods, different studies [25, 76, 77] presented the rheological and compression tests (as shown in Figure 2-10) for buildability quantification. Through a series of rheological tests, Le et al. [70] concluded that there is a range of material strength for material printability assessment. This range is highly dependent on the material mix. If lower than this range, the fresh materials are too wet, and segregation will occur in the pipe-pump-nozzle system. The extruded materials cannot sustain shape due to excessive deformation. If higher than this range, the cementitious materials are difficult to be extruded and printed continuously. The ‘uniaxial compression’ test is another method proposed for buildability quantification. For example, Di Carlo [78] presented a compression test to quantify the structural buildability of cylinder samples. Kazemian et al. [79] proposed a cylinder stability test for rapid comparative assessment of compositions’ impact on build-up capacity. In these tests, they regard the layers that are printed on the top of each other act as the compressive loading applied to the specimen. Panda et al. [77, 80, 81] defined the shape retention parameter to quantify the structural shape stability. They reported that, if the stand-off distance is reduced, the dimensional accuracy of printed structure is negatively affected [26].



(a)

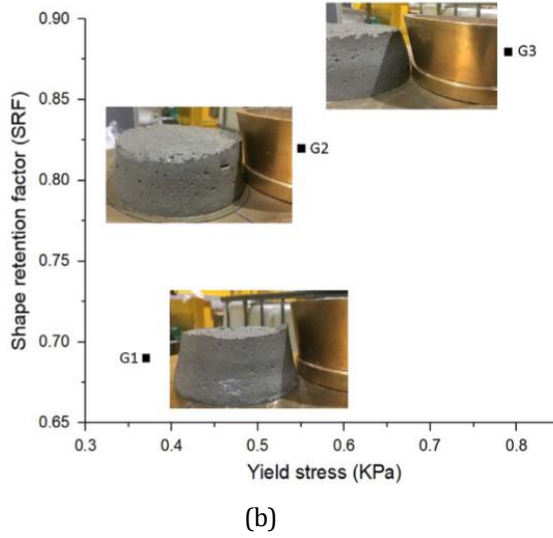


Figure 2-10 Two types of experimental methods for buildability quantification (a) a schematic diagram of shear vane with measuring positions [70] (b) compression test: relationship between SRF and yield stress of the printable cementitious materials [77]

2.4.2 Analytical models

To assess the structural buildability during the printing process, some analytical methods are proposed. These analytical models can be divided into two categories: rheological models and solid mechanics models. The major contribution towards rheological model comes from Roussel [29]. He explored how a series of material properties, such as yield stress, elastic modulus, viscosity, and structuration rate, influence the printability [29]. Proposed criteria evaluate the rheological requirements and examine the final geometrical dimensions of a single layer, which include the surface cracking and structural instability. To measure the structural build-up rate, Roussel adopted the parameter A_{thix} [28] and static yield stress σ_0 to predict the material yielding using Eq. 2-4.

$$\tau_0 t_{rest} = \tau_{0,t=0} + A_{thix} t_{rest} \quad \text{Eq. 2-4}$$

Here, the t_{rest} refers to the resting time after material deposition and $\tau_{0,t=0}$ refers to the material initial yield stress. It should be pointed that the sheared extruded material has a lower static yield stress than the unsheared one because of the breakdown of the connection among cement particles, as explained in Section 2.3.2. A_{thix} is the yield stress development due to the structuration and flocculation. According to the time range considered, the material development can be described by a linear or non-linear tendency [82, 83]. Further investigations into thixotropy and other rheological properties have been conducted, providing a theoretical basis for research in this field [22, 84-90]. These rheological models are mainly used to characterize the extrusion

and pumping processes from the standpoint of material rheology. Kruger et al. [90-93] found that re-flocculation of the cement particle network must be taken into account once the printable materials are subjected to high shear stress. They presented a bi-linear model to describe the evolution of material yield stress, which determines the material yielding during the printing process. The impact of two mechanisms (namely, re-flocculation (R_{thix}) and structuration (A_{thix})) are considered with aspects to thixotropic behaviour of printable materials. The time-dependent yield stress shown in Figure 2-11 can be mathematically expressed as follows:

$$\begin{aligned}\tau_s(t) &= \tau_{D,i} + R_{thix}t \quad \text{for } t \leq t_{rf} \\ \tau_s(t) &= \tau_{s,i} + A_{thix}(t - t_{rf}) \quad \text{for } t > t_{rf} \\ t_{rf} &= \frac{\tau_{s,i} - \tau_{D,i}}{R_{thix}}\end{aligned}\tag{Eq. 2-5}$$

where $\tau_s(t)$ is the static or the apparent yield stress of the printed material after agitation. $\tau_{s,i}$ and $\tau_{D,i}$ stand for initial static and dynamic yield stress of printed material, respectively, which can be measured with rheological tests; t_{rf} means the time range in which re-flocculation occurs.

Perrot et al. [69, 82] proposed a similar analytical model to define the optimal build-up rate considering material yielding. Their model predicts the critical printing height based on the instantaneous material strength, as shown in Eq. 2-6. If the stress in the bottom layer reaches the material strength, plastic collapse is assumed to occur.

$$H_{critical} = \frac{\sqrt{3}\tau_0(t_{pr})}{\rho g}\tag{Eq. 2-6}$$

Here, the t_{pr} refers to the printing time after material deposition. Similarly, Wangler et al. [94] computed the maximal horizontal printing velocity $V_{r,max}$, as shown in Eq. 2-7.

$$V_{r,max} = \frac{\sqrt{3}LA_{thix}}{\rho gH_{layer}}\tag{Eq. 2-7}$$

where L refers to the contour length. In contrast to other analytical models, this analytical model studies the impact of structural geometry on the prediction of plastic collapse dominant failure mode.

However, in addition to plastic collapse, elastic buckling is also important for buildability quantification [25, 76]. Roussel [29] presented an analytical model to predict the critical printed height for buckling failure, mathematically described as:

$$H_{c,buck} \simeq \left(\frac{8EI}{\rho gA}\right)^{1/3}\tag{Eq. 2-8}$$

Where E and I refer to the material stiffness and second moment of inertia, and A refers to the horizontal rectangular cross-section area. Then, this model is improved through the consideration of printing geometry. When it comes to wall structure with the I equal to $\delta^3/12$ (δ refers to the width of wall), this equation can be rewritten as:

$$H_{c,buck} \simeq \left(\frac{2E\delta^2}{3\rho g} \right)^{1/3} \quad \text{Eq. 2-9}$$

Although some other studies also attempted to use similar models to quantify structural build-up [69], the geometry and structural heterogeneity are still difficult to consider [22, 92, 95-98].

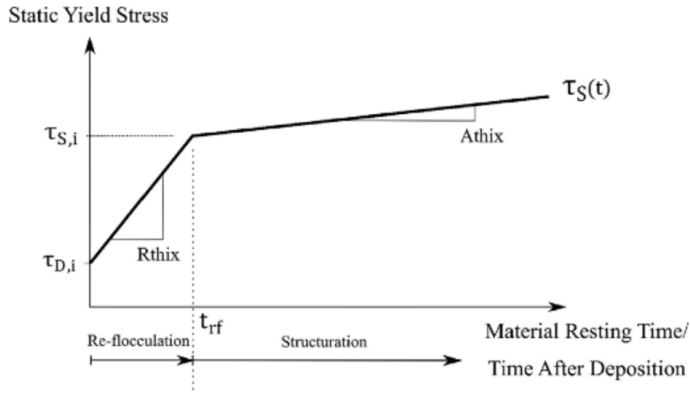


Figure 2-11 The development of static yield stress as a function of the concrete age considering the re-flocculation and structuration, the different stages can be mathematically described by Eq. (2-4) [93]

To incorporate the above-mentioned factors, a mechanistic model presented by Suiker [74] considers a series of parameters, i.e., time-dependent material stiffness and strength, printing velocity, boundary conditions, the structural imperfections and non-uniform gravitational loading. Two failure modes (i.e., elastic buckling and plastic collapse, as shown in Figure 2-12), are considered to analyze the build-up performance of a wall structure [72-74]. As explained in Suiker's model [73, 74], the criterion in Eq. 2-10 can be used to examine whether straight wall structures fail due to elastic buckling or plastic collapse during printing process.

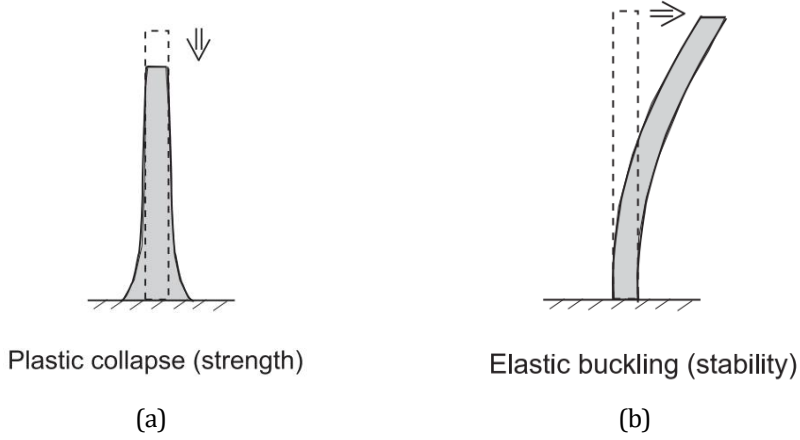


Figure 2-12 Wall failure mode during printing process [74] (a) plastic collapse due to material yielding, which is dominant by material strength (b) elastic buckling due to the structural instability, which is dominant by material stiffness

$$\frac{\bar{l}_{cr}}{\bar{l}_p} < \bar{\Lambda} : \text{elastic buckling}$$

$$\frac{\bar{l}_{cr}}{\bar{l}_p} > \bar{\Lambda} : \text{plastic collapse}$$

Eq. 2-10

$$\text{with } \bar{\Lambda} = \left(\frac{h}{D_0} \right) \frac{\sigma_{p,0}}{(\rho g)^{2/3}}$$

In which, the dimensionless parameter Λ refers to “failure mechanism indicator”. Based on this model, the failure mechanism is codetermined by a series of factors, including wall thickness h , initial material yield strength $\sigma_{p,0}$, initial bending stiffness D_0 of the printed wall structure, material density ρ and the gravitational acceleration g .

In contrast to other analytical models, this mechanical model studies the impact of more influencing factors on buildability. Several printing geometries, including the wall structure [74], rectangular [72], and square structures [73] are used for model validation. This model predicts the critical printing height close to the experimental results.

The primary advantages of Suiker’s model lie in its simplicity of use and time efficiency. However, this model has the same limitation as other analytical models, e.g., being applicable only for specific printing geometries. Additionally, it does not apply to printing geometries other than wall structures. In contrast, the numerical models can explore the impact of geometric features and material heterogeneity on structural analysis during printing process. Such kind of tools also can replace or at least reduce the resource and time-consuming trial-and-error testing. Thus, it is essential to

present the numerical tools for buildability quantification. After material deposition, the printed filaments are at rest, behaving roughly like elasto-visco-plastic materials subject to gravitational loading. Two kinds of theories, namely, fluid and solid mechanics, are adopted in numerical models.

2.4.3 Numerical models

Computational fluid dynamics (CFD) models based on fluid mechanics have been used to investigate the effect of constitutive relationships (such as generalized Newtonian fluid and elasto-visco-plastic fluid) on cross-sectional geometry of a printed layer [99], as shown in Figure 2-13. Furthermore, the relationship between the layer geometry and a series of printing parameters, including printing velocity and nozzle height, has been studied as well [100-103]. The CFD is capable to describe the filament instability and tearing induced by the imbalance between the nozzle movement speed and the material flow (as shown in Figure 2-14), enabling the design of an optimal extrusion process [102]. In addition, a CFD model has also been used to simulate the non-uniform material deposition at corners during printing process, as illustrated in Figure 2-15. So far, the majority of CFD models focused on the extrusion process or geometry prediction of a single printing layer. Recently, the stability and deformation of multiple layers are simulated as well by means of this method, as shown in Figure 2-16. However, CFD models have not been used for buildability quantification.

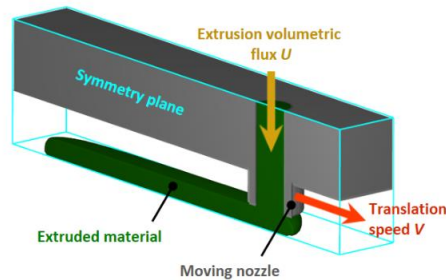


Figure 2-13 A schematic diagram of 3D printing simulation using the CFD model [103]

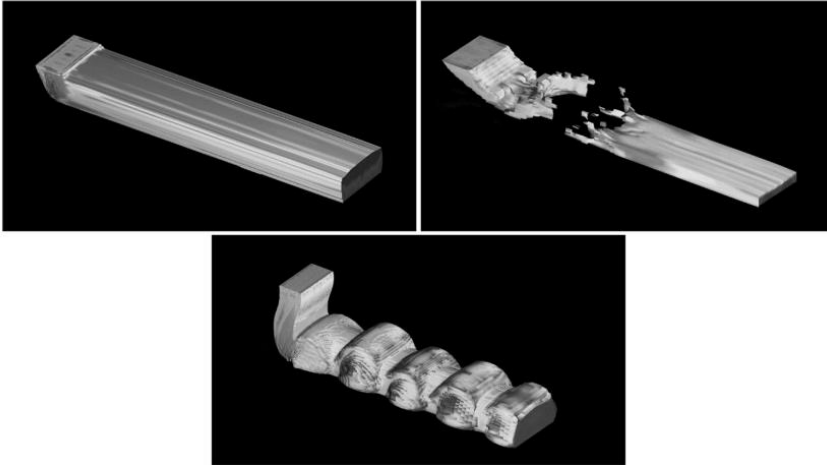


Figure 2-14 Simulation of individual layer printing using CFD with possible printing results, i.e., nominal extrusion, filament tearing and filament buckling [102]

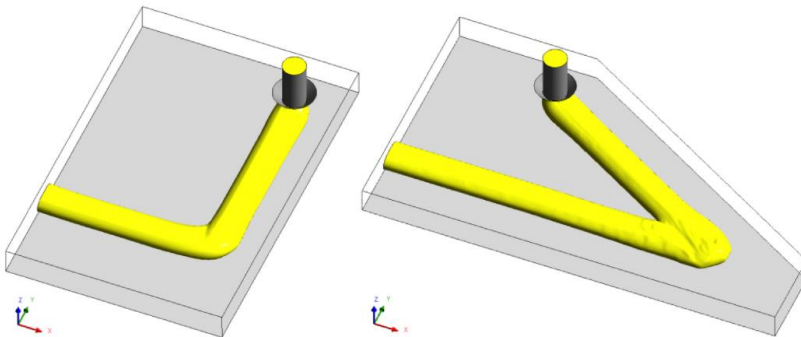
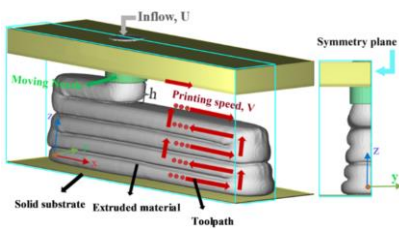
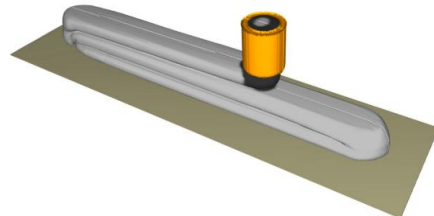


Figure 2-15 Simulation of material deposition at corner during printing process; the left is the ideal material deposition with the corner equal to 90-degree and the right one is the non-ideal material deposition with the corner equal to 30-degree



(a)



(b)

Figure 2-16 Simulation of stability and deformation of multi-layers in 3D concrete printing using CFD model (a) a wall with five layers [99]; (b) a numerical case with three layers [101]

To better understand the structural failure during printing process, a Finite element method (FEM) based model using the ABAQUS package has been developed by Wolfs et al. [71, 72, 75] to quantify the structural buildability. This 3D printing model can simulate two typical failure modes, i.e., plastic collapse and elastic buckling, during printing process. The time-dependent material characteristics and Mohr-Coulomb failure criterion are employed for plastic collapse simulation. The material properties are derived from the uniaxial compression and shear tests at different material ages. This 3D printing model applies the model change option in ABAQUS to mimic the layer-by-layer printing process. In each analysis step, the material properties (strength and stiffness in this case) develop with the printing time to account for the impact of hydration. A geometric nonlinear analysis is carried out to consider the impact of large deformation on the structural analysis. Once any point of the printed structure reaches the material strength, the printed structure is regarded as having failed and the critical printed height is calculated. This model can qualitatively reproduce the experimental results, as shown in Figure 2-17. However, there is a large quantitative disagreement with the printing experiment, almost 60%. This difference is mainly due to the neglect of localized damage, stress redistribution and non-uniform gravitational loading. In terms of buckling, Wolfs et al. [75] first performed linear buckling analysis to get possible buckling modes. An initial imperfection based on the first-mode instability was obtained and then incorporated into numerical model for nonlinear buckling analysis. A quantitative agreement with printing test can be derived. However, the buckling failure modes produced by the FEM-based method are different from those observed from the printing tests, as shown in Figure 2-18. For wall structure, an asymmetric buckling failure mode can be observed from experiment, which is different from the symmetric failure mode in the numerical analysis. For rectangular layout, the buckling failure occurs close to the end of the structure while the numerical model produces buckling failure in the middle of the rectangular structure. The possible reason to these differences is the neglect of non-uniform gravitational loading in 3D printing simulations. The buckling failure mode of analyzed object is determined by the initial imperfection in the numerical analyses. To reproduce the experimentally observed failure mode for elastic buckling, researchers from Ghent university [104] tried to incorporate the non-uniform gravitational loading into the buckling analysis of wall structures, and asymmetric failure of buckling response can be derived. However, there is no published work which describes the relationship between the non-uniform gravitational loading, geometric nonlinearity and buckling failure during printing process. Previous studies demonstrate that the FEM-based method is able to reproduce the experimentally derived results for 3D concrete printing. However, some model limitations exist and need to be addressed.

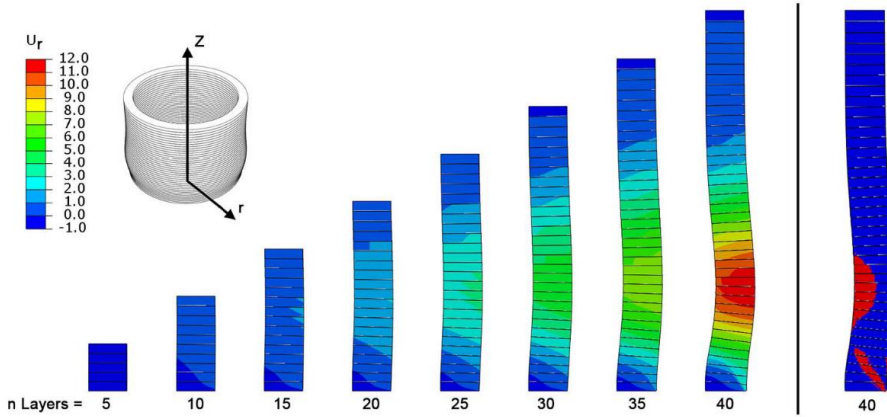


Figure 2-17 FEM-based numerical model for plastic collapse failure model simulation vis hollow cylinder structure [71]

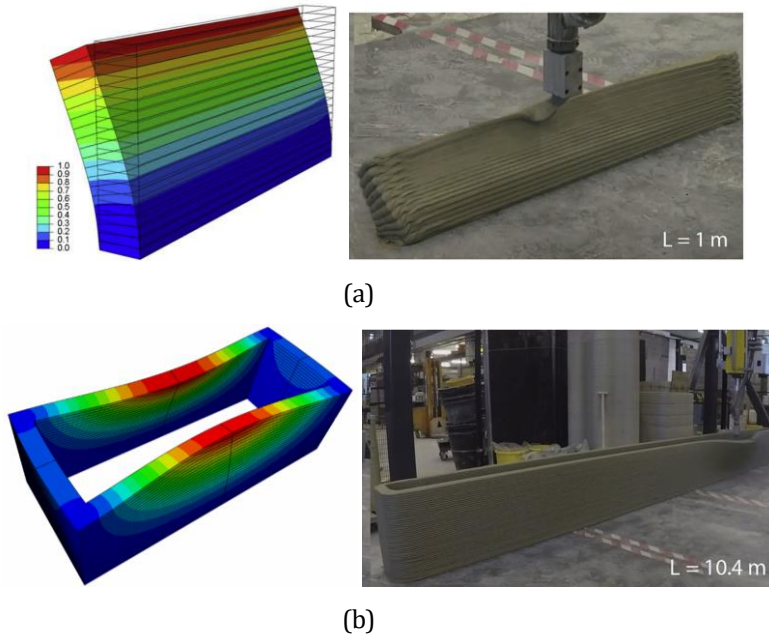


Figure 2-18 Typical buckling failure mode during printing process [52] (a) wall structure (b) rectangular structure [In each subfigure, the left is the numerical analysis and the right is the experimental result]

Using this FEM-based method model as a base, Ooms et al. [105-107] proposed a parametric tool to create input files for 3D printing models without extensive manual modelling. This parametric tool automizes pre-processing step for structural analysis of 3DCP, especially for complex printing geometries. The general methodology of this parametric tool is shown in Figure 2-19. Using this technique, they split each printing layer into several segments and studied the impact of non-uniform gravitational

loading on failure height. Furthermore, they also investigated the different interaction methods (i.e., tie constraints and contact-based interactions) on structural deformation. A schematic diagram of these two interaction methods can be found in Figure 2-20. In addition, they investigated the model change interaction for structural analysis during printing process, which allows for the simulation of deactivation and reactivation of printed segments. Based on their finding, the option (i.e., model change interaction with strain) is the only choice for buildability quantification of 3DCP for the FEM-based 3D concrete model.

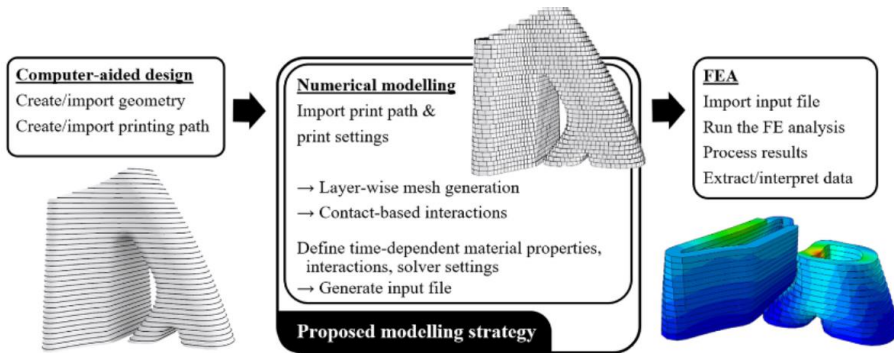


Figure 2-19 General methodology of the proposed method for 3DCP simulation [105]

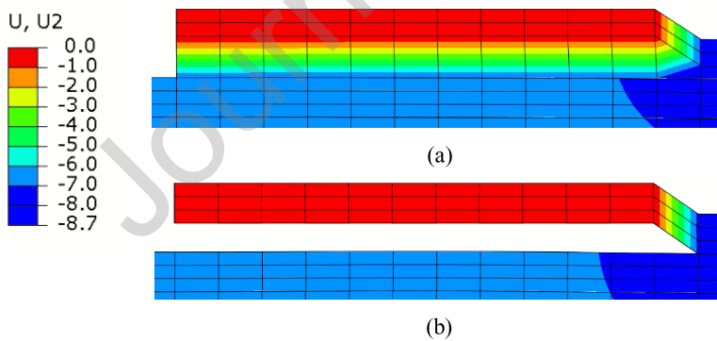


Figure 2-20 Different interactions in ABAQUS: (a) tie constraints (b) contact-based interactions [105]

Similar to Ooms et al.'s research, Nguyen-Van et al. proposed a novel computational framework to model the structural buildability of complex triply periodic minimal surface via the given toolpath [108]. The general procedure is shown in Figure 2-21. Using this technique, the effect of printing velocity on critical printed height and vertical deformation is studied.

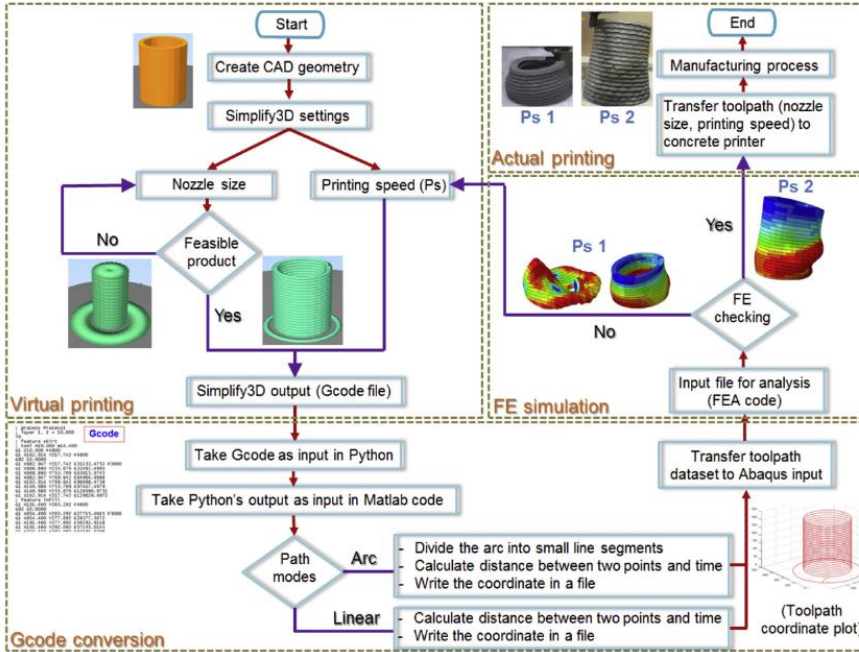


Figure 2-21 The general procedure for the computational framework for 3D concrete printing [108]

Besides the above-mentioned research, some other works are performed to analyze influencing factors during the printing process. This includes the improved FEM models [105, 106, 109] and other novel methods [105, 107, 110, 111]. For instance, to investigate the impact of viscoelasticity at finite strain for buildability quantification, Nedjar [112] incorporated the viscosity and geometric nonlinearity into the FEM model for buildability quantification. In his model, viscosity refers to early age creep, which is simulated via an internal variable method. The evolution of early creep is modelled through a generalized Maxwell model. Furthermore, the incremental algorithm is also incorporated into his model based on the Lagrangian formulation for buildability quantification. For model validation, a hollow cylinder structure and a wall structure were used. The predicted structural failure of these two printing geometries can be found in Figure 2-22. The biggest improvement of this model is the incorporation of the viscosity of printable cementitious materials into the 3D printing model. However, the model is similar to the FEM-based 3D printing model proposed by Wolfs et al. The localized damage and non-uniform gravitational loading during printing process are not taken into account. Besides, the viscosity adopted in these numerical analyses does not correspond to that of a printable cementitious material.

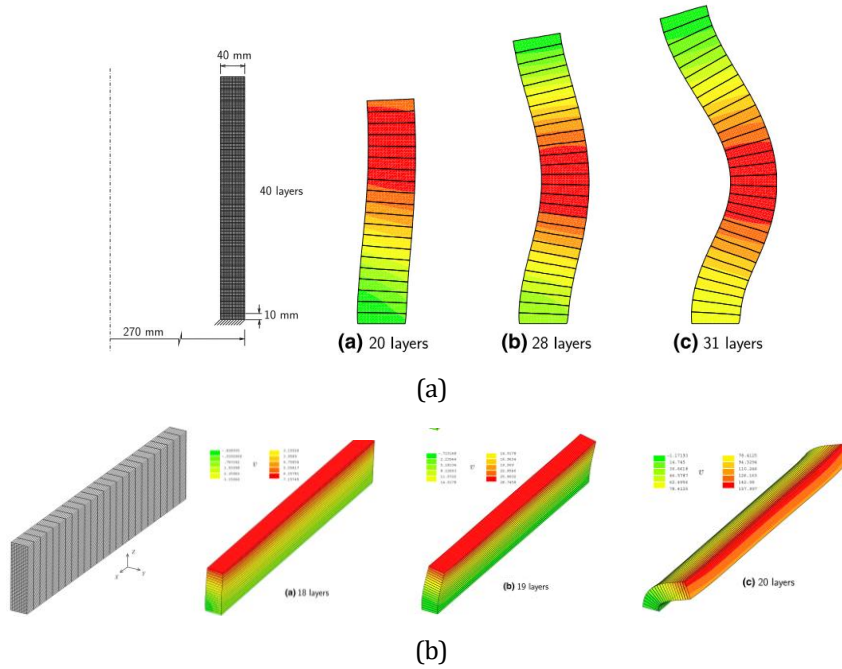


Figure 2-22 Numerical simulations for 3D concrete printing (a) hollow cylinder (b) wall structure [112]

Besides Nedjar's 3D printing model with incremental viscoelasticity, a chemo-mechanical model on the basis of FEM is presented for buildability quantification of 3DCP [109]. This model accounts for several important features of the printable cementitious concrete at a fresh stage, including early-age creep, plasticity and ageing effect due to hydration. In particular, the hydration process of cementitious material after the deposition is described by a modified affinity hydration model. The contribution of this model is to bridge the chemical reaction with structural analysis during printing process.

In addition to FEM-based 3D printing model, Particle Finite Element Method [113] has also been used for layer shape prediction and printing parameters optimization. This method is Lagrangian-based Particle Finite Element Method using a Bingham constitutive model. This approach allowed for the numerical analysis of flow processing simulations with different process and material parameters. Laboratory 3D-printing experiments which measure the layer geometries are used for model validation. The numerical result can be found in Figure 2-23. However, similar to the CFD method, the model has been applied only to the layer deformation prediction not to buildability quantification.

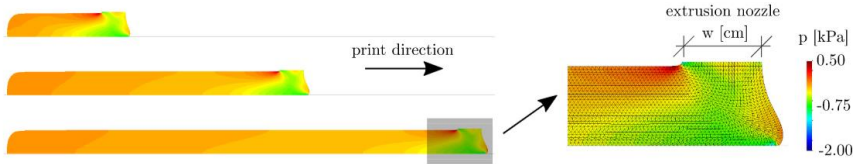


Figure 2-23 Stress distribution of numerical analysis of a single printing layer after material deposition using Particle Finite Element Method [113]

The previous research demonstrate that the 3D printing models listed in Table 2-1, are beneficial tools regarding the prediction of structural deformation and buildability quantification of 3DCP. However, based on the published research, most models simulate extrusion-based 3D printing process. As soon as any point of the printed structure reach the material strength, the structure is considered to have failed. In that way, these models might underestimate the critical printing height of printed structure because the material yielding might only locally occur and the stress-redistribution can happen to ensure the printed structure avoids failure. Additionally, 3DCP is a continuous printing process, in which the gravitational load is gradually applied to the printed system. Thus, non-uniform stress distribution may occur. In addition, the printing material undergoes a layer-by-layer extrusion. A 3D printing process will likely cause the material to have more variable mechanical properties (such as strength and stiffness) compared to casting process [75]. Due to the material variation and non-uniform gravitational loading, some localized damage may occur, thereby affecting structural buildability. However, till now, no method considering these factors is found in the published literature. It is necessary to incorporate the material heterogeneity, non-uniform gravitational loading, localized damage and stress redistribution into 3D printing model for buildability quantification.

In FEM-based model, in order to simulate elastic buckling during printing process, a bifurcation linear buckling analysis is first conducted to get the geometric imperfection. Then, this imperfection is introduced into initial model for non-linear buckling analysis [75]. Consequently, a symmetric mode of buckling failure can be obtained through nonlinear analyses regarding structural stability of wall and rectangular structures. To reproduce the experimentally observed asymmetric buckling failure, a new method with the incorporation of geometric nonlinearity should be developed.

The numerical models based on solid mechanics rely on the assumption that the behaviour of the material is elasto-plastic. This implies that only instantaneous strain is considered during the printing process, while time-dependent deformation is neglected. This delayed deformation is induced by the creep, plastic and autogenous shrinkage, and consolidation settlement under distributed compressive loading and increases with printing time. Herein, the term ‘early-age creep’ is used to describe this time-dependent deformation. In the published research, several early-age creep tests of 3D printable mortar/paste have been performed [114, 115]; experiments indicate

that early-age creep makes for about 7% of the viscoelastic deformation of the tested sample [115]. Therefore, early-age creep needs to be incorporated into 3D printing model to explore its effects on the prediction of structural deformation and the buildability quantification. Further research that investigates the impact of early-age material behaviour, such as plastic and autogenous shrinkage on buildability quantification is recommended.

Table 2-1 Different methodologies for buildability quantification in 3D concrete printing

Theory	Model description	Model application	Limitation	Main contributors	Others
1	Rheology/ Analytical model	Analytical models consider the development of materials properties and printing velocity to estimate structural failure due to plastic collapse while the printing process	Geometry limitation, structural variability	Roussel [29]	[78, 84-87]
	The model proposes several rheological requirements on printable materials considering flocculation-induced thixotropy and chemical reaction			Kruger et al. [88, 92, 96]	
	The model accounts for the re-flocculation and structuration thixotropy mechanisms			Perrort et al. [69]	
2	Solid mechanics/ Analytical model	The model proposes linear and non-linear curing function			
3	CFD /Numerical model	The mechanistic model includes a series of printing parameters for the prediction of elastic buckling and plastic collapse	Geometry limitation, structural variability	Suiker [73, 74]	[78, 116]
4	Solid mechanics/ Numerical model	Computational fluid dynamics models use generalized Newtonian fluid and elastic-viscous-plastic fluid constitutive relationship	Buckling failure, localized damage	R. Comminal et al. [99-101]	[102]
		The relationship between the cross-sectional shape of printing segments and printing parameters, including printing speed, nozzle height, and extrusion force is established			
4	Solid mechanics/ Numerical model	FEM-based numerical models adopt time-dependent elastic-plastic behavior and Mohr-Coulomb criterion	Localized damage, structural failure criterion	Wolfs et al. [71, 72, 75]	[87, 105, 107, 109, 117-119]
		Incremental viscoelasticity at finite strains for the modelling of 3D concrete	Plastic collapse and elastic buckling	Nedjar [112]	[109]

2.5 CONCLUSIONS

This chapter summarizes the basic principles of different stages in 3DCP, which include pumping, extrusion, and building-up process. A review of the current strategies for buildability quantification is given from three aspects, including experimental investigations, analytical modelling and numerical simulations. Based on the presented state of art on methods for buildability quantification of 3DCP, some conclusions can be drawn:

- Experiments and analytical methods for buildability quantification of 3DCP have been proposed in the literature. However, experiments are labour-and-time consuming, while the applicability of analytical models is limited to specific printing geometries.
- Numerical methods have been a promising tool to analyze the structural behaviour during printing process. A reliable numerical model can be utilized to investigate the structural behaviour and optimize the printing parameters and material design. However, there are obvious limitations to current numerical models. Some important factors such as localized damage and stress redistribution are not considered. Therefore, current numerical methods are not accurate enough to predict the structural behaviours of 3DCP in the fresh state. More efforts are needed in the development and improvement of numerical methods for the buildability quantification of 3DCP.
- Due to the simplicity of current 3D printing models, almost all the reviewed models only take the time-dependent stiffness and strength into account for buildability quantification. The time dependent behaviours such as early-age creep and shrinkage may also significantly affect structural buildability and should be analyzed.

In the following chapters, a new 3D printing model based on lattice model will be presented to characterize the structural behaviour of 3DCP during printing process. An experimental program will also be developed to measure the early-age creep behaviour to provide input parameters of this 3D printing model.

REFERENCES

- [1] Gerbert P, Castagnino S, Rothballer C, Renz A, F. R., The transformative power of building information modeling, 2016. March 08).
- [2] B.G. de Soto, I. Agustí-Juan, J. Hunhevicz, S. Joss, K. Graser, G. Habert, B.T. Adey, Productivity of digital fabrication in construction: Cost and time analysis of a robotically built wall, *Automation in construction* 92 (2018) 297-311.
- [3] C. Harty, Implementing innovation in construction: contexts, relative boundedness and actor - network theory, *Construction management and economics* 26(10) (2008) 1029-1041.
- [4] A. Bonoli, S. Zanni, F. Serrano-Bernardo, Sustainability in building and construction within the framework of circular cities and european new green deal. The contribution of concrete recycling, *Sustainability* 13(4) (2021) 2139.
- [5] U.N.D.o. Economic, S.A.P. Division, *World Population Prospects: The 1998 Revision*, United Nations Publications 1999.
- [6] T. Wangler, N. Roussel, F.P. Bos, T.A. Salet, R.J. Flatt, Digital concrete: a review, *Cement and Concrete Research* 123 (2019) 105780.
- [7] R.A. Buswell, W.L. de Silva, S. Jones, J. Dirrenberger, 3D printing using concrete extrusion: A roadmap for research, *Cement and Concrete Research* 112 (2018) 37-49.
- [8] T. Salet, Z. Ahmed, F. Bos, H. Laagland, 3D printed concrete bridge, 3rd International Conference on Progress in Additive Manufacturing, Pro-AM 2018, 2018, pp. 2-9.
- [9] Y. He, Y. Zhang, C. Zhang, H. Zhou, Energy-saving potential of 3D printed concrete building with integrated living wall, *Energy and Buildings* 222 (2020) 110110.
- [10] D. Asprone, F. Auricchio, C. Menna, V. Mercuri, 3D printing of reinforced concrete elements: Technology and design approach, *Construction and Building Materials* 165 (2018) 218-231.
- [11] A. Siddika, M.A.A. Mamun, W. Ferdous, A.K. Saha, R. Alyousef, 3D-printed concrete: Applications, performance, and challenges, *Journal of Sustainable Cement-Based Materials* 9(3) (2020) 127-164.
- [12] S. Pessoa, A.S. Guimarães, S.S. Lucas, N. Simões, 3D printing in the construction industry-A systematic review of the thermal performance in buildings, *Renewable and Sustainable Energy Reviews* 141 (2021) 110794.
- [13] D. Dey, D. Srinivas, B. Panda, P. Suraneni, T. Sitharam, Use of industrial waste materials for 3D printing of sustainable concrete: A review, *Journal of Cleaner Production* (2022) 130749.
- [14] G. Ma, R. Buswell, W.R.L. da Silva, L. Wang, J. Xu, S.Z. Jones, Technology readiness: a global snapshot of 3D concrete printing and the frontiers for development, *Cement and Concrete Research* 156 (2022) 106774.
- [15] M. Batikha, R. Jotangia, M.Y. Baaj, I. Mousleh, 3D concrete printing for sustainable and economical construction: A comparative study, *Automation in Construction* 134 (2022) 104087.
- [16] T. Wangler, R.J. Flatt, First RILEM International Conference on Concrete and Digital Fabrication-Digital Concrete 2018, Springer 2018.
- [17] F.P. Bos, S.S. Lucas, R.J. Wolfs, T.A. Salet, Second RILEM International Conference on Concrete and Digital Fabrication: Digital Concrete 2020, Springer Nature 2020.
- [18] Richard Buswell, Ana Blanco, Sergio Cavalaro, P. Kinnell, Third RILEM International Conference on Concrete and Digital Fabrication, Springer 2022.

- [19] K. Vallurupalli, N. Farzadnia, K.H.J.C. Khayat, C. Composites, Effect of flow behavior and process-induced variations on shape stability of 3D printed elements–A review, (2021) 103952.
- [20] V.N. Nerella, V. Mechtcherine, Studying the printability of fresh concrete for formwork-free concrete onsite 3D printing technology (CONPrint3D), 3D Concrete Printing Technology, Elsevier 2019, pp. 333-347.
- [21] Y.W.D. Tay, Y. Qian, M.J. Tan, Printability region for 3D concrete printing using slump and slump flow test, Composites Part B: Engineering 174 (2019) 106968.
- [22] Y. Zhang, Y. Zhang, W. She, L. Yang, G. Liu, Y. Yang, Rheological and harden properties of the high-thixotropy 3D printing concrete, Construction and Building Materials 201 (2019) 278-285.
- [23] G.H.A. Ting, T.K.N. Quah, J.H. Lim, Y.W.D. Tay, M.J. Tan, Extrudable region parametrical study of 3D printable concrete using recycled glass concrete, Journal of Building Engineering 50 (2022) 104091.
- [24] P. Zhi, Y.-C. Wu, Q. Yang, X. Kong, J. Xiao, Effect of spiral blade geometry on 3D-printed concrete rheological properties and extrudability using discrete event modeling, Automation in Construction 137 (2022) 104199.
- [25] C. Joh, J. Lee, T.Q. Bui, J. Park, I.-H. Yang, Buildability and mechanical properties of 3D printed concrete, Materials 13(21) (2020) 4919.
- [26] V.N. Nerella, M. Krause, V. Mechtcherine, Direct printing test for buildability of 3D-printable concrete considering economic viability, Automation in Construction 109 (2020) 102986.
- [27] B. Panda, N. Mohamed, N. Ahamed, S.C. Paul, G. Bhagath Singh, M.J. Tan, B. Šavija, The effect of material fresh properties and process parameters on buildability and interlayer adhesion of 3D printed concrete, Materials 12(13) (2019) 2149.
- [28] N. Roussel, A thixotropy model for fresh fluid concretes: theory, validation and applications, Cement and Concrete Research 36(10) (2006) 1797-1806.
- [29] N. Roussel, Rheological requirements for printable concretes, Cement and Concrete Research 112 (2018) 76-85.
- [30] D. Feys, How much is bulk concrete sheared during pumping?, Construction and Building Materials 223 (2019) 341-351.
- [31] M. Choi, N. Roussel, Y. Kim, J. Kim, Lubrication layer properties during concrete pumping, Cement and Concrete Research 45 (2013) 69-78.
- [32] S.D. Jo, C.K. Park, J.H. Jeong, S.H. Lee, S.H. Kwon, A computational approach to estimating a lubricating layer in concrete pumping, Computers materials and continua 27(3) (2012) 189.
- [33] G. De Schutter, D. Feys, Pumping of fresh concrete: insights and challenges, RILEM Technical Letters 1 (2016) 76-80.
- [34] D. Feys, K.H. Khayat, R. Khatib, How do concrete rheology, tribology, flow rate and pipe radius influence pumping pressure?, Cement and Concrete Composites 66 (2016) 38-46.
- [35] V. Mechtcherine, F.P. Bos, A. Perrot, W.L. da Silva, V. Nerella, S. Fataei, R.J. Wolfs, M. Sonebi, N. Roussel, Extrusion-based additive manufacturing with cement-based materials–Production steps, processes, and their underlying physics: A review, Cement and Concrete Research 132 (2020) 106037.
- [36] D. Feys, G. De Schutter, K.H. Khayat, R. Verhoeven, Changes in rheology of self-consolidating concrete induced by pumping, Materials and Structures 49(11) (2016) 4657-4677.
- [37] N. Roussel, G. Ovarlez, S. Garrault, C. Brumaud, The origins of thixotropy of fresh cement pastes, Cement and Concrete Research 42(1) (2012) 148-157.

- [38] M. Choi, K. Park, T. Oh, Viscoelastic properties of fresh cement paste to study the flow behavior, *International Journal of Concrete Structures and Materials* 10(3) (2016) 65-74.
- [39] D. Kaplan, F. de Larrard, T. Sedran, Design of concrete pumping circuit, *ACI materials journal* 102(2) (2005) 110.
- [40] J. Vosahlik, K.A. Riding, D. Feys, W. Lindquist, L. Keller, S. Van Zetten, B. Schulz, Concrete pumping and its effect on the air void system, *Materials and Structures* 51(4) (2018) 1-15.
- [41] A. Das, Y. Song, S. Mantellato, T. Wangler, R.J. Flatt, D.A. Lange, Influence of pumping/extrusion on the air-void system of 3D printed concrete, *RILEM International Conference on Concrete and Digital Fabrication*, Springer, 2020, pp. 417-427.
- [42] V. Nerella, M. Näther, A. Iqbal, M. Butler, V. Mechtcherine, Inline quantification of extrudability of cementitious materials for digital construction, *Cement and Concrete Composites* 95 (2019) 260-270.
- [43] A. Perrot, D. Rangeard, V.N. Nerella, V. Mechtcherine, Extrusion of cement-based materials-an overview, *RILEM Technical Letters* 3 (2018) 91-97.
- [44] M.K. Mohan, A. Rahul, G. De Schutter, K. Van Tittelboom, Extrusion-based concrete 3D printing from a material perspective: A state-of-the-art review, *Cement and Concrete Composites* 115 (2021) 103855.
- [45] X. Cao, S. Yu, H. Cui, Z. Li, 3D Printing Devices and Reinforcing Techniques for Extruded Cement-Based Materials: A Review, *Buildings* 12(4) (2022) 453.
- [46] K. El Cheikh, S. Rémond, N. Khalil, G. Aouad, Numerical and experimental studies of aggregate blocking in mortar extrusion, *Construction and Building Materials* 145 (2017) 452-463.
- [47] B. Panda, G.B. Singh, C. Unluer, M.J. Tan, Synthesis and characterization of one-part geopolymers for extrusion based 3D concrete printing, *Journal of cleaner production* 220 (2019) 610-619.
- [48] L. Hass, F. Bos, Bending and pull-out tests on a novel screw type reinforcement for extrusion-based 3D printed concrete, *RILEM International Conference on Concrete and Digital Fabrication*, Springer, 2020, pp. 632-645.
- [49] J. Sanjayan, R. Jayatilakage, P. Rajeev, Vibration induced active rheology control for 3D concrete printing, *Cement and Concrete Research* 140 (2021) 106293.
- [50] J.H. Jo, B.W. Jo, W. Cho, J.-H. Kim, Development of a 3D printer for concrete structures: laboratory testing of cementitious materials, *International Journal of Concrete Structures and Materials* 14(1) (2020) 1-11.
- [51] N. Roussel, J. Spangenberg, J. Wallevik, R. Wolfs, Numerical simulations of concrete processing: from standard formative casting to additive manufacturing, *Cement and Concrete Research* 135 (2020) 106075.
- [52] R. Wolfs, Experimental characterization and numerical modelling of 3D printed concrete: controlling structural behaviour in the fresh and hardened state, *Eindhoven University of Technology*, 2019.
- [53] A. Kazemian, X. Yuan, O. Davtalab, B. Khoshnevis, Computer vision for real-time extrusion quality monitoring and control in robotic construction, *Automation in Construction* 101 (2019) 92-98.
- [54] V. Mechtcherine, A. Michel, M. Liebscher, T. Schmeier, Extrusion-based additive manufacturing with carbon reinforced concrete: Concept and feasibility study, *Materials* 13(11) (2020) 2568.

- [55] Y. Tao, A. Rahul, K. Lesage, Y. Yuan, K. Van Tittelboom, G. De Schutter, Stiffening control of cement-based materials using accelerators in inline mixing processes: possibilities and challenges, *Cement and Concrete Composites* 119 (2021) 103972.
- [56] Y. Tao, A. Rahul, M.K. Mohan, K. Van Tittelboom, Y. Yuan, G. De Schutter, Blending performance of helical static mixer used for twin-pipe 3D concrete printing, *Cement and Concrete Composites* 134 (2022) 104741.
- [57] Y. Tao, M.K. Mohan, A. Rahul, Y. Yuan, G. De Schutter, K. Van Tittelboom, Stiffening controllable concrete modified with redispersible polymer powder for twin-pipe printing, *Cement and Concrete Research* 161 (2022) 106953.
- [58] L. Reiter, T. Wangler, A. Anton, R.J. Flatt, Setting on demand for digital concrete—principles, measurements, chemistry, validation, *Cement and Concrete Research* 132 (2020) 106047.
- [59] C. Maltese, C. Pistolesi, A. Bravo, F. Cella, T. Cerulli, D. Salvioni, A case history: Effect of moisture on the setting behaviour of a Portland cement reacting with an alkali-free accelerator, *Cement and Concrete Research* 37(6) (2007) 856-865.
- [60] J. Zhang, S. Xu, W. Li, High shear mixers: A review of typical applications and studies on power draw, flow pattern, energy dissipation and transfer properties, *Chemical Engineering and Processing: Process Intensification* 57 (2012) 25-41.
- [61] R. Thakur, C. Vial, K. Nigam, E. Nauman, G. Djelveh, Static mixers in the process industries—a review, *Chemical engineering research and design* 81(7) (2003) 787-826.
- [62] D. Rauline, J.-M. Le Blévec, J. Bousquet, P. Tanguy, A comparative assessment of the performance of the Kenics and SMX static mixers, *Chemical Engineering Research and Design* 78(3) (2000) 389-396.
- [63] F. Bos, R. Wolfs, Z. Ahmed, T. Salet, Additive manufacturing of concrete in construction: potentials and challenges of 3D concrete printing, *Virtual and Physical Prototyping* 11(3) (2016) 209-225.
- [64] A. Perrot, A. Pierre, V. Nerella, R. Wolfs, E. Keita, S. Nair, N. Neithalath, N. Roussel, Mechtcherine, From analytical methods to numerical simulations: A process engineering toolbox for 3D concrete printing, *Cement and Concrete Composites* 122 (2021) 104164.
- [65] C.D. Ghent, Elastic buckling vs plastic collapse in concrete printing, Youtube, https://www.youtube.com/watch?v=2FdIRk_79x4&t=1s, 2020.
- [66] L. Reiter, T. Wangler, N. Roussel, R.J. Flatt, The role of early age structural build-up in digital fabrication with concrete, *Cement and Concrete Research* 112 (2018) 86-95.
- [67] W.R. Leal da Silva, H. Fryda, J.-N. Bousseau, P.-A. Andreani, T.J. Andersen, Evaluation of early-age concrete structural build-up for 3D concrete printing by oscillatory rheometry, *International Conference on Applied Human Factors and Ergonomics*, Springer, 2019, pp. 35-47.
- [68] M. Chen, L. Yang, Y. Zheng, Y. Huang, L. Li, P. Zhao, S. Wang, L. Lu, X. Cheng, Yield stress and thixotropy control of 3D-printed calcium sulfoaluminate cement composites with metakaolin related to structural build-up, *Construction and Building Materials* 252 (2020) 119090.
- [69] A. Perrot, D. Rangeard, A. Pierre, Structural built-up of cement-based materials used for 3D-printing extrusion techniques, *Materials and Structures* 49(4) (2016) 1213-1220.
- [70] T.T. Le, S.A. Austin, S. Lim, R.A. Buswell, A.G. Gibb, T. Thorpe, Mix design and fresh properties for high-performance printing concrete, *Materials and structures* 45(8) (2012) 1221-1232.
- [71] R. Wolfs, F. Bos, T. Salet, Early age mechanical behaviour of 3D printed concrete: Numerical modelling and experimental testing, *Cement and Concrete Research* 106 (2018) 103-116.

- [72] R. Wolfs, A. Suiker, Structural failure during extrusion-based 3D printing processes, *The International Journal of Advanced Manufacturing Technology* 104(1-4) (2019) 565-584.
- [73] A.S. Suiker, R.J. Wolfs, S.M. Lucas, T.A. Salet, Elastic buckling and plastic collapse during 3D concrete printing, *Cement and Concrete Research* 135 (2020) 106016.
- [74] A.S.J. Suiker, Mechanical performance of wall structures in 3D printing processes: Theory, design tools and experiments, *International Journal of Mechanical Sciences* 137 (2018) 145-170.
- [75] R. Wolfs, F. Bos, T.J.C. Salet, Triaxial compression testing on early age concrete for numerical analysis of 3D concrete printing, *Cement and Concrete Composites* 104 (2019) 103344.
- [76] L. Casagrande, L. Esposito, C. Menna, D. Asprone, F. Auricchio, Effect of testing procedures on buildability properties of 3D-printable concrete, *Construction and Building Materials* 245 (2020) 118286.
- [77] B. Panda, M.J. Tan, Experimental study on mix proportion and fresh properties of fly ash based geopolymers for 3D concrete printing, *Ceramics International* 44(9) (2018) 10258-10265.
- [78] T. Di Carlo, B. Khoshnevis, A. Carlson, Experimental and numerical techniques to characterize structural properties of fresh concrete, *ASME International Mechanical Engineering Congress and Exposition*, American Society of Mechanical Engineers, 2013, p. V009T10A062.
- [79] A. Kazemian, X. Yuan, E. Cochran, B. Khoshnevis, Cementitious materials for construction-scale 3D printing: Laboratory testing of fresh printing mixture, *Construction and Building Materials* 145 (2017) 639-647.
- [80] B. Panda, S.C. Paul, N.A.N. Mohamed, Y.W.D. Tay, M.J. Tan, Measurement of tensile bond strength of 3D printed geopolymer mortar, *Measurement* 113 (2018) 108-116.
- [81] S.C. Paul, Y.W.D. Tay, B. Panda, M.J. Tan, Fresh and hardened properties of 3D printable cementitious materials for building and construction, *Archives of Civil and Mechanical Engineering* 18(1) (2018) 311-319.
- [82] A. Perrot, A. Pierre, S. Vitaloni, V. Picandet, Prediction of lateral form pressure exerted by concrete at low casting rates, *Materials and Structures* 48(7) (2015) 2315-2322.
- [83] T. Lecompte, A. Perrot, Non-linear modeling of yield stress increase due to SCC structural build-up at rest, *Cement and Concrete Research* 92 (2017) 92-97.
- [84] F.A. Cardoso, V.M. John, R.G. Pileggi, Rheological behavior of mortars under different squeezing rates, *Cement and Concrete Research* 39(9) (2009) 748-753.
- [85] M. Chen, L. Li, Y. Zheng, P. Zhao, L. Lu, X. Cheng, Rheological and mechanical properties of admixtures modified 3D printing sulphoaluminate cementitious materials, *Construction and Building Materials* 189 (2018) 601-611.
- [86] H. Jeong, S.-J. Han, S.-H. Choi, Y.J. Lee, S.T. Yi, K.S. Kim, Rheological property criteria for buildable 3D printing concrete, *Materials* 12(4) (2019) 657.
- [87] R. Jayathilakage, J. Sanjayan, P. Rajeev, Direct shear test for the assessment of rheological parameters of concrete for 3D printing applications, *Materials and Structures* 52(1) (2019) 1-13.
- [88] J. Kruger, S. Zeranka, G.J.C. van Zijl, B. Materials, An ab initio approach for thixotropy characterisation of (nanoparticle-infused) 3D printable concrete, 224 (2019) 372-386.
- [89] J. Kruger, S. Zeranka, G.J.A.i.C. van Zijl, 3D concrete printing: a lower bound analytical model for buildability performance quantification, 106 (2019) 102904.
- [90] J. Kruger, A. du Plessis, G. van Zijl, An investigation into the porosity of extrusion-based 3D printed concrete, *Additive Manufacturing* 37 (2021) 101740.

- [91] J. Kruger, M. van den Heever, S. Cho, S. Zeranka, G. van Zijl, High-performance 3D printable concrete enhanced with nanomaterials, *Proceedings of the International Conference on Sustainable Materials, Systems and Structures: New Generation of Construction Materials*, RILEM Publications SARL Rovinj, Croatia, 2019, pp. 533-540.
- [92] J. Kruger, S. Zeranka, G. van Zijl, 3D concrete printing: a lower bound analytical model for buildability performance quantification, *Automation in Construction* 106 (2019) 102904.
- [93] J. Kruger, S. Zeranka, G. van Zijl, An ab initio approach for thixotropy characterisation of (nanoparticle-infused) 3D printable concrete, *Construction and Building Materials* 224 (2019) 372-386.
- [94] T. Wangler, E. Lloret, L. Reiter, N. Hack, F. Gramazio, M. Kohler, M. Bernhard, B. Dillenburger, J. Buchli, N. Roussel, Digital concrete: opportunities and challenges, *RILEM Technical Letters* 1 (2016) 67-75.
- [95] B. Panda, C. Unluer, M.J. Tan, Investigation of the rheology and strength of geopolymer mixtures for extrusion-based 3D printing, *Cement and Concrete Composites* 94 (2018) 307-314.
- [96] J. Kruger, S. Zeranka, G. van Zijl, Quantifying constructability performance of 3D concrete printing via rheology-based analytical models, *Rheology and Processing of Construction Materials*, Springer 2019, pp. 400-408.
- [97] M. Briffaut, F. Benboudjema, J.-M. Torrenti, G. Nahas, Concrete early age basic creep: Experiments and test of rheological modelling approaches, *Construction and Building Materials* 36 (2012) 373-380.
- [98] Y. Qian, S. Kawashima, Use of creep recovery protocol to measure static yield stress and structural rebuilding of fresh cement pastes, *Cement and Concrete Research* 90 (2016) 73-79.
- [99] M.T. Mollah, R. Comminal, M.P. Serdeczny, D.B. Pedersen, J. Spangenberg, Stability and deformations of deposited layers in material extrusion additive manufacturing, *Additive Manufacturing* (2021) 102193.
- [100] M.P. Serdeczny, R. Comminal, D.B. Pedersen, J. Spangenberg, Numerical simulations of the mesostructure formation in material extrusion additive manufacturing, *Additive Manufacturing* 28 (2019) 419-429.
- [101] R. Comminal, W.R.L. da Silva, T.J. Andersen, H. Stang, J. Spangenberg, Modelling of 3D concrete printing based on computational fluid dynamics, *Cement and Concrete Research* 138 (2020) 106256.
- [102] R.J. Wolfs, T.A. Salet, N. Roussel, Filament geometry control in extrusion-based additive manufacturing of concrete: The good, the bad and the ugly, *Cement and Concrete Research* 150 (2021) 106615.
- [103] R. Comminal, M.P. Serdeczny, N. Ranjbar, M. Mehrli, D.B. Pedersen, H. Stang, J. Spangenberg, Modelling of material deposition in big area additive manufacturing and 3D concrete printing, *Joint Special Interest Group Meeting between Euspen and ASPE Advancing Precision in Additive Manufacturing, The European Society for Precision Engineering and Nanotechnology* (2019) 151-154.
- [104] C.D. Ghent, Numerical simulation of 3D concrete printing processes, 2019.
- [105] T. Ooms, G. Vantghem, R. Van Coile, W. De Corte, A parametric modelling strategy for the numerical simulation of 3D concrete printing with complex geometries, *Additive Manufacturing* 38 (2021) 101743.
- [106] G. Vantghem, T. Ooms, W. De Corte, FEM modelling techniques for simulation of 3D concrete printing, *arXiv preprint arXiv:06907* (2020).

- [107] G. Vantighem, T. Ooms, W. De Corte, VoxelPrint: A Grasshopper plug-in for voxel-based numerical simulation of concrete printing, *Automation in Construction* 122 (2021) 103469.
- [108] V. Nguyen-Van, B. Panda, G. Zhang, H. Nguyen-Xuan, P. Tran, Digital design computing and modelling for 3-D concrete printing, *Automation in Construction* 123 (2021) 103529.
- [109] Q. Wang, X. Ren, J. Li, A Chemo-Mechanical Model for Predicting the Buildability of 3d Printed Concrete, Available at SSRN 4147420.
- [110] Z. Chang, Y. Xu, Y. Chen, Y. Gan, E. Schlangen, B. Šavija, A discrete lattice model for assessment of buildability performance of 3D - printed concrete, *Computer - Aided Civil Infrastructure Engineering* 36(5) (2021) 638-655.
- [111] B. Nedjar, On a geometrically nonlinear incremental formulation for the modeling of 3D concrete printing, *Mechanics Research Communications* 116 (2021) 103748.
- [112] B. Nedjar, Incremental viscoelasticity at finite strains for the modelling of 3D concrete printing, *Computational Mechanics* 69(1) (2022) 233-243.
- [113] J. Reinold, V.N. Nerella, V. Mechtcherine, G. Meschke, Extrusion process simulation and layer shape prediction during 3D-concrete-printing using the Particle Finite Element Method, *Automation in Construction* 136 (2022) 104173.
- [114] Y. Chen, Z. Li, S. Chaves Figueiredo, O. Çopuroğlu, F. Veer, E. Schlangen, Limestone and Calcined Clay-Based Sustainable Cementitious Materials for 3D Concrete Printing: A Fundamental Study of Extrudability and Early-Age Strength Development, *Applied Sciences* 9(9) (2019) 1809.
- [115] L. Esposito, L. Casagrande, C. Menna, D. Asprone, F. Auricchio, Early-age creep behaviour of 3D printable mortars: Experimental characterisation and analytical modelling, *Materials and Structures* 54(6) (2021) 1-16.
- [116] B. Panda, J.H. Lim, M.J. Tan, Mechanical properties and deformation behaviour of early age concrete in the context of digital construction, *Composites Part B: Engineering* 165 (2019) 563-571.
- [117] R. Jayathilakage, P. Rajeev, J. Sanjayan, Extrusion rheometer for 3D concrete printing, *Cement and Concrete Composites* 121 (2021) 104075.
- [118] R. Jayathilakage, P. Rajeev, J. Sanjayan, Yield stress criteria to assess the buildability of 3D concrete printing, *Construction and Building Materials* 240 (2020) 117989.
- [119] M. Mengesha, A. Schmidt, L. Göbel, T. Lahmer, Numerical Modeling of an Extrusion-Based 3D Concrete Printing Process Considering a Spatially Varying Pseudo-Density Approach, *RILEM International Conference on Concrete and Digital Fabrication*, Springer, 2020, pp. 323-332.

3. A DISCRETE LATTICE MODEL FOR ASSESSMENT OF BUILDABILITY PERFORMANCE OF 3D PRINTED CONCRETE

In this chapter, a discrete lattice beam model is adjusted to study the printing process and quantify the buildability of 3D concrete printing. This model simulates structural failure by incorporating the element birth technique, time-dependent development of stiffness and strength, printing velocity, non-uniform gravitational load and localized damage of the printed object. Using this model, parametric analyses on non-uniform gravitational load and randomly distributed material properties are first conducted to assess their impact on the failure-deformation response and the critical printing height. Then, two 3D printing experiments (i.e., a hollow cylinder and a square wall layout) from the literature are adopted for model validation. Modelling of the printed structures reproduces the correct failure-deformation modes, but the quantitative agreement on the buildability could be improved. Possible reasons for the quantitative discrepancy are discussed in the end.

3.1 INTRODUCTION

In extrusion-based 3D concrete printing, the cementitious materials are extruded from the nozzle to build a computer-designed object using a robotic arm. After deposition, the material should be strong enough to retain the shape and avoid collapse under self-weight and the gravitational load from subsequent printing layers. Considering the 3D printing is a continuous process, the non-uniform stress distribution, material heterogeneity and structural localized damage might affect the structural buildability. However, no published approaches [1-5] have taken these effects into account.

To investigate the above-mentioned factors on buildability quantification, this chapter adjusts the discrete lattice model to quantify the structural buildability. In this numerical model, a new failure criterion is proposed and adopted for buildability quantification. To mimic the continuous printing process, the element birth technique is adopted and utilized for investigating the influence of non-uniform gravitational load. Besides, the randomly distributed material properties (i.e., stiffness and strength) are assigning to different lattice elements based on the Gauss distribution. Their quantitative impact on critical printing height is analyzed and a typical plastic collapse failure mode can be reproduced. This numerical analysis demonstrates the feasibility of discrete lattice for assessment of buildability performance of 3D printed concrete.

3.2 MODEL OVERVIEW

An overview of the numerical approach based on the lattice model is presented in Figure 3-1, which comprises six branches. In the flowchart, k and K stand for the local and global stiffness matrix, respectively. T is the transformation matrix used to relate local and global coordinate systems. L and D are the global load vector and displacement vector, respectively.

Branch A: Establish a numerical model for 3DCP. The details are given in Section 3.2.1 to Section 3.2.8.

Branch B: Assemble the global stiffness matrix K , the load vector L and displacement vector D based on the current printing time. When reaching the pre-determined printing time, the corresponding printing pieces are activated and the inner elements within these activated printing pieces are then assigned with age-dependent stiffness and strength.

Branch C: Calculate the nodal forces. After the printing pieces activation, the self-weight of these parts and the boundary conditions (as indicated in Section 3.2.5) are applied to the current system. Then, a conjugate gradient solution procedure is utilized for displacement solution; the parallel computation is employed to improve the computing efficiency and enable the modelling of a large lattice system.

Branch D: Update the analysis model and check the system stability. Through the conjugate gradient solution, nodal displacements are found and used to determine stresses in the lattice elements. Afterwards, all critical elements (i.e., those reaching the compressive/tensile strength) are removed from the lattice mesh. The removal of these elements stands for localized damage during the printing process. The solution procedure within this time step repeats until no additional elements rupture and the system stabilizes. Eventually, the system state is regarded as a failure when reaching the pre-determined system failure criterion. The structural failure criterion can be found in Section 3.2.7.

Branch E: Output the system displacement and localized damage.

Branch F: Describe the system failure criterion, as stated in Section 3.2.8.

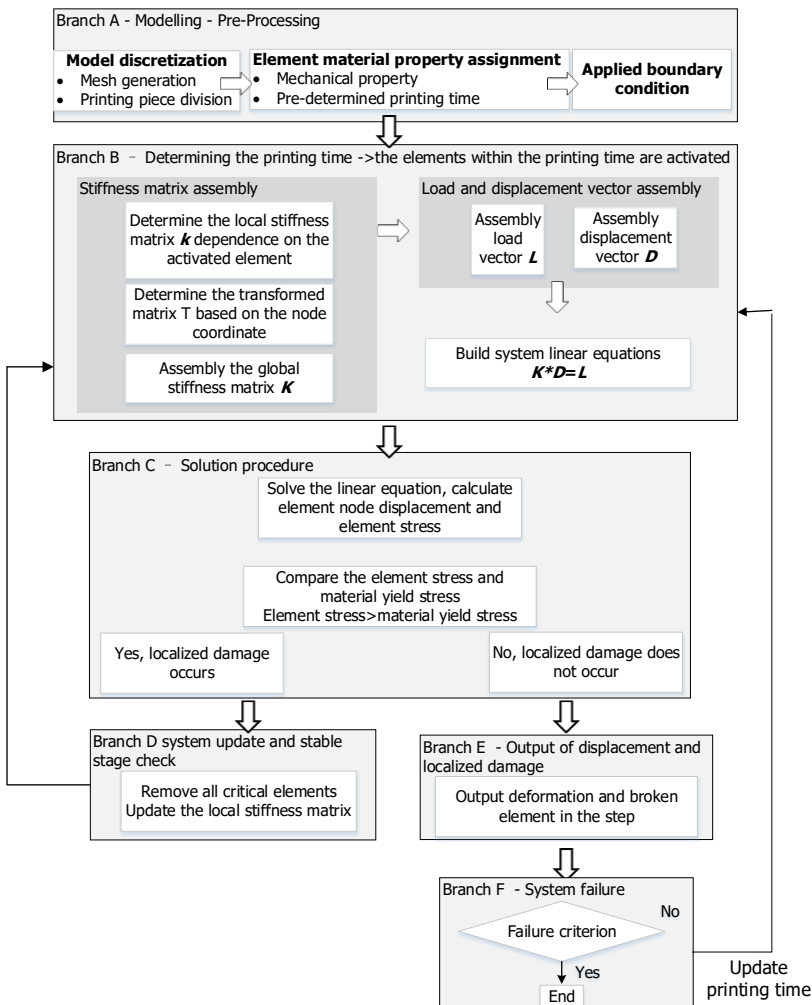


Figure 3-1 A general procedure for simulating the concrete 3D printing process using the lattice model

3.2.1 Model Establishment

In the lattice model, the continuum object is represented by a lattice mesh. When establishing a numerical model such as that of a cylindrical structure, the cubical domain is first divided into a number of cubic cells, representative of the continuum system. Then, sub-cells are generated in the middle of each cell. Nodes are then randomly positioned within each sub-cell using a pseudorandom number generator [6]. The ratio between the length of the sub-cell and the cell is defined as the mesh randomness, the representative of the mesh disorder. Considering that printable cementitious materials are not completely isotropic, the randomly distributed material properties are mimicked through irregularities of the network geometry [6-9]. Based on our previous research, randomness of 0.2 is adopted in this study to avoid large variations in lengths of individual lattice elements [10]. As soon as the lattice nodes are generated in the cubical domain (as shown in Figure 3-2 (a)), the target printed object is then established in this domain, as indicated in Figure 3-2 (b). After that, the nodes within the printed object are retained for model discretization while the outside nodes are deleted, as shown in Figure 3-2 (c).

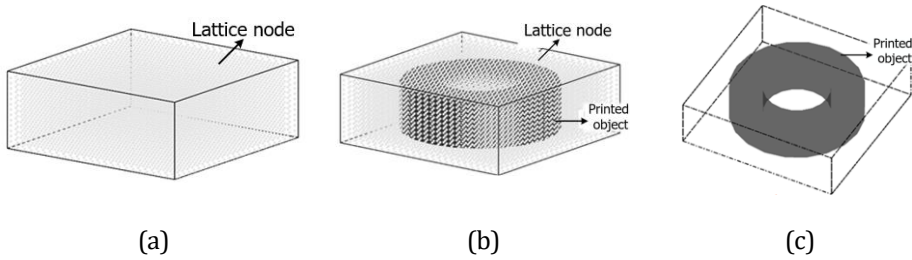


Figure 3-2 Schematic view of lattice model establishment (a) lattice nodes in the cubical domain (b) printed object mapping (c) final printed object

3.2.2 Model Discretization

After the model establishment, the target object can be defined using a set of lattice nodes. Employing these lattice nodes, the printed structure is discretized as a network of beam elements. An example of model discretization is shown in Figure 3-3 (a). Delaunay triangulation is then performed to establish the node connectivity [11].

A 3D printed object is manufactured by a layer-by-layer printing process. In this numerical model, the printed object comprises a series of layers, representative of the continuous printing process (as shown in Figure 3-3 (b)). To account for the non-uniform gravitational load that occurs during the printing of a single layer, each layer is subsequently divided into a series of printing pieces (as shown in Figure 3-3 (c)). Regarding the interface between different printing pieces, tie constraint is utilized, which means that different printing pieces share the same nodes and there is no relative motion between two neighboring pieces.

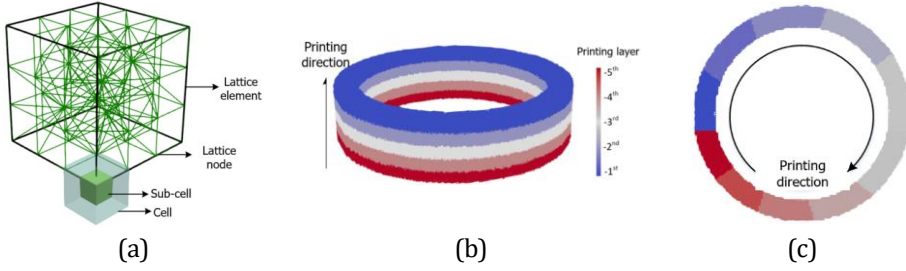


Figure 3-3 (a) Schematic view of lattice model generation (b) Schematic view of printing object with different printing layers [cubic cell number: 25000] (c) diagram on printing sequence for each layer [cubic cell number: 5000]

3.2.3 Element Birth Technique

The continuous printing process is simulated using the element birth technique, in which elements are activated according to the printing time. Each element has an initial time t_0 less than zero and this initial time is determined by the element's location in printed system. This initial time for the specific element can be derived based on

$$t_0 = \frac{-\Delta d}{v} \quad \text{Eq. 3-1}$$

where the Δd represents the placement distance to the starting point of the printed structure; and v is the printing velocity.

During the printing process, the element-time label t increases by an incremental time step. Once the current printing time t is more than zero for a given printing segment, the elements representing that segment are activated.

3.2.4 Properties Of Lattice Elements

Since the ratio between the length and cross-section of the lattice beam is generally low in the lattice network, Timoshenko beam elements are utilized to account for the shear deformation. To simulate the development of the mechanical properties in time due to hydration, the lattice beams are assigned time-dependent stiffness and strength properties. The development of mechanical properties can be derived from experiments such as compression tests, direct shear tests [12] and triaxial compression tests [13]. At present, two types of relations have been proposed in the literature to account for the development of mechanical properties of printable concretes at a very early age: a linear relationship [12-16] and an exponentially-decaying relationship between the strength/stiffness and curing time [2, 14, 17, 18]. In principle, both types of relations can be incorporated into the lattice model to define the stiffness and strength development in time.

3.2.5 Non-Uniform Gravitational Load

In the 3D printing process, the material strength competes with the gradual increasing load, codetermining the buildability performance. In principle, little is known about the actual loads acting on the object during printing [19]. The most significant load is certainly the self-weight, the magnitude of which can be established relatively easily. However, the effects of the kinematic pressure from the filament deposition and non-uniform gravitational load caused by the deposition process have not been quantitatively studied.

In general, the non-uniform gravitational load is ascribed to the continuous printing process during the printing period of a single layer. Since printing is a continuous process, the deadweight loading for the newly printed layer is gradually transferred into the whole system, resulting in the non-uniform loading force in the vertical direction. Consequently, this non-uniform gravitational load may threaten the overall stability of the object being printed, allowing fewer layers to be printed than otherwise expected. However, this influence has not been studied in any of the previous prediction models [5, 12, 20-23]. To account for the continuous printing process, each printing layer is divided into several sequential printing pieces (as indicated in Figure 3-4). In the numerical analysis, the value and position of system gravity are associated with the number of activated printing pieces. Thus, the influence of non-uniform gravitational load can be investigated through the number of printing pieces, as shown in Section 3.2.5.

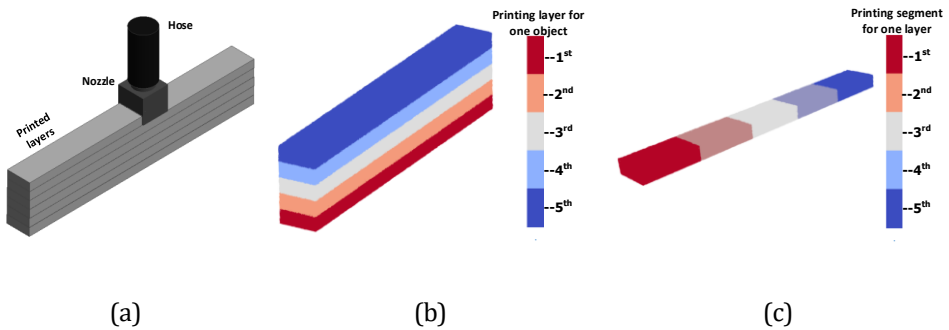


Figure 3-4 (a) Schematic view of 3D printing object with sequence printing (b) 3D printing model in lattice (c) layer division

In the lattice model, the structure heterogeneity is taken into account from two aspects, namely, model discretization and randomly distributed material properties. The model discretization, as described in Sections 3.2.3 and 3.2.4, generates randomly distributed lattice nodes that are connected by beam elements with different lengths and orientations. These parameters introduce geometric heterogeneity into the system. For 3DCP, the gravitational load is applied to the system as nodal forces. As beforementioned, the continuum system is discretized by a series of lattice nodes connected by the Timoshenko beams using the Delaunay triangulation. Given that the Voronoi tessellation is used to partition the domain, the volume of each Voronoi cell is used to assess the self-weight load for the corresponding nodal force [24], as shown in

Figure 3-5. This volume can then be used to determine the equivalent gravitational force acting on each node in the mesh as:

$$f = V \times \rho \times g \quad \text{Eq. 3-2}$$

where the f represents the nodal force; V and ρ are the nodal volume and unit weight of the material, respectively; g is gravity acceleration ($g \approx 9.8 \text{ m/s}^2$).

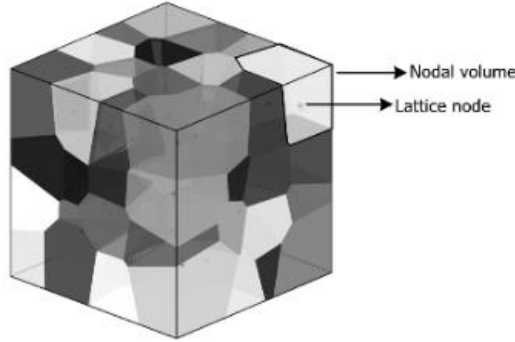


Figure 3-5 Voronoi diagram for a given set of nodes within a cubic domain

3.2.6 Element Failure Criterion

As discussed before, the printing object is discretized by a series of lattice beams. Herein, the removal of lattice beams is utilized to account for localized damage that occurs during the additive manufacturing process. Again, in 3DCP, two competing parameters determine whether an object can be successfully printed or not. Specifically, the increasing strength and stiffness need to keep up with the gradually increasing load as more layers are deposited from the nozzle. The former can be incorporated into the lattice model through the development of mechanical properties in time and the latter can be reflected via the incremental load in each step. Subjected to non-uniform gravitational load and boundary conditions, linear elastic calculations are performed to determine the stress distribution within the lattice mesh. The element failure criterion, consisting of normal force and bending moment determines the critical element and is given as:

$$\sigma = \alpha_N \frac{F}{A} + \alpha_M \frac{(|M_i|, |M_j|)_{\max}}{W} \quad \text{Eq. 3-3}$$

$$\sigma_{\text{yield}} \leq \sigma$$

Here, F is the normal force in the lattice beam element; M_i and M_j stand for the bending moments in the local coordinate system; and σ_{yield} stands for the material yield stress. Specifically, a lattice element is assumed to break in compression or tension in accordance with the maximal stress theory, where the limiting stresses are represented by the uniaxial compressive and tensile strengths [14, 20]. A is the element cross-sectional area, and W is the section modulus ($W = \pi D^3/32$, where D is

the effective diameter of the lattice element). The coefficients α_N and α_M are the normal force factor and the bending influence factor, which control the degrees to which normal force and bending moment govern the failure mode. The value for α_N is commonly adopted as 1.0 [25-27], and the α_M value is set to 0.05 in agreement with the literature [6, 10, 26, 28-30].

3.2.7 Structural Failure Criterion

In previous 3D printing models [12, 20], the structure is considered to have failed when any point of the printed object has reached the material yielding. This failure criterion may be reasonable for a homogeneous system under uniform loading. Under non-uniform loading, however, the point reaching the yield strength generally causes only localized damage instead of system failure. The printed structure may still be able to retain the shape and allow for the printing process to continue since some stress redistribution could occur. Therefore, this kind of failure criterion may underestimate the buildability performance under the complex printing geometry or the non-uniform gravitational loading.

To accurately model the printing process and quantify the buildability, a different structural failure criterion should be established. In 3DCP experiments, the structures usually fail because of the system instability or material yielding. This means that a relatively large offset occurs between the new printing layer and the designed position. As a consequence, the next printing layer cannot be placed into the printed system. Even if the object somehow does not collapse, such excessive deformation may be considered a 'failure' when the aim is to print a predefined geometry, since the printing process is usually pre-programmed and does not correct for such deviations. In this numerical model, failure occurs when the lateral offset of a layer surpasses the width of an individual layer (i.e., when the next printing layer fails to find a position to be placed into the printed system), as indicated in Figure 3-6. This printing process stops since the structure has reached the maximum printing height.

Regarding a point in the structure reaching the limiting stress in tension or compression, the corresponding element will be removed from the printed object, representative of the localized damage during the printing process. Such local damage is typically accompanied by stress redistribution, which allows for the printing process to continue. In other words, by modeling failure as an incremental process, rather than as a single event, the critical printing height is less likely to be underestimated.

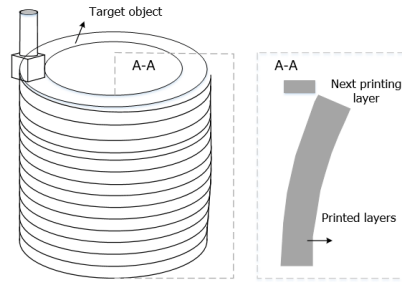


Figure 3-6 Structural failure for 3DCP due to large offset of the top layer

3.2.8 Failure Mode

Due to the absence of moulds, the object may collapse during the printing process. A model must be able to capture the typical failure modes to quantify buildability performance. Herein, using the lattice model, plastic collapse results from the accumulation of local damage in the lower layers, as depicted in Figure 3-7. The details related to the calibration of input parameters and experimental validation are given in the next section.

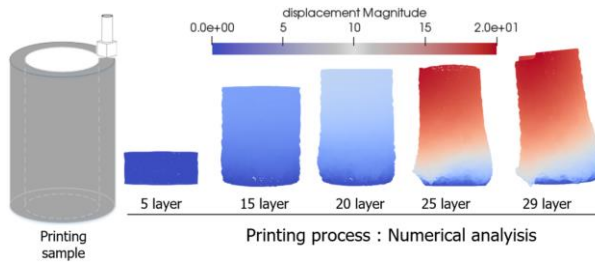


Figure 3-7 Plastic collapse dominant failure mode for 3D printing. The plotted greyscale indicates the displacement magnitude (unit: mm)

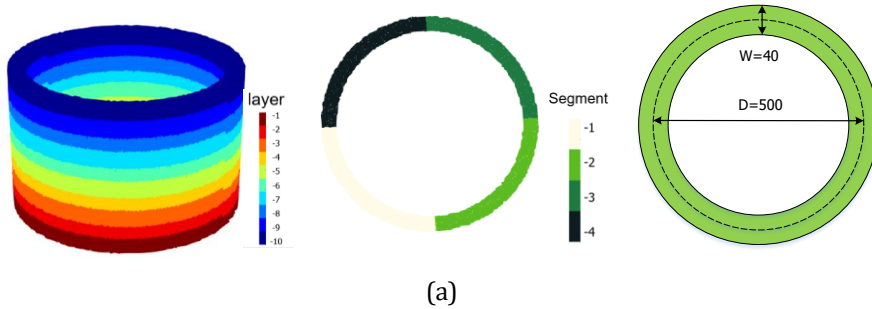
3.2.9 Model Applicability

In this model, the solution procedure is based on the lattice beam model with the assumption of the linear elastic theory and small deformation. In practical applications of concrete 3D printing, the onset of elastic buckling or plastic collapse is the only thing that matters in a 3D printing experiment. Once the system fails, excessive deformation will occur. In that sense, large deformation is not relevant for predicting the critical printing height. Some structures, such as the wall geometry, are sensitive to elastic buckling. For these structures, geometric nonlinearity plays a significant role in buildability quantification since even a small offset can introduce significant stress in the structure. Other geometries usually fail due to material yielding. This chapter focuses on the plastic collapse dominant failure mode with a relatively short printing time. The second-order effects are not considered, and structural instability due to the loss of geometry (e.g., elastic buckling) will be studied in Chapter 5.

In addition to mechanical analysis, in practice, the process of 3DCP is influenced by hydro-thermal phenomena through a combination of cement hydration (and associated heat development and cooling), shrinkage (autogenous, plastic and drying) and viscoelastic deformation (creep). All of these factors may, to a certain extent, influence the buildability quantification, especially for cases with long printing time. The influence of most of these factors has not yet been experimentally studied and is poorly understood. The present model can therefore be seen as an initial processing step for buildability performance quantification. Extensive investigations on the aforementioned factors are beyond the scope of this chapter and will be studied in the following chapters.

3.3 NUMERICAL ANALYSES

The experimental validation of the lattice model for buildability quantification is performed by simulating two printing geometries (see Figure 3-8) using two types of materials, namely, Figure 3-8 (a) a cylindrical geometry with material model A and Figure 3-8 (b) a square structure with material model B. The 3DCP numerical analyses are performed in three steps using the lattice model. First, the computational uniaxial compression tests are carried out for calibration of the time-dependent stiffness and strength. Then, two printing parameters including the non-uniform gravitational load and randomly distributed material properties are quantitatively analyzed to study their impact on the printing characteristics, namely the critical printing height and failure mode. On the basis of these parametric analyses and calibrated time-dependent material properties, two 3D printing numerical campaigns are carried out for model validation, in which the derived printing characteristics are compared with experimental results from the literature.



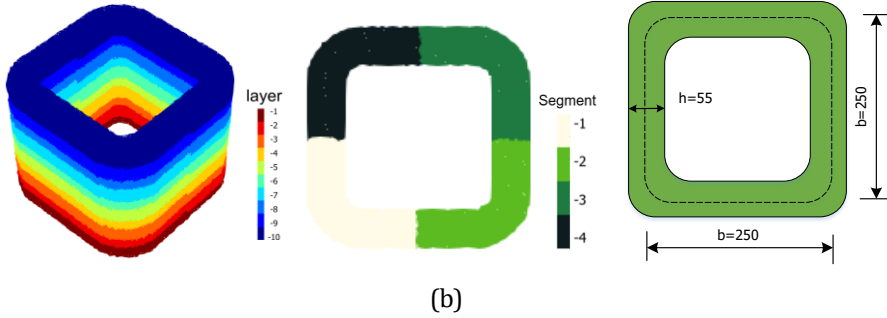


Figure 3-8 Dimensions of the printing objects (a) cylinder structure (b) square structure. The rounding radius for the corners of the square structure is 50 mm. (unit: mm)

3.3.1 Computational Uniaxial Compression Test

In this section, the unconfined uniaxial compression tests (UUCT) are simulated to calibrate the time-dependent stiffness and strength of lattice elements. As previously noted, two types of printable materials are considered. Material model A is regarded as the case study to demonstrate the detailed steps for parameter calibration.

During the 3D printing process, cementitious materials undergo a transition from a fluid-like stage to a solid-like stage at an early age. The development of yield stress (static yield stress to be more precise) can be regarded as the transition between these two stages. When it comes to buildability performance, the material is actually in the transition process, in which the cement hydration continues, impacting the physical and rheological behavior. To be specific, when the material stress reaches the yield stress, the hydrate bridges between percolated cement particles break and they flow. As a consequence, the printable materials display a viscous behaviour and the shear rate is proportional to dynamic yield stress based on the plastic viscosity. [4, 21, 31, 32]. Once the structure reaches the critical weight load, it will collapse. In such a “load-controlled” situation, further stress redistribution within the whole system is not possible, as explained by [14]. It can be concluded that the yield stress plays a dominant role in the final printing characteristics. Therefore, in the initial stage of this model developed in this chapter, the local post-peak behavior is not considered: only the material yield stress and elastic modulus are considered for the buildability performance quantification.

Regarding the determination of material properties at different curing times, five computational uniaxial compressive tests from the literature [12] are simulated to determine the properties of lattice elements to reflect the time-dependent material properties. In the experiment, the printable material is cast into steel cylindrical molds and undergoes a compaction process three times on a 30 Hz vibration table for a homogeneous sample realization. Then, cylindrical samples with a diameter of 70 mm and a height of 140 mm are loaded through an INSTRON setup in which a Teflon sheet is placed on both sides of the specimen to minimize the friction at the supports. The

corresponding mechanical properties for fresh concrete at $t=0, 15, 30, 60$, and 90 min are tested.

Because the printable material subjected to the uniaxial compression test undergoes a compaction process, a homogeneous sample with increased strength and stiffness and decreased compressibility is achieved, as explained by [12]. For the computational uniaxial compression test, a numerical model of a cylinder structure with the same size as the experimental specimen is created. Considering the computational time and accuracy, a cell size of 5 mm is selected in the numerical campaign. The model in UUCT consists of 4317 nodes and 30614 Timoshenko beam elements. Considering the low friction support condition in the experiments, radial deformation of the top and bottom boundary conditions is free. Nodal displacements on one side are applied and the opposite side is fixed, as shown in Figure 3-9.

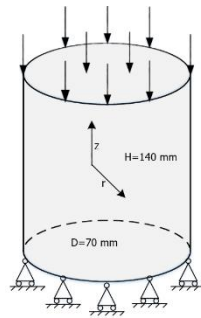


Figure 3-9 Computational compressive test. Loading is applied in the z -direction

In the lattice model, there are four input parameters that determine the material properties: elastic modulus, shear modulus, compressive strength, and tensile strength. The compressive strength is assumed to be 10 times higher than tensile strength considering the fact that the cementitious materials have a higher resistance to compressive loading than tensile loading [33, 34]. Concerning the calibration process, Young's modulus can be computed dependent on the initial slope of the curve, and the compressive strength is calibrated based on the peak load. The detailed calibration process is based on the previously published research on hardened cementitious materials and may need to be reassessed in the future [10].

After calibration, the time-dependent stiffness and strength used in the lattice model are listed in Figure 3-10. Note that, in general, the local mechanical properties of the individual lattice element differ from the global ones [35]. For example, the lattice element mechanical properties with the compressive strength equal to 10.96 kPa , elastic modulus equal to 77.9 kPa are calibrated by the computational uniaxial compression test in 0 min . The derived Young's modulus and compressive strength are compared to the experimental data, see Figure 3-10. In the literature, two types of "curing" functions have been proposed for describing the development of early age mechanical properties of 3DCP: linear curing and exponentially-decaying curing

functions [14, 17]. Here, the linear function is adopted for the material properties calibration based on the previous research [12]. The development of the time-dependent strength and stiffness within the first 90-min can be determined as indicated by the black solid lines shown in Figure 3-10 and the R^2 values are calculated through the linear regression function and the average experimental results on different concrete stages.

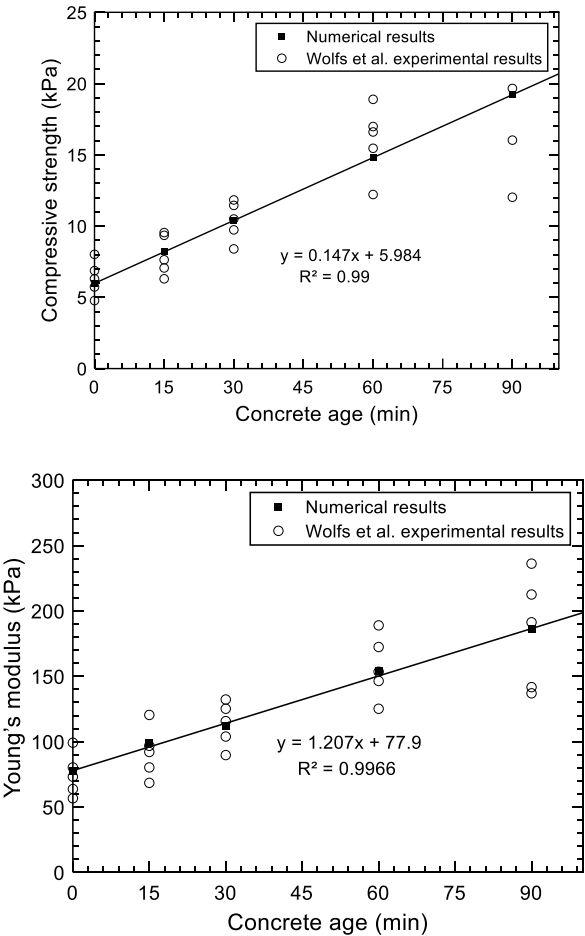


Figure 3-10 Comparison between the experimental and numerical result of the compression test for material model A, with concrete age 0 to 90min [12]

Table 3-1 Calibrated lattice element parameters for material model A with a range of time 0 to 90 min

Local mechanical properties of individual element			Computational uniaxial compression test	
Concrete	Elastic	Compressive	Elastic	Compressive

age (min)	modulus (kPa)	strength (kPa)	modulus (kPa)	strength (kPa)
0	77.9	10.96	77.9	5.98
15	99.0	15.01	99.0	8.19
30	111.7	19.04	111.7	10.39
60	154.0	27.12	154.0	14.80
90	186.0	35.21	186.0	19.21

The time-dependent stiffness and strength for lattice elements are described using the following linear relation,

$$\begin{aligned} E^A(t) &= 77.9 + 1.21 \cdot t \\ f_c^A(t) &= 10.96 + 0.27 \cdot t \end{aligned} \quad \text{Eq. 3-4}$$

$$\begin{aligned} E^B(t) &= 48.56 + 2.61 \cdot t \\ f_c^B(t) &= 5.2 + 0.6 \cdot t \end{aligned} \quad \text{Eq. 3-5}$$

where E represents Young's modulus [kPa], which affects the elastic deformation; f_c stands for the material compressive strength [kPa] and t is curing time within 90 minutes; the superscripts A and B stand for the material type.

3.3.2 Parametric Analyses

As mentioned in Section 3.3.1, the cylinder specimen for UUCT underwent a compaction process [12]. This vibration process reduces the local porosity, breaks the material internal structure, and promotes the re-flocculation and structuration process, thereby probably resulting in a (relatively) homogeneous sample with higher material strength compared to the one in the 3D printing process. The material in the 3D printing process goes through a pump and is extruded through a hose and a nozzle which may also result in higher local porosity [36]. Consequently, the material subjected to a 3D printing process will probably have lower mechanical properties (i.e., strength, stiffness) and larger variations in randomly distributed material properties. Thus, considering the variability of material properties may therefore be crucial for realistic buildability quantification of 3DCP. Besides, as discussed in Section 3.2.3 and Section 3.2.5, the continuous printing process in the experiment leads to the non-uniform gravitational load to the structure. This type of loading condition leads to localized damage, which may eventually result in structural failure.

In the following sections, the influence of non-uniform gravitational load and randomly distributed material properties are investigated for buildability quantification.

3.3.2.1 Non-uniform Gravitational Load

In this section, the impact of non-uniform gravitational load on the printing characteristics and geometry will be quantitatively analyzed. Two kinds of geometries under various non-uniform gravitational load scenarios (see

Table 3-3) are analyzed. For the numerical analysis, each printing layer is divided into several printing pieces, which stands for the continuous printing process in the experiment and reflects the influence of non-uniform gravitational load, as explained in Section 3.2.5. Here, seven numerical models with a different number of printing pieces and geometries are established to study their impact on the printing characteristics, and the corresponding input parameters can be found in Table 3-2 Input parameters for the numerical analyses on non-uniform gravitational load. The model with a number equal to 1 means that one layer is added into the system in each step, while the model with a piece number equal to 10 will divide one layer into 10 sequential pieces to print. Note that the high friction at the bottom is applied as a boundary condition.

Table 3-2 Input parameters for the numerical analyses on non-uniform gravitational load

geometry	Parameter	Value
Cylinder	Density	2070 kg·m ⁻³
	Diameter	500 mm
	Layer thickness	40 mm
	Layer height	10 mm
	Randomness	0.2
	Cell size	5 mm
	Printing time per layer	18.6 s
	Material model	A
Square	Density	2100 kg·m ⁻³
	Side length	250 mm
	Layer thickness	55 mm
	Layer height	10 mm
	Randomness	0.2
	Cell size	5 mm
	Printing time per layer	9.6 s
	Material model	B

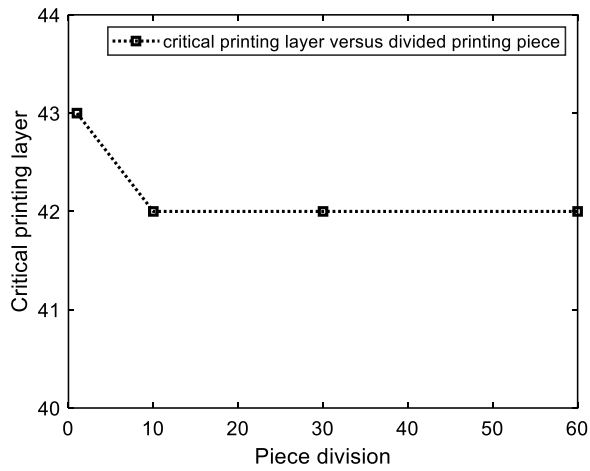
Table 3-3 Numerical models for non-uniform gravitational load investigation

Model	Geometry	Number of printing pieces per layer	Printing time per piece (s)
1	Cylinder	1	18.6
2		10	1.86
3		30	0.62
4		60	0.31
5	Square	1	9.6

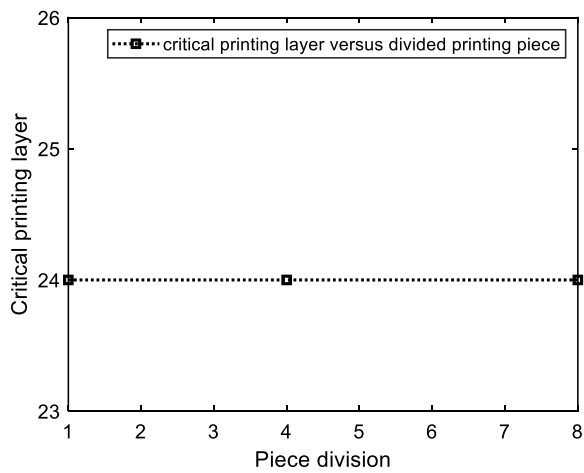
6	4	2.4
7	8	1.2

Figure 3-11 provides the critical printing height for two kinds of printing geometries. It can be illustrated from a that the non-uniform gravitational load decreases the number of printing layers at failure for the cylinder structure. The critical printing height converges to a stable value by increasing the number of printing pieces. On the other hand, the non-uniform gravitational load plays a negligible influence on the square wall layout as shown in Figure 3-11 (b). Regarding the failure mechanism, the non-uniform gravitational load may reduce the critical printing height due to the uneven displacement of each layer. Specifically, the non-uniform gravitational load introduces uneven stress in each layer, leading to localized damage to the structure. On the other hand, the model with more printing pieces updates the system mechanical property in a finer time step, as a consequence, stronger loading capacity for each layer is accompanied. These two opposing factors codetermine the critical printing height. Which one plays a more significant role depends on the printing geometry, the printing time and mechanical properties development. Based on this numerical analysis, it is observed that the non-uniform gravitational load influences the critical height for the model with a relatively low printing speed or the numerical campaign with a relatively large size while the non-uniform loading hardly affects the printing critical height for the objects with fast printing speed and small printing size.

Figure 3-12 shows the ultimate global failure related to the influence of non-uniform gravitational load, clearly showing that non-uniform gravitational load influences the final failure mode. For the model under uniform gravitational load, namely model 1 and model 5, the system deforms in an axial-symmetric way. In contrast, the failure zone in all models subjected to non-uniform loading arises from the non-uniform stress distribution to the structure, resulting in non-uniform deformation per layer. Consequently, the radial deformation in the top area increases, such that the next printing layer may fail to be placed on the system within the printing accuracy.



(a)



(b)

Figure 3-11 Relation between the printing divisions per layer and printing characteristics (a) cylinder geometry (b) square wall layout

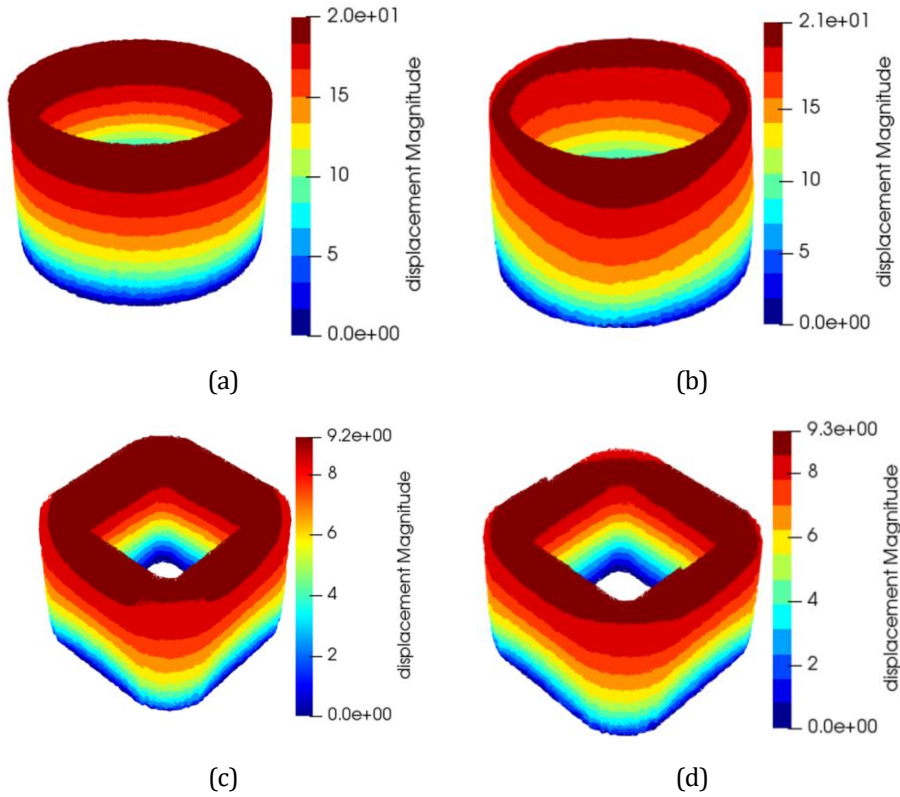


Figure 3-12 Failure mode for 3D printing simulation with non-uniform gravitational load influence (unit: mm) (a) Model 1 (b) Model 2 (c) Model 5 (d) Model 6

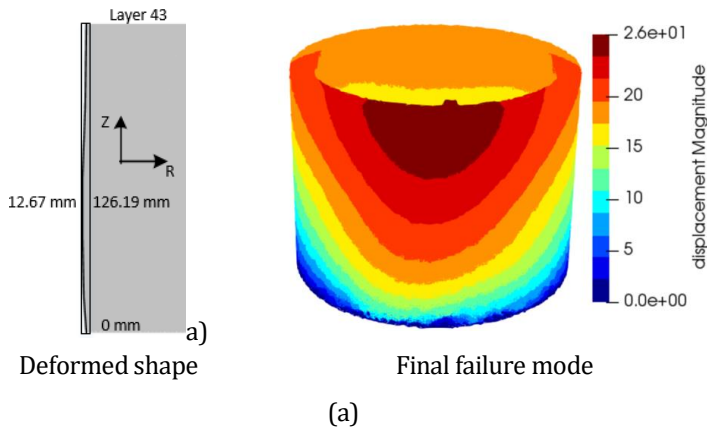
3.3.2.2 Randomly Distributed Material Properties

As mentioned before, two methods are used to introduce spatial variability within the printed system: random placement of the lattice nodes (within each sub-cell) and random assignment of the material properties using Gaussian distributions. Due to the nature of the printing process, variability of the material properties might be high, yet this phenomenon remains scarcely investigated. Although investigations regarding the effects of vibration on early age concrete have been performed [37, 38], they mainly focused on the 7 d or 28 d material strength influenced by the vibration. Some studies do provide information about the strength measured 24 hours after casting, but this is far beyond the timeframe of a concrete 3D printing process [39].

Herein, randomly distributed material properties are introduced into the 3D printing model. Specifically, the beam elements have compressive/tensile strength values that are randomly determined from a Gaussian distribution (with an average value of 10.96 kPa for the case of compressive strength at $t = 0$ s). This is an effective means for assessing the potential influence of material heterogeneity, in lieu of more advanced representations of material heterogeneity. Although the value of Young's

modulus should correlate with strength, it is taken as constant herein at a given printing time for single variable comparison. Two standard deviation values, i.e., 2 kPa and 3 kPa, are chosen for qualitatively evaluating the effect of randomly distributed material properties on the buildability performance of 3D printing. During the printing process, the compressive strength and Young's modulus increase with the printing time following the growth rate given by Equation (4). For the material strength distribution, compressive strength is assumed to be 10 times greater than tensile strength for each element, as discussed before. Note that, concerning the Gaussian distribution, a limited number of elements should be assigned with negative strength values, which is not physically possible. Therefore, those elements are removed from the mesh prior to the analysis.

Two numerical analyses of the hollow cylinder are performed with the same loading and boundary conditions as described in Section 3.3.1. Figure 3-13 shows the maximum radial displacement and the ultimate failure-deformation mode for these two examples before failure. It can be concluded that allowing for disorder in the lattice system, in terms of strength variation, reduces the number of layers that can be printed. To be specific, heterogeneous material behavior leads to the non-uniform displacement for the same layer under self-weight. Some points of the target object reach their strength limits producing localized damage. The accumulation of localized damage leads to extensive deformation, progressive collapse, and eventually system failure. Increasing the standard deviation of strength reduces the achievable printing height. Introducing strength variations also produces a more asymmetric failure mode relative to that of the homogeneous model. It can be stated that, in practice, the printing process should aim to ensure a homogeneous material deposition (e.g., in terms of density and porosity) to maximize buildability.



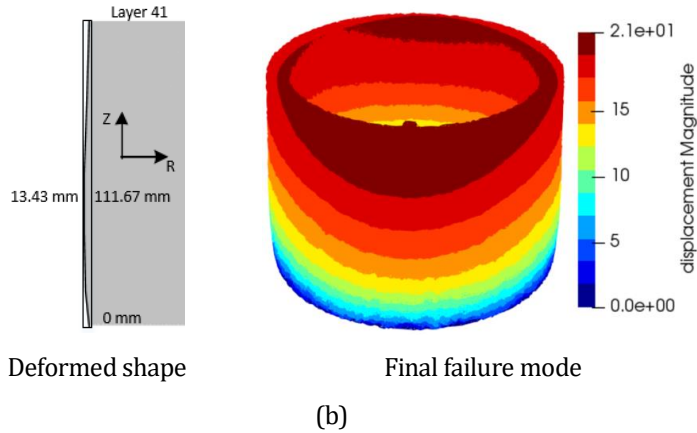


Figure 3-13 Failure-deformation and final failure modes for differing material strength distributions (a) model with standard deviation value of 2 kPa (b) model with standard deviation value of 3 kPa [unit: mm]

3.3.3 Model Validation

In this section, two 3D printing experimental campaigns, namely, a cylinder and a square structure, are modeled employing the lattice model for buildability quantification, as indicated in Figure 3-8.

3.3.3.1 Cylinder Geometry

A cylinder structure with a diameter of 500 mm, a thickness of 40 mm, and a layer height of 10 mm is modeled to quantify buildability performance. The details about cylinder geometry can be found in Figure 3-8 (a) and Table 3-2. The numerical model is in line with the specimen in the trial printing [12], as indicated in Figure 3-14a. In the numerical program, each layer is subdivided into 60 pieces for sequential printing reflecting the non-uniform gravitational load during the printing process. The interface between the different pieces is modeled using tie constraint, as described in Section 2.2. The computational printing process advances until structural failure. More specifically, as soon as the linear elastic calculation fails to converge, the next printing piece in the numerical analysis cannot be placed due to the excessive deformation, as described in Section 2.7. The time interval between two layers is set to 0.31 min, determined by the printing speed in the experimental campaign. The development of material stiffness and strength depends on the age of the printing piece. For example, after the placement of 5 layers, the initial printing piece in the first layer is 1.55 min old and the corresponding mechanical properties are assigned to this piece, while the current printing piece is assigned the initial mechanical properties (i.e., those corresponding to $t = 0$ min). In the UUCT [12], the printable materials show a standard deviation value equal to 1.07 kPa for UUCT. Based on this global standard deviation, a standard deviation of 1.96 kPa for the lattice elements can be derived and this value is adopted in this numerical analysis.

In the 3D printing model, the cell size is set to 5 mm, the same as the computational unconfined uniaxial compression test. Using the same cell size can eliminate the influence of element size on the material properties. Each layer consists of 5000 nodes connected by around 360000 beam elements. Concerning the boundary condition, the bottom layer is fixed to model the high frictional resistance of the printing bed, corresponding to the conditions of the experiment [12]. The relevant gravitational load with the average material density of 2070 kg/m^3 is calculated by employing Equation (2).

Figure 3-14 shows the maximum structural deformation affiliated with the printing process and ultimate global failure. Specifically, the final failure-deformation is affected by the lateral restraint in the radial direction and increasing non-uniform gravitational load. The stepwise addition of printing pieces causes eccentric loading, introducing bending moment to the system. The element stresses increase under loading, such that the randomly assigned strength values are exceeded at some locations, causing localized damage. This localized damage negatively affects the structural stability and significantly governs the critical printing height. Eventually, the system fails at the 41st printing layer, with the radial deformation equal to 14.42 mm, which occurs at the corresponding z position of 115.36 mm.

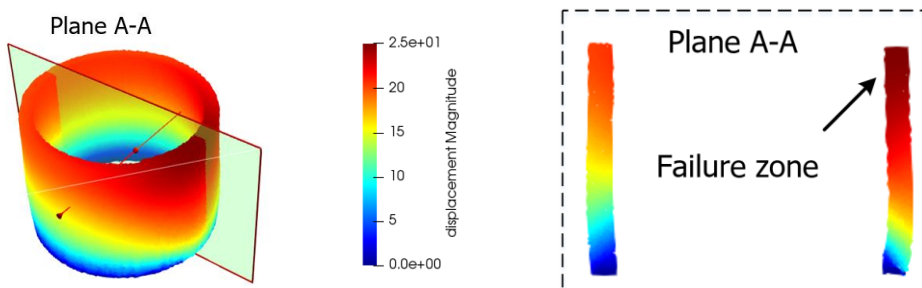


Figure 3-14 Failure-deformation mode during the printing process (unit: mm)

Figure 3-15 shows the relation between the radial deformation and corresponding position in the z-direction, clearly showing a gradual increase of radial deformation as more layers are printed. The model with a total of 41 filament layers is successfully printed with a total building height of around 410 mm within 12.71 min. Concerning the printing process, excessive deformation occurs when placing 41st layer and the system eventually collapses after the placement of the 42nd layer. The excessive radial deformation of the top area at the layer 41 stage is noticeable, demonstrating that the current printing layer cannot be placed in the pre-determined position. Thus, the object fails to ensure the printing quality and meet printing accuracy due to the excessive deformation in the top zone therefore the 41st layer is regarded as the critical printing height. The maximum radial deformation and the corresponding z position are derived from the stage before the system collapse (i.e., layer 41). The final failure mode is dominated by the accumulation of damage leading to plastic collapse.

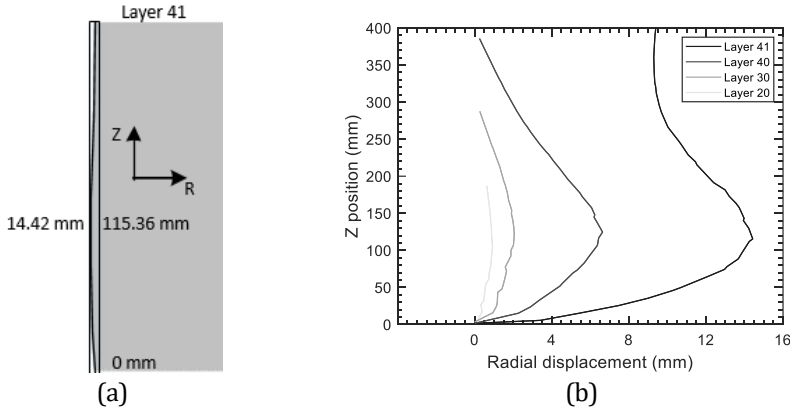


Figure 3-15 Lattice model results deformed shape of cylinders (a) final deformed shape (b) deformed shape after the placement of different printing layers

Table 3-4 gives a comparison of the final printing characterizations between the newly developed lattice model, and the FEM and experimental result from the literature [12]. The average number of 41 layers derived from the lattice model overestimates the experimental findings for critical printing height (29 layers) by 41.38%. The numerical average radial deformation before failure is equal to 14.42, which yields a relative difference below 1% with the experimental values. The corresponding z position is 115.36 mm, which differs from the experimental result by less than 6%.

There is good general agreement between the results presented herein and those of the FE model employed by [12]. In particular, both sets of results overestimate the critical printing height, but provide accurate estimates of maximum radial displacement and the height at which it occurs. This agreement is remarkable considering the large fundamental differences between the modeling approaches.

The fact that both, differing modeling approaches overestimate the critical printing height suggests that there are aspects of the printing process that are underappreciated. The remaining discrepancy between the lattice model results and experimental data might be that the numerical analysis ignores extra loading from updated structural deformation; besides, the influence of manufacturing imperfections in the printing process is also another possibility. Since the failure of cylindrical structures is notoriously sensitive to imperfections in geometry [40-42], the initial imperfections or the defection caused by the additional loading may decrease the critical printing height due to similar forms of structural instability. To obtain a better quantitative agreement result on buildability, a different algorithm which can reflect the impact of non-equilibrium force due to the updated system will be developed in Chapter 4.

Furthermore, experimental techniques are needed for determining the in-situ properties of the printed materials. The use herein of UUCT data, obtained from specimens that were consolidated through vibration, may be another source of error.

Table 3-4 The overview of printing characterizations between the current lattice model and previous simulations and experiments

Parameter		Layer value	Relative error
Critical printing height	Experiment	29	--
	Wolfs et al.	46	58.62%
	Lattice	41	41.38%
Max radial deformation (mm)	Experiment	15.3	--
	Wolfs et al.	13.89	10.87%
	Lattice	14.42	5.75%
Z position of max radial deformation (mm)	Experiment	114.7	--
	Wolfs et al.	115.8	1%
	Lattice	115.36	<1%

3.3.3.2 Square Structure

In this section, a relatively small square wall structure with the layer width equal to 250 mm and a corner radius of 50 mm, is simulated for model validation and buildability quantification. Additional information about this model can be found in Figure 3-8 (b) and Table 3-2.

In the numerical campaign, the bottom layer is fixed to correspond with the high friction on the print bed [20]. The time to place one layer is set to 9.6s, determined by the printing speed in the experimental campaign. Each layer consists of around 4300 nodes, connected by around 31000 lattice beams; each layer is divided into four printing pieces, which enables representation of the non-uniform gravitational load. The time-dependent material stiffness and strength are described using Equation (5): material model B. The nodal force is calculated based on the average material density of 2100 kg.m^{-3} employing Equation (2).

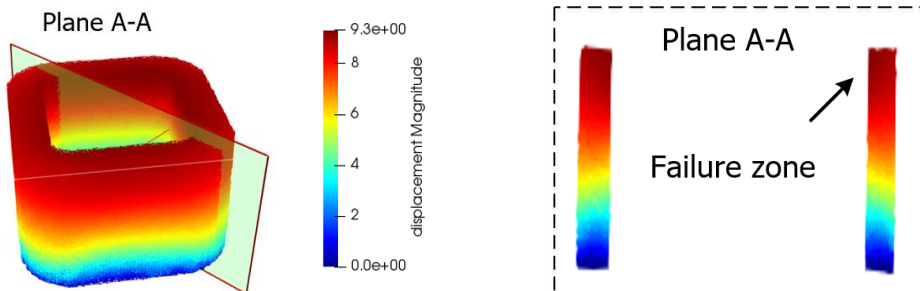


Figure 3-16 Final failure mode for square wall layout (unit: mm) (a) Final failure mode (b) localized damage

Figure 3-16 shows the failure-deformation mode and the localized damage in-plane A-A. A comparison with experimental data is given in Table 3-5. As for the analyses of the cylindric structure, under the gradually increasing gravity load, the lattice elements eventually exceed the material strength, causing localized damage in the printed object. This kind of damage negatively affects the structural stability and governs the critical number of printing layers. Eventually, the system fails at the printing of the 24th layer because of the accumulation of damage in the bottom layer. The lattice model is verified via comparison with the experimental results of Suiker et al [20]. With respect to critical printing height, there is a relative difference of around 10% (Table 3-5), which is smaller than the relative difference observed for the cylinder structure. The square layout might be less sensitive to imperfections generated by the printing process, but this possibility will be further studied in Chapter 4.

Table 3-5 Number of layers at plastic collapse for square wall layout

Parameter		Value	Relative error
Critical printing height	Experiment	218.5 mm	--
	Lattice	240 mm	9.84 %

3.4 CONCLUSIONS

In this chapter, the lattice model is adopted to quantify the buildability of 3DCP. This model, incorporating an element birth technique, the time-dependent nature of the mechanical properties, printing velocity, non-uniform gravitational load and localized damage of the printed object, is able to reproduce the plastic collapse failure modes reported in the literature. Using this model, computational uniaxial compression tests are first conducted to calibrate the time-dependent material stiffness and strength in the range of 0 to 90 min. Thereafter, parametric analyses regarding the non-uniform gravitational load and randomly distributed material properties are conducted to evaluate their impact on printing characteristics, including the failure-deformation response and critical printing height. Based on the calibrated material properties and parametric analyses results, the model is finally validated by comparison with two well-documented 3D printing experiments from the literature. The main conclusions are summarized below.

A new failure criterion for buildability quantification is proposed and applied in the numerical model. Failure of the system is assumed to occur when the next printing layer fails to be placed on the current printed system. This failure criterion allows for the occurrence and accumulation of localized damage. Relative to single event, stress-based failure criteria, the proposed criterion provides a more realistic measure of critical printing height.

In the 3DCP numerical analysis, structural heterogeneity of the printed object can be approximated in two ways. Firstly, the random positioning of nodes within the

sub-cells produces an irregular lattice. This leads to nonuniform stresses in the elements even under uniform loading. Secondly, the strength properties of the lattice elements are randomly assigned, according to a Gaussian distribution, to mimic the material heterogeneity. A higher standard deviation value causes a lower critical printing height based on the parametric analysis results.

By means of the element birth technique, the continuous printing process can be simulated realistically. The quantitative influence of non-uniform gravitation load can be reflected through the number of segments for each layer. The non-uniform gravitational load influenced the critical printing height of the cylindrical model, which was relatively large in size and constructed with relatively low printing velocity. The effect of non-uniform loading affected less the critical printing height of the square structure.

Lattice modeling of the square structure and cylinder structure produce the correct failure-deformation patterns and quantitative agreement with experimental data with respect to critical printing height and maximum lateral displacement of the printed structure.

In this chapter, a new numerical method is proposed to quantify the buildability of 3DCP. Compared with current published numerical and analytical models, this present lattice model is the first that studies the impact of localized damage, non-uniform gravitational loading and randomly distributed material properties for buildability quantification. It can be seen as an intermediate step toward accurate buildability quantification.

However, the lattice model results are comparable to those of the FE models. The tendency for all models to overestimate the critical printing height suggests there are aspects of the printing process, which requires further study. According to the newly published research [20], the additional force due to deformed geometry and related imperfection during the printing process may be a neglected factor in the current numerical models. A potential solution is to incorporate an incremental method as this algorithm can compute the non-equilibrium force caused by structure deformation. Using this method, the imperfection that occurred during the printing process can be simulated and the quantitative agreement is possible be improved. This is further explored in chapter 4.

REFERENCES

- [1] R. Wolfs, Experimental characterization and numerical modelling of 3D printed concrete: controlling structural behaviour in the fresh and hardened state, Eindhoven University of Technology, 2019.
- [2] T. Wangler, E. Lloret, L. Reiter, N. Hack, F. Gramazio, M. Kohler, M. Bernhard, B. Dillenburger, J. Buchli, N. Roussel, Digital concrete: opportunities and challenges, RILEM Technical Letters 1 (2016) 67-75.
- [3] T. Di Carlo, B. Khoshnevis, A. Carlson, Experimental and numerical techniques to characterize structural properties of fresh concrete, ASME International Mechanical Engineering Congress and Exposition, American Society of Mechanical Engineers, 2013, p. V009T10A062.
- [4] N. Roussel, Rheological requirements for printable concretes, Cement and Concrete Research 112 (2018) 76-85.
- [5] J. Kruger, S. Zeranka, G. van Zijl, 3D concrete printing: A lower bound analytical model for buildability performance quantification, Automation in Construction 106 (2019) 102904.
- [6] Z. Qian, Multiscale modeling of fracture processes in cementitious materials, Delft University of Technology, Delft, The Netherlands, 2012.
- [7] S. Berton, J.E. Bolander, Crack band model of fracture in irregular lattices, Computer Methods in Applied Mechanics and Engineering 195(52) (2006) 7172-7181.
- [8] J.E. Bolander, N. Sukumar, Irregular lattice model for quasistatic crack propagation, Physical Review B 71(9) (2005) 094106.
- [9] H. Zhang, B. Šavija, E. Schlangen, Combined experimental and numerical study on micro-cube indentation splitting test of cement paste, Engineering Fracture Mechanics 199 (2018) 773-786.
- [10] Z. Chang, H. Zhang, E. Schlangen, B. Šavija, Lattice Fracture Model for Concrete Fracture Revisited: Calibration and Validation, Applied Sciences 10(14) (2020) 4822.
- [11] M. Yip, J. Mohle, J. Bolander, Automated modeling of three - dimensional structural components using irregular lattices, Computer - Aided Civil Infrastructure Engineering 20(6) (2005) 393-407.
- [12] R. Wolfs, F. Bos, T. Salet, Early age mechanical behaviour of 3D printed concrete: Numerical modelling and experimental testing, Cement and Concrete Research 106 (2018) 103-116.
- [13] R. Wolfs, F. Bos, T. Salet, Hardened properties of 3D printed concrete: The influence of process parameters on interlayer adhesion, Cement and Concrete Research 119 (2019) 132-140.
- [14] A.S.J. Suiker, Mechanical performance of wall structures in 3D printing processes: Theory, design tools and experiments, International Journal of Mechanical Sciences 137 (2018) 145-170.
- [15] B. Panda, J.H. Lim, M.J. Tan, Mechanical properties and deformation behaviour of early age concrete in the context of digital construction, Composites Part B: Engineering 165 (2019) 563-571.
- [16] S.C. Paul, Y.W.D. Tay, B. Panda, M.J. Tan, Fresh and hardened properties of 3D printable cementitious materials for building and construction, Archives of Civil and Mechanical Engineering 18(1) (2018) 311-319.
- [17] A. Perrot, D. Rängeard, A. Pierre, Structural built-up of cement-based materials used for 3D-printing extrusion techniques, Materials and Structures 49(4) (2016) 1213-1220.

- [18] P. Billberg, Form pressure generated by self-compacting concrete, Proceedings of the 3rd international RILEM symposium on self-compacting concrete, RILEM PRO33 Reykjavik, Iceland, 2003, pp. 271-280.
- [19] V. Mechtcherine, F.P. Bos, A. Perrot, W.L. da Silva, V. Nerella, S. Fataei, R.J. Wolfs, M. Sonebi, N. Roussel, Extrusion-based additive manufacturing with cement-based materials—Production steps, processes, and their underlying physics: A review, *Cement and Concrete Research* 132 (2020) 106037.
- [20] A.S. Suiker, R.J. Wolfs, S.M. Lucas, T.A. Salet, Elastic buckling and plastic collapse during 3D concrete printing, *Cement and Concrete Research* 135 (2020) 106016.
- [21] N. Roussel, J. Spangenberg, J. Wallevik, R. Wolfs, Numerical simulations of concrete processing: from standard formative casting to additive manufacturing, *Cement and Concrete Research* 135 (2020) 106075.
- [22] R. Wolfs, A. Suiker, Structural failure during extrusion-based 3D printing processes, *The International Journal of Advanced Manufacturing Technology* 104(1-4) (2019) 565-584.
- [23] J. Kruger, S. Cho, S. Zeranka, C. Viljoen, G. van Zijl, 3D concrete printer parameter optimisation for high rate digital construction avoiding plastic collapse, *Composites Part B: Engineering* (2019) 107660.
- [24] Y. Pan, A. Prado, R. Porras, O.M. Hafez, J.E. Bolander, Lattice modeling of early-age behavior of structural concrete, *Materials* 10(3) (2017) 231.
- [25] E. Schlangen, E.J. Garboczi, Fracture simulations of concrete using lattice models: computational aspects, *Engineering fracture mechanics* 57(2-3) (1997) 319-332.
- [26] H. Zhang, B. Šavija, S. Chaves Figueiredo, M. Lukovic, E. Schlangen, Microscale Testing and Modelling of Cement Paste as Basis for Multi-Scale Modelling, *Materials (Basel)* 9(11) (2016).
- [27] H. Zhang, B. Šavija, S.C. Figueiredo, E. Schlangen, Experimentally validated multi-scale modelling scheme of deformation and fracture of cement paste, *Cement and Concrete Research* 102 (2017) 175-186.
- [28] M. Vassaux, F. Ragueneau, B. Richard, A. Millard, Compressive behavior of a lattice discrete element model for quasi-brittle materials, *Computational Modelling of Concrete Structures* 1 (2014) 335-344.
- [29] E. Schlangen, Experimental and numerical analysis of fracture processes in concrete, Delft University of Technology, Delft, The Netherlands, 1993.
- [30] Z. Qian, E. Schlangen, G. Ye, K. van Breugel, Modeling Framework for Fracture in Multiscale Cement-Based Material Structures, *Materials (Basel)* 10(6) (2017).
- [31] N. Roussel, G. Ovarlez, S. Garrault, C. Brumaud, The origins of thixotropy of fresh cement pastes, *Cement and Concrete Research* 42(1) (2012) 148-157.
- [32] R.A. Buswell, W.L. da Silva, F.P. Bos, H. Schipper, D. Lowke, N. Hack, H. Kloft, V. Mechtcherine, T. Wangler, N. Roussel, A process classification framework for defining and describing Digital Fabrication with Concrete, *Cement and Concrete Research* 134 (2020) 106068.
- [33] H. Zhang, Y. Xu, Y. Gan, E. Schlangen, B. Šavija, Experimentally validated meso-scale fracture modelling of mortar using output from micromechanical models, *Cement and Concrete Composites* 110 (2020) 103567.
- [34] H. Zhang, B. Šavija, E. Schlangen, Towards understanding stochastic fracture performance of cement paste at micro length scale based on numerical simulation, *Construction and Building Materials* 183 (2018) 189-201.

- [35] A. Delaplace, R. Desmorat, Discrete 3D model as complimentary numerical testing for anisotropic damage, *International Journal of Fracture* 148(2) (2007) 115.
- [36] Y. Chen, K. Jansen, H. Zhang, C.R. Rodriguez, Y. Gan, O. Çopuroğlu, E. Schlangen, Effect of printing parameters on interlayer bond strength of 3D printed limestone-calcined clay-based cementitious materials: An experimental and numerical study, *Construction and Building Materials* 262 (2020) 120094.
- [37] M.R. Dunham, A.S. Rush, J.H. Hanson, Effects of induced vibrations on early age concrete, *Journal of performance of constructed facilities* 21(3) (2007) 179-184.
- [38] A.J. Hulshizer, A.J. Desai, Shock vibration effects on freshly placed concrete, *Journal of Construction Engineering Management* 110(2) (1984) 266-285.
- [39] C. Zhang, F. Hu, S. Zou, Effects of blast induced vibrations on the fresh concrete lining of a shaft, *Tunnelling underground space technology* 20(4) (2005) 356-361.
- [40] W.T. Koiter, On the stability of elastic equilibrium, *National Aeronautics and Space Administration* 1967.
- [41] H. Leipholz, J.W. Hutchinson, Theory of Elasticity, *Journal of Applied Mechanics* 42(4) (1975) 911-911.
- [42] J.C. Amazigo, B. Budiansky, Asymptotic formulas for the buckling stresses of axially compressed cylinders with localized or random axisymmetric imperfections, *J. Appl. Mech.* 39(1) (1972) 179-184.

4. EFFECT OF DEFORMED GEOMETRY AND INDUCED DAMAGE ON STRUCTURAL FAILURE OF PLASTIC COLLAPSE

In this chapter, a different numerical approach for buildability quantification in the lattice model is presented: the incremental loading method (or the incremental method for short). With the incremental method, the loading is applied in increments to the deformed printing system. Through this method, the impact of localized damage and deformed printing geometry on the structural failure of plastic collapse for 3DCP can be taken into account. A hollow cylinder structure and square layout are utilized for model validation. The predictions are compared with numerical results obtained using the load-unload method (presented in Chapter 3). The lattice model based on incremental method is able to predict the correct failure mode; furthermore, better quantitative agreement of critical printing height can be obtained compared to the load-unload method (from Chapter 3). These numerical analyses demonstrate that the incremental solution is an accurate method for buildability quantification since it can account for the nonequilibrium force induced by the deformed printing geometry and localized damage.

4.1 INTRODUCTION

In recent studies, several numerical methods have been proposed for the buildability quantification of 3DCP [1-4]. They usually reproduce the correct failure-deformation mode qualitatively while a quantitative agreement with the experimental results could be improved. The majority of published numerical models follow the same fundamental principle but may use different failure criteria and different forms of material stiffness and strength evolution (i.e. linear or exponentially-decaying curing function). Although these numerical models are deemed more accurate than the analytical models, some issues remain. Rather, these models have not incorporated at least one or even several printing parameters, such as geometrical imperfections, non-uniform gravitational loading, material heterogeneity, and deformed structure and localized damage. These influence factors have different effects on the structural buildability. For instance, the deformed geometry usually induces non-equilibrium force to the current printed system, resulting in stress redistribution and damage. Particularly if a complex 3D geometry is analyzed, some localized damage may occur in layers other than the bottom one during the printing process, resulting in structural failure.

To incorporate this kind of damage into the numerical analysis and achieve a good quantitative agreement with experimental results, herein the incremental method (IM) and the updated Lagrangian method are incorporated into the lattice model to quantify structural buildability for 3D concrete printing. In this way, non-equilibrium force and related damage can be taken into account and an integrated discrete lattice model for plastic collapse failure mode can be completed. Structural instability due to elastic buckling is not discussed herein and will be explored in Chapter 5.

4.2 MODEL DESCRIPTION

4.2.1 Model introduction and applicability

In this chapter, the incremental method is introduced into the discrete lattice beam model to predict the structural failure of plastic collapse. The impact of localized damage and deformed geometry is reflected in the form of a nonequilibrium force. This proposed model applies to objects with a short printing time from first minutes after casting to initial setting time, in which the material is in a fresh stage. The model is based on the assumptions of solid mechanics, and printed materials are considered in a solid-state. The fracture behavior of concrete in a fluid state is not simulated, despite the fact that it is an important factor in the extrusion process. In addition, the viscous behavior is not considered, and the model in this chapter is therefore not consider time-dependent deformation, namely early-stage shrinkage and creep. In relation to viscous deformation, relevant experimental data of fresh printing materials are required to provide input parameters for the numerical analysis. However, to the best of the authors' knowledge, no reliable published work reveals the mechanisms

behind these. This is therefore beyond the scope of Chapter 4 and will be addressed in Chapters 6, 7 and 8.

4.2.2 Model generation and discretization

Figure 4-1 gives an overview of pre-processing steps of 3DCP analysis, which includes model generation, discretization, material properties assignment, and failure criterion, as described in Chapter 3. Both the load-unload (Chapter 3) and incremental method share the same procedures for structural analysis.

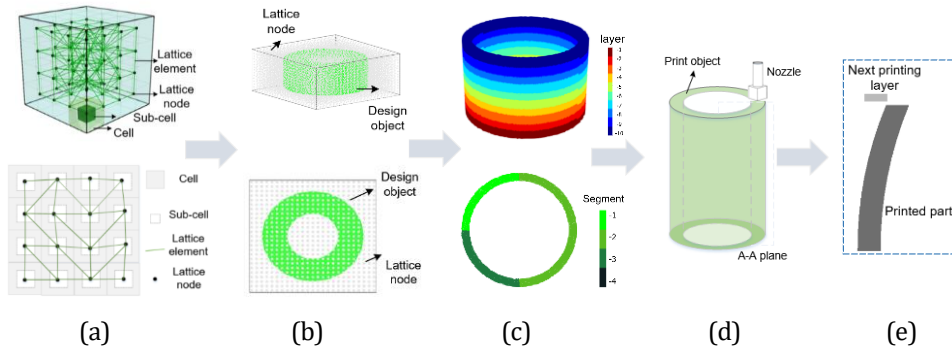


Figure 4-1 Flowchart of lattice modelling on 3DCP (a) model generation (b) model establishment (c) layer division (d) structural analysis (e) structural failure criterion

4.3 RECAPITULATION OF LOAD-UNLOAD AND INCREMENTAL METHODS

4.3.1 Overview

The modeling of fracture in cementitious materials has been under development over the past decades. Two different non-iterative solving methods will be discussed in this Chapter, i.e., the incremental method (IM) and load unload method (LU).

The LU method removes the applied loading after each analysis step, and then loads the system by a load increment which results in breakage of exactly one element. This solution procedure is repeated until a global stopping criterion is reached. Fundamentally, the linear concept of the ‘event-by-event’ is preserved in the load-unload method; no iterations are needed, and the algorithm always converges. Figure 4-2 (a) shows a simulation result of a uniaxial compressive test of hardened concrete obtained using the load-unload method. Considering that the analysis at each step is always conducted based on the undeformed state, the assembling of the stiffness matrix is only done once through the entire analysis. This algorithm has been introduced into the lattice model for fracture analysis [5-8] due to its robustness and simplicity.

Unlike the LU, the IM presented herein considers the influence of deformed geometry and non-proportional loading. In each analysis step, incremental load is applied to the deformed system obtained in the previous analysis step. Subjected to

the incremental load, some elements may break, resulting in a disequilibrium force; the stress redistribution is then conducted until a static equilibrium state is reached again; after that, the incremental load of the following analysis step is imposed on the system and the solution procedure continues until the final criterion is reached. Figure 4-2 (b) shows an example of the response of a uniaxial compressive test derived using IM. This method is not only valid for non-proportional loading issues but also for time-dependent problems [9].

There is however one drawback of IM, which is that the displacement that is used as feedback should be defined a priori. The displacement of the nodes that are chosen should always increase and no snap-backs can be simulated. As a consequence, this method is therefore step-dependent. In case of situations in which it is sure that the displacement always seems to increase, like in the case of early age material and 3D concrete printing, the method (IM) is valid. In case of large deformations in the material and progressive deformation IM is of course a much better option than LU, because node coordinates can be updated to reflect the deformed shape and stress redistribution can be included in a better way by disequilibrium forces.

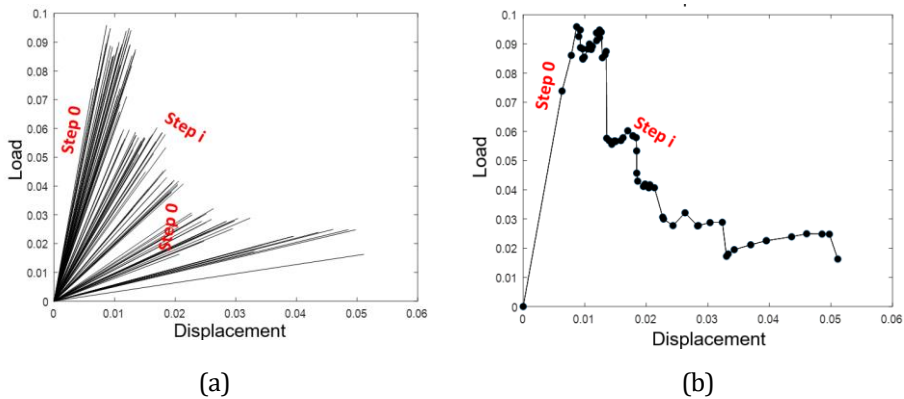


Figure 4-2 Schematic diagram towards load-displacement curve using two methods (a) load-unload method (b) incremental method.

4.3.2 Case study: computational uniaxial compression test

During printing, localized damage has a substantial impact on plastic collapse of structure failure. The primary goal of this case study is to highlight the difference between two numerical solution approaches (i.e., LU and IM) regarding the damage analysis through computational uniaxial compression tests. The investigated objectives involve the fracture performance and crack information, including the number of cracks, as well as their distribution and sequence. If different damage information is obtained, these two methods may show different performance in buildability quantification of 3DCP. In contrast to the load-unload method, the incremental approach considers the influence of a number of parameters, including

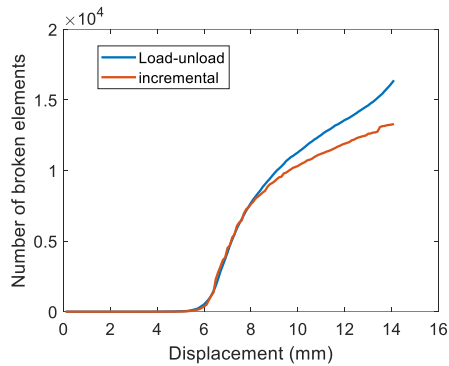
the deformed geometry, induced non-equilibrium force and non-proportional loading. Intuitively, it should better mimic the actual printing process.

First, computational uniaxial compression tests are performed to see how two approaches (i.e., LU and IM) affect numerical results, including the load-displacement curve and fracture information. Three groups of input parameters are utilized, representative of concretes for different hardening times, as shown Table 4-1. All models are cylinder-shaped with the dimension of 70 mm diameter and 140 mm height.

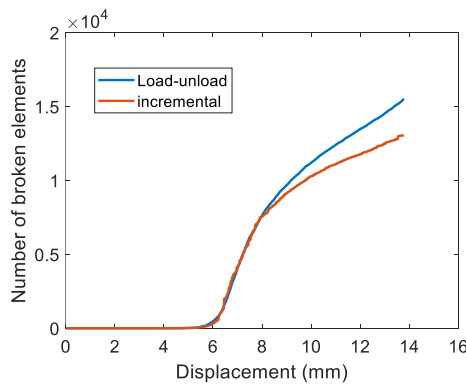
Table 4-1 Computational uniaxial compression tests with different material properties

Case	Input material properties			Predicted peak load using two methods		Model Difference
	E (MPa)	f_t (KPa)	f_c (KPa)	LU (N)	IM (N)	
1	0.05	0.71	7.1	14,375	13,780	4.32%
2	0.1	1.42	14.2	28,980	27,836	4.11%
3	10,000	10,000	100,000	202,770	204,260	-0.73%

*: E : elastic modulus; f_t : material tensile strength; f_c : material compressive strength; Difference = $(IM-LU)*100\%/IM$;



(a)



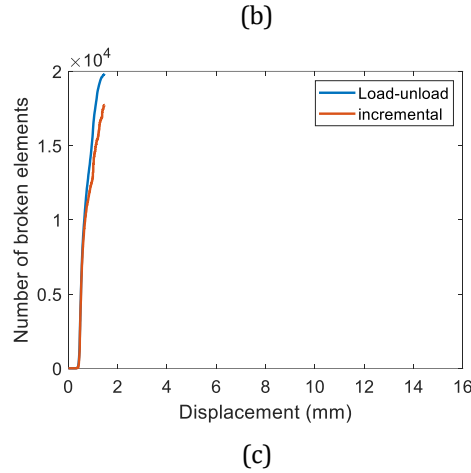


Figure 4-3 Number of broken elements with displacement (a) model 1 (b) model 2 (c) model 3

There is a small difference in peak load for the three models with different material properties, as shown in Figure 4-3. Model 3 with the lowest material properties results in the largest variance between these two methods (4.32%). Figure 4-3 provides the number of broken elements versus displacement using LU and IM analyses. Overall, these results show a discrepancy in the crack information obtained from two methods. A similar trend has previously been reported by Eliáš [10] (who considered hardened concrete). An increase in the discrepancy in the number of broken elements can be found with increased displacement. These discrepancies are due to the impact of deformed geometry and the influence of the nonequilibrium force induced by the localized damage. This case study demonstrates that the inclusion of nonequilibrium force and deformed geometry affects the peak load and the crack information, both of which are relevant for early-age concrete.

4.4 MODEL METHODOLOGY ON 3D CONCRETE PRINTING

4.4.1 Load-unload method

In Chapter 3, the lattice model to analyze the structural failure of the plastic collapse of 3DCP was presented. The load-unload solution method computes the structural deformation based on transient material stiffness; however, the ‘real’ structural deformation is a summation including a series of incremental displacements. Therefore, this solution algorithm underestimates structural deformation. On the other hand, the unloading procedure provides a convenient and robust solution, as a prize, the non-equilibrium due to structural deformation is neglected. As a consequence, the predicted critical printing height is likely higher than the real one.

4.4.2 Incremental analysis

In this chapter, an enhancement of the incremental method is proposed to simulate non-proportional loading characteristics and capture the correct layer deformation based on the updated Lagrange approach.

4.4.3 Theoretical framework

Compared to the load-unload approach, the incremental method applies the gravitational load in increments. In each step, the incremental displacement is computed based on the incremental gravitational load from newly printed segments. Thus, the layer deformation is a summation of a series of incremental displacements which need to be computed based on the time-dependent material stiffness. Meanwhile, the delta displacement induced by the incremental load is also computed, altering the printed geometry. Thus, a stress distribution occurs, bringing an additional force to the printed system. Within this analysis step, this stress redistribution needs to be conducted until no further damage occurs. In that way, at this time step, the stable stage is reached and the printing process proceeds. The total analysis procedures are schematically described can be found in Figure 4-5.

4.4.4 Model implementation

The model implementation based on the incremental analysis can be divided into five branches: A, B, C, D, and E, as indicated in Figure 4-5. The model initialization, fracture check, and structural failure criterion in 3DCP are identical to those in the previously published study using load-unload method in Chapter 3. The numerical solution and stress redistribution owing to deformed geometry and damage, on the other hand, are new in this approach.

Branch A: model initialization

After model establishment and discretization, numerical analyses of structural failure are conducted using the incremental method. The element stiffness and strength of printing segments are first computed based on the corresponding printing time to assemble the system stiffness matrix K .

Branch B: load increment

In each analysis step, the incremental load is the difference between the gravitational loading of printed segments and element force, which is affected by the generation of localized damage and the change of printing geometry. Subject to the disequilibrium force, a series of linear analyses are conducted to derive the incremental displacement, leading to the renewal of the internal force and the printing geometry. Here, the second-order Runge-Kutta method is adopted for solving the system of equations, and parallel computing is used for computational efficiency.

Branch C: Fracture check

During the printing process, layers of cementitious materials are placed on top of each other without the use of formwork to support and stabilize the printed object. Although this is an advantage from a sustainability and economic point of view, it also

raises the risk of crack occurrence. Regarding the buildability quantification of 3DCP, the element removal mechanism is adopted to mimic the localized damage during the printing process. Once the material yield stress is reached, these elements will be marked as critical elements and removed from the system computed through the equation.

Branch D: localized damage and stress redistribution

When removing critical elements from the system, the material stiffness and strength of those elements is set to zero, thereby resulting in a disequilibrium force to the current printing system. Subsequently, stress redistribution is then performed for another iteration. As soon as no damage occurs, the iterative computation of this step stops, indicating that a stable stage is derived for the deformed printing geometry.

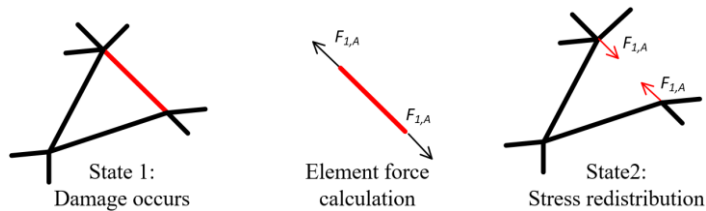


Figure 4-4 A diagram for stress redistribution due to damage

Branch E: structural failure criterion

After each analysis step, the structural failure criterion as described in section 3.2.7 (Chapter 3) is utilized to assess whether the printed object fails or not. Once the structural failure criterion is reached, the critical printing height will be determined; otherwise, the numerical analysis will continue until structural failure.

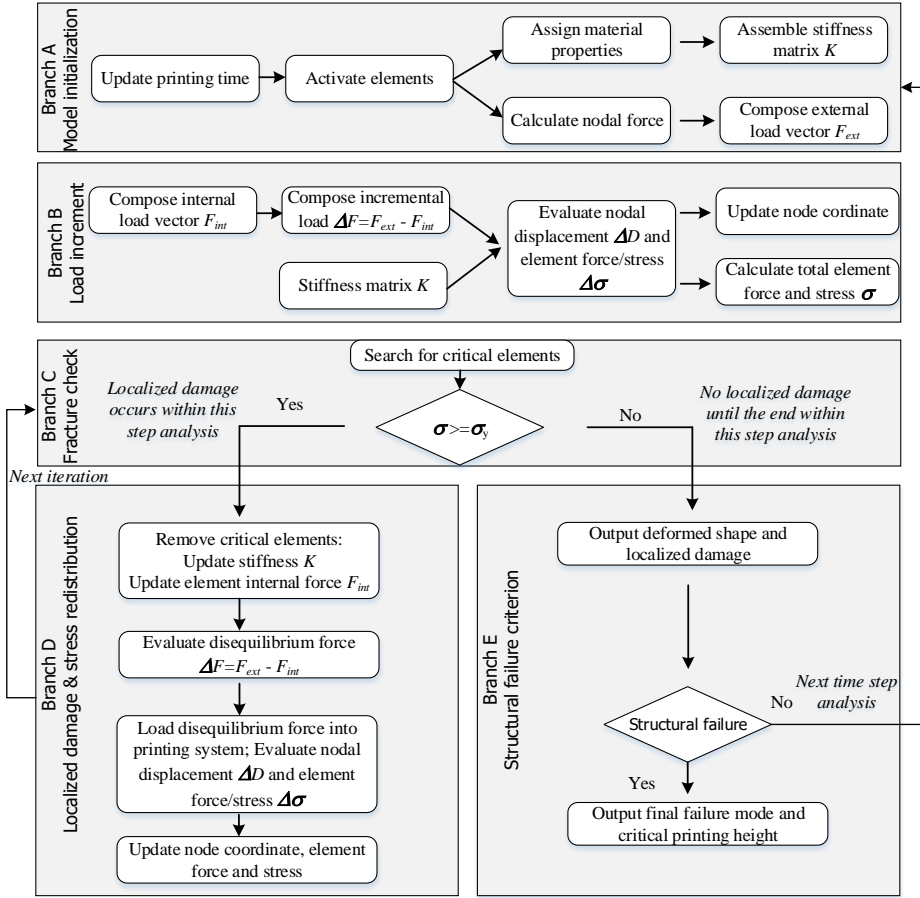


Figure 4-5 Flowchart of the developed incremental algorithm on 3DCP

This algorithm is similar to the incremental sequentially linear analysis in which the applied load is kept in the system and the next reference load is added for the exact one element broken [11, 12]. However, two points of difference should be noted: first, the geometry will be updated based on the derived incremental displacement after each iteration solution; second, more than one element is removed within one analysis step. Through the incremental method, the effect of the disequilibrium force due to the occurrence of localized damage and change of printing geometry on buildability quantification can be investigated.

4.5 NUMERICAL ANALYSES

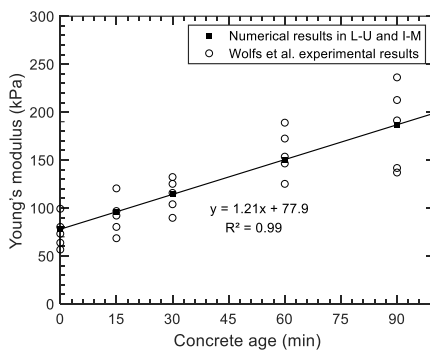
This section studies the impact of the non-equilibrium force caused by localized damage and deformed printing geometry on the structural failure of plastic collapse

for 3D concrete printing using the lattice model with the incremental solution. The effect of disequilibrium force on buildability quantification is studied through the comparison with numerical results using the load-unload method from Chapter 3; and model performance is evaluated compared to the experimental results from the literature [13, 14].

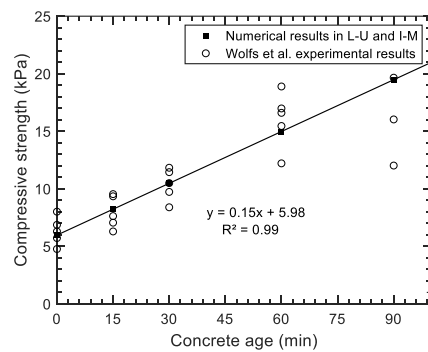
For buildability quantification, computational uniaxial compression tests are first conducted to calibrate the material properties, i.e., the material stiffness and strength. Structural analyses of plastic collapse are then performed to assess when and how the printed objects fail. Several failure-based characterizations, consisting of failure-deformation mode, critical printing height, and localized damage, are used to evaluate the predictive performance of the load-unload and incremental methods for 3DCP.

4.5.1 Model calibration

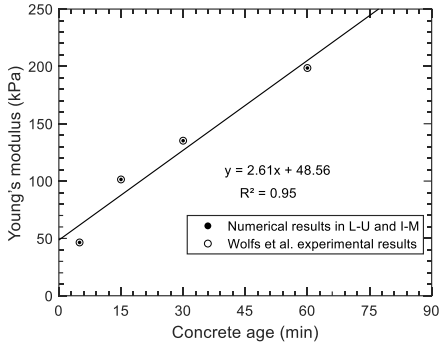
The model formation and calibration process follow the same procedure as Section 3.3.1 (Chapter 3). The numerical results derived from the computational uniaxial compression test are shown in Figure 4-6 along with the test data. The relevant material properties of lattice elements are obtained from the calibration process, and are then adopted as input parameters for buildability quantification. Eq. 4-1 to Eq. 4-4 mathematically describe time-dependent Young's modulus and compressive strength of the lattice elements using linear functions. A linear relation seems valid at very early age, although at later age the development will slow down with time. Note that there are some differences in terms of calibrated material properties between load-unload and incremental methods. This is because the incremental solution updates the system stiffness matrix after each analysis step, thus the disequilibrium force induced by deformed geometry can be taken into account. In contrast, the load-unload method always simulates the structural behaviour based on the initial system state.



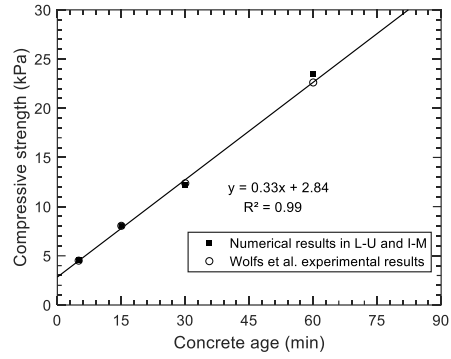
(a)



(b)



(c)



(d)

Figure 4-6 Compressive strength and Young's modulus development from experimental results and lattice model, with concrete age 0 to 90 min

$$E^{A,LU}(t) = 77.9 + 1.21 \cdot t$$

$$f_c^{A,LU}(t) = 10.96 + 0.27 \cdot t$$
Eq. 4-1

$$E^{B,LU}(t) = 48.56 + 2.61 \cdot t$$

$$f_c^{B,LU}(t) = 5.2 + 0.6 \cdot t$$
Eq. 4-2

$$E^{A,IM}(t) = 77.9 + 1.21 \cdot t$$

$$f_c^{A,IM}(t) = 12.02 + 0.28 \cdot t$$
Eq. 4-3

$$E^{B,IM}(t) = 48.56 + 2.61 \cdot t$$

$$f_c^{B,IM}(t) = 4.63 + 0.75 \cdot t$$
Eq. 4-4

Here, t is defined as the printing time; E is Young's modulus of lattice elements, determining elastic deformation within each time frame during the printing process; f_c is the material compressive strength, codetermining the localized damage together with tensile strength; superscripts A and B refer to different types of printing materials; LU and IM refer to load-unload and incremental approach, respectively.

4.5.2 Model validation

4.5.2.1 Hollow cylinder structure

To study the effect of deformed geometry and induced damage on structural buildability, the same printing cases, i.e., a hollow cylinder structure with 500 mm diameter, 40 mm thickness, and 10 mm layer height (as shown in Figure 3-8), are employed for buildability quantification during the printing process. This numerical case is in accordance with the printing trials in the literature [13]. This numerical analysis adopts high friction as the boundary condition at the bottom, and divides

each layer into 4 printing segments to mimic non-uniform gravitational loading due to the sequential printing process in actual trials, see Figure 3-8. More details on this can be found in Chapter 3.

4.5.2.2 Large Square structure

Because cylindrical geometry is sensitive to imperfections for structural analysis [15, 16], a square layout is therefore also used for model validation. The dimensions of the square structure are given in Figure 3-8 i.e., layer height of 10 mm, and a radial corner of 50 mm. The model information and validation has been described in Chapter 3.

In relation to the printing velocity, the interval time between two layers is 0.31 min and 0.16 min for the hollow cylinder and the square structure, respectively, in accordance with the printing speed in the actual tests. Lattice modeling of plastic collapse is carried out in two steps. The first step concerns the development of material properties, in which new printing elements are activated and material stiffness and strength develop following a linear function, as described in Eq. 4-1 to Eq. 4-4. For instance, when assuming the interval time between two segments is 0.62 min, the total printing time reaches 3.1 min after deposition of 5 printing segments. Consequently, the first printing segment is assigned properties corresponding to 0.31 min, age while the 5th segment has the properties of 0 min. (here the time 0 is defined as the earliest time extruded from the nozzle) The second step concerns structural analyses during the printing process, as explained in section 4.4, where the two algorithms, LU and IM, are employed for buildability quantification. The numerical analyses continue until the structural failure criterion is reached, i.e., the next printing segment fails to be placed on deformed geometry.

In 3DCP, there is a standoff distance between the printed structure and the nozzle. This is the height difference between the bottom of the nozzle and the top of the printed structure. Depending on this distance, two subcategories of the printing processes for extrusion-based materials can be distinguished. If the standoff distance is positive, the printed materials are extruded from the nozzle and placed on the deformed structure. In that case, the gravitational load due to the printed segments mainly affects the structure deformation. Once this distance is negative, the newly printed segments are extruded to the printed structure under the gravitational load and compressive pressure from the nozzle. This pressure significantly affects the structure deformation, and must be considered in the model when quantifying the structure buildability in such an instance. In these two printing experiments, the new printing segments are placed on the deformed structure without the pressure force (i.e. with a positive standoff distance), as described in the literature [13, 14].

4.5.3 Numerical results

Figure 4-7 shows radial deformation and the occurrence of localized damage during the printing process, showing that a growing number of printing layers result

in a larger radial deformation. In addition, an increasing amount of damage can also be observed from the deformed printing geometry. This is attributed to the non-uniform gravitational loading from successive printing segments, and due to the disequilibrium force caused by the generation of localized damage and the change of printing geometry. To be specific, a new printing segment is placed on the deformed printing system, resulting in more localized damage and a larger structural deformation. This influence may, in turn, affect the non-uniform state of stress which can result in structural collapse. In the end, the majority of lattice elements in the bottom layers break (as shown in Figure 4-8), leading to structural failure of plastic collapse. Concerning the system deformation (defined as the square root computed through the displacements in three translations, x , y , and z , i.e., the $\sqrt{x^2 + y^2 + z^2}$) zone with maximal deformation derived from the load-unload method is close to the top area, as shown in Figure 4-8 (a). However, the incremental method predicts maximum deformation near the middle of the cylinder height, as shown in Figure 4-8 (b), while numerous broken elements also can be observed due to large radial deformation in Figure 4-8 (c). Comparison with the experimental results from the literature (Figure 4-8 (d)) indicates that the incremental method better reproduces the failure-deformation mode [13]. In relation to the generation of localized damage, Figure 4-9 (a) indicates that the number of broken elements obtained with the incremental method is higher than that obtained using the load-unload solution under the same gravitational loading condition. Thus, the incremental method (IM) predicts a lower critical printing layer than the load-unload method (LU). Eventually, the printing object fails due to material yielding.

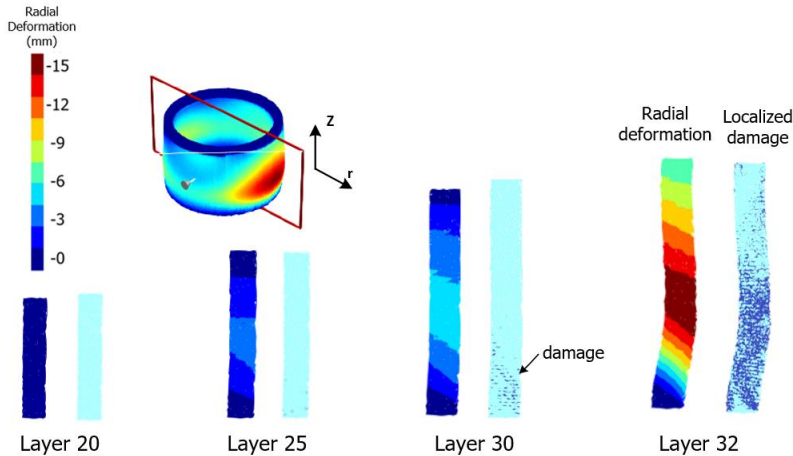


Figure 4-7 Lattice model results deformed shape and occurrence of localized damage for hollow cylinder structure using the incremental method

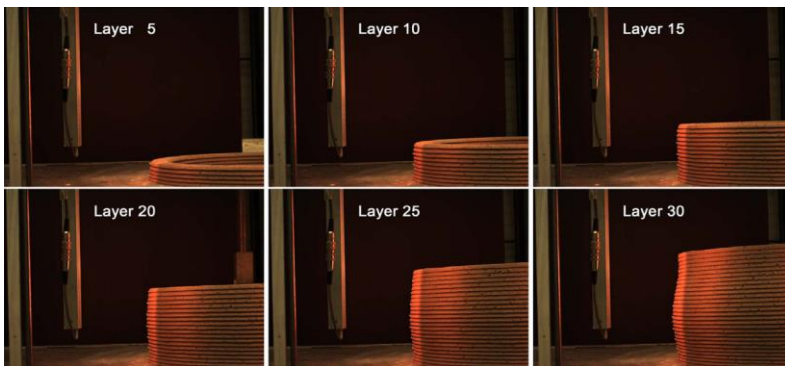
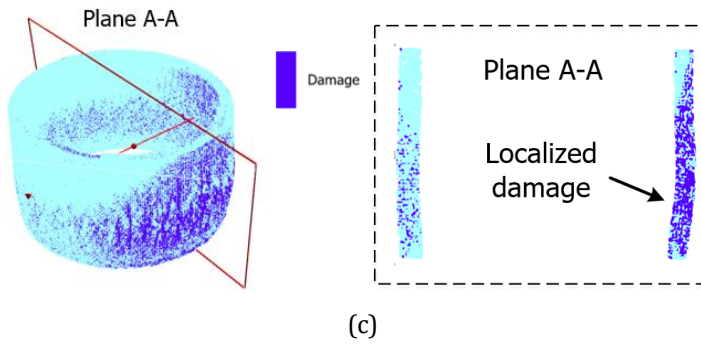
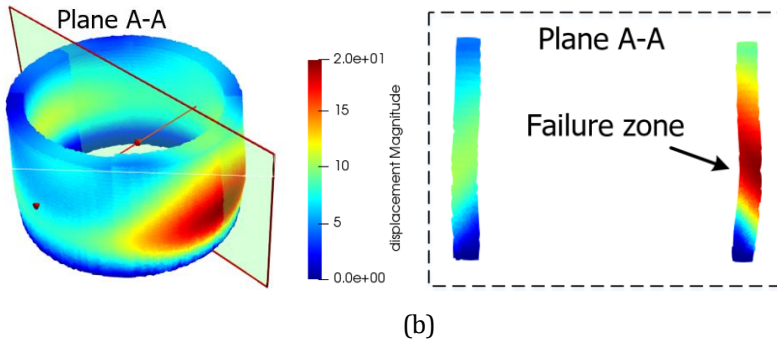
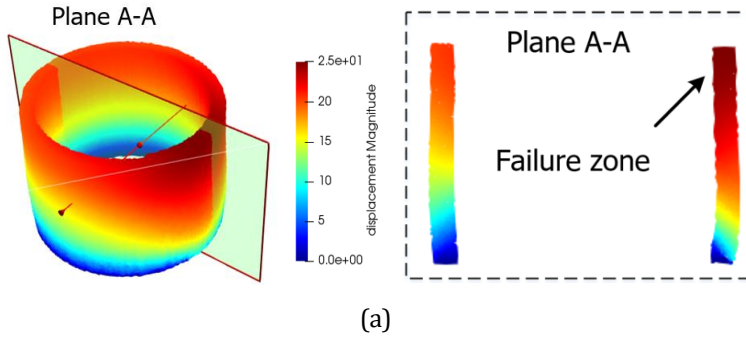


Figure 4-8 Final-deformation mode of hollow cylinder structure (a) load-unload method (41st layer) [Chapter 3] (b) incremental method: failure deformation (32nd layer) (the structural deformation is magnified to see. Unit: mm) (c) incremental method: localized damage (32nd layer) (d) experimental results. Reproduced from [13]. Copyright 2018, Elsevier

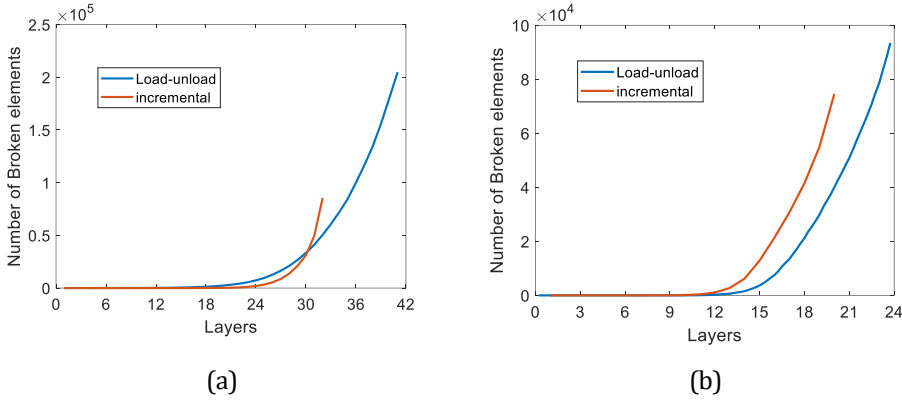
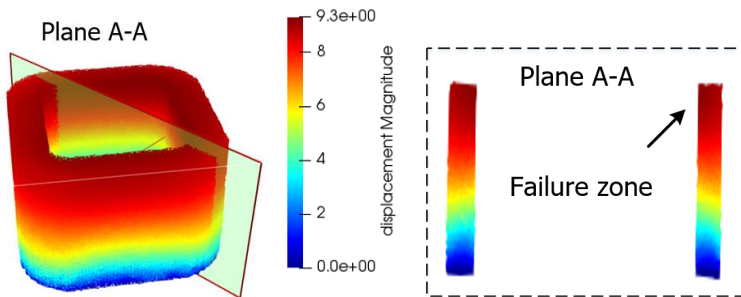


Figure 4-9 Generation of localized damage during the printing process (a) hollow cylinder structure (b) square structure

Figure 4-9 (b) describes the generation of localized damage versus the printing layers for the large square structure. Compared to the load-unload method, more broken elements are obtained using the incremental solution, which is attributed to the inclusion of disequilibrium force and updating of nodal coordinates with increasing deformation, thereby taking into account the occurrence of large deformation. Figure 4-10 provides the failure-deformation mode and the occurrence of localized damage of the square layout using the two algorithms. Although the two approaches predict different failure zones with maximal deformation, the failure-deformation modes, characterized by localized damage and excessive deformation, are comparable. Eventually, numerous lattice elements within the bottom layers break, leading to the structural failure of plastic collapse, as illustrated in Figure 4-10 (c). This failure mode with an obvious cross-section increasing on the bottom layers can be easily observed from Figure 4-10 (b), which is in accordance with the experimental findings as shown in Figure 4-10 (d) [14].



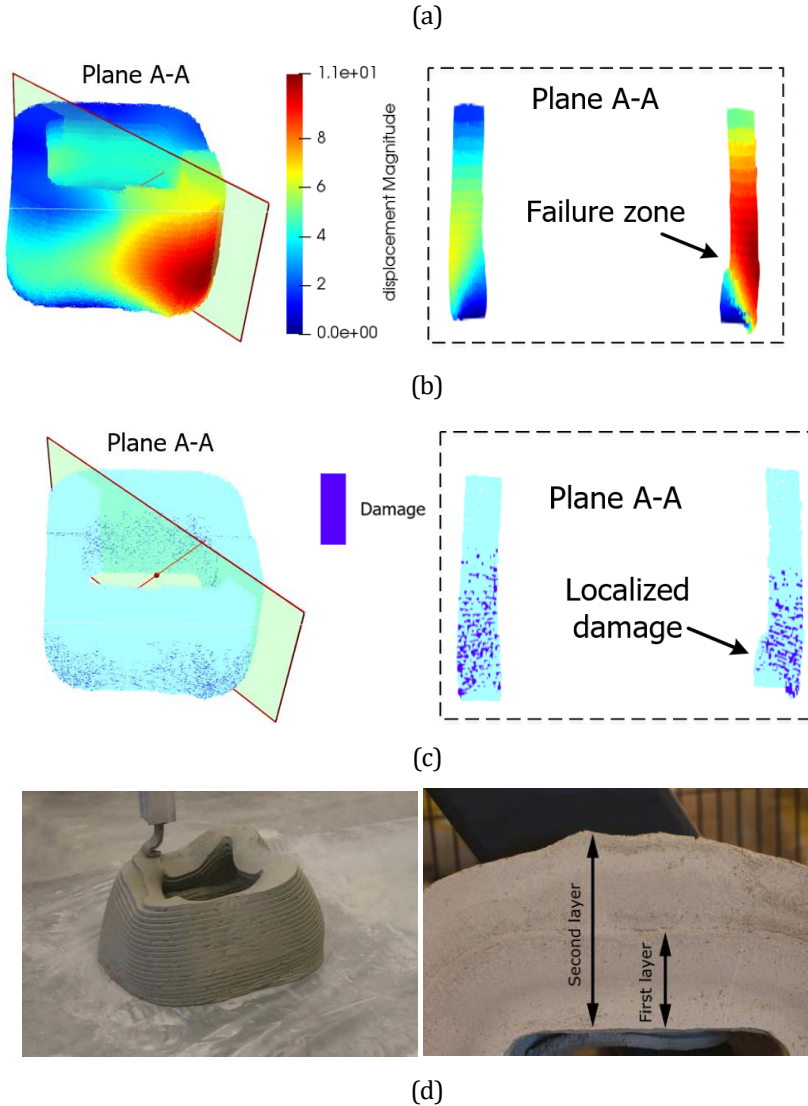


Figure 4-10 Final-deformation mode of square structure (a) load-unload method (24th layer) [Chapter 3] (b) incremental method: failure deformation (20th layer) (the structural deformation is magnified to see. Unit: mm) (c) incremental method: localized damage (20th layer) (d) experimental results. Reproduced from [14]. Copyright 2020, Elsevier

Table 2 lists a series of failure characterizations, consisting of critical printing height, maximum radial deformation, and corresponding z position among lattice model using the load-unload (Chapter 3) and the incremental method, the FEM model from Wolfs et al. [13], and the experimental results [13, 14]. Differences are obtained between the experimental data and the different simulation methods. These differences are expected also because of variation of material properties and

circumstances when performing the experiments. The most important, however, is to conclude is that the IM method predicts the same failure mechanism as in the experiment and is therefore, in that sense, better than the LU method.

Table 2 Overview of failure-deformation results of the cylinder and square structures, including critical printing height, radial deformation, and corresponding height

Object	Parameter	Value	Relative error
Hol- low cylin- der	Critical printing height	Experiment	29 layers
		Load-unload method	41 layers
		Incremental method	32 layers
		Wolfs et al.	46 layers
	Max radial deformation (mm)	Experiment	15.3 mm
		Load-unload method	14.42 mm
		Incremental method	14.9 mm
		Wolfs et al.	13.89 mm
	Z position of max radial deformation (mm)	Experiment	114.7 mm
		Load-unload method	115.36 mm
		Incremental method	128.09 mm
		Wolfs et al.	115.8 mm
Square	Critical printing height	Experiment	218.5 mm
		Load-unload method	240 mm
		Incremental method	200 mm

4.6 DISCUSSION

When comparing the predicted critical heights from the lattice model using the two approaches, the numerical results indicate that the incremental method predicts a lower critical printing height than the load-unload method, which is ascribed to consideration of deformed geometry and disequilibrium force. Specifically, the total deformation of the printing structure is determined by the transient material stiffness using the load-unload method. However, the layer deformation is a summation including a series of incremental displacements which should be computed based on the time-dependent material stiffness. Besides, based on the deformed printing geometry, the disequilibrium force induced by the geometry change and damage generation can be included using the incremental solution. Considering that the lattice model with incremental approach reproduces the correct failure-deformation mode

as well as better quantitative agreement result with experimental data, it can be considered as a more precise method for buildability quantification of 3DCP.

However, compared to experimental results, some discrepancy is still present. The incremental solution underestimates printing height of the hollow cylinder structure while the opposite is observed for the square layout. This difference is attributed to exclusion of geometric imperfections and possible underestimation of material properties used as input in the model. The development of material properties is obtained using the green strength test, in which printable materials are actually cast and therefore undergo a compaction process [13, 14]. This may result in a low early-stage material stiffness and strength within the time frame of the first 30 mins compared to the actual printed material [17]. Furthermore, viscoelastic effects like creep and relaxation are not taken into account, while both will be present in the green strength testing, but also during printing. Consequently, the critical printing height is underestimated. To obtain more reliable input parameters, some improvements on the material testing procedures may be needed; however, this is beyond the scope of current research.

The underestimation of the number of critical layers can be found from square geometry while the opposite is found for hollow cylinder structure, which can be attributed to another factor; namely, presence of geometric imperfections induced by the extrusion and printing process. In 3DCP, two types of imperfections may be generated during the printing process; the first one comes from the manufacturing process, given the fact that printable materials cannot be smoothly extruded from the nozzle; the second one is localized damage. The model presented in this chapter only allows for localized damage that is generated due to the loading conditions, but neglects imperfections resulting from the printing procedure. The critical printing height may therefore be overestimated using the lattice model with the incremental solution, especially for the hollow cylinder structure. This is because the cylinder geometry is much more sensitive to imperfections compared with the square structure [14, 18]. If presence of imperfections such as large air voids or layer tearing and the development of shrinkage stresses during the manufacturing process are taken into account, a better quantitative agreement with experimental data may be achieved.

4.7 CONCLUSIONS

This chapter investigates the influence of disequilibrium force due to localized damage and deformed printing geometry on the structural failure of plastic collapse by incorporating incremental methods into the lattice model. A series of novel insights and conclusions can be reached as below:

Compared to the load-unload method (In Chapter 3), the incremental method considers disequilibrium force via generation of localized damage and the change of printing geometry. In the computational uniaxial compression test, the inclusion of

this kind of force results in different peak load and crack information, and the influence is more significant for early-age cementitious materials.

For 3D concrete printing analysis, the load-unload method (presented in Chapter 3) underestimates the layer deformation based on instantaneous material stiffness. The layer deformation is a summation including a series of incremental displacements which should be computed based on the time-dependent material stiffness. The lattice model with an incremental approach is more accurate in capturing the structural deformation during the printing process.

The incremental approach reproduces more accurately the failure-deformation mode as well as quantitatively agreement results with experimental data. This is due to the consideration of the deformed geometry and the inclusion of nonequilibrium force. A small deviation between lattice modeling using the incremental method and the experimental results can be found. This is likely because of the underestimated material properties from testing, and disregarding the impact of geometrical imperfections generated during the extrusion and printing process.

These numerical results demonstrate that the incremental solution is a more suitable method for buildability quantification since it can account for the nonequilibrium force induced by the deformed printing geometry and localized damage. Using this method, a typical plastic collapse failure mode can be obtained and a good quantitative agreement on critical printing height can be achieved.

However, the plastic collapse failure mode is not the only failure mode that may occur during printing process of 3DCP; elastic buckling is the other common failure mode. To study the buckling-dominant failure mode, an algorithm which considers the impact of geometric nonlinearity will be discussed in Chapter 5.

REFERENCES

- [1] T. Ooms, G. Vantighem, R. Van Coile, W. De Corte, A parametric modelling strategy for the numerical simulation of 3D concrete printing with complex geometries, *Additive Manufacturing* 38 (2021) 101743.
- [2] G. Vantighem, T. Ooms, W. De Corte, FEM modelling techniques for simulation of 3D concrete printing, *arXiv preprint arXiv:06907* (2020).
- [3] R. Jayathilakage, P. Rajeev, J. Sanjayan, Yield stress criteria to assess the buildability of 3D concrete printing, *Construction and Building Materials* 240 (2020) 117989.
- [4] M. Mengesha, A. Schmidt, L. Göbel, T. Lahmer, Numerical Modeling of an Extrusion-Based 3D Concrete Printing Process Considering a Spatially Varying Pseudo-Density Approach, *RILEM International Conference on Concrete and Digital Fabrication*, Springer, 2020, pp. 323-332.
- [5] H.J. Herrmann, A. Hansen, S. Roux, Fracture of disordered, elastic lattices in two dimensions, *Physical Review B* 39(1) (1989) 637.
- [6] E. Schlangen, E.J. Garboczi, Fracture simulations of concrete using lattice models: computational aspects, *Engineering fracture mechanics* 57(2-3) (1997) 319-332.
- [7] Z. Pan, R. Ma, D. Wang, A. Chen, A review of lattice type model in fracture mechanics: theory, applications, and perspectives, *Engineering Fracture Mechanics* 190 (2018) 382-409.
- [8] E. Schlangen, J.G.M. Van Mier, Simple lattice model for numerical simulation of fracture of concrete materials and structures, *Materials and Structures* 25(9) (1992) 534-542.
- [9] B. Jurkiewicz, J.-F. Destrebecq, A. Vergne, Incremental analysis of time-dependent effects in composite structures, *Computers & structures* 73(1-5) (1999) 425-435.
- [10] J. Eliáš, Generalization of load-unload and force-release sequentially linear methods, *International Journal of Damage Mechanics* 24(2) (2015) 279-293.
- [11] C. Yu, P. Hoogenboom, J. Rots, Extension of incremental sequentially linear analysis to geometrical non-linearity with indirect displacement control, *Engineering structures* 229 (2021) 111562.
- [12] J. Eliáš, P. Frantík, M. Vořechovský, Improved sequentially linear solution procedure, *Engineering fracture mechanics* 77(12) (2010) 2263-2276.
- [13] R. Wolfs, F. Bos, T. Salet, Early age mechanical behaviour of 3D printed concrete: Numerical modelling and experimental testing, *Cement and Concrete Research* 106 (2018) 103-116.
- [14] A.S. Suiker, R.J. Wolfs, S.M. Lucas, T.A. Salet, Elastic buckling and plastic collapse during 3D concrete printing, *Cement and Concrete Research* 135 (2020) 106016.
- [15] W.T. Koiter, On the stability of elastic equilibrium, *National Aeronautics and Space Administration* 1967.
- [16] J.C. Amazigo, B. Budiansky, Asymptotic formulas for the buckling stresses of axially compressed cylinders with localized or random axisymmetric imperfections, *J. Appl. Mech.* 39(1) (1972) 179-184.
- [17] R. Wolfs, F. Bos, T.J.C. Salet, Triaxial compression testing on early age concrete for numerical analysis of 3D concrete printing, *Cement and Concrete Composites* 104 (2019) 103344.
- [18] A.S.J. Suiker, Mechanical performance of wall structures in 3D printing processes: Theory, design tools and experiments, *International Journal of Mechanical Sciences* 137 (2018) 145-170.

5. MODELLING OF ELASTIC BUCKLING FAILURE IN 3DCP

This chapter explores the buckling failure during the printing process of 3DCP by incorporating the geometric nonlinearity into previously developed discrete lattice beam model. The computational uniaxial compression tests were first conducted to calibrate age-dependent elastic modulus and yield stress. Subsequently, analyses of the 3D printing process of a free wall structure and a square layout were performed. The model can reproduce the asymmetry of buckling failure accurately without introducing any initial geometric imperfection. A good quantitative agreement in terms of critical printing height is found between the numerical results and experiments from the literature.

5.1 INTRODUCTION

In 3DCP, the extrusion-based printing process can generally be divided into two processing steps: material deposition and structural build-up [1-6]. This first stage concerns pumping of the printable material from the pump to the printhead, in which material elastic/plastic viscosity is crucial. After material deposition, the printed layers should be stiff enough and strong enough to retain the self-weight and gravitational loading of subsequent layers without excessive deformation or collapse [7]. In general, two competing failure modes are frequently reported: plastic collapse through material yielding and structural instability by local or global buckling [8-11]. Plastic collapse failure is characterized by maximum stress of the critical layer reaching the material yield stress, while elastic buckling is determined by a loss of geometrical stability.

The majority of published numerical or analytical models concern purely strength-based material yielding, whereas structural failure of a printed object is sometimes a result of local or global buckling, as illustrated by printing trials in the literature [2, 12]. Predicting the buckling response is therefore also crucial for structure build-up.

The remaining numerical models predict buckling failure mode by introducing geometrical imperfections into the initial model which is derived from a bifurcation linear buckling analysis. Using this method, an asymmetric mode of buckling failure can be obtained through nonlinear analyses regarding structural stability of wall and rectangular structures. However, the predicted failure mode is different from the experimentally observed one.

In order to fill these gaps, geometric nonlinearity is introduced into the previously developed discrete lattice model for simulating the buckling failure mode during 3DCP. This modified lattice model incorporates time-dependent mechanical properties, different printing velocities, material heterogeneity, localized damage, non-uniform gravitational loading, deformed geometry and geometric nonlinearity. Using this newly proposed model, asymmetric buckling failure can be simulated without introducing initial geometrical imperfections. As will be shown, this can be attributed to a combined effect of geometric nonlinearity and system heterogeneity, including mesh randomness of model discretization, localized damage, and printing segment division.

5.2 MODEL OVERVIEW

In this chapter, the geometric nonlinearity is introduced into the lattice model based on the incremental algorithm. The application of this improved model includes prediction on plastic collapse and elastic buckling. The viscous behavior is not considered, and the model in this chapter is therefore not capable of time-dependent deformation, such as early-age creep. This will be studied in the following chapters. In terms of the pre-processing steps of 3DCP analysis, this model shares the same

procedures with the previous method. The details can be found in Section 3.2 (Chapter 3).

5.3 GEOMETRIC NONLINEARITY

In previous chapters, lattice model for 3DCP showed that it can reproduce the plastic collapse failure mode and is in quantitative agreement with experimental data. However, it was not applicable to elastic buckling, considering the failure mechanism is generally induced by local or global geometrical stability. Therefore, assessing structural failure of elastic buckling might be possible if geometric nonlinearity is introduced into the lattice model [2, 13].

5.3.1 Theoretical framework

In this research, the implementation of geometric nonlinearity considers kinematic descriptions in principle while physical non-linearity due to material development is considered through updating the material stiffness matrix. By means of virtual displacement formula and second-order elastic analysis, the effect of finite deformations and displacements in structural analysis can be accounted for through the following equations [14, 15],

$$\begin{aligned} (K_t + K_g) \Delta D &= \Delta F \\ \Delta F &= F_{ex} - F_{in} \end{aligned} \quad \text{Eq. 5-1}$$

in which the ΔF and ΔD are incremental loading and displacement of printing system, respectively. For structural analysis of 3DCP, this incremental force can be computed based on the external load F_{ex} and the internal element force F_{in} .

In the model, K_t is the material stiffness matrix, dependent on Young's modulus (E) (transient material properties during printing process) and B_L (strain-displacement relation), which is computed based on strain condition and interpolation function (as described in equation Eq. 5-2). More specifically, G includes the differentials towards every strain measure and condition while H contains the interpolation function. The geometric stiffness matrix K_g is updated on the basis of kinematic descriptions and derived element force after each analysis step; the C represents 2nd Piola–Kirchhoff stress in matrix form, and BNL is the shape function in non-linear form considering incremental loading, mathematically described as follows [14]:

$$\begin{aligned}
B_L &= GH \\
K_t &= \int_0^l B_L^T E B_L^T dx \\
K_g &= \int_0^l B_{NL}^T C_t B_{NL}^T dx
\end{aligned}
\tag{Eq. 5-2}$$

5.3.2 Numerical implementation

The pre-processing procedures of the numerical analysis have been described in Section 3.2 (Chapter 3) and the corresponding solution flowchart concerning geometric nonlinearity will be explained in this section. The extended lattice model with geometric nonlinearity for buildability quantification of 3DCP encompasses six branches: A, B, C, D, E and F, as indicated in Figure 5-1.

In this flowchart, the k and K stand for local and global stiffness matrix, respectively. To be specific, subscripts ' t ' and ' g ' refer to material stiffness and geometric stiffness matrix. The T is the transformation matrix transferring the local domain to the global domain. The L and D are the global load and displacement vectors, respectively. The subscript i^{th} stands for the analysis step. Also, σ and $\Delta\sigma$ are the cumulative element stress and incremental element stress within one analysis step. The structural deformation δ is a summation including a series of incremental displacements $\Delta\delta$. The F refers to load vector, and subscript 'ext' and 'int' stand for the external load due to gravitational loading and internal load stored in the printing system derived from the last known equilibrium stage. The ΔF is derived disequilibrium force between the external load and the internal load.

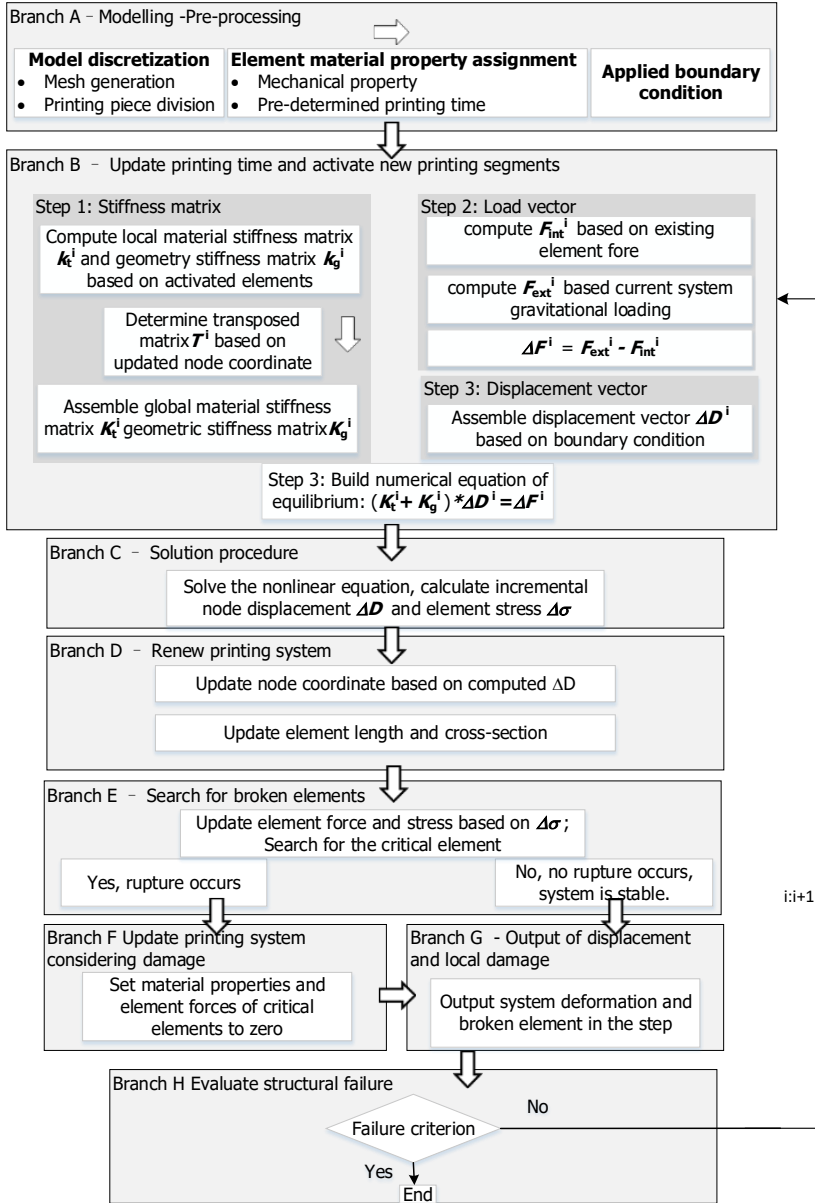


Figure 5-1 Implementation of geometric nonlinearity in the lattice model

Branch A: Modelling procedure.

A brief introduction has been given in Section 2, and detailed information can be found from previous research [16].

Branch B: Update printing time and activate new printing segments considering geometric nonlinearity.

B1: In the lattice model, layers of a printed object can be subdivided into different segments, allowing for sequential printing process. These time-based segments will be activated immediately once the pre-determined time is reached. They are subsequently assigned with material behaviors, which grow in a linear or an exponentially decaying fashion. For instance, if the interval period between two segments is 1 min; after 5 segments, the initial one is characterized by 5-min material properties, the 3rd printing segment also is assigned with 3-min old stiffness and strength, and so on.

B2: Once transient material properties are assigned to corresponding elements, the element stiffness matrix k in the local coordinate system can be assembled. Combined with the transformation matrix T , the global tangent stiffness matrix K_t and geometry stiffness matrix K_g of each activated element can also be derived, as mathematically expressed in the Eq. 5-3. Typically, the K_t is a linear elastic component and determined by transient material properties while K_g , the geometry stiffness matrix, is relevant to the 2nd Piola-Kirchhoff stress and calculated based on element force, as discussed above.

$$\begin{aligned} K_g &= T^T k_g T \\ K_t &= T^T k_t T \end{aligned} \quad \text{Eq. 5-3}$$

Branch C: Structural analysis in each time step.

C1: The numerical analysis of printing process is based on lattice model using an updated Lagrangian method and the numerical equation of equilibrium (i.e., Eq. 5-1) is solved using the midpoint Runge-Kutta method [15]. A parallel computation approach has been adopted for computing efficiency, clearly showing model feasibility for large scale structural analysis.

Branch D: Update printing system based on solved displacement.

D1: The node coordinates are updated as well on the basis of obtained ΔD using an updated Lagrangian method. Then, the element length is recalculated based on new node coordinate, and the cross-section is updated considering constant element volume.

Branch E: Search for broken elements & Branch F: update printing system considering localized damage

After the solution procedure, derived nodal displacement are utilized for determining the elemental stresses. Afterwards, critical elements are immediately removed from the mesh according to the same element failure criterion (Chapter 4 Equation (1)), and their internal forces are also released.

Branch G: Output structure deformation and localized damage after one-step analysis

Branch H: Evaluate system failure.

H1: In the numerical procedure, the numerical analysis of buildability quantification will be performed until the structural failure criterion (as described in Section 3.2.7, Chapter 3) is reached. For each analysis step, the next printing segment is placed on the designed/original position instead of being adjusted along with deformed geometry, and this solution method is in accordance with actual trials [12, 17]. As soon as the next printing segment is successfully placed on top of the current system, the printing process will proceed, in which the printing time updates and a new printing segment is activated.

In the next analysis step, the deformed shape is utilized as the reference frame and the incremental equation will be built here with relation to Updated Lagrangian formulation [18]. It should be mentioned that a series of parameters, including stiffness matrix, external and internal loading, must be updated based on this reference geometry.

The necessity of matrix modification, consisting of stiffness matrix K_t and geometry matrix K_g , is also required given deformed structure. On the one hand, presence of localized damage produced in the previous analysis step reduces the material properties of critical elements to zero, which is detrimental to the printing system; the sequential printing process, on the other hand, activates more printing segments and linearly or exponentially enhances the material properties of existing elements. The geometric stiffness matrix allowing for the effect of geometric nonlinearity on structure analysis, and material stiffness standing for localized damage and material development, are computed based on the element force, updated material properties and deformed structure. The contradictory effect of material development and occurrence of localized damage results in uncertain prediction of buildability and their influence will take effect in next step analysis.

The load vector of internal force also renews after each step, which can be attributed to two aspects. First, the incremental gravitational loading is applied on the system, which causes the element internal forces to evolve. Second, the updated transformation matrix T results in orientation variation of beam elements, leading to a different internal load force vector in the global domain.

Based on the updated printing system, the numerical analysis of buildability quantification will be continuously performed to assess when and how the printed object fails.

5.4 NUMERICAL MODEL

In this section, we perform numerical analyses of structural instability through two layouts sensitive to buckling failure: a free wall and a large square structure [19, 20], as indicated in Figure 5-2. In relation to buildability quantification, computational uniaxial compression tests are first performed to calibrate essential material behaviors such as stiffness and strength [17, 20]. The calibrated material properties

are subsequently employed for structural build-up in which failure-deformation mode, as well as critical printing height, is predicted [19]. Herein, this study adopted experimental campaigns, including material tests and 3D printing trials, from Wolfs et al. [17, 19] for model calibration and validation.

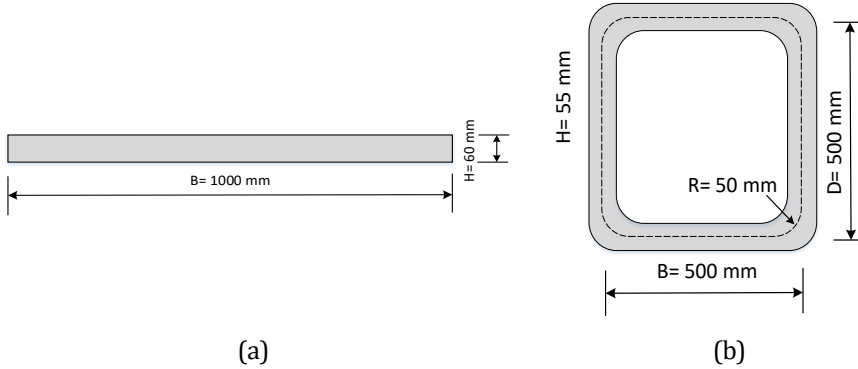


Figure 5-2 Geometrical characteristics of the free wall and rectangular structure for 3DCP (a) free wall structure (b) rectangular layout, both viewed from the top

5.4.1 Model calibration: computational uniaxial compression test

Similar to the model calibration procedure presented in previous chapters, the uniaxial compression tests from the literature [2, 17] is utilized to calibrate model parameters. In this study, two types of materials are employed for 3DCP: material A for the free wall structure and the material B for the square layout. The detailed calibration process can be found from Chapter 3.

The calibrated elastic modulus and compressive strength are listed on Table 5-1. In contrast to experimental results. The numerical results are in excellent agreement with the experimental findings, which proves this numerical model has accurately derived material stiffness and strength of fresh concrete. These time-dependent material properties are therefore adopted and then can be utilized for formulation of curing function. Two time-dependent material properties, i.e., a linear and an exponential relationship, are often adopted for time-dependent material properties. Considering the exponential yield stress evolution can describe a smooth transition from initial linear increase to exponential evolution [21, 22], it is adopted herein to describe age-dependent material properties (i.e., elastic modulus and compressive strength). It should also be noted that some experimental results show considerable scatter, which is attributed to the compaction process. The material usually does not undergo a compaction procedure during the printing process. However, green strength tests on the material B are conducted after a compaction process. The published research indicates [2] that there is a difference between samples subjected to a compaction process and those that are not. The influence becomes more pronounced with concrete age. Thus, the aging time above than 30 min is not taken into account during calibration process. Here, the material A without compaction

process enables to identify curing function according to all calibrated results, while regarding material B only transient material properties under 15 and 30 min are adopted for material development to eliminate experimental scatter induced by compaction process. This identified material development will be taken as time-dependent material properties for structure analysis of buckling response in next section. There is no doubt that the fitting function of time-dependent material properties would be more reliable given more available data. A possible way to accomplish this is to perform green strength tests without compaction. However, this is beyond the scope of the current work. On the basis of calibrated material properties listed in Table 5-1, the time-dependent material behaviors of lattice elements can be described as Eq. 5-4 and Eq. 5-5.

Table 5-1 Calibrated mechanical properties with a range of time 0 to 90 min

Material type	Input material properties in lattice model			Computational uniaxial compression test	
	Concrete age (min)	Young's modulus (kPa)	Compressive strength (kPa)	Young's modulus (kPa)	Compressive strength (kPa)
A	15	60.20	7.35	60.20	7.29
	30	104.08	10.00	104.08	9.97
	60	128.57	12.86	128.57	12.71
	90	197.96	20.92	197.96	20.87
B	15	101.41	8.05	101.41	7.89
	30	135.21	12.37	135.21	12.62

$$E_c^A = 55.97e^{0.0142t}$$

$$f_c^A = 22.76e^{0.0127t}$$

Eq. 5-4

$$E_t^B = 76.31e^{0.019t}$$

$$f_t^B = 11.10e^{0.0458t}$$

Eq. 5-5

Here, the E represents the elastic modulus, determining the elastic deformation; f_c stands for the material compressive strength.

5.4.2 Model validation

5.4.2.1 Free wall structure

Model validation of buckling response starts from a free wall structure printed with material A, the dimensions of which are 1000 mm length and 60 mm width [20,

23]. The printing velocity equal to 6250 mm/min was employed. The detailed information about this free wall structure is given in Table 5-2.

Table 5-2 Printing process parameters for wall structure

Parameter	Value
Wall thickness (mm)	60 mm
Concrete density (kg/m ³)	2100
Printing velocity (mm/s)	6250 mm/min
Initial material stiffness (kPa)	55.97 kPa
Initial material strength (kPa)	22.7 kPa

Prior to structural analysis of buckling failure, each printing layer, including 4000 lattice nodes connected by around 35,000 Timoshenko beams, is divided into three printing segments to study the impact of non-uniform gravitational loading based on Chapter 3. It means that sequential printing segments are continuously added alongside each other with a time frame of numerical analysis, as described in Section 2. Rather, mesh resolution of 5 mm, which is line with computational uniaxial compression test, has been characterized for the purpose of elimination of mesh size effect on buildability quantification. The layer height of 10 mm is therefore adopted in this numerical analysis, slightly different than the experiment (9.5 mm). A fully fixed support was utilized on the bottom to capture high friction caused by printing bed in the trials. In terms of loading condition, nodal forces representing gravitational load are determined by the material density (2100 kg/m³) and the volume of each Voronoi cell, as described in Chapter 3. One point should be noted, unlike the FEM analyses of buckling failure in 3DCP discussed above, no geometric imperfection is introduced into the printed object in advance. The structure failure due to elastic buckling is therefore a combined effect of localized damage and non-uniform gravitational loading due to sequential printing process.

The typical failure mode of free wall structure is depicted in Figure 5-3, indicating this failure-deformation mode is dominated by elastic buckling. Figure 5-4 provides the comparison of localized damage before and after structure failure. In relation to the critical printing height, failure occurred at 18th layers, while no excessive deformation could be observed before the final failure, as illustrated from Figure 5-3 (a). This is attributed to the combined effect of heterogeneity consisting of non-uniform loading and mesh randomness, in accordance with localized damage of a printed object during an actual process. Further exploration goes to failure process and mechanism observed from the numerical analysis: although homogeneous material properties are assigned to lattice elements, the printed object still shows strong heterogeneity caused by the random lattice mesh and non-uniform application of gravitational load (i.e., division in printing segments). This expedites localized damage and loss of geometrical stability, in which the former governs the plastic

collapse, while the latter is crucial for elastic buckling. Under the effect of system buckling, a growing number of broken elements also can be observed from Figure 5-4 (b).

In comparison with experimental results from the literature [2, 12], this model not only reproduces the experimentally derived failure-deformation mode accurately without introducing initial geometric imperfections, but also predicts the experimental results well in quantitative terms. Specifically, when placing the 18th layer into original position, the offset between the design position and deformed geometry is larger than the width of an individual layer. It can be observed that the final failure occurred at the 18th layer, and that the critical printing height is 180 mm, around 12% lower than the test data (i.e., 204.25 mm). A deviation of up to 20% is not exceptional, considering that the input material properties are calibrated by uniaxial compression experiments, where significant scatter exists (i.e., the relative standard deviations up to 21% for elastic modulus and around 17% for the yield stress).

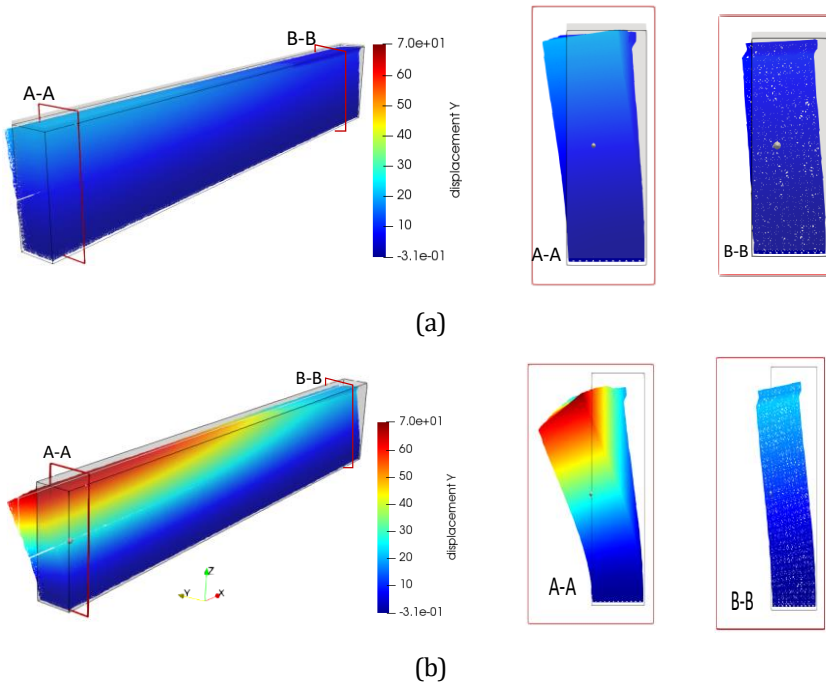


Figure 5-3 Failure by elastic buckling of a free wall structure (a) before failure (b) after failure

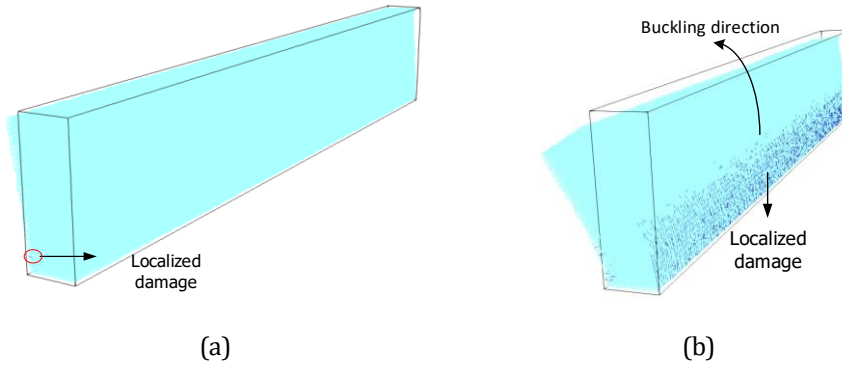


Figure 5-4 Localized damage (shown in black) for wall structure (a) before failure (b) after failure

Table 5-3 Experimental value and model prediction of the critical printing height for free wall and rectangular structure

Printed sample	Experiment	Lattice model	Relative difference
Free wall	204.25 mm	180 mm	-11.87%
Square structure	261.14 mm	230 mm	-11.92%

5.4.2.2 A large square structure

In this section, a square structure (side = 500 mm and width = 55 mm) was modeled through material B with an exponential material evolution [19, 23], and the relevant parameters are listed in Table 5-4. Each layer of the square structure, consisting of 8000 lattice nodes connected by around 61000 Timoshenko beams, includes four segments to coincide with the continuous printing process. Like the above modeled free wall structure, a fully fixed boundary condition and the same solution of nodal force have been employed, as well as the mesh fineness. Similar to the wall structure, no initial geometric imperfection is introduced for numerical analysis of structural stability.

Table 5-4 Printing process parameters for square layout

Parameter	Value
Wall thickness (mm)	55
Model length/B (mm)	500
Model width/D (mm)	500
Concrete density (kg/m^3)	2100
Printing velocity (mm/s)	83.3
Initial material strength (kPa)	11.10
Initial material stiffness (kPa)	76.31

The typical failure mode of the square structure is shown in Figure 5-5, and comparison with experimental data associated with printing height is indicated in Table 5-3. Figure 5-6 provides the comparison of localized damage before and after structure failure.

Regarding the failure process, dead weight of the stepwise increasing layers induced some damage near to the bottom (as indicated in Figure 5-6 (a)), thereby exacerbating structural instability. The rectangular structure fails after the 23rd printing layer due to out-of-plane displacement in A-A plane, predicting critical printing height equal to 230 mm. Furthermore, significant localized damage can be observed near the buckling zone, as depicted in Figure 5-6 (b). In contrast to experimental result with 261.125 mm, a deviation around 12% can be derived, i.e., less than 20%. It is therefore concluded that the model for the square structure not only can reproduce the correct buckling-dominant failure mode, but also that the critical printing height is in good quantitative agreement with the experiments.

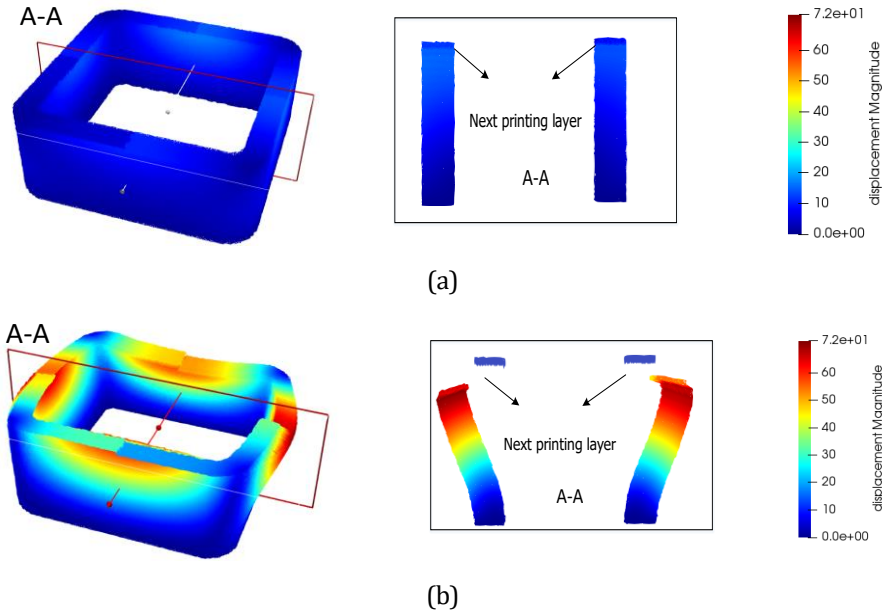


Figure 5-5 Failure by elastic buckling in the numerical analysis of rectangular layout structure
(a) before failure (b) after failure

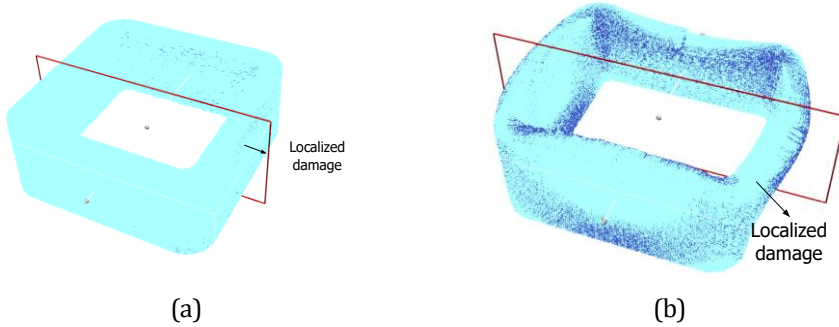


Figure 5-6 Localized damage for square structure (a) before failure (b) after failure

5.5 DISCUSSION

The above numerical analyses indicate that the extended lattice model enables correct simulations with respect to structural buckling failure, qualitatively similar to printing trials from the literature [2, 12]. In relation to the critical printing height computed for these two structures, deviations of 11.87% and 11.97% were derived for the free wall and square layout, respectively.

When it comes to the failure process, some localized damage occurs first, detrimental to structural stability. Subjected to heterogeneity, including mesh randomness and non-uniform gravitational loading, numerical models are likely to fail because of combined failure mode, here the elastic buckling plays a dominant influence. In addition, this kind of buckling response also causes more localized damage to printed systems in return, as observed from Figure 5-4 (b) and Figure 5-6 (b). It can be concluded that structural failure of concrete during 3D printing is a complex combination of plastic collapse and elastic buckling. Assessing build-up performance of printed system merely considering one of them will likely result in errors since their interaction, which actually exists in print trials, is ignored.

In this study, a comparison between the numerical analyses and experimental results strengthens the necessity to correctly characterize the behavior of printing materials. Specifically, time-dependent material behaviors of 3D printed concrete are characterized through the uniaxial compression test, in which up to 20% material variation has been experimentally reported [2, 12]. Considering that structural analyses of printed objects are performed based on the average material stiffness and strength of green strength tests, the deviation on buildability quantification around 12% can be considered an excellent quantitative agreement.

Nonetheless, the critical printing heights computed from lattice model are lower than those in actual print trials in both validation cases. This suggests that there are some effects that are not incorporated into numerical analyses which may positively affect the build-up performance. Three possible reasons may be hypothesized. First, the material stiffness and strength experimentally established by green strength test

in the literature might be lower than real values in 3D printing trials due to the compaction influence, especially for material B. Besides, the unconfined compression test is utilized to characterize material stiffness, while a fully fixed boundary condition is employed in printing trials. In reality, low friction in terms of boundary condition might cause a reduction in material stiffness [2].

The 3D printing process also causes the material to heat up, which is ascribed to the friction in the mixer-pump and the hose. This may influence the mechanical and rheological behaviors [24] due to speeding up of the hydration process, especially for larger objects with a longer printing process. Recently, an outcome of the ultrasound tests conducted by Wolfs et al. [2] showed an influence of temperature on structural properties of 3D printing materials at the early age.

The time-dependent deformation at early stage, consisting of shrinkage and creep, may also affect the structural stability by means of stress redistribution and local deformation. But to the best of our knowledge, the influence of early-stage shrinkage and creep on buildability has yet to be explained. More experimental research work is essential to be first performed for behind mechanism or input parameters of numerical analyses.

5.5.1 Model limitation and possible extension

In this research, the geometric nonlinearity has been incorporated into lattice model combined with different features of heterogeneity, the structural instability of buckling response can be reproduced and quantitative agreements with experimental data also can be computed by the extended lattice model.

In contrast to the FEM analysis of Wolfs et al. [2, 23], this model can reproduce the buckling failure without a bifurcation analysis or introducing an initial geometrical imperfections. This shows that the buckling response is a combined effect of system heterogeneity and geometry loss during the printing process. Furthermore, for both geometries used for validation, the experimentally observed asymmetry of failure mode can be derived without introducing any initial geometric imperfection; the structural failure due to elastic buckling is attributed to the combined effect of localized damage, geometric nonlinearity and non-uniform gravitational load.

Regarding the limitations of the model and possible future extensions, the updated Lagrangian method and linear elastic assumption have been adopted for solution procedure and material properties, and the structural instability can be simulated through this extended lattice model. However, the viscoelastic properties of fresh 3D printed concrete, including early-age creep and shrinkage, also cannot be simulated using this model. However, more recently, several numerical methods, including experimentally informed lattice model proposed by Gan et al. [25], and lattice modeling the drying shrinkage proposed by Gao et al. [26, 27], showcase the possibility to incorporate viscoelastic behavior into lattice fracture model.

Although potential solutions for time-dependent deformation at early ages are available in terms of numerical analyses, there is no literature available that reveals the mechanisms of these effects in 3D printable concretes and their impact on buildability quantification; a comprehensive study of these factors is a topic of ongoing research and the corresponding analyses will also be incorporated into lattice model in the future.

5.6 CONCLUSIONS

In this chapter, geometric nonlinearity is incorporated into the lattice model to quantify the buildability of printing objects by considering the elastic buckling failure mechanism. The computational uniaxial compression tests were first carried out to calibrate the time-dependent material properties. Subsequently, two buckling-sensitive geometries, a free wall structure and a rectangular layout, were adopted for model validation. Based on the results presented, a number of conclusions and novel points are summarized below:

In 3DCP, several heterogeneity characteristics of printing objects affect the structural stability. When subjected to non-uniform gravitational loading, some localized damage due to material yielding might occur to the printing objects, thereby expediting structural failure. To study their impact on buildability quantification, these heterogeneities should be incorporated into numerical or analytical models.

Using this model, the asymmetric buckling failure mode can be reproduced without introducing any initial geometrical imperfection and bifurcation linear buckling analysis, which are of necessity for published FEM-based models for buildability quantification in 3DCP.

Lattice modelling of printing objects is not only able to reproduce experimentally derived failure modes qualitatively, but also to agree quantitatively with experimental results.

During model validation, some discrepancy between numerical predictions and experimental results is observed. This can be attributed to underestimated material properties, temperature influence and early-age material behavior. This results in differences between the data used for the input (i.e., measured on cast specimens) and the real (i.e., extruded/printed) material properties. It may be useful to devise a better testing methodology that considers the intricacies of the 3D printing process and their influence on the mechanical properties.

This chapter demonstrates that structural failure through elastic buckling for 3DCP can be reproduced by considering non-uniform gravitational loading using lattice model with geometric nonlinearity instead of introducing initial geometric imperfections.

In Chapters 3-5, the most common failure modes in 3DCP i.e., plastic collapse and elastic buckling during the printing process, have been simulated using the discrete

lattice model. In the coming chapters, the dependent-deformation, i.e., creep, will be incorporated into the model to study their effects on the early-age behavior of 3D printed concrete.

REFERENCES

- [1] A. Perrot, A. Pierre, V. Nerella, R. Wolfs, E. Keita, S. Nair, N. Neithalath, N. Roussel, Mechtcherine, From analytical methods to numerical simulations: A process engineering toolbox for 3D concrete printing, *Cement and Concrete Composites* 122 (2021) 104164.
- [2] R. Wolfs, F. Bos, T.J.C. Salet, Triaxial compression testing on early age concrete for numerical analysis of 3D concrete printing, *Cement and Concrete Composites* 104 (2019) 103344.
- [3] R. Wolfs, F. Bos, T. Salet, Hardened properties of 3D printed concrete: The influence of process parameters on interlayer adhesion, *Cement and Concrete Research* 119 (2019) 132-140.
- [4] V.N. Nerella, S. Hempel, V. Mechtcherine, Effects of layer-interface properties on mechanical performance of concrete elements produced by extrusion-based 3D-printing, *Construction and Building Materials* 205 (2019) 586-601.
- [5] V.N. Nerella, M. Krause, V. Mechtcherine, Direct printing test for buildability of 3D-printable concrete considering economic viability, *Automation in Construction* 109 (2020) 102986.
- [6] Y. Chen, S.C. Figueiredo, Z. Li, Z. Chang, K. Jansen, O. Çopuroğlu, E. Schlangen, Improving printability of limestone-calcined clay-based cementitious materials by using viscosity-modifying admixture, *Cement and Concrete Research* 132 (2020) 106040.
- [7] N. Roussel, J. Spangenberg, J. Wallevik, R. Wolfs, Numerical simulations of concrete processing: from standard formative casting to additive manufacturing, *Cement and Concrete Research* 135 (2020) 106075.
- [8] F. Bos, R. Wolfs, Z. Ahmed, T. Salet, Additive manufacturing of concrete in construction: potentials and challenges of 3D concrete printing, *Virtual and Physical Prototyping* 11(3) (2016) 209-225.
- [9] R.A. Buswell, W.L. de Silva, S. Jones, J. Dirrenberger, 3D printing using concrete extrusion: A roadmap for research, *Cement and Concrete Research* 112 (2018) 37-49.
- [10] J. Kruger, S. Zeranka, G. van Zijl, 3D concrete printing: a lower bound analytical model for buildability performance quantification, *Automation in Construction* 106 (2019) 102904.
- [11] B. Nematollahi, M. Xia, J. Sanjayan, Current Progress of 3D Concrete Printing Technologies, *Proceedings of the 34th International Symposium on Automation and Robotics in Construction (ISARC)*, 2017.
- [12] A.S. Suiker, R.J. Wolfs, S.M. Lucas, T.A. Salet, Elastic buckling and plastic collapse during 3D concrete printing, *Cement and Concrete Research* 135 (2020) 106016.
- [13] T. Ooms, G. Vantyghem, R. Van Coile, W. De Corte, A parametric modelling strategy for the numerical simulation of 3D concrete printing with complex geometries, *Additive Manufacturing* 38 (2021) 101743.
- [14] C. Yu, P. Hoogenboom, J. Rots, Extension of incremental sequentially linear analysis to geometrical non-linearity with indirect displacement control, *Engineering structures* 229 (2021) 111562.
- [15] Przemieniecki, J. S., *Matrix structural analysis*, Courier Corporation 1985.
- [16] Z. Chang, Y. Xu, Y. Chen, Y. Gan, E. Schlangen, B. Šavija, A discrete lattice model for assessment of buildability performance of 3D - printed concrete, *Computer - Aided Civil Infrastructure Engineering* 36(5) (2021) 638-655.
- [17] R. Wolfs, F. Bos, T. Salet, Early age mechanical behaviour of 3D printed concrete: Numerical modelling and experimental testing, *Cement and Concrete Research* 106 (2018) 103-116.

- [18] R. De Borst, M.A. Crisfield, J.J. Remmers, C.V. Verhoosel, *Nonlinear finite element analysis of solids and structures*, John Wiley & Sons 2012.
- [19] A.S.J. Suiker, Mechanical performance of wall structures in 3D printing processes: Theory, design tools and experiments, *International Journal of Mechanical Sciences* 137 (2018) 145-170.
- [20] R. Wolfs, Experimental characterization and numerical modelling of 3D printed concrete: controlling structural behaviour in the fresh and hardened state, Eindhoven University of Technology, 2019.
- [21] A. Perrot, D. Rangeard, A. Pierre, Structural built-up of cement-based materials used for 3D-printing extrusion techniques, *Materials and Structures* 49(4) (2016) 1213-1220.
- [22] B. Panda, J.H. Lim, M.J. Tan, Mechanical properties and deformation behaviour of early age concrete in the context of digital construction, *Composites Part B: Engineering* 165 (2019) 563-571.
- [23] R. Wolfs, A. Suiker, Structural failure during extrusion-based 3D printing processes, *The International Journal of Advanced Manufacturing Technology* 104(1-4) (2019) 565-584.
- [24] J.-Y. Petit, K.H. Khayat, E. Wirquin, Coupled effect of time and temperature on variations of yield value of highly flowable mortar, *Cement and concrete research* 36(5) (2006) 832-841.
- [25] Y. Gan, C. Romero Rodriguez, H. Zhang, E. Schlangen, K. van Breugel, B. Šavija, Modeling of microstructural effects on the creep of hardened cement paste using an experimentally informed lattice model, *Computer - Aided Civil and Infrastructure Engineering* 36(5) (2021) 560-576.
- [26] P. Gao, Y. Chen, H. Huang, Z. Qian, E. Schlangen, J. Wei, Q. Yu, Effect of relative humidity on drying-induced damage in concrete: A comparative study of digital image correlation and lattice modelling, *Materials and Design* 196 (2020) 109128.
- [27] P. Gao, Y. Chen, H. Huang, Z. Qian, E. Schlangen, J. Wei, Q. Yu, Investigation of drying-induced non-uniform deformation, stress, and micro-crack propagation in concrete, *Cement and Concrete Composites* 114 (2020) 103786.

6. EARLY-AGE CREEP: EXPERIMENTS AND ANALYTICAL MODELLING

This chapter proposes an experimental setup to characterize the early-age creep of 3D printable mortar. The testing protocol comprises quasi-static compressive loading-unloading cycles, with 180-second holding periods in between. An analytical model based on a double power law was used to establish the relationship between creep compliance, hardening time and loading duration. Subsequently, this analytical model was validated by comparison to uniaxial compression tests in which loading is increased incrementally, i.e., in steps, showing a good quantitative agreement. Minor differences between the two results were noted, most notably at the beginning of the test. This is because the determination of creep compliance for 3D printable mortar at fresh stage depends on the load level. In the end, the volumetric strain of tested samples from uniaxial compressive test is used to explain why the compressive loading affects the creep deformation.

6.1 INTRODUCTION

The 3D printable materials differ from conventional cementitious materials in several aspects: (1) high paste volume; (2) low water to cement (w/c) ratio; (3) addition of viscosity-modifying agent (VMA) [1-3]. These features affect the visco-elastic properties of 3D printable materials in their fresh state; for example, the high paste volume will make shrinkage and creep more pronounced compared to traditional concrete [4]. Moreover, the layer-by-layer extrusion process may result in increased porosity compared to casting [5]. This creates more free space for water movement and may result in higher creep [6]. Thus, understanding the time-dependent deformation of the cementitious materials used in 3DCP is crucial. This type of deformation occurs during the printing process and consists of basic creep, autogenous shrinkage, plastic shrinkage, and the consolidation settlement under compressive load. Since this delayed deformation certainly continues to increase over time under constant compressive loading for cementitious materials at fresh stage, the term ‘early-age creep’ is utilized to define this delayed strain in this PhD project.

Some explorations about the early-age behaviour of 3D printable materials comes from uniaxial compression tests conducted by Esposito et al. [7] and rheological tests performed by Chen et al. [8]. However, the effects of hydration, loading rate, and load level on the determination of creep compliance are not controlled during the testing process. In addition, the relationship between creep compliance with hardening time and loading duration is not known. Therefore, it is difficult to incorporate these experimental data into a numerical or analytical model and investigate their effect on the structural deformation prediction and failure mode simulation.

To capture this kind of delayed deformation during the printing process, herein an early-age creep testing approach is proposed. Then, a relationship between early-age creep and printing time using analytical modelling is established and experimentally validated. Given that the total deformation is what is observed during printing process, this research, therefore, does not distinguish the contribution of each factor (i.e., autogenous shrinkage, drying shrinkage, basic creep and consolidation settlement) to the result. Thus, the proportion of each factor and their influence mechanism on the final deformation is outside of the scope of this study.

6.2 MATERIALS AND METHODS

6.2.1 3D printable mortar

6.2.1.1 Mix design

Here, a printable mortar was designed. To ensure the stiffness and strength after material deposition, a low w/c ratio is utilized for mix design [9, 10]. The 0.0024% of hydroxypropyl methylcellulose-based VMA is also added to the material to increase its viscosity in order to fulfil the criteria of pumpability [11]. Consequently, this material

can be extruded from the nozzle without blocking it. The mix design is given in Table 6-1.

Table 6-1 Compositions of 3D printable materials utilized in this study [kg/m³]

Cement	Water	VMA	Sand (0.01-0.02 mm)	w/c ratio	Cement type
1140	342	0.83	770	0.3	I

6.2.1.2 Pumpability and buildability test

The most straightforward method to assess the printability of cementitious materials is through laboratory tests for pumpability and buildability, as suggested by Le et al. [12]. Fig. 6-1 illustrates the extrusion-based mortar 3D printer utilized in this study. This printer employs a gantry system and a 3D printed plastic nozzle is equipped on the gantry frame to move along in the x - y plane for printing. The print-table can move along the z axis to raise or lower itself to the designed height. The effective printing size is 480 mm (l), 480 mm (w), and 500 mm (h), and the maximum volume of printing material in a batch is 1.5 L. Table 6-2 describes the procedures for sample preparation and buildability test.

Figure 6-2 (a) depicts mortar being extruded from the nozzle. It can be observed that mortar can be smoothly extruded from the nozzle without blockage, which demonstrates its good pumpability. Then, the buildability of this material is evaluated through printing a hollow cylinder geometry and a free wall structure. After 20 layers of deposition, the hollow cylinder geometry with a 150 mm diameter and 6 mm layer height was successfully produced in around 20 mins, as illustrated in Figure 6-2 (b). The critical printing height of the free wall structure was then investigated in the second test, as shown in Figure 6-2 (c). This wall structure, composed of extruded layers with 15 mm width, 4 mm thickness and 350 mm length, failed due to the out-of-plane displacement (i.e., elastic buckling failure mode) at 34 layers. A suitable pumpability and buildability performance can be observed through these three tests. Then, further experimental programs on early-age material characteristics, consisting of green strength and creep behaviour, will be introduced.

Table 6-2 Mixing procedures for the fresh mortar preparation and testing

	Mixing procedures
-2:00	Mix dry blends at low speed using a HOBART mixer
0:00	Add water during mixing
4:00	Stop, start to fill the barrel of the printer
4:00-20:00	Preparation before printing
20:00	Start printing

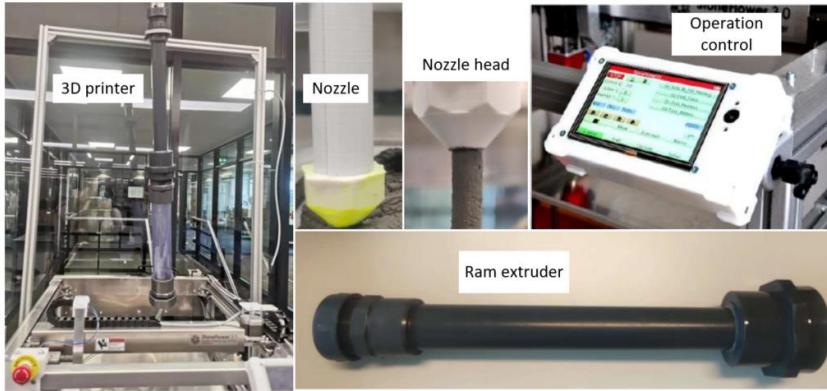


Fig. 6-1 The 3D printer used in this study, and its components

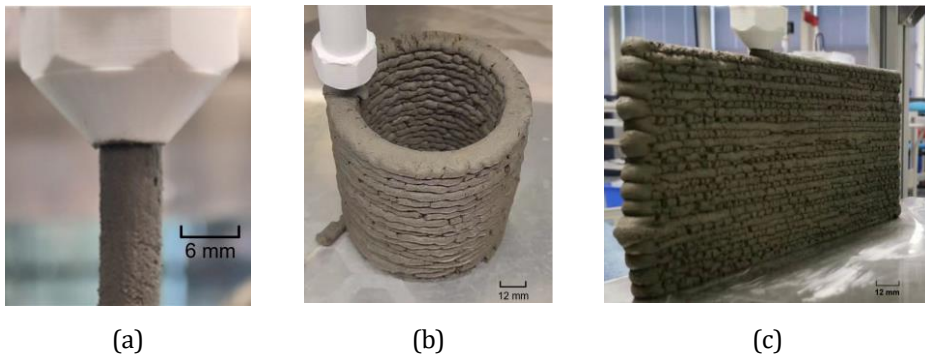


Figure 6-2 Printability quantification of designed material (a) pumpability test (b) buildability test: hollow cylinder structure (c) buildability test: wall structure

6.2.2 Experimental methods

Cement paste generally plays a significant influence in the creep of mortar and concrete [22]. Creep of Portland cement paste is highly co-determined by the porosity and calcium silicate hydrates (C-S-H). Macroscale experiments to evaluate the creep evaluation of hardened cementitious materials usually adopt a low creep loading, below 30% or 45% of compressive strength [13, 14], which aims to exclude the influence of damage on creep measurement. This load ratio is generally adopted for creep analysis of hardened cementitious material; however, it might need to be revised for cementitious materials at fresh stage.

6.2.2.1 Green strength test

The green strength tests were carried out to measure the compressive strength of 3D printable material in the fresh stage [15]. The displacement-controlled compression tests were performed on cylindrical samples, which were 70 mm in height (h) and 70 mm in diameter (d), at a rate of 0.5 mm/s in an Instron equipped

with a 150 N load cell with an accuracy of 0.1 N. This test was performed at multiple fresh mortar ages of $t=20$ and 30 min. Here, $t=0$ was defined as the moment when the water was added to the dry mixture. The displacement is measured through the stroke of the machine. The experimental load-displacement curves and computed stress-strain curves are given in Figure 6-3. The material compressive strength is found to be around 5.1 kPa. The sample stress under a load of 5 N is below 1.7 kPa, which is less than 30% of early-age compressive strength. This stress level is thought to be outside of the non-linear creep domain, which often results in microcracks within the tested samples [16, 17]. On the other hand, this load level results in the creep deformation that can be measured with a high accuracy within the machine sensitivity.

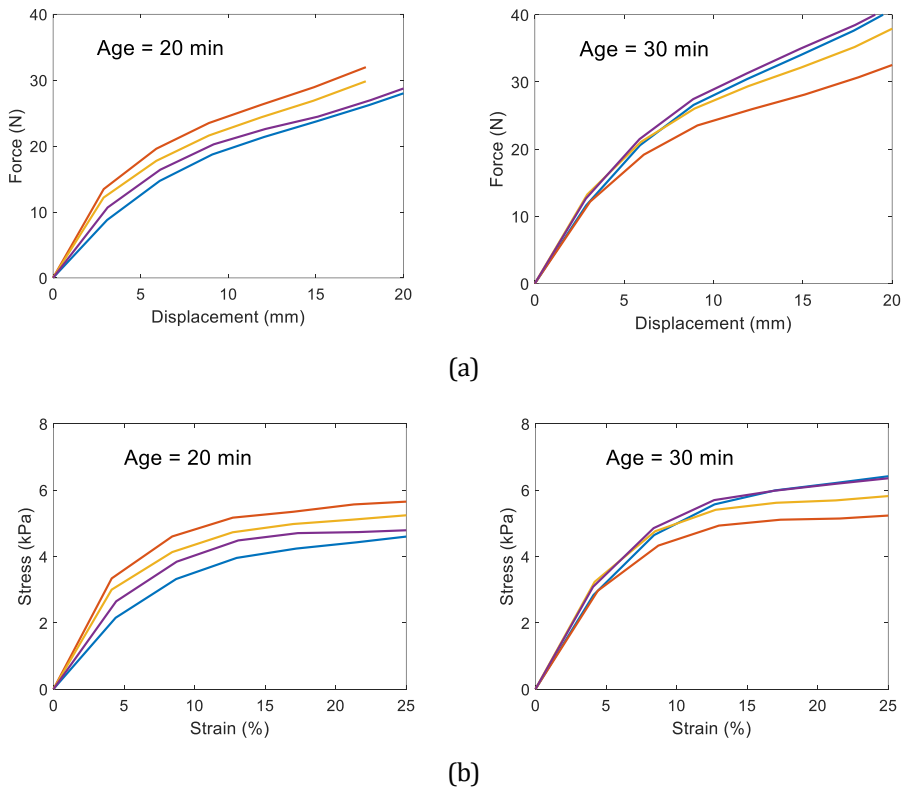


Figure 6-3 Green strength test results (a) load-displacement curves (b) stress-strain curves (different colors represent different samples)

6.2.2.2 Creep test

6.2.2.2.1 Sample preparation

Early-age creep tests under uniaxial compressive loading were performed on cylindrical specimens. The samples are designed with the h/d ratio of 1 to minimize or

eliminate the risk of structural instability during testing. The sample preparation included mixing, placement, and compaction, which take around 10 minutes in total. Subsequently, the prepared samples are placed in the mould for approximately 10 minutes with a sealed cover on the top. The sample for the creep test is then demolded using specialized demolding equipment (as illustrated in Figure 6-4 (a)). This ensures that the sample remains upright, thereby preventing the occurrence of eccentric loading. Oil is used in the mold to reduce friction. In addition, this minimizes the water loss. The absence of bleeding during sample preparation and testing process shows that there is sufficient VMA to ensure water retention [11].

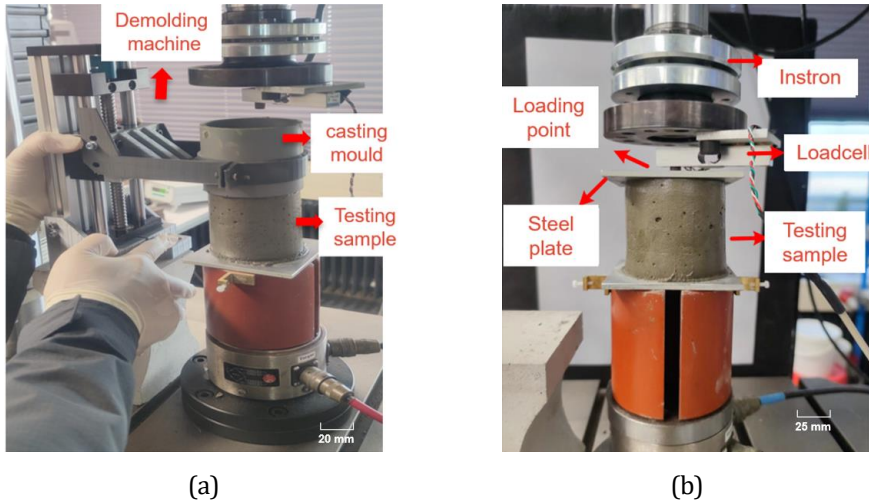


Figure 6-4 Self-developed experimental setup (a) demolding setup (b) creep test setup

6.2.2.2.2 Creep testing

Here, a quasi-static compressive loading-unloading cycle test is performed to characterize the early-age creep of 3D printable material. The test is based on the research of Irfan-ul-Hassan et al. [18]. Since it is difficult to keep the top surface of the testing specimen completely flat in the fresh stage, a rotation boundary condition is introduced into the creep setup. For the loading to remain centric, the compressive loading is transferred from a loading point to a rotatable steel plate. Therefore, the creep loading can be applied to the whole upper surface with a minimum of localized damage. The relative humidity (RH) and the environmental temperature were measured and remained constant during the testing process, i.e., 40% RH and 32 °C. Thus, the plastic shrinkage due to the water loss and temperature fluctuation can be significantly reduced.

This study aims to experimentally derive the creep deformation of 3D printable materials at different hardening times, which refers to clearly different microstructures due to the hydration process and consolidation settlement under a compressive load distribution. The early-age creep experimental program consists of

quasi-instantaneous compressive loading-unloading cycles, as well as 180-second (3 minutes) holding periods in each step. Each cycle takes 10 mins. The loading duration (3 mins) is short enough such that the micro-structure remains unaltered during each three-minute creep test. In the remaining seven minutes, a compressive force of 0.5 N ensures that the sample remains upright. The creep strain rates induced by this stable load decay quickly, such that they can be neglected compared to the significantly larger creep strain captured during the three-minute testing process. The early-age creep tests were performed at multiple fresh mortar ages in the range of 20 to 90 min after material casting.

An infinite loading speed is desirable for a creep test, which is, of course, not possible. Herein, a force-controlled approach is utilized, with a prescribed loading rate of 2.5 N/s, which corresponds to a stress rate of around 1 kPa/s. The overall loading time is 2 s. This quick loading rate ensures that the loading duration is around two orders of magnitudes less than the subsequent constant loading duration of 180 s. Unloading is performed via a force-controlled stress rate, amounting to 1 MPa/s. Following an initial acceleration and before the piston's final deceleration, a constant creep loading is kept on the tested sample during 180 s loading duration. Figure 6-5 shows the physical force path and displacement measured during a loading-unloading creep test. Structural deformation during one loading-unloading event is depicted in Figure 6-6.

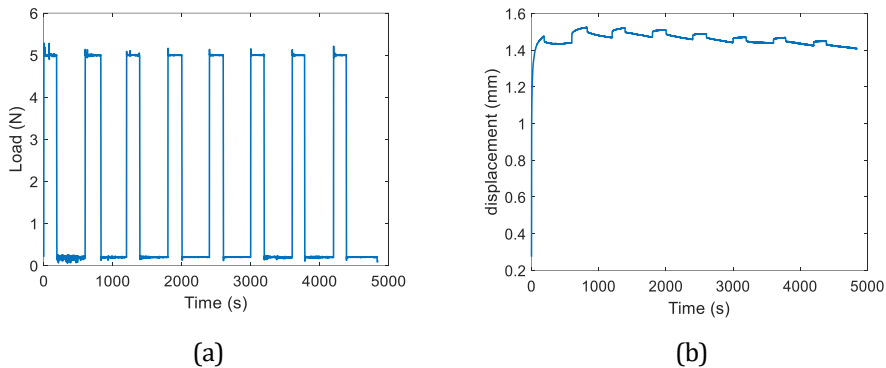


Figure 6-5 Typical force reading capture during the creep test (a) loading path (b) structural deformation (Note that the time 0 in the figures refers to the mortar age of $t=20$ min)

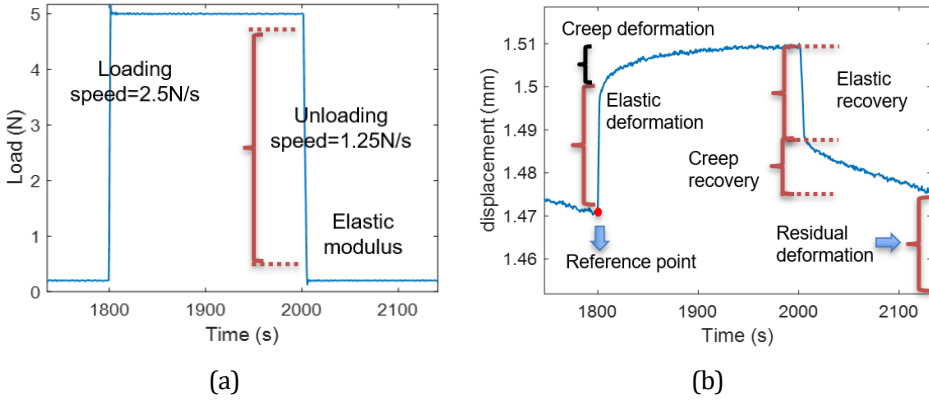


Figure 6-6 Typical loading path and structural deformation in one cycle (a) loading path (b) structural deformation

6.3 ANALYTICAL MODELLING

6.3.1 Theoretical background

The early-age creep deformation is a time-dependent process under constant loading. Since the creep loading in this study is below 30% of green strength, the tested sample is assumed to be undamaged. The entire loading path includes a series of loading steps, and creep is assumed to be independent of one another under various loading steps. Therefore, the previous loading condition does not affect the creep deformation in subsequent stages. As a result, the entire creep response of the printed segments at all time steps can be computed based on the Boltzmann superposition principle, as described in Eq. 6-1.

$$\varepsilon(t) = \int_0^t J(t - \tau, \tau) d\sigma(\tau) \quad \text{Eq. 6-1}$$

Here, J refers to the creep compliance function determined by the hardening time (τ) and loading duration ($t - \tau$); $\Delta\sigma$ is the incremental stress, which may alter due to hydration process and loading condition. Creep occurs in hardened cementitious materials due to the slip between C-S-H particles in a shear process where water acts as lubricant [6, 19]. However, the mechanism behind early-age creep is unknown. While herein an experimental program to investigate the early age creep and analyze creep compliance using the linear viscoelastic theory is proposed, study of governing mechanisms of this behaviour is beyond the scope of this study.

In 3DCP, each printed segment experiences increasing loading due to the subsequent printing layers. The stress history of each printed segment can therefore be divided into a series of loading stages with the time interval Δt . The creep force is applied to the testing sample at the beginning of the interval, and remains constant until the end of the interval (as shown in Figure 6-7 (a)). During the entire printing

process, the structural deformation shows a significant development, including the elastic and creep deformation. The red lines in Figure 6-7 (b) represent the instantaneous elastic deformation caused by the incremental creep load at the onset of each time interval, whereas the black lines refer to the creep evaluation under constant loading at this time interval.

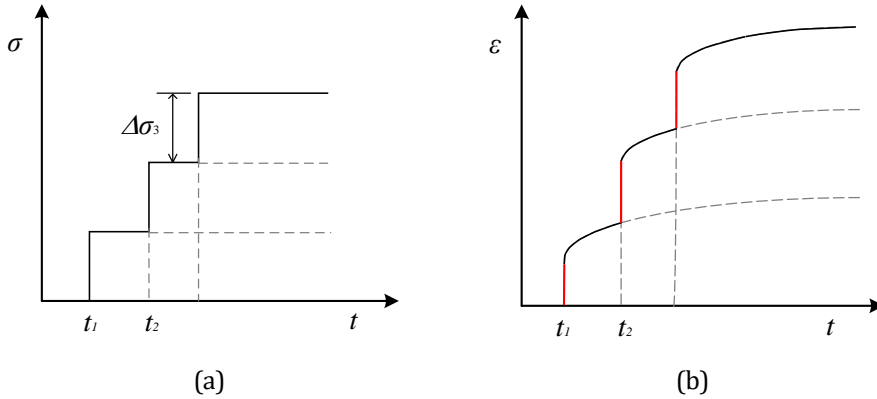


Figure 6-7 Illustration of creep evaluation based on Boltzmann superposition principle: (a) loading history (b) system deformation

Followed by Eq. 6-1, the creep evolution after t_3 is the summation of all the strain curves (i.e., dashed grey curves in Figure 6-7 (b)) which can be expressed as:

$$\varepsilon(t) = \sigma_1 J(t - t_0, t_0) + (\sigma_2 - \sigma_1) J(t - t_1, t_1) + (\sigma_3 - \sigma_2) J(t - t_2, t_2) \quad \text{Eq. 6-2}$$

It can be illustrated that a creep compliance function related to hardening and loading duration is required for structural deformation prediction. In this research, early-age creep experiments at multiple fresh mortar ages will be used to describe this relationship using an analytical model.

6.3.2 Quantification of creep behaviour

Figure 6-5 (b) shows the measured deformation of the tested sample when subjected to compressive creep loading. The initial loading-unloading step causes a comparatively significant proportional plastic deformation. One of the potential causes may be the collapse of macropores/large air voids as a result of the compressive loading. This type of irreversible deformation is not taken into consideration in the creep analysis in order to decrease or eliminate its influence on the computation of creep compliance. When analyzing the experimental data, the second loading-unloading step is where the creep analysis begins, and the initial displacement at the onset of this loading duration is taken as the reference point for this step's creep computation.

In this work, the creep behavior at different fresh mortar ages under constant loading is characterized using a power-law expression as described in Eq. 6-3 [20].

$$\begin{aligned}\varepsilon(t-t_0, t_0) &= \sigma \times C(t-t_0, t_0) \\ C(t-t_0, t_0) &= 1/E_e + 1/E_c \times (t-t_0)^b\end{aligned}\quad \text{Eq. 6-3}$$

Here, E_e is the elastic modulus, E_c refers to the creep modulus, and b is the creep power-law exponent. Through the evaluation of the minimal square creep strain between experimental findings and the analytical model, a set of creep coefficients, comprising creep modulus, elastic modulus, and creep exponent, can be fitted for each creep interval time [18]. This is further discussed in Section 6.4.4.

The relationship between creep compliance and loading time at different hardening times can be determined using Eq. 6-3. The effect of hardening time on the prediction of creep compliance, however, is not well captured or reflected by the fitted power-law function. A double power law expression based on two international standard codes, Euro Code 2 [31] and ACI-209R [32], offers a solution to this problem, and their formulation can be described as:

$$J(t-\tau, \tau) = 1/E(\tau) + C_0 C_1(\tau) C_2(t-\tau) \quad \text{Eq. 6-4}$$

Here, C_0 is a coefficient related to general material properties and microstructure formation as a result of hydration, which is also affected by external conditions like temperature and relative humidity; C_1 is a power function used to study the impact of hardening time (τ) on creep compliance; and C_2 is a power function determined by the non-ageing/loading duration ($t-\tau$) [21].

6.3.3 Determination of unloading elastic modulus

The unloading procedure in this quasi-static compressive creep test is utilized to determine the unloading elastic modulus [20]. Figure 6-6 illustrates the unloading part, in which that the middle part of the curve is used for the calculation of unloading elastic modulus, while discarding the top 10% and the bottom 5% of the unloading curve to minimize error [18], as illustrated in Figure 6-6 (b). Through dividing the residual force reading by the cross-section area of the cylindrical specimen, which is equal to 3846.5 mm², it is possible to calculate the imposed stress. The structural strains can be computed through dividing the machine output displacement by the sample height, which is 70 mm. As a result, the unloading elastic modulus can be determined.

6.4 RESULTS

The proposed early-age creep test provides quantification of temporal evolution of unloading elastic modulus and creep of 3D printable mortar in the time range of 30 to 90 min with a 10-min interval. Three samples are used for the test and all three exhibit similar properties.

6.4.1 Unloading elastic modulus

Figure 6-6 (b) shows the elastic recovery during the unloading process, indicating that this printable material is in viscous-elastic-plastic state. As described in Section 3.2, the unloading elastic modulus can be determined through the calculation of elastic recovery through each cycle's unloading process. Figure 6-8 illustrates how the time-dependent unload elastic modulus grows monotonically with material age. A linear fit can be found, as shown in Figure 6-8. It should be noted that the R -square value is computed between the regression and average experimental data for each time point.

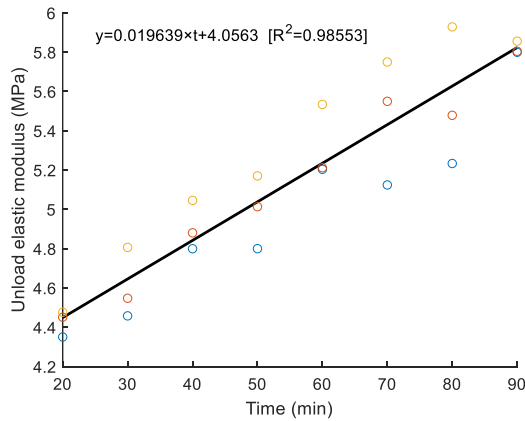
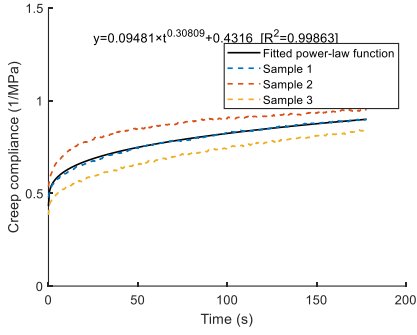


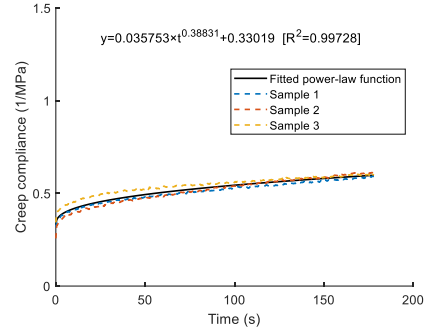
Figure 6-8 Time-dependent unloading elastic modulus

6.4.2 Creep compliance curves

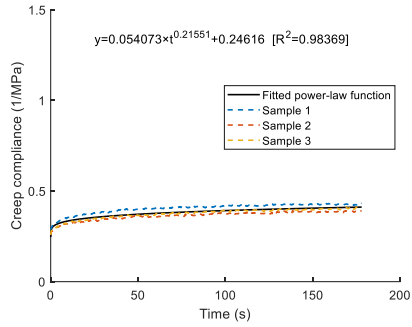
As previously mentioned, the power-law function, as described in Eq. 6-3 is adopted to fit the early-age creep behaviour in the time range from 30 to 90 mins after material deposition. When calibrating the analytical model, the objective function is determined by the R -square value, which reflects the difference between the mean experimental data from three testing specimens and the power-law regression. Figure 6-9 shows the temporal evolution of the creep modulus and calibrated power-law functions at various material ages.



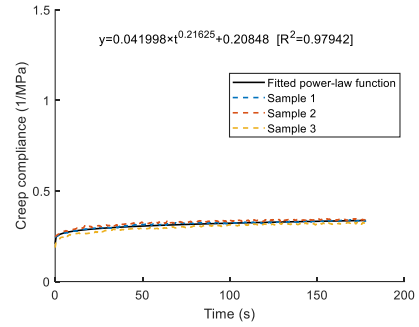
(a) 30 min



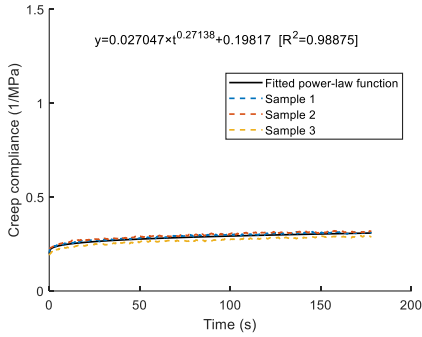
(b) 40 min



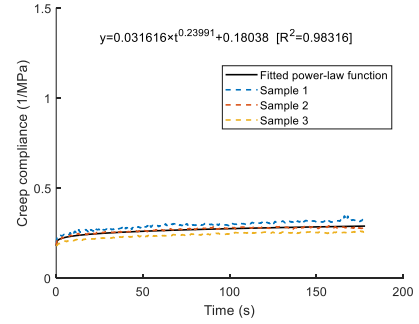
(c) 50 min



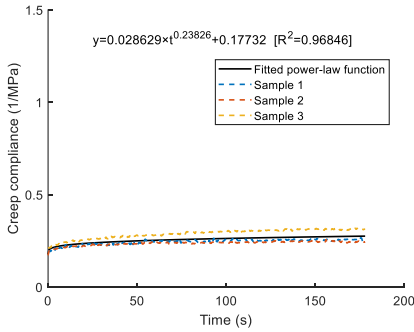
(d) 60 min



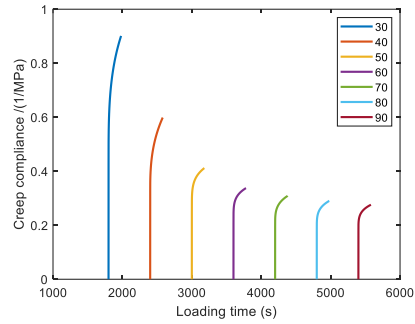
(e) 70 min



(f) 80 min



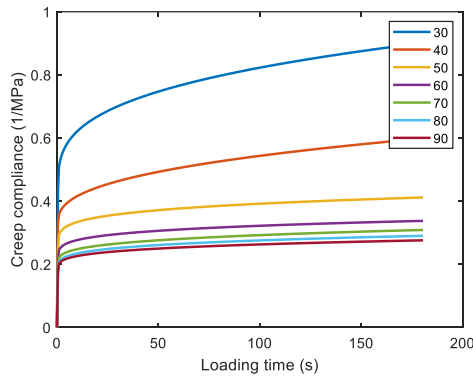
(g) 90 min



(h) Different material ages

Figure 6-9 Time dependent creep compliance at different aging time

It can be seen in Figure 6-9 that the power-law function can fit the early-age creep behaviour with high R^2 . Figure 6-10 describes the development of time-dependent creep parameters with hardening time. Both the creep modulus and elastic modulus increase with the hardening time. Note that this type of delayed deformation differs from the basic creep in hardened cementitious materials. As previously discussed, it is determined by the combined effect of hydration process and consolidation settling under compressive stress distribution. However, this experimental program makes it possible to mimic the time-dependent deformation that occurs in printing trials, which is what we want to measure.



(a)

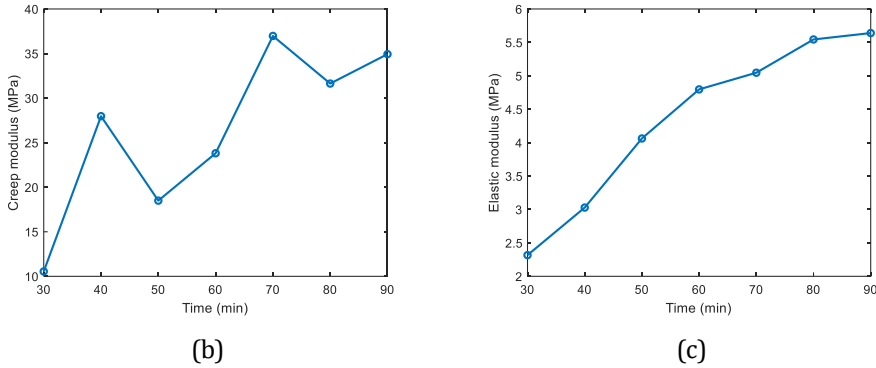


Figure 6-10 Evolution of creep parameters with the increasing age of printable material (a) creep compliance curves at different ages (b) creep modulus with hardening time (c) elastic modulus with hardening time

Based on the experimentally derived creep deformation, analytical modelling was used to compute the creep compliance at different ages. However, the creep deformation during the printing process is associated with mortar age and loading duration, thus a clear relationship between creep compliance and hardening time and loading duration is required.

6.4.3 Creep compliance surface

The influence of hardening time and loading duration on creep deformation can be reflected in a creep compliance surface, as discussed in Section 6.3.2. Here, a double law power expression in Eq. 6-4 is used to describe this relationship. The smallest square root (i.e., the difference between the fitted function surface and experimental data) can be obtained using the optimal creep parameters, which are composed of C_1 , C_2 , C_3 and E . Figure 6-11 describes the fitted creep compliance surface after optimization process.

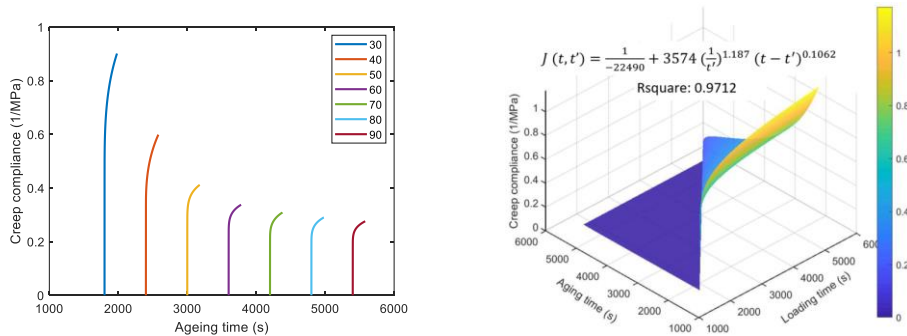


Figure 6-11 Fitted creep compliance surface (a) dataset for function fitting (b) fitted creep compliance surface

6.4.4 Evolution of early-age material properties with hardening time

In this study, this specialized experimental program consists of a 180 s loading period, in which the microstructure remains unaltered due to flocculation and structuration. The experimental results at multiple material ages refer to the different stages of the hydration process. The evolution of unloading elastic modulus and creep modulus describes the impact of hydration process on the material properties. In 3DCP, the printable materials are extruded from the nozzle and placed on the printed structure. The hydration process continues throughout this stage, resulting in varying microstructures. From a microstructural perspective, the flocculation and structuration processes make the printed materials display the initial material characteristic such as yield stress and elastic behaviour. The mixing and pumping processes disperse the cement particles throughout the printing process. After flocculation, these particles connect to form a network that can transfer stress. The elastic material behaviour results from attractive colloidal force while the viscous property is primarily caused by the interstitial water between the cement grains. Although the printable mortar is still in the rest state, solid bridges between the interconnected particles are formed when hydrate nucleation occurs at pseudo-contact points in the network of particles. The structuration process strengthens the bonding among inter-particle connections and causes the loss of workability [22]. Additionally, it can be seen that a stronger framework eventually develops at the microscopic level along with the hydration process. As a result, the elastic modulus increases at the macroscopic level with hydration time, as does creep modulus.

Besides the hydration process, the consolidation settlement under compressive loading is another influential factor for the measured early-age creep in this study. A lot of free space exists between the dispersed cement particles. These dispersed particles are gradually compacted and eventually collapse when subjected to compressive force. This compaction process is similar to the consolidation settlement in soil mechanics [23, 24]. If more voids are compressed, less deformation space may be found. The entire structure has a higher material density as a result.

6.5 MODEL VALIDATION

The fitted creep compliance surface allows predicting creep deformation with the loading condition and printing time as inputs. To verify if this analytical model can predict the early-age creep deformation during printing process, an incremental loading test is designed to mimic the loading condition in 3DCP. The cylindrical sample is the same size as in the previous creep test. Figure 6-12 describes the loading path and obtained structural deformation. The first loading step results in a significant plastic deformation, like the early-age creep test. When analyzing the structural deformation, the onset point of the second loading step is taken as the moment at which data analysis begins.

For creep prediction, the entire loading process can be divided into a series of loading sequences, each assumed to remain constant from the onset of time interval to

the end. As a result, early-age creep under various loading conditions is independent of one another. Thus, the entire creep response of this sample at all time steps can be computed based on the Boltzmann superposition, as described in Section 6.3.1. The total deformation of the sample is a summation consisting of elastic and creep portions.

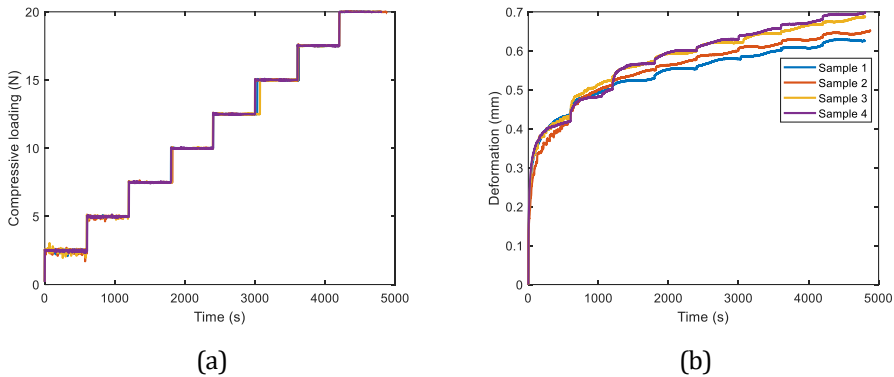


Figure 6-12 Compressive creep test with incremental loading (a) loading path (b) structural deformation (Note that the time 0 in the figures refers to the mortar age of $t=20$ min)

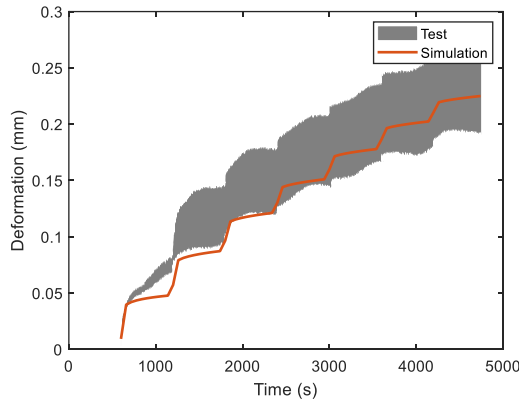


Figure 6-13 The comparison results between the analytical solution and experimental result (Note that the time 0 in the figures refers to the mortar age of $t=20$ min)

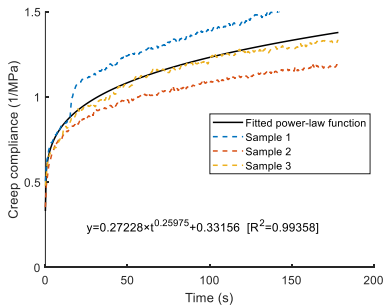
Figure 6-13 demonstrates that analytical modelling of the early-age creep can quantitatively reproduce the experimental results. This indicates that the analytical modelling can account for the stress history and reproduce the time-dependent deformation during the printing process. However, there is some discrepancy between the analytical solution and the experimental data in the initial phase. The variability of the creep data from compressive test could be one of the causes. In particular, the creep loading lower than 30% of compressive strength is used to determine the early-age creep behaviour. This is because that stress level is within the

linear creep domain, which excludes the impact of damage on the time-dependent deformation. However, as discussed before, this assumption originates from creep analysis of hardened cementitious materials. The validity of this assumption may be challenged for cementitious materials in the fresh stage, in which the creep mechanism is possibly different. In the following section, more creep tests with various loading magnitudes are conducted to study the impact of load level on the creep compliance.

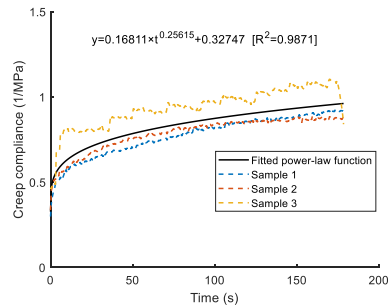
6.6 DISCUSSION

6.6.1 The impact of load level on creep compliance curves

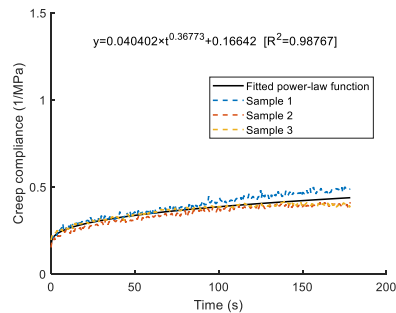
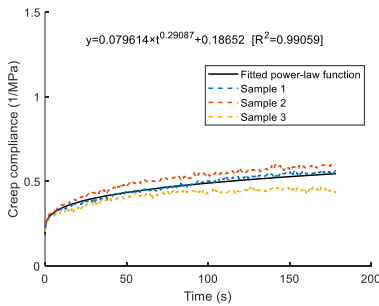
Herein, the same experimental program but with different compressive loading (i.e., 2.5 N and 10 N) is used to characterize the early-age creep at the multiple mortar ages: $t=30, 40, 50, 60$ mins. Figure 6-14 and Figure 6-15 show the experimental findings as well as the calibrated creep curves based on the power-law function. R square reflects the difference between the mean experimental data from three testing specimens and the power-law regression. The fitted results demonstrate that the power-law expression is able to represent the evaluation of early-age creep under different magnitudes of compressive loading. Figure 6-16 describes the evolution of elastic modulus and creep modulus with hardening time at different loading conditions. The experimental finding verifies the previous conclusion, i.e., both the elastic and creep modulus increase with the hardening time.



30 min

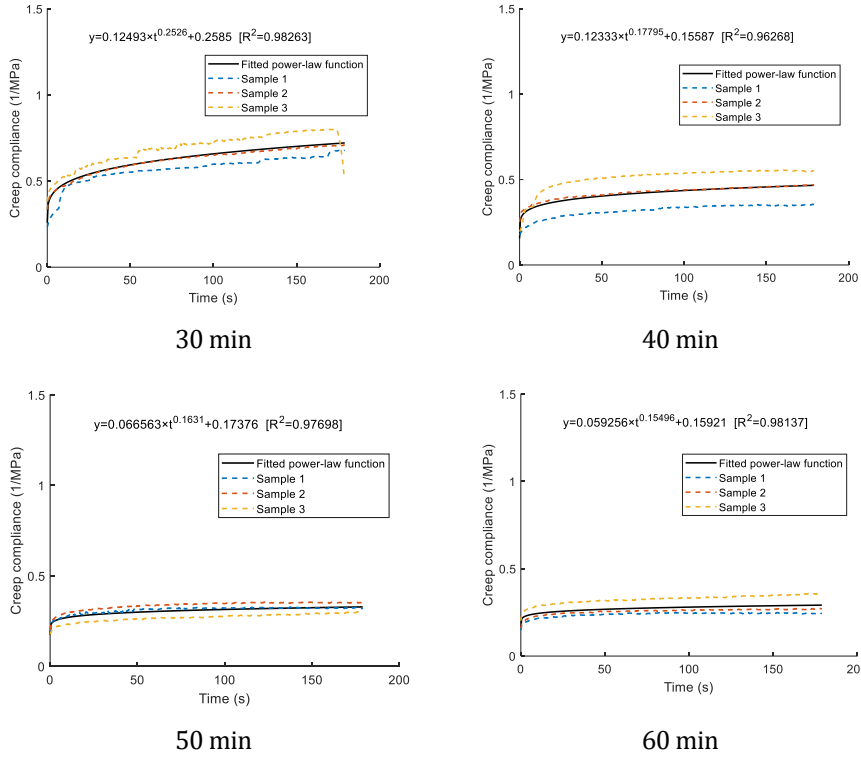


40 min



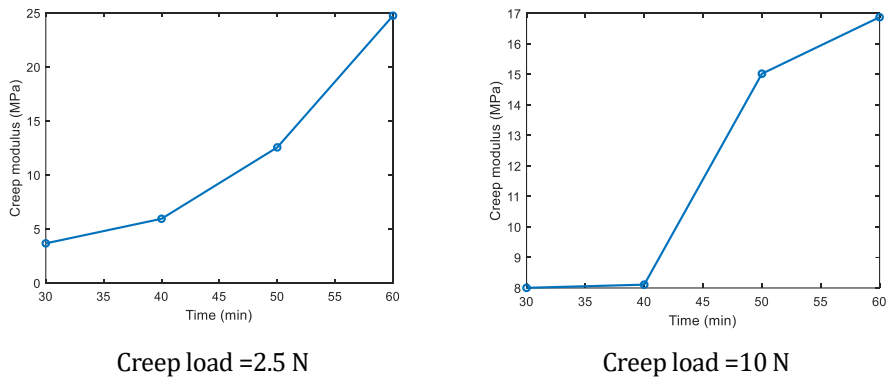
50 min 60 min

Figure 6-14 Creep compliance curves with the compressive load of 2.5 N



50 min 60 min

Figure 6-15 Creep compliance curves with the compressive loading of 10 N



(a)

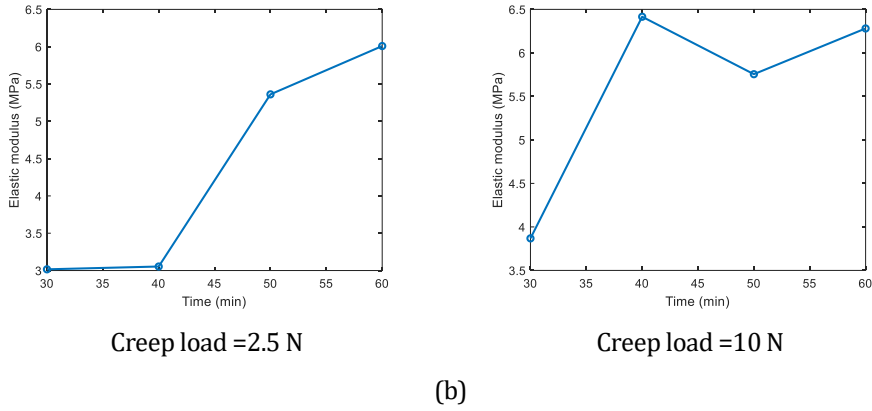


Figure 6-16 The relationship between the creep parameters and hardening time (a) creep modulus (b) elastic modulus

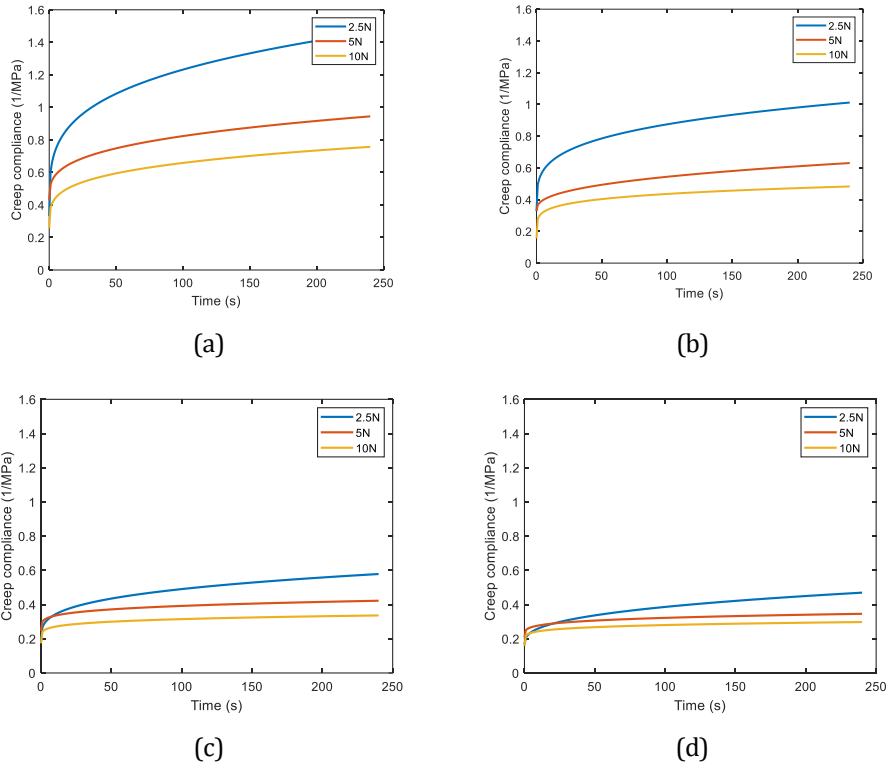


Figure 6-17 The creep compliance curves with different compressive loading (a) 30min (b) 40 min (c) 50 min (d) 60 min

Figure 6-17 shows a comparison of creep compliance with different loading magnitudes for sample ages from 30 to 60 mins. It is found that the creep compliance

decreases as the loading increases. This can help to explain a slight discrepancy between the experimental results and analytical prediction, most notably at the beginning of the test. It is possible that the creep compliance for 3D printable mortar in the fresh stage depends on the load level. More specifically, experimental results from the creep test under 5 N are used to determine the creep compliance. However, the validation test adopts incremental compressive loading starting at 2.5 N with a 2.5 N increment. At the beginning of the test, the compressive load applied to the sample is below 5 N. However, the creep compliance surface obtained from 5 N is adopted to predict the creep deformation. A small difference between the testing results and analytical prediction therefore can be observed. The reason is unclear. To the best of the authors knowledge, only one published article focused on the impact of loading magnitude on the creep compliance [8]. Experimental results from [17], shown in Figure 6-18, conflict with the trends observed herein. In that work, a very small shear force is applied to 3D-printed cement composites using a rheometer to characterize the early-age creep. Their experiments show that the creep compliance increases with the applied shear stress. The rheological test measures the bonding force among particles, which is attributed to flocculation and structuration. In the rheological test, a higher shear stress can create more microcracks, therefore, creep increases with the stress level. In contrast, the uniaxial compression test measures the creep evolution with the consideration of the compaction process of the internal pores. The creep deformation is somewhat similar to the time-dependent deformation of 3D printed segments with high porosity [5, 25]. During the test, the impact of pores or air voids will be reflected through the creep behaviour in macroscale. The higher compressive stress compacts more pores within the tested sample. With the increased compressive load, there are less voids within the tested sample which can be compressed, thereby resulting in less creep. Compared to the rheological test, this kind of uniaxial compression test mainly reflects the impact of compressed internal voids within the tested sample on creep evolution.

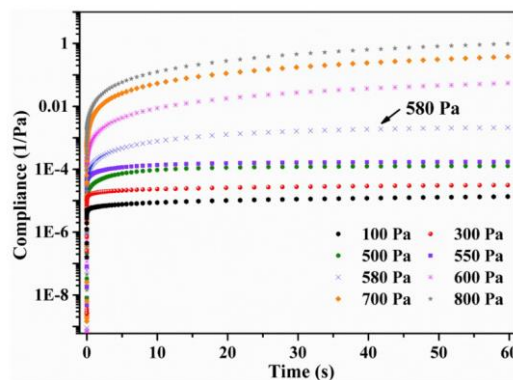


Figure 6-18 Typical creep curves of cementitious materials obtained using rheometer using various shear stress, reproduced from [8].

6.6.2 Volumetric strain under incremental compressive loading

To further investigate why the load level affects the creep compliance, an experimental program is designed to characterize the volumetric strain under the compressive force. Figure 6-19 shows the experimental setup. Two samples are used to test the repeatability of the testing protocol. During the testing process, a camera is utilized to capture sample deformation, and an incremental vertical compressive load is applied at the rate of 0.01 mm/s. The volume of the tested sample in each step is computed based on the horizontal and vertical deformation.

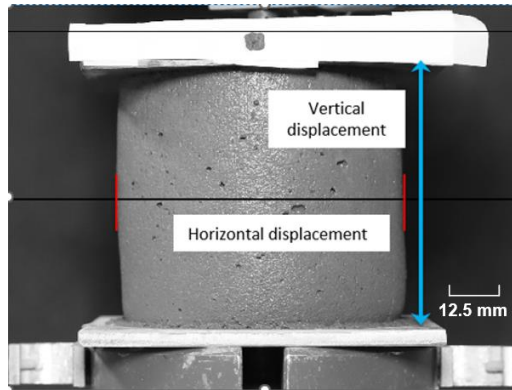


Figure 6-19 Experimental set-up for volumetric strain capture

Figure 6-20 (a) describes the normalized volumetric strain, which is defined as the ratio between the loaded sample volume and the initial one, versus structural vertical strain. It can be observed that the lowest normalized volumetric strain occurs at structural strain about 1%. This suggests that the free space, consisting of voids between cement particles, is compacted under the compressive loading until that vertical strain reaches 1%. After that, a transition of the measured curves can be found, and lateral expansion is observed due to the Poisson's effect. It can be concluded that the lots of internal pores within the tested sample are compressed before the transition point. After that, fewer pores are available to be filled under the compressive load, therefore, less creep deformation for a unit increment in creep load will be derived. Figure 6-20 (b) gives a relationship between compressive loading with structural vertical strain. It can be easily found the equivalent compressive loading at 1% sample strain is below 5 N. According to this inflexion point, as indicated in Figure 6-20 (a), the samples are easily compressed up to a structural vertical strain of 1%, whereas after that point, specimens with collapsed large pores are more difficult to compress under a unit compressive loading.

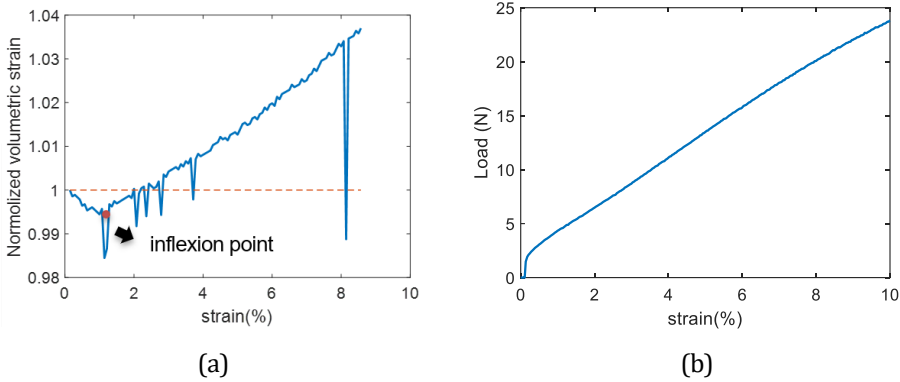


Figure 6-20 Volumetric strain between the experimental program (a) volumetric strain versus sample strain (b) applied force with sample strain

6.7 CONCLUSIONS

In this study, an experimental setup was proposed to characterize the early-age elastic and creep behaviour of 3D printable mortar. The experimental program consists of quasi-static compressive loading-unloading cycles as well as 180-second holding periods in between. Based on the experimental results, a double power-law model is established to describe the relationship between creep compliance and hardening, loading duration. Subsequently, this analytical model was validated by comparison to uniaxial compression tests with incremental loading. Based on this research, the following conclusions can be drawn:

- The printable mortar at fresh stage is visco-elastic plastic; the elastic recovery can be observed during the unloading process and the unloading elastic modulus also can be derived;
- The power-law expression can describe the early-age creep behaviour; both the elastic modulus and the creep modulus increase with hydration time; the possible reasons include consolidation settlement under compressive loading and the hydration process, consisting of flocculation and structuration;
- Analytical modelling of early-age creep behaviour during printing reproduces the experimental results quantitatively; it demonstrates the feasibility of proposed method for time-dependent structural deformation prediction in 3DCP; A small discrepancy between the analytical solution and the experimental data can be found, especially in the initial phase. This is because the underestimation of creep compliance due to the magnitude of creep loading;
- The higher compressive stress indeed results in a lower creep compliance. The inverse tendency can be found from the rheological test in the literature. This is because the different measured characteristics

towards these two methods. In the rheological test, a higher shear stress can create more microcracks, therefore, creep increases with the stress level. In contrast, this uniaxial compression test mainly reflects the impact of compaction process and internal pore on creep evolution.

Through this study, the time-dependent deformation during the printing process in 3DCP can be precisely predicted through a combination of analytical modelling and experimental investigation. Further research will be conducted to study the impact of early-age creep evolution on the prediction of structural deformation and buildability quantification during the printing process of 3DCP.

REFERENCES

- [1] S.A. Nair, S. Panda, M. Santhanam, G. Sant, N. Neithalath, A critical examination of the influence of material characteristics and extruder geometry on 3D printing of cementitious binders, *Cement and Concrete Composites* 112 (2020) 103671.
- [2] B. Lu, Y. Weng, M. Li, Y. Qian, K.F. Leong, M.J. Tan, S. Qian, A systematical review of 3D printable cementitious materials, *Construction and Building Materials* 207 (2019) 477-490.
- [3] M.K. Mohan, A. Rahul, K. Van Tittelboom, G. De Schutter, Rheological and pumping behaviour of 3D printable cementitious materials with varying aggregate content, *Cement and Concrete Research* 139 (2021) 106258.
- [4] F. Bos, R. Wolfs, Z. Ahmed, T. Salet, Additive manufacturing of concrete in construction: potentials and challenges of 3D concrete printing, *Virtual and Physical Prototyping* 11(3) (2016) 209-225.
- [5] Y. Chen, Z. Chang, S. He, O. Çopuroğlu, B. Šavija, E. Schlangen, Effect of curing methods during a long time gap between two printing sessions on the interlayer bonding of 3D printed cementitious materials, *Construction and Building Materials* 332 (2022) 127394.
- [6] B.T. Tamtsia, J.J. Beaudoin, Basic creep of hardened cement paste A re-examination of the role of water, *Cement and Concrete Research* 30(9) (2000) 1465-1475.
- [7] L. Esposito, L. Casagrande, C. Menna, D. Asprone, F. Auricchio, Early-age creep behaviour of 3D printable mortars: Experimental characterisation and analytical modelling, *Materials and Structures* 54(6) (2021) 1-16.
- [8] M. Chen, B. Liu, L. Li, L. Cao, Y. Huang, S. Wang, P. Zhao, L. Lu, X. Cheng, Rheological parameters, thixotropy and creep of 3D-printed calcium sulfoaluminate cement composites modified by bentonite, *Composites Part B: Engineering* 186 (2020) 107821.
- [9] F.P. Bos, Z.Y. Ahmed, E.R. Jutinov, T.A.M. Salet, Experimental Exploration of Metal Cable as Reinforcement in 3D Printed Concrete, *Materials (Basel)* 10(11) (2017).
- [10] Y. Chen, S.C. Figueiredo, Z. Li, Z. Chang, K. Jansen, O. Çopuroğlu, E. Schlangen, Improving printability of limestone-calcined clay-based cementitious materials by using viscosity-modifying admixture, *Cement and Concrete Research* 132 (2020) 106040.
- [11] M. Lachemi, K. Hossain, V. Lambros, P.-C. Nkinamubanzi, N. Bouzoubaa, Performance of new viscosity modifying admixtures in enhancing the rheological properties of cement paste, *Cement and Concrete Research* 34(2) (2004) 185-193.
- [12] T.T. Le, S.A. Austin, S. Lim, R.A. Buswell, A.G. Gibb, T. Thorpe, Mix design and fresh properties for high-performance printing concrete, *Materials and structures* 45(8) (2012) 1221-1232.
- [13] R. Vrijdaghs, M. di Prisco, L. Vandewalle, Uniaxial tensile creep of a cracked polypropylene fiber reinforced concrete, *Materials Structures* 51(1) (2018) 1-12.
- [14] N. Ranaivomanana, S. Multon, A. Turatsinze, Tensile, compressive and flexural basic creep of concrete at different stress levels, *Cement and Concrete Research* 52 (2013) 1-10.
- [15] R. Wolfs, F. Bos, T. Salet, Early age mechanical behaviour of 3D printed concrete: Numerical modelling and experimental testing, *Cement and Concrete Research* 106 (2018) 103-116.
- [16] M.F. Ruiz, A. Muttoni, P.G. Gambarova, Relationship between nonlinear creep and cracking of concrete under uniaxial compression, *Journal of Advanced Concrete Technology* 5(3) (2007) 383-393.

- [17] P. Rossi, J.-L. Tailhan, F. Le Maou, L. Gaillet, E. Martin, Basic creep behavior of concretes investigation of the physical mechanisms by using acoustic emission, *Cement and Concrete Research* 42(1) (2012) 61-73.
- [18] M. Irfan-ul-Hassan, B. Pichler, R. Reihnsner, C. Hellmich, Elastic and creep properties of young cement paste, as determined from hourly repeated minute-long quasi-static tests, *Cement and Concrete Research* 82 (2016) 36-49.
- [19] H. Ye, Creep mechanisms of calcium-silicate-hydrate: an overview of recent advances and challenges, *International Journal of Concrete Structures Materials* 9(4) (2015) 453-462.
- [20] P. Karte, M. Hlobil, R. Reihnsner, W. Dörner, O. Lahayne, J. Eberhardsteiner, B. Pichler, Unloading - based stiffness characterisation of cement pastes during the second, third and fourth day after production, *Strain* 51(2) (2015) 156-169.
- [21] C. Européen, Eurocode 2: Design of concrete structures—Part 1-1: General rules and rules for buildings, British Standard Institution, London: , 2004.
- [22] N. Roussel, Rheological requirements for printable concretes, *Cement and Concrete Research* 112 (2018) 76-85.
- [23] W.Q. Feng, J.H. Yin, A new simplified Hypothesis B method for calculating consolidation settlements of double soil layers exhibiting creep, *International Journal for Numerical and Analytical Methods in Geomechanics* 41(6) (2017) 899-917.
- [24] D. Nash, S. Ryde, Modelling consolidation accelerated by vertical drains in soils subject to creep, *Géotechnique* 51(3) (2001) 257-273.
- [25] J. Kruger, A. du Plessis, G. van Zijl, An investigation into the porosity of extrusion-based 3D printed concrete, *Additive Manufacturing* 37 (2021) 101740.

7. LATTICE MODELLING OF EARLY-AGE CREEP

In this chapter, a new numerical method is proposed to analyze the early-age creep of 3D printed segments with the consideration of stress history. The integral creep strain evaluation formula is first expressed in a summation form using the superposition principle. The experimentally derived creep compliance surface is then employed to calculate the creep strain in the lattice model based on the stored stress history. These strains are then converted into element forces and applied to the analyzed object. The entire numerical analysis consists of a sequence of linear analyses, and the viscosity is modelled using the imposed local forces. The model is based on the incremental algorithm, and one of its main advantages is the straightforward implementation of stress history. The creep test with incremental compressive loading from Chapter 6 is utilized to validate the model. Numerical modelling of early-age creep agrees well with experimental data, demonstrating the feasibility of the lattice model for early-age creep analysis under incremental compressive loading. In addition, a numerical analysis of a printed segment is carried out to demonstrate the impact of early-age creep on the prediction of structural viscoelastic deformation occurring during printing process. The numerical result highlights the necessity of creep for the accurate prediction of viscoelastic deformation of 3D printed concrete.

7.1 INTRODUCTION

In 3DCP, the structural deformation during printing process is codetermined by the instantaneous and time-dependent deformation. The former refers to the elastic-plastic deformation, while the latter refers to the delayed strain, namely, early-age creep mentioned in Chapter 5. Only a few published models investigate the impact of early-age creep on the prediction of structural deformation of 3DCP. Based on the published research, the majority of the creep models are applicable to hardened cementitious materials subjected to constant loading [1-3]. Li et al. [4] have proposed a numerical method to explore the early-age viscoelastic behaviour of hydrating cement paste based on the computer-generated microstructural models. Han et al. [5] presented a nonlinear model to predict early-age creep of concrete (about 2 days) subjected to compressive load. However, early-age creep of conventional cementitious materials, in general, refers to the moment after the final or at least the initial setting time. At that stage, the hydration products grow along with the surface of the cement particles, eventually forming a solid particle skeleton. Creep in the fresh stage (i.e., after casting or deposition from the nozzle in case of extrusion-based 3D printing) has not been considered in the concrete modelling literature.

This chapter aims to propose a numerical method to predict the evolution of early-age creep of 3D printed segments while allowing for stress history of individual elements. The creep analysis consists of a sequence of linear analyses, in which the elastic and creep coefficients are determined based on creep tests. The viscosity can be simulated via an imposed local force, which is similar to the effective elastic modulus method proposed by Bažant [6-8]. A series of non-ageing/ageing creep tests are then employed for model validation.

7.2 METHODOLOGY

This section summarizes the fundamental theory of viscoelasticity and analytical models for prediction of creep compliance. The method for computing the creep strain of each element will next be presented with the computed creep compliance and stored element stress as inputs. At the end of this section, the incorporation of creep strains into the lattice model with an incremental algorithm is discussed.

7.2.1 Theoretical background

Laboratory studies of 3DCP demonstrate that the structural deformation of printed segments at fresh stage tends to increase when the gravitational loading is maintained at a constant level. The term "early-age creep" is commonly used to describe this phenomenon.

To describe the early-age creep under incremental compressive loading, the stress history must be considered. However, storing the entire stress history will result in a high computational cost and extensive memory use. To address this issue,

numerous methods have been proposed to simplify the computation of creep strain, such as the rate-type creep approach [9, 10], effective modulus method [11], ageing coefficient method [12], parallel creep method [13], and others [14]. Using these methodologies, the integral stress-strain relation of creep evolution can be converted into new formulations that only store a limited number of history variables instead of the entire loading history. For instance, the continuous creep function is transformed into the Dirichlet series approximation using the rate-type technique. However, the Dirichlet series expansion involves numerous empirical parameters which are difficult to identify correctly [15].

Herein, a numerical model to predict this delayed deformation during the printing process is proposed; it does not distinguish the contribution of some influential factors like plastic and autogenous shrinkage, nor the consolidation settlement under compressive stress. The creep behaviour of cementitious materials can be analyzed using linear viscoelasticity, which enables the consideration of the entire stress history. The eq. (6-2) explains how to compute the creep strain of lattice elements by means of Boltzmann superposition principle.

It must be noted that the Boltzmann superposition is only valid if each period is assumed to be independent. In other words, previous loading steps do not affect the creep response resulting from the applied force at later stages. The superposition principle is valid given that all the principal stresses are below 40-50% of uniaxial strength [16, 17]. In that case, the analyzed object is not damaged, and linear elasticity is valid [17]. When it comes to a higher stress level, a damage law must be incorporated into the numerical model for non-linear creep behaviour description [6, 18].

7.2.2 Lattice model implementation

Section 7.2.1 briefly describes how to compute the creep strain of lattice elements. In this section, these computed strains will be converted into element forces and applied to the elements. This approach is termed 'local force method' herein. The detailed procedures about model implementation can be found in Figure 7-1.

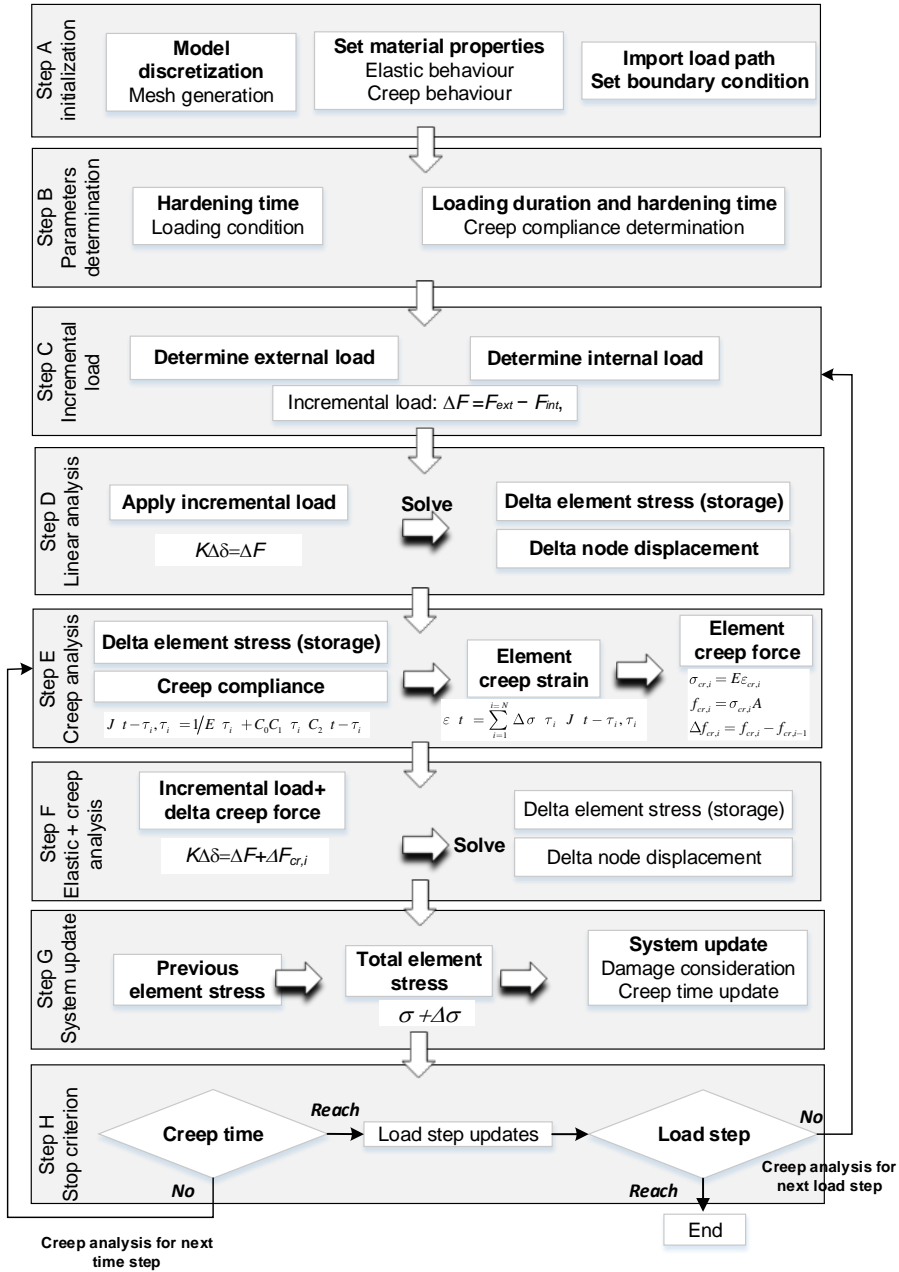


Figure 7-1 Flowchart about Lattice model on creep analysis

This flowchart describes how lattice model simulates the viscoelasticity behaviour of 3D printable mortar, which includes 8 steps, A, B, C, D, E, F, G, and H.

Step A: Model discretization.

Model discretization is the same with the 3D printing model. The relevant material properties are assigned to the beam elements. Besides, the designed load path is imported into the lattice model as the external boundary for creep and fracture analysis.

Step B: Determination of creep parameters

When it comes to the creep analysis, the creep compliance plays a significant role, and can be computed with the hardening time and loading duration as inputs. The obtained creep compliance is then incorporated with the superposition principle for the calculation of element creep strain, as expressed by Eq. 6-2.

Step C: Incremental load.

The difference between the external and internal loading is defined as a disequilibrium force in the incremental algorithm, as expressed by Eq. 5-1. The former refers to the loading condition imported from the load path while the latter is computed considering the internal force as well as element orientation.

Step D: Linear analysis.

In this step, the numerical equation is solved by means of the conjugate gradient method.

Step E and F: Creep analysis.

Given the known creep compliance and obtained delta element stress, the creep strain of individual elements can be computed based on Eq. 6-1. These element strains are then converted into axial forces. The difference between two steps' creep forces is defined as incremental creep force in each analysis step. These forces are calculated as:

$$\begin{aligned}\sigma_{cr,i} &= E\varepsilon_{cr,i} \\ f_{cr,i} &= \sigma_{cr,i}A \\ \Delta f_{cr,i} &= f_{cr,i} - f_{cr,i-1}\end{aligned}\tag{Eq. 7-1}$$

Here, E refers to the elastic modulus of printable mortar and A is the area of cross-section of lattice beam. f and σ are element force and stress for creep analysis. This derived delta creep force $\Delta f_{cr,i}$ is then applied to the lattice element, as shown in Figure 7-2, together with the previously computed disequilibrium force in each step. These applied local forces enable the simulation of time-dependent deformation. In this study, this kind of solution approach is defined as 'local force method'. Using this method, the entire viscoelastic analysis can be conducted by solving a series of fictitious elastic problems. This is similar to the effective modulus approach proposed by Bažant [8], with the exception that the local force instead of the effective modulus is updated in each analysis step.

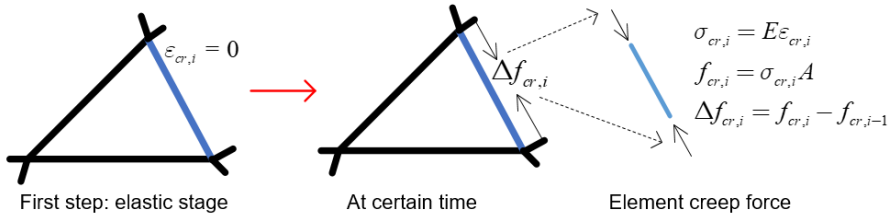


Figure 7-2 The creep deformation and local axial force of an individual beam element.

Step G: System update.

In the lattice model, the entire simulation process consists of a sequence of linear analysis steps, in which the lattice beam is assumed to be linear elastic. The comparative stress within the individual element can be computed using Eq. 3-3. When the element stress is lower than the material strength (compressive or tensile), the Boltzmann superposition is valid because the element is in an undamaged state. Once the stress exceeds the material strength, this element will be removed from the mesh system, allowing for damage initialization and propagation. Creep analysis with the inclusion of element removal mechanism is adopted in the model to simulate the creep evolution under high load level (i.e., higher than 40%-50 % material strength).

In each analysis step, those elements whose stress is higher material strength will be removed from the system, representing a series of cracks. A group of equivalent element forces, consisting of normal force, shear force, bending moment and torsion, is utilized to replace this removed element for stress redistribution. The system stiffness is then updated considering the broken elements. In this way, the non-linear material behavior can be simulated in a sequence of linear analysis steps.

Step H: Stop criteria.

For creep analysis under various loading conditions, two stop criteria are utilized. The first one regulates the timing of each loading component. When the numerical analysis reaches the loading duration of a given step, it moves into the following step. The entire numerical analysis stops until the whole load path is applied to the mesh system.

7.2.3 Model applicability

This newly proposed model adopts the local force method to simulate the viscosity behaviour of cementitious materials, similar to the effective elastic modulus method [6]. The model is based on the incremental algorithm and one of the main advantages is the straightforward implementation of stress history consideration. Besides, this method significantly reduces the computational cost and memory intensity since it stores just one stress parameter (i.e., element comparative stress) at each step of the analysis. In addition, the lattice model adopts the linear elastic analysis for individual steps. Once the computed stress is below material strength,

there is no damage to individual elements. Thus, those lattice elements are in the elastic stage, the Boltzmann superposition for creep strain computation of each element is always valid. As a result, the lattice model with element removal technique and the incremental algorithm is valid for creep analysis of cementitious materials under high load levels.

7.3 MODEL VALIDATION

7.3.1 Comparison with the analytical solution

In this section, the predicted results from the lattice model are compared with the analytical solution. In addition, step size sensitivity analysis is carried out to investigate its influence on deformation prediction. The model dimension is 100 by 100 mm with a mesh resolution of 1 mm. Each load step must be independent; damage is therefore not considered in this numerical case study. Three different step sizes, namely, 1s, 3s, and 5s, are used for the sensitivity analysis. Eq. 7-2 describes the input creep function, and the initial hardening time is 2400 s. The load path includes two parts, as shown in Figure 7-3 (a).

$$J(t - \tau_i, \tau_i) = 1/4.2254 + 59.75 \times \tau_i^{1.055} \times (t - \tau_i)^{0.1193} \quad \text{Eq. 7-2}$$

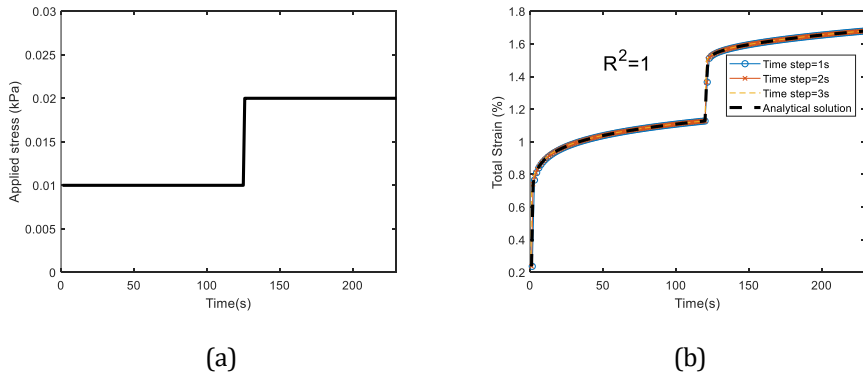


Figure 7-3 Creep analysis on incremental compressive load (a) load path (b) structural strain

Figure 7-3 (b) shows a comparison between the analytical solution and predicted results using the lattice model with different step sizes. It can be concluded that all of them reproduce the analytical solution quantitatively, namely $R^2 = 1$. It means this newly proposed model can account for the impact of stress history and accurately describe the creep behaviour of cementitious materials.

7.3.2 Early-age creep test of 3D printable mortar

7.3.2.1 Non-ageing creep tests

The non-ageing creep tests conducted in Chapter 6 are adopted for model validation. Detailed information about the sample preparation and testing process can be found in Chapter 6.

Here, the power-law function is assumed and directly adopted to fit the creep evolution of experimental findings for 3D printable materials. The creep compliance function can therefore be expressed by Eq. 7-3.

$$J(t - \tau_0, \tau_0) = 1/E_e(\tau_0) + 1/E_c(\tau_0)(t - \tau_0)^\beta \quad \text{Eq. 7-3}$$

Here, E_e and E_c refer to the elastic and creep modulus of all lattice beams; β is the creep exponent. The fitted power-law expressions are then introduced into the lattice model as inputs for creep strain computation of beam elements.

The 3D numerical model is built with a mesh size of 3 mm, which consists of 10,255 lattice nodes connected by 74,195 Timoshenko beams. The radial deformation at the top and bottom sides are fixed to mimic the high friction boundary in the real test. The analyzed object is subjected to the uniaxial compressive force of 5 N. Figure 7-4 (b) gives the schematic diagram of the numerical model for creep analysis.

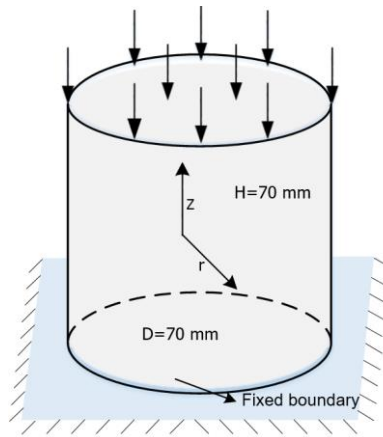
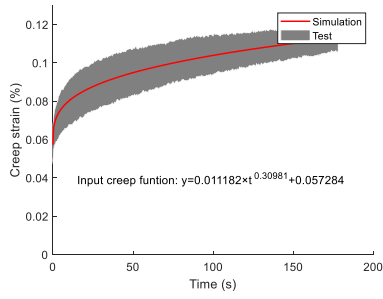
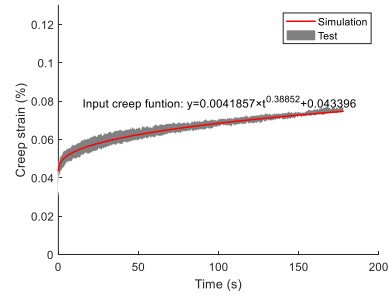


Figure 7-4 Schematic diagram of creep simulation

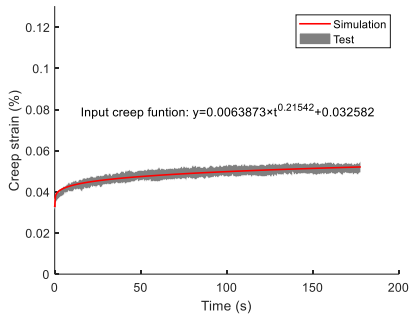
Simulated creep deformation is then compared with experimental findings. Figure 7-5 shows the comparisons between the experimental results and numerical predictions. It can be seen that lattice modelling of the early-age creep is in good agreement with experimental data. This demonstrates the feasibility of the lattice model on non-ageing creep evolution of cementitious materials in the fresh stage.



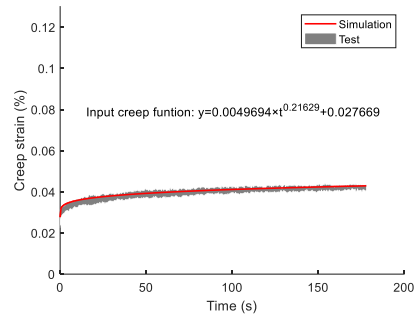
(a)



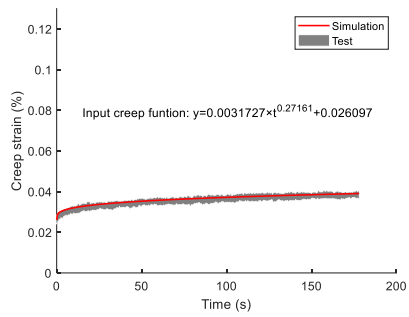
(b)



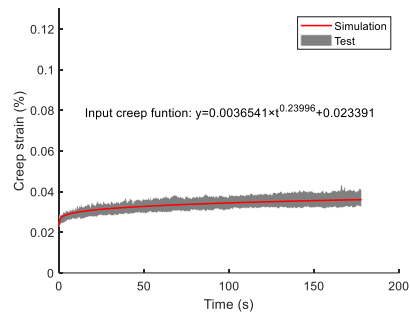
(c)



(d)



(e)



(f)

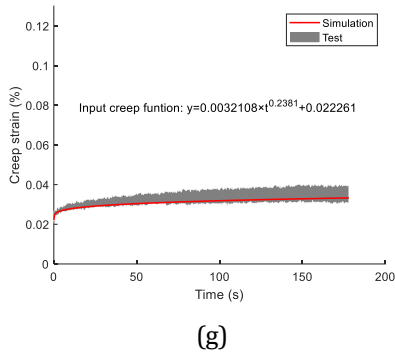


Figure 7-5 The comparison between experimental finding and numerical results on early-age creep evolution at multiple mortar ages. (a) 30 min (b) 40 min (c) 50 min (d) 60 min (e) 70 min (f) 80 min (g) 90 min

7.3.2.2 Ageing creep test

In this section, the ageing creep test with incremental loading condition is utilized to verify whether this newly proposed model can reproduce the creep evolution under the incremental compressive loading. The input parameters can be derived from Figure 7-6 and Figure 6-11. Figure 7-7 shows a comparison between the simulation and the experiments in relation to the creep deformation subjected to incremental compressive loading. Lattice modelling of early-age creep evolution can reproduce the experimental results. This quantitative agreement suggests that this newly proposed model enables to account for the effect of time-dependent material properties and the stress history, thereby producing a similar early-age creep deformation with the actual test. Although the modelling results are similar to the experiments, some discrepancy between the predicted values and experimental data can still be found, particularly at the beginning of the loading stage. The main cause is due to the impact of load level on creep compliance determination, which is examined experimentally in Chapter 6.

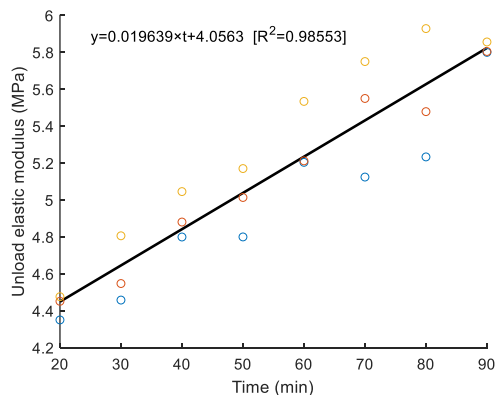


Figure 7-6 Time-dependent elastic modulus for creep analysis through lattice model

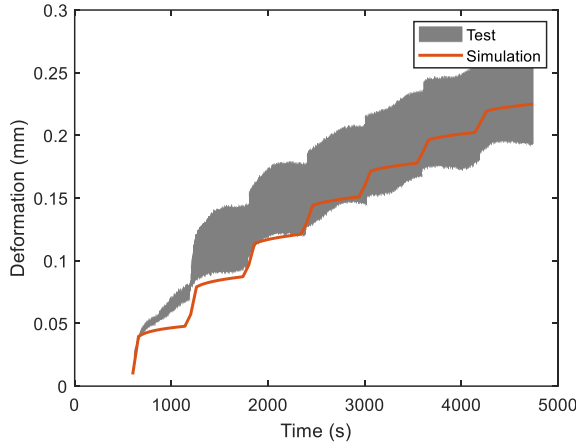


Figure 7-7 Comparison between lattice modeling and experimental result for early-age creep analysis

7.4 DISCUSSION

The above numerical analyses show that the proposed model can account for the stress history and simulate the creep behaviour of cementitious materials from fresh to hardened stages. In this section, the impact of hardening time and loading duration on creep analysis will be quantified through a series of numerical simulations. Subsequently, the early-age deformation of printed segments will be modelled to study the effect of creep on the prediction of structural deformation.

7.4.1 Hardening time and loading duration

In 3DCP, a specific printed segment may experience different loading situations during the printing process (namely, constant, unloading and loading situations). During the loading period, the hardening time and loading duration codetermine the creep evolution. When it comes to the unloading process, the creep recovery plays a significant role in predicting the structural response and understanding the mechanism of creep behaviour.

In this section, a 3D numerical model with a diameter of 70 mm and a height of 70 mm is built. The mesh size equal to 3 mm is adopted. The whole model consists of 10,255 lattice nodes connected by 74,195 Timoshenko beams. The step size is set to 6 s in these analyses. Detailed information about these numerical analyses can be found in Table 7-1. The input parameters about creep compliance are mathematically described in the following equation.

$$J(t - \tau_i, \tau_i) = 1/4.6453 + 23260 \times \tau_i^{1.363} \times (t - \tau_i)^{0.1167} \quad \text{Eq. 7-4}$$

These numerical cases adopt the elastic modulus as constant values to ensure the single variable analysis. A loading-unloading process is utilized to explore the model feasibility to simulate the creep recovery and investigate the impact of time (hardening time and loading duration) on creep analyses.

Table 7-1 Parametric analyses of early-age creep with different loading duration and hardening times

Case	Applied force (N)	Hardening time (s)	Loading duration (s)	Unload force (N)
1	5	1800	300	0.5
2	5	1800	600	0.5
3	5	1800	900	0.5
4	5	180	600	0.5
5	5	18000	600	0.5

Figure 7-8 describes the creep development of cementitious materials with different input parameters. It can be illustrated that both the loading duration and hardening time affect the creep evolution. Given the loading duration extends three times, the final strain of analyzed sample increases from 0.1814% to 0.2027%. The final system strain with 180 seconds of hardening time is more than 100 times larger than that with 18000 seconds of hardening time, indicating that the hardening time has a greater impact on creep evolution than the loading duration. In 3DCP, the hardening time refers to the moment when the printable materials are extruded from the nozzle and placed on the print bed. It can be inferred that the initial printing time may highly affect the structural deformation during printing process. Relevant numerical analyses are essential to explore the impact of early-age creep on the prediction of structural deformation in 3DCP. In addition, the elastic and creep recovery can be observed during the unloading process, which demonstrates that the proposed model is able to simulate the creep recovery behaviour of cementitious materials.

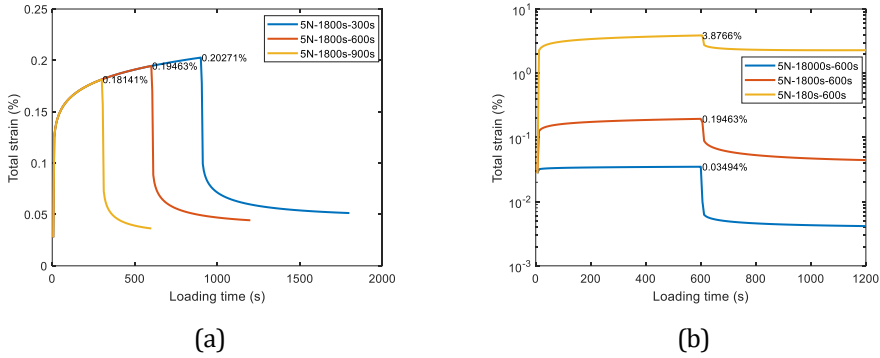


Figure 7-8 Lattice modelling the creep evolution with various hardening time and loading duration (a) loading duration (b) hardening time

7.4.2 Creep analysis of a 3D printed segment

During the printing process, cementitious materials are extruded from the nozzle and placed on the deformed geometry, as described in Figure 7-9. The compressive force from the subsequent printing layers is applied to one specific printed segment. Together with the self-weight, these forces codetermine the structural deformation, which includes the elastic, plastic, and time-dependent deformation.

This section will study the early-age creep influence on structural viscoelastic deformation. The model presented in the previous section is adopted and the creep compliance described in Figure 7-6 (b) is utilized. It should be noted that the elastic modulus is taken as constant value during the numerical process. Figure 7-9 (a) describes the loading path of this printed segment, and Figure 7-9 (b) demonstrates the structural deformation with or without the consideration of creep. It should be noted that the red and orange curves refer to the creep evolution with different ageing times (namely, 600 s and 1800 s). It can be seen that the structural deformation with the consideration of creep increases significantly compared to that not considering creep. In particular, the strain in the model with the ageing time equal to 600 s is more than 20 times larger than the one without creep. This demonstrates the necessity of considering creep for predicting the deformation of a printed system. In next chapter, early-age creep will be incorporated into the 3DCP model for buildability quantification to study its impact structural deformation prediction.

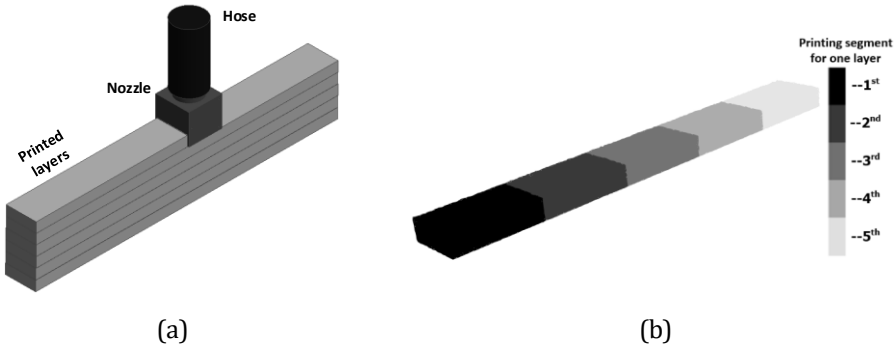


Figure 7-9 Schematics of the printing process (a) entire printing process (b) one specific printed segment within one printing layer

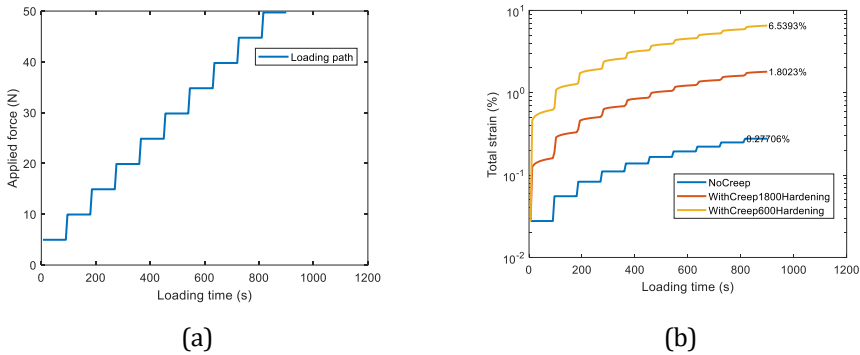


Figure 7-10 Numerical analysis the deformation development of one specific printed segment (a) loading path (b) vertical structural deformation

7.5 CONCLUSIONS

In this chapter, a numerical method was proposed to analyse the early-age creep of 3D printable mortar. The creep compliance surface and time-dependent material behaviours obtained from Chapter 6 were taken as input parameters. The model was then validated through a creep test with incremental compressive loading. Below are some insights and conclusions.

- The local force method is suitable for simulating the viscoelastic behavior of cementitious materials. One of the main advantages of this approach is the straightforward implementation of stress history. This solution method requires no approximation of the creep constitutive law, and reproduces exactly with the solution;
- The superposition principle is incorporated into the lattice model based on the incremental algorithm. The entire simulation of creep includes a sequence of linear analyses. Lattice modelling of the early-age creep is in

good agreement with experimental results. It demonstrates the model ability for creep analysis of 3D printable mortar under incremental/constant compressive loading;

- When predicting structural deformation of 3D printed concrete, hardening time has a greater influence on the determination of creep development than loading duration. In comparison to the model without early-age creep consideration, the numerical result shows a very different prediction on viscoelasticity deformation. This highlights the necessity of considering creep for accurate prediction of viscoelastic deformation for 3D printing concrete.

REFERENCES

- [1] R. De Borst, Smeared cracking, plasticity, creep, and thermal loading—A unified approach, *Computer methods in applied mechanics and engineering* 62(1) (1987) 89-110.
- [2] S. Murakami, Y. Liu, M. Mizuno, Computational methods for creep fracture analysis by damage mechanics, *Computer methods in applied mechanics and engineering* 183(1-2) (2000) 15-33.
- [3] H. Alberg, D. Berglund, Comparison of plastic, viscoplastic, and creep models when modelling welding and stress relief heat treatment, *Computer methods in applied mechanics and engineering* 192(49-50) (2003) 5189-5208.
- [4] X. Li, Z. Grasley, E.J. Garboczi, J.W. Bullard, Modeling the apparent and intrinsic viscoelastic relaxation of hydrating cement paste, *Cement and Concrete Composites* 55 (2015) 322-330.
- [5] B. Han, H.-B. Xie, L. Zhu, P. Jiang, Nonlinear model for early age creep of concrete under compression strains, *Construction and Building Materials* 147 (2017) 203-211.
- [6] Z.P. Bazant, R. L'Hermite, Mathematical modeling of creep and shrinkage of concrete, (1988).
- [7] Z.P. Bažant, Prediction of concrete creep and shrinkage: past, present and future, *Nuclear engineering and Design* 203(1) (2001) 27-38.
- [8] Z.P.J.A.C.I. Bazant, Prediction of concrete creep effects using age-adjusted effective, 69(4) (1972) 212-217.
- [9] G. Di Luzio, L. Cedolin, C. Beltrami, Tridimensional long-term finite element analysis of reinforced concrete structures with rate-type creep approach, *Applied Sciences* 10(14) (2020) 4772.
- [10] S.-G. Kim, Y.-S. Park, Y.-H. Lee, Rate-type age-dependent constitutive formulation of concrete loaded at an early age, *Materials* 12(3) (2019) 514.
- [11] K. Kovler, Drying creep of concrete in terms of the age-adjusted effective modulus method, *Magazine of Concrete Research* 49(181) (1997) 345-351.
- [12] Z. Cheng, R. Zhao, Y. Yuan, F. Li, A. Castel, T. Xu, Ageing coefficient for early age tensile creep of blended slag and low calcium fly ash geopolymer concrete, *Construction and Building Materials* 262 (2020) 119855.
- [13] Y.-S. Park, Y.-H. Lee, Y. Lee, Description of concrete creep under time-varying stress using parallel creep curve, *Advances in Materials Science and Engineering* 2016 (2016).
- [14] M.A. Pisani, Behaviour under long-term loading of externally prestressed concrete beams, *Engineering structures* 160 (2018) 24-33.
- [15] Z.P. Bažant, S. Prasannan, Solidification theory for concrete creep. II: Verification and application, *Journal of Engineering mechanics* 115(8) (1989) 1704-1725.
- [16] P. Rossi, J.-L. Tailhan, F. Le Maou, L. Gaillet, E. Martin, Basic creep behavior of concretes investigation of the physical mechanisms by using acoustic emission, *Cement and Concrete Research* 42(1) (2012) 61-73.
- [17] M.F. Ruiz, A. Muttoni, P.G. Gambarova, Relationship between nonlinear creep and cracking of concrete under uniaxial compression, *Journal of Advanced Concrete Technology* 5(3) (2007) 383-393.
- [18] Z.P. Bažant, B. H., Crack band theory for fracture of concrete, *Matériaux et construction* 16(3) (1983) 22.

8. THE IMPACT OF EARLY-AGE CREEP ON BUILDABILITY OF 3D PRINTED CONCRETE

This chapter incorporates the local force method, presented in chapter 7, into the 3D printing model to study the impact of early-age creep for buildability quantification. This enables to study the impact of early-age creep on typical failure modes, i.e., structural instability due to buckling and plastic collapse resulting from material yielding. The green strength and early-age creep tests are first employed to characterize the visco-elastic-plastic material properties. The model is then validated with the comparison to printing experiment in relation to critical printing height and failure mode. A series of parametric analyses are subsequently performed to quantify the influence of early-age creep on various printing geometries in which different failure modes are dominant. The numerical results highlight the significance of initial printing time and material mix design for predicting the buildability of 3D printing of concrete. In the end, an explanation about how creep affects structural buildability is given from the perspective of localized damage and creep strain.

8.1 INTRODUCTION

In 3DCP, numerical modelling has proved to be a beneficial tool with regard to the prediction of structural deformation and buildability quantification. However, numerical models based on solid mechanics mostly rely on the assumption that the behaviour of the material is elastic-plastic [1-3]. This implies that only instantaneous strain is considered during the printing process, while time-dependent deformation is neglected. This delayed deformation is induced by the basic creep, plastic and autogenous shrinkage, and consolidation settlement under distributed compressive loading and increases with printing time, as shown in Chapter 6 and Chapter 7. In this chapter, the terminology of 'early-age' is used to describe this time-dependent deformation. In the published research, several early-age creep tests of 3D printable mortar/paste have been performed [4, 5]. The experimental finding indicates that early-age creep makes for about 7% of the viscoelastic deformation of the tested sample [4]. Therefore, it is clear that the early-age creep needs to be incorporated into 3D printing model to explore its effects on the prediction of structural deformation and the buildability quantification.

To the best of the authors' knowledge, only one published work fill this research gap [6]. Here, the previously developed lattice model is employed to investigate the impact of early-age creep on structural analysis during printing process. The uniaxial compression test and early-age creep test in Chapter 6 are utilized to calibrate the input material properties. The model is then validated by comparison to a 3D printing experiment using wall structure. The quantitative effect of early-age creep on structural analysis is determined through a series of parametric analyses. In the end, an explanation about how creep affects structural buildability is given from the perspective of localized damage and creep strain.

8.2 MODEL IMPLEMENTATION

Chapter 7 presents a 'local force method' for simulating the early-age creep of cementitious materials under different loading conditions (i.e., constant, loading and unloading). In this approach, the creep strains of lattice elements are first computed with the stored element stresses and creep compliance as inputs. The derived results are then converted into element force and applied to the analyzed object. In this chapter, the detailed procedures on how to incorporate the local force method into 3D printing model for structural analysis during printing process will be given. This method is based on the buckling model proposed in Chapter 5. The numerical implementation consists of seven steps: A, B, C, D, E, F and G, as shown in Figure 8-2.

In the schematic diagram, the k and K refer to the local and global system stiffness matrix, which consists of material stiffness k_t/K_t and geometric stiffness k_g/K_g . The superscript ' t ' stand for the printing time, which determines the viscoelasticity material property and gravitational loading from the activated printing segments.

Detailed information abouts Step A, B and C can be found in Chapter 5.

Step A: Model generalization

Step B: Material properties determination

Step C: Structure analysis of printed segments

The transient material properties are introduced into the 3D printing model for the material stiffness matrix determination. The computed element stresses are then used as incremental stresses for creep strain computation. The derived incremental displacement is utilized to update the printing geometry.

Step D: Local force computation

With the known creep compliance and stored element stress as inputs, the creep strain of lattice elements can be derived, as described in Chapter 7. Subsequently, these computed strains are transferred into axial forces, which refers to the local force in this study. Given that this numerical analysis adopts the incremental solution, the difference about creep force between two steps are then calculated, as described in Eq. 7.2.1.

Step E: Viscoelastic analysis

Together with the incremental load, the local forces in incremental formulation are applied to the lattice system to simulate the viscoelasticity behaviour of printed structure, as shown in Figure 8-1.

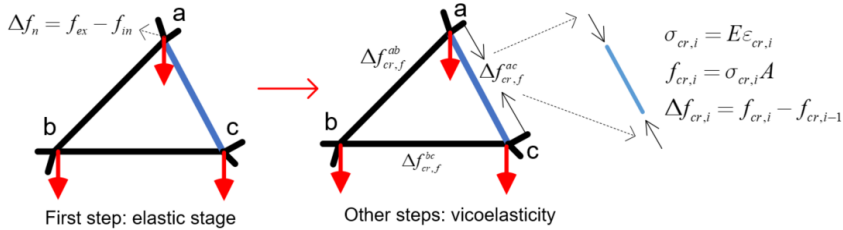


Figure 8-1 The viscoelasticity analysis of an individual beam element

Step F: System updates

The nodal displacement derived from Step C is utilized to update the numerical model. Meanwhile, critical elements in which element stresses are higher than the material strength (tensile or compressive) are removed from the lattice mesh.

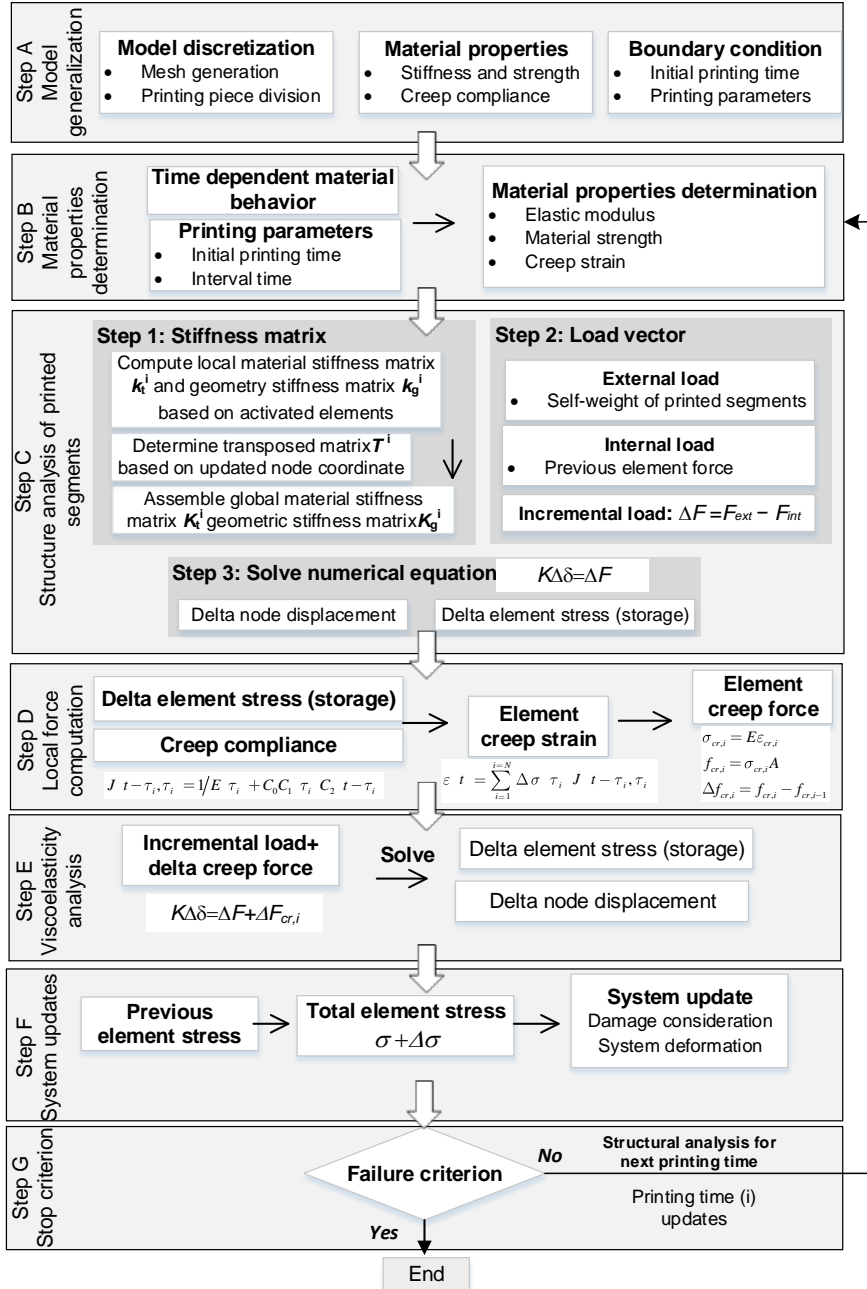


Figure 8-2 Flowchart about the 3D printing model with creep consideration

Step F: Stop criterion

At the end of each step analysis, the structural failure criterion mentioned in Section 3.2.5 is adopted to determine whether or not the analyzed model fails. The numerical analysis continues until the structural failure criterion is met. In that case, the predicted critical printing layer will be given, as well as the failure mode.

8.3 NUMERICAL ANALYSIS

In this section, a numerical study is carried out to evaluate the lattice model with the incorporation of geometric nonlinearity, early-age creep, and localized damage for predicting the buildability of 3DCP. The model performance will be quantified through the comparison to printing experiment, which consists of the critical printing height and failure mode.

8.3.1 Model calibration

3D printable mortar/paste behaves approximately as a visco-elastic-plastic material. After material deposition, the printed segments are at rest for the majority of the duration of the printing process [7]. The instantaneous and time-dependent deformation codetermine the structural deformation. The former is associated with the elasto-plastic material behaviour, and the unconfined uniaxial compression/green strength test is commonly used to determine time-dependent stiffness and strength. The latter, on the other hand, refers to the early-age creep, which is caused by a combination of basic creep, autogenous and plastic shrinkage, and consolidation settlement. To describe this viscoelastic behavior, early-age creep tests are generally performed to provide the creep compliance required in this local force method.

8.3.1.1 Green strength test

This section gives a brief overview of the model calibration on the early-age material stiffness and strength of 3D printable mortar at fresh stage. The uniaxial compression tests taken from Chapter 6 are utilized to calibrate the time-dependent material properties. The cylinder sample with a height of 70 mm and diameter of 70 mm is utilized in this test. This sample geometry is inherited from the early-age creep test and allows for the occurrence of eccentric loading during the testing process. In view of computational convenience of solution accuracy, the mesh resolution equal to 1 mm is employed, creating a model composed of 10,255 lattice nodes connected by 74,195 beam elements. To account for the fact that cementitious materials have a higher resistance to compressive loading than tensile loading, the compressive strength is assumed to be 10 times that of the tensile strength throughout the calibration procedure. Details of the calibration process can be found in Chapter 3. The calibrated time-dependent material properties of lattice elements are expressed as:

$$\begin{aligned}
 E(t) &= 53 + t \\
 f_c(t) &= 20.54 + 0.5 \cdot t \\
 f_t(t) &= 2.054 + 0.05 \cdot t \quad [\text{kPa}]
 \end{aligned}
 \tag{Eq. 8-1}$$

Here, t refers to the hardening/printing time (min); E is the material stiffness, i.e., 'elastic modulus' from the green strength test. f_c and f_t refer to the material compressive and tensile strength, respectively.

8.3.1.2 Early-age creep test

In this section, the early-age creep tests are adopted to calibrate the viscoelasticity of the printable materials. This experimental program consists of quasi-instantaneous compressive loading-unloading cycles, as well as 180-second (3 minutes) holding periods. The experimental results from non-ageing creep test (as shown in Figure 6-11 (a)), are employed to fit a creep compliance surface (as shown in Figure 6-11 (b)), which describes the relationship between the creep compliance and loading duration and hardening time. This fitted double power law function (as expressed in Figure 6-11 (b)) is then incorporated into 3D printing model as the creep coefficients to simulate the viscoelasticity behaviour.

8.3.2 Model validation

A wall structure with the 350 mm length, 15 mm width, and 4 mm layer height is employed for buildability quantification with the consideration of early-age creep, as shown in Figure 8-3. The printing velocity is set to 600 mm/min in this experiment to avoid instability and tearing of the extruded filament caused by the imbalance speed between nozzle movement and material flow. More detailed information about the 3D printer, printable mortar, and the printing process can be found Chapter 6.

A numerical model with the wall layout printing geometry is created to simulate the printing experiment, as shown in Figure 8-4 (a). This numerical model divides each printing layer into three segments (as shown in Figure 8-4 (b)) to mimic the non-uniform gravitational loading condition caused by the continuous printing process and employs high friction as the boundary condition during structural analysis. To minimize the effects of mesh size, this wall structure uses the same mesh resolution, i.e., 1 mm, which is in accordance with the computational green strength and early-age creep test. In the end, a wall structure is built, each layer of which is composed of 21,060 lattice nodes connected by 157,950 elements.

The structural analysis for buildability quantification is conducted with the time-dependent material stiffness and strength, as well as creep compliance as inputs. The critical printing height and the structural failure mode are two commonly used criteria for model validation. Lattice modelling of the printing process reproduces the

buckling dominant failure mode, which is similar to experimental findings. In relation to the critical printing height, the wall structure fails at the 34th layer due to the out-of-plane displacement in the printing test. In contrast, lattice model predicts that this wall structure fails at 32nd layer. There is around 5% difference between the numerical prediction and the experimental result. It can be inferred that this 3D printing model can reproduce the experimentally derived failure mode and relatively accurately predict the critical printing height.

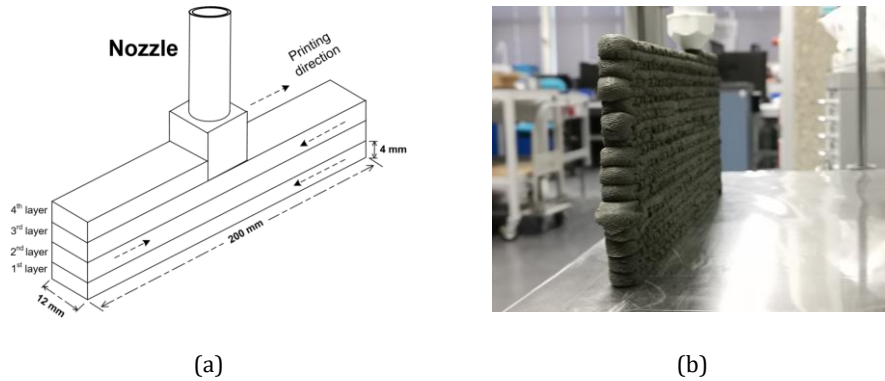


Figure 8-3 Wall structure for 3DCP (a) schematic diagram for designed wall structure (b) 3D printing test

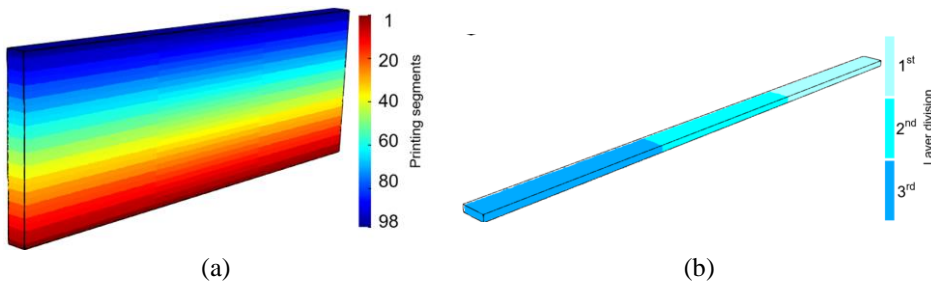


Figure 8-4 A numerical model with wall structure for 3DCP (a) layers of numerical model (b) layer division

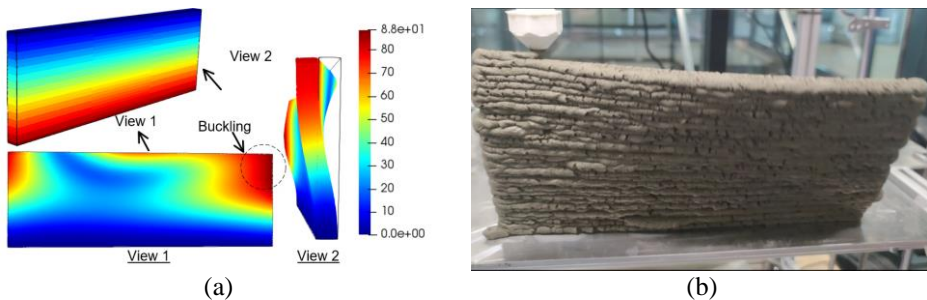


Figure 8-5 Typical failure mode for wall structure (a) numerical modeling (b) experimental result

8.4 DISCUSSIONS

Lattice modelling of wall structure shows similar results with experimental findings in terms of the critical printing height and failure mode. The impact of early-age creep on buildability quantification will then be quantitatively analyzed through a variety of printing geometries which are dominant by different failure modes. In the end, the relevant explanation of these impacts will be given from the perspective of system damage and the proportion of creep strain.

8.4.1 Factors influencing creep compliance at early age

Hardening time, loading duration, and material characteristics are the main factors that determine the creep compliance. Chapter 7 demonstrates that the hardening time outweighs the loading duration for creep prediction of 3D printed segments. In this section, the creep compliance function with various ageing times will be incorporated into the 3D printing model to investigate its impact on structural analysis during printing process. Here, the simulation cases with ageing time of 2100 s are regarded as the references, which are consistent with printing trials conducted in Chapter 6. In addition, the experimental results in published research indicate that the early-age creep accounts for more than 1% of the overall deformation at resting time of 0 min [4], which is roughly 100 times greater than our previous test result in Chapter 6. This difference suggests a significant impact of material mix design on early-age. Herein, the numerical cases with 100-time augmented creep coefficient C_0 are conducted to investigate the creep due to material properties on buildability quantification during printing process.

8.4.2 Failure modes

This numerical analysis allows for three typical failure modes: elastic buckling, plastic collapse, and a combination of the two. The hollow cylinder structures with different sizes are taken as the designed printing geometries. These numerical cases employ the time-dependent material properties expressed in Eq. 8-1 as well as same creep compliance coefficients, described in Eq. 7-4, including material properties C_0 , aging time exponent C_1 and loading duration coefficient C_2 . Table 8-1 summarizes the input parameters and failure information of all cases. Each printing layer is divided into 4 printed segments for non-uniform gravitational loading consideration. The numerical examples with the identical geometry share the same input model, making it possible to remove the influence of mesh disorder on printing process simulation. The failure step, failure mode, and deformed structure are provided to quantify the creep impact on 3D printing simulation. It should be noted that the failure step in this chapter refers to the critical printing step, in which the analyzed object reaches the structural failure criterion and fails.

Table 8-1 Summary of numerical cases for creep analysis

Nr.	Size (mm)	Creep	Failure	Failure	Difference
-----	-----------	-------	---------	---------	------------

	L/D	W	H	Ageing time (s)	Amplification C_0	mode	step	(%)
1				No creep	0		166	0
2	100	12	12	36	1	Plastic	165	0.6%
3				2100	1	collapse	166	Ref
4				2100	100		88	46.99%
5				No creep	0		123	0
6	200	12	12	36	1	Combined	122	0.81%
7				2100	1		123	Ref
8				2100	100		79	62.6%
9				No creep	0		70	0
10	400	12	12	36	1	Elastic	70	0
11				2100	1	buckling	70	Ref
12				2100	100		60	14.29%

Noted: L: Length; D: Diameter; H: layer height; Difference refers to the deviation between the reference model with the analyzed one.

8.4.3 Numerical results

Figure 8-6 describes the failure modes of all cases listed in Table 8-1. When comparing the numerical examples with or without creep inclusion (i.e., 1 and 3, 5 and 7, as well as 9 and 11), it can be illustrated that the creep effect on structural analysis of 3DCP might well be ignored in the context of this 3D printable material. In terms of the impact of ageing time, the failure steps obtained from numerical cases (i.e., 2, 6 and 10) indicate that an early ageing time makes the designed structures easier to fail. Although this difference (i.e., 0%, 0.6% and 0.81%) is small, it also should be pointed out that the structures in which plastic collapse is the dominant failure mode are affected more than those in which buckling is dominant. When comparing such numerical samples with different creep coefficient C_0 , significant differences (i.e., 46.99, 62.6% and 14.29%) in critical printing height can be found. Figure 8-6 shows the numerical cases with augmented creep coefficient C_0 reproduce different failure models with others. These numerical results show that the impact of creep on the structural buildability differs depending on the printing materials. It can be concluded that early-age creep must be considered for buildability quantification of 3DCP for printable materials with high creep.

Comparing the numerical cases (i.e., 4, 8 and 12) with augmented creep deformation to the reference ones (i.e., 3, 7 and 11), Figure 8-7 shows the deformed shape of hollow cylinder structures under different printing steps. Figure 8-8 provides the damage information for structural analysis during the printing process. The numerical cases with larger creep coefficients result in more localized damage. As a result, a lower critical printing height is found. In contrast to material yielding dominant failure mode, the buckling determined failure geometry is less affected by creep deformation. This is because the material stiffness instead of the strength determines the critical printing height for such kind of printing structure.

In contrast, the numerical finding indicates that the early-age creep without augmented creep coefficient shows a limited influence on structural deformation for the reference cases (i.e., 3, 7 and 11). The possible reason is that the creep accounts for small deformation to the deformed structure, therefore, its impact can be neglected. Figure 8-9 provides the ratio between the creep to total strain for all beam elements during the numerical analysis for case 3. This small ratio (i.e., roughly 1%) suggests that there is a limited contribution from early-age creep to the entire deformation. Figure 8-10 describes the creep evolution of a randomly chosen element during the structural analysis. Although the creep evolution of this lattice element increases during the numerical analysis, the creep strain is still limited until the system eventually fails. As a result, the buildability quantification and structural deformation of 3DCP remain almost unchanged with the consideration of early-age creep.

During the numerical analysis, positive incremental element stresses (namely, tensile stress) can sometimes be observed (as shown in Figure 8-10 (a)), which means that this selected element is sometimes exposed to the incremental tensile stress. This basic reason for this phenomenon is that the continuous extrusion process results in some printed segments subject to different loading conditions (namely, loading and unloading situations). It also reveals the printed segment during printing process is not always increased but sometimes varies based on printing parameters and geometry. Thus, it requires the proposed model to account for the loading-unloading situation in element scale. The research in chapter 7 has demonstrated that the 'local force method' is able to mimic the creep behaviour under various loading conditions. Thus, the creep impact of buildability quantitation of 3DCP can be accurately analyzed.

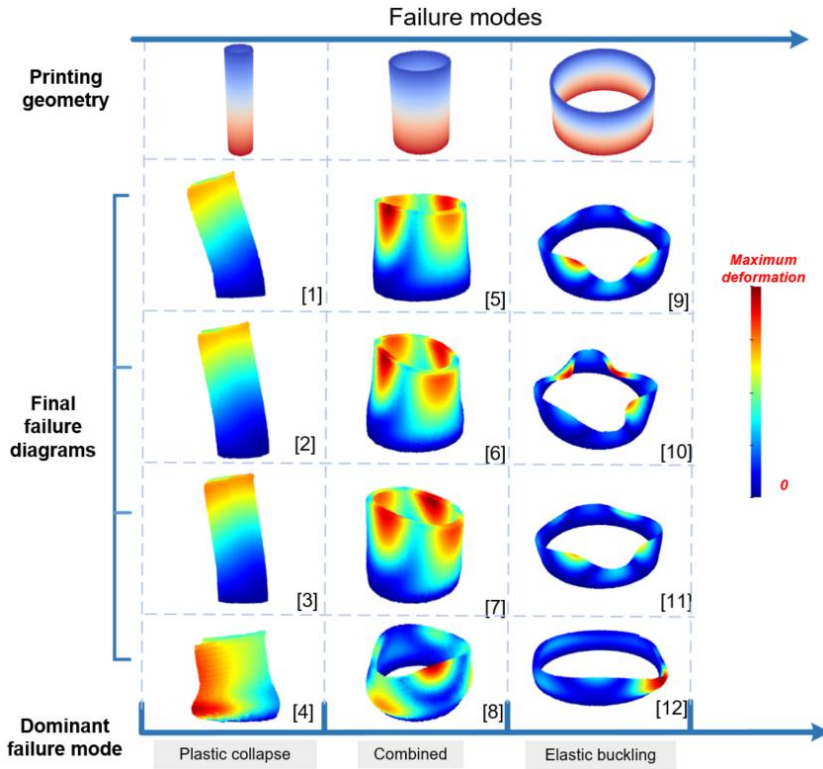
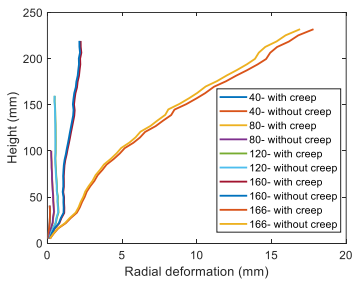
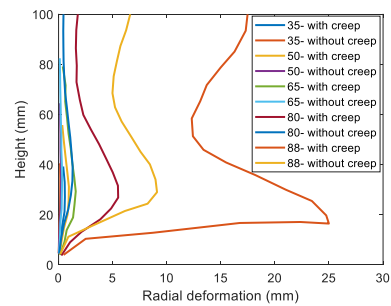


Figure 8-6 Failure modes of listed numerical cases



(a)



(b)

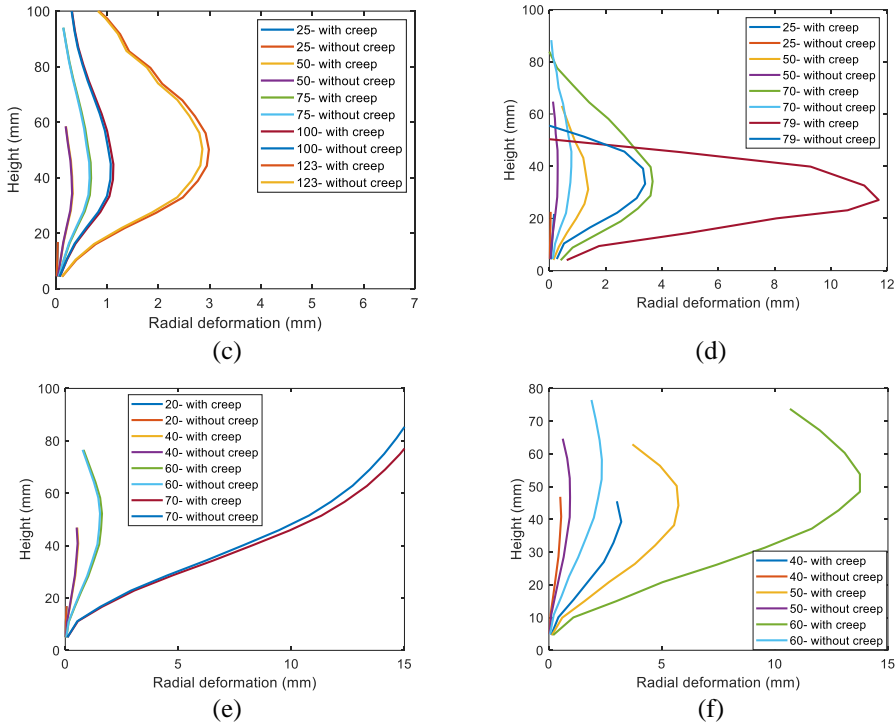
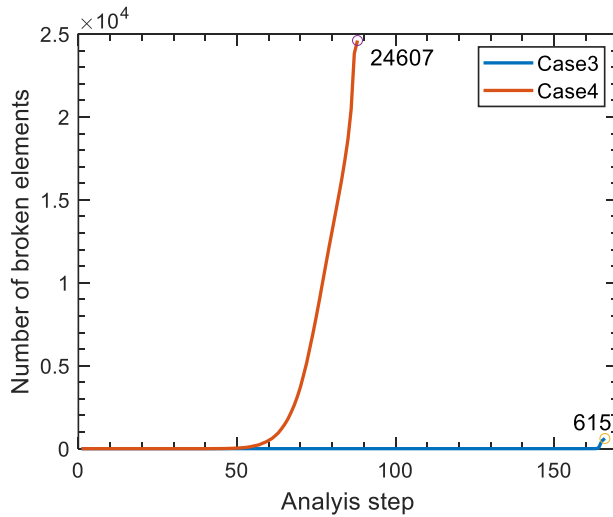
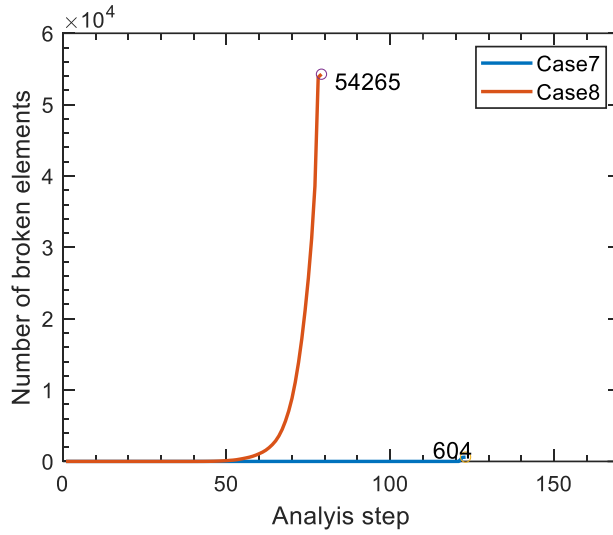
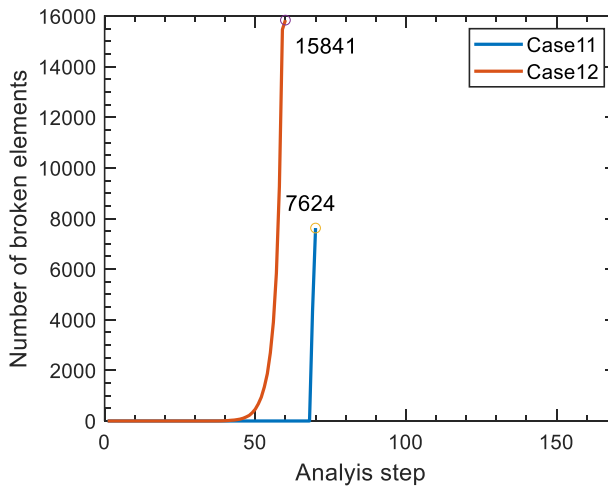


Figure 8-7 Radial deformation versus height (a) case 3; (b) case 4; (c) case 7; (d) case 8; (e) case 11; (f) case 12





(b)



(c)

Figure 8-8 Damage information during numerical analysis for different failure modes (a) plastic collapse (b) combined failure mode (c) elastic buckling

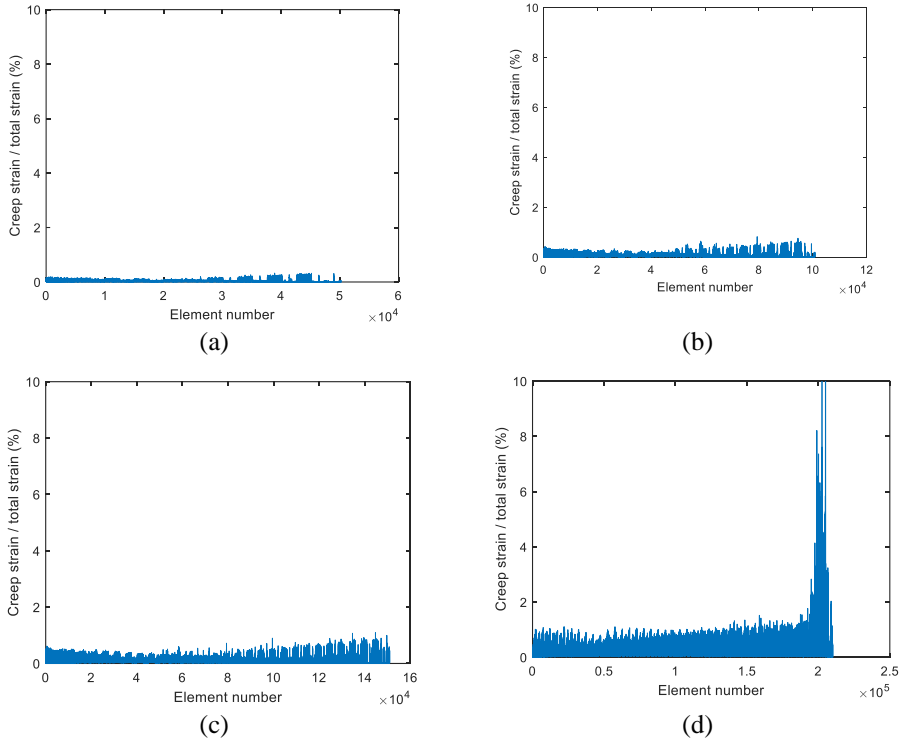


Figure 8-9 Creep strain during numerical analysis for case 3 (a) 40 step (b) 80 step (c) 120 step (d) 166 step

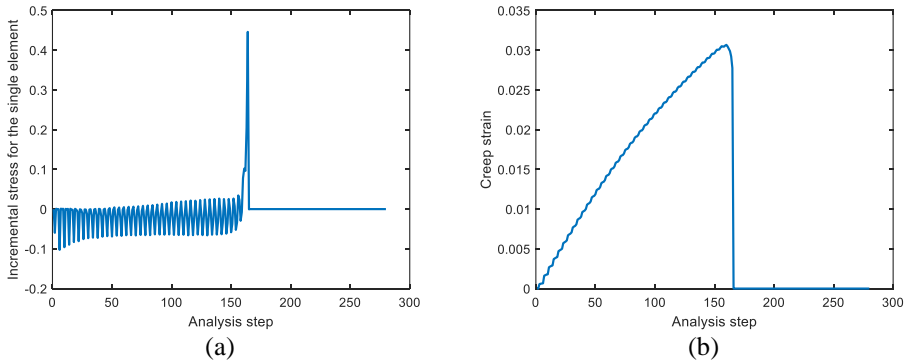


Figure 8-10 Creep behaviour of randomly chosen lattice element (a) incremental element stress (b) creep evolution

8.5 CONCLUSIONS

In this chapter, the local force method is incorporated into previously proposed 3D printing model to study the impact of early-age creep on structural analysis. The green strength and early-age creep tests are first employed to characterize the

viscous-elastic-plastic material properties of lattice elements. A printing experiment is then utilized to validate the model. After that, a series of parametric analyses are performed to investigate how the early-age creep affects the structural analysis of 3DCP, ranging from the critical printing height, failure mode, and structural deformation. Based on this research, some insights and conclusions can be reached:

- The presented 3D printing model can simulate the early-age creep behaviour under various loading conditions. In comparison to printing experiment, it not only can reproduce buckling dominant failure modes but also predicts the experimentally derived critical printing height accurately;
- In terms of the impact of hardening time on structural analysis, the failure height obtained from numerical cases indicate that an early ageing time makes the designed structures easier to fail. However, this influence is limited (i.e., 0%, 0.6% and 0.81%), because the elastic-plastic deformation determines the structural deformation, not creep. In contrast to buckling determined geometries, the collapse dominant structures are more affected.
- The creep impact on the structural buildability differs depending on the printing materials. When introducing a large creep compliance function into the 3D printing model, the critical printed height decreases significantly. In relation to different failure modes, the buildability of the elastic buckling failure mode declines with increasing creep compliance, but the typical failure model remains almost unchanged; in contrast, the buildability of the plastic collapse failure mode increases with creep compliance and the creep deformation also affects the failure mode.

REFERENCES

- [1] R. Wolfs, F. Bos, T. Salet, Early age mechanical behaviour of 3D printed concrete: Numerical modelling and experimental testing, *Cement and Concrete Research* 106 (2018) 103-116.
- [2] A.S.J. Suiker, Mechanical performance of wall structures in 3D printing processes: Theory, design tools and experiments, *International Journal of Mechanical Sciences* 137 (2018) 145-170.
- [3] A.S. Suiker, R.J. Wolfs, S.M. Lucas, T.A. Salet, Elastic buckling and plastic collapse during 3D concrete printing, *Cement and Concrete Research* 135 (2020) 106016.
- [4] L. Esposito, L. Casagrande, C. Menna, D. Asprone, F. Auricchio, Early-age creep behaviour of 3D printable mortars: Experimental characterisation and analytical modelling, *Materials and Structures* 54(6) (2021) 1-16.
- [5] M. Chen, B. Liu, L. Li, L. Cao, Y. Huang, S. Wang, P. Zhao, L. Lu, X. Cheng, Rheological parameters, thixotropy and creep of 3D-printed calcium sulfoaluminate cement composites modified by bentonite, *Composites Part B: Engineering* 186 (2020) 107821.
- [6] Q. Wang, X. Ren, J. Li, A Chemo-Mechanical Model for Predicting the Buildability of 3d Printed Concrete, Available at SSRN 4147420.
- [7] N. Roussel, Rheological requirements for printable concretes, *Cement and Concrete Research* 112 (2018) 76-85.

9. RETROSPECTION, CONCLUSIONS AND RECOMMENDATIONS

In this chapter, a brief overview of this thesis work is given. Then follow the general conclusions. In the end, some recommendations for further work are indicated.

9.1 RETROSPECTION

Over the past decade, additive manufacturing has been a revolutionary technology which generates enormous interest in both industry and academia. 3DCP, an automated construction method, can manufacture a computer-designed model through material deposition. Although this technique shows enormous potential, full adoption in construction sector is still far due to the lack of fundamental knowledge regarding material behaviors of printable cementitious materials, as explained in Chapter 2. To fill this knowledge gap, investigations on material and mechanical properties of 3DCP are required. For this reason, the first goal of this thesis was to present a method to simulate the build-up stage.

To achieve this research goal, a numerical tool based on the lattice model was developed to quantify the structural buildability during the printing process. This model takes a series of factors into account, which include the printing velocity, time-dependent material properties, non-uniform gravitational loading, geometric nonlinearity, localized damage, early-age creep and stress redistribution. By means of this model, three typical failure modes, namely plastic collapse, elastic buckling and a combination thereof, can be reproduced. The impact of printing parameters and material properties on buildability quantification can be quantitatively analyzed. Given a specific printing geometry, this numerical tool can be further used to design and optimize the printing scheme.

9.2 CONCLUSIONS

This thesis analyzes the structural behaviour and early-age material properties of 3DCP in the fresh state. The main research can be divided into two parts, a) lattice modelling of printing process on buildability quantification; b) investigation of early-age creep behaviour for 3D printable materials. This thesis presents a promising numerical tool to engineers and researchers to quantify the structural buildability of 3DCP. It also proposes an experimental method to measure the early-age creep evolution of 3D printable cementitious materials and study its impact on structural behaviour during the printing process. General conclusions are given below:

The 3D printing model based on the lattice fracture model is a promising tool for buildability quantification of 3DCP. The original lattice model, which can avoid the singularity-related issues in fracture analyses, can simulate the localized damage which occurs during the printing process. The incorporation of geometric nonlinearity allows the 3D printing model to consider buckling as well. The element birth technique, proposed in Chapter 3, can mimic the continuous printing process of 3DCP, allowing for the non-uniform gravitational loading. The quantitative influence of non-uniform gravitation load can be reflected through the number of printing segments for each layer. The calculated critical printing height decreases and converges to a constant value with the increased number of divided printing segments for each layer.

The non-uniform gravitational loading and geometric nonlinearity are two significant factors for simulation of buckling failure. This newly proposed model, incorporating all the above-mentioned factors, can predict the experimentally observed failure modes and critical printing height. On the one hand, the impact of material properties and printing parameters on buildability quantification can be directly analyzed via this numerical tool without a series of trial-and-error tests. On the other hand, understanding the effect of each factor on buildability quantification provides instructive feedback towards the exploitation and improvement of other 3D printing models.

The incremental method is considered to be a more accurate method to quantify buildability during the printing process compared to load-unload method. The load-unload approach computes structural deformation in each step based on the instantaneous material stiffness. As a result, this numerical solution underestimates the structural deformation and ignores the stress redistribution that occurs due to deformed geometry. In contrast, the incremental method computes the layer deformation as a series of incremental displacements which are derived based on time-dependent material stiffness. It can reproduce more accurate failure mode in terms of plastic collapse. This is due to the consideration of deformed geometry and the inclusion of nonequilibrium force. The understanding of the stress redistribution is extremely important for the simulation of plastic collapse. It also explains the large quantitative discrepancy between previous FEM-based numerical simulations and experimental results [1].

The experimental program consisting of quasi-static compressive loading-unloading cycles can characterize early-age creep of 3D printable mortar. The elastic modulus, creep deformation and elastic recovery can be obtained using this experimental method. The magnitude of creep load plays a significant role in creep compliance determination. Unexpectedly, a higher compressive stress results in a lower creep compliance. This is opposite from what has been observed from rheological tests in the literature [2]. This is because these two experimental methods measure the early-age creep considering different factors. In the rheological test, a higher shear stress can create more microcracks, therefore, creep increases with the stress level. In contrast, this uniaxial compression test proposed in this thesis mainly reflects the impact of the compaction process and internal pores on the creep evolution. Using the experimental method presented in this thesis, the early-age creep for other kinds of printable cementitious materials can be directly examined. The relationship between creep compliance and time (i.e., loading duration and hydration time) can, therefore, be built for creep prediction.

The 'local force method' is suitable for simulating the viscoelastic behaviour of cementitious materials. One of the main advantages of this approach is the straightforward implementation of stress history. This solution method requires no approximation of the creep constitutive law and reproduces the same result as the analytical solution. The superposition principle is incorporated into the lattice model

based on the incremental algorithm. The entire simulation of creep includes a sequence of linear analyses. Lattice modelling results of the early-age creep are close to experimental results. This demonstrates the ability of the model for creep analysis of 3D printable mortar under incremental/constant compressive loading. Therefore, this simulation method can be incorporated into other numerical models to study the viscosity effect on mechanical and fracture analysis without introducing numerous empirical parameters which are difficult to identify correctly.

The impact of early-age creep on the buildability quantification depends on the printing material and the print geometry. When introducing a large creep deformation into the 3D printing model, the critical printing height decreases. Compared to elastic buckling, the structures dominant by plastic collapse are more affected by the early-age creep with respect to the failure-deformation mode and the critical printing height. These numerical analyses reveal the influence of early-age creep on structural buildability in terms of different printing geometries and material designs.

9.3 RECOMMENDATION FOR FUTURE RESEARCH

In this research, a new 3D printing model is proposed to quantify buildability. However, there are still some points for model improvement. Further research is recommended as follows.

First, this 3D printing model does not incorporate the impact of cold joints or the high porosity in the interface zone, which occurs due to water loss and hydration process. Thus, this model is only suitable to printing cases with short printing time in which the cold joint effect can be ignored. In the future, the impact of cold joints should be considered.

In addition, as discussed in Chapter 2, one of the advantages of 3DCP technique is to eliminate the use of formwork. This leads to increased water loss during the manufacturing process. As a result, more localized damage can occur due to plastic shrinkage [3-7]. Therefore, considering the moisture transfer in the 3D printing model is recommended.

Given that there are different extrusion methods, an additional compressive force discussed in Chapter 2 sometimes occurs. For example, if the standoff distance is smaller than the layer height, the local compression may occur, thereby significantly affecting the structural stability and mechanical properties through interlayer porosity. To the best knowledge of the author, there is no published research focusing on this kind of loading. Further research is recommended to study its impact on structural behaviour during the printing process.

Furthermore, the numerical model developed in this thesis can be combined with optimization methods such as topology optimization to search for the optimal printing parameters with the maximum critical printing height as the objective function. In addition, it also can be incorporated with some advanced machine

learning methods, such as the active learning [8] or reinforcement learning [9] for mix design and printing parameter optimization.

REFERENCES

- [1] R. Wolfs, F. Bos, T. Salet, Early age mechanical behaviour of 3D printed concrete: Numerical modelling and experimental testing, *Cement and Concrete Research* 106 (2018) 103-116.
- [2] M. Chen, B. Liu, L. Li, L. Cao, Y. Huang, S. Wang, P. Zhao, L. Lu, X. Cheng, Rheological parameters, thixotropy and creep of 3D-printed calcium sulfoaluminate cement composites modified by bentonite, *Composites Part B: Engineering* 186 (2020) 107821.
- [3] M.S. Khan, F. Sanchez, H. Zhou, 3-D printing of concrete: Beyond horizons, *Cement and Concrete Research* 133 (2020) 106070.
- [4] M.K. Mohan, A. Rahul, G. De Schutter, K. Van Tittelboom, Extrusion-based concrete 3D printing from a material perspective: A state-of-the-art review, *Cement and Concrete Composites* 115 (2021) 103855.
- [5] V.N. Nerella, S. Hempel, V. Mechtcherine, Effects of layer-interface properties on mechanical performance of concrete elements produced by extrusion-based 3D-printing, *Construction and Building Materials* 205 (2019) 586-601.
- [6] N. Roussel, A thixotropy model for fresh fluid concretes: theory, validation and applications, *Cement and Concrete Research* 36(10) (2006) 1797-1806.
- [7] N. Roussel, Rheological requirements for printable concretes, *Cement and Concrete Research* 112 (2018) 76-85.
- [8] M. Liang, Z. Chang, S. He, Y. Chen, Y. Gan, E. Schlangen, B. Šavija, Predicting early - age stress evolution in restrained concrete by thermo - chemo - mechanical model and active ensemble learning, *Computer - Aided Civil and Infrastructure Engineering* (2022).
- [9] F. Sui, R. Guo, Z. Zhang, G.X. Gu, L. Lin, Deep reinforcement learning for digital materials design, *ACS Materials Letters* 3(10) (2021) 1433-1439.

SUMMARY

For some decades now, additive manufacturing has been a revolutionary technology which generates enormous interest in both industrial and academic applications. 3D concrete printing (3DCP), an automated construction method, is able to manufacture the computer-designed model through material deposition. This innovative technique can considerably accelerate the construction process, and make it economically and technically feasible to implement complex structural elements in practice. Although this technique shows a promising future, full adoption in construction sector is still far from possible due to the absence of fundamental knowledge about printable material and structural analysis during or after printing process.

In 3DCP, the material after deposition should be strong enough to retain the shape and avoid collapse under self-weight and the gravitational load from subsequent printing layers. This is defined as buildability, which is codetermined by the printing parameters and material properties. The most straightforward method to assess the buildability of cementitious materials is the printing tests. Through a series of printing trials, a conservative program may be guaranteed while experimental methods are time-and-labor consuming. Therefore, this research aims to propose a 3D printing model to give a full understanding on the buildability and mechanical properties. To accomplish this research objective, this PhD research was carried out in two steps:

First, to fully understand the failure mechanism and quantify the structural buildability, a 3D printing model based on the lattice model is proposed. This newly developed model incorporates a series of influential factors, including the printing velocity, time-dependent material properties, gravitational loading, geometric nonlinearity, localized damage, element birth technique, geometric nonlinearity and stress redistribution. By means of this model, the localized damage and stress redistribution during the printing process can be taken into account for buildability quantification. Meanwhile, the asymmetric buckling failure mode can be reproduced without introducing any initial geometrical imperfection and bifurcation linear buckling analysis, which are of necessity for published FEM-based models for buildability quantification in 3DCP.

To investigate the impact of early-age creep on buildability analysis, a specialized experimental setup is designed to characterize the early-age creep of 3D printable mortar. An analytical model based on a double power law is used to establish the relationship between creep and loading duration and ageing time. A local force method based on the Boltzmann superposition principle is proposed to simulate the

early-age creep behaviour. Then, this simulation idea is incorporated into the 3D printing model to study the impact of early-age creep on buildability quantification.

Based on the research work, a new numerical method for buildability quantification is proposed. This research gives a deep insight of material and structural behaviour of 3D concrete printing in the fresh state. Based on this work, further research about the structural design and printing parameters optimization can be performed. Such a numerical model will be beneficial to the application of 3DCP in construction industry, from the printing performance quantification and printing parameters optimization.

SAMENVATTING

Al enkele decennia is additive manufacturing een revolutionaire technologie die een enorme belangstelling wekt voor zowel industriële als academische toepassingen. 3D-betonprinten (3DCP), een geautomatiseerde constructiemethode, kan het door de computer ontworpen model vervaardigen door middel van materiaaldepositie. Deze innovatieve techniek kan het bouwproces aanzienlijk versnellen en het economisch en technisch haalbaar maken om complexe constructieve elementen in de praktijk te realiseren. Hoewel deze techniek een veelbelovende toekomst biedt, is volledige acceptatie in de bouwsector nog verre van mogelijk vanwege het gebrek aan fundamentele kennis over printbaar materiaal en structurele analyse tijdens of na het printproces.

In 3DCP moet het materiaal na plaatsing sterk genoeg zijn om de vorm te behouden en instorting onder het eigen gewicht en de zwaartekracht van volgende lagen te voorkomen. Dit wordt gedefinieerd als bouwbaarheid, die mede wordt bepaald door de printparameters en materiaaleigenschappen. De eenvoudigste methode om de bouwbaarheid van cementgebonden materialen te beoordelen, zijn de printproeven. Door een reeks drukproeven kan een conservatief programma worden gegarandeerd, terwijl experimentele methoden tijdrovend en arbeidsintensief zijn. Daarom heeft dit onderzoek tot doel een 3D-printmodel voor te stellen om een volledig inzicht te krijgen in de bouwbaarheid en mechanische eigenschappen. Om dit onderzoeksdoel te bereiken, is dit promotieonderzoek in twee stappen uitgevoerd:

Ten eerste, om het faalmechanisme volledig te begrijpen en de structurele bouwbaarheid te kwantificeren, wordt een 3D-printmodel voorgesteld op basis van het lattice model. Dit nieuw ontwikkelde model bevat een reeks invloedrijke factoren, waaronder de printsnelheid, tijdsafhankelijke materiaaleigenschappen, zwaartekrachtbelasting, geometrische niet-lineariteit, plaatselijke schade, elementgeboortetechniek, geometrische niet-lineariteit en herverdeling van spanning. Door middel van dit model kan de gelokaliseerde schade en herverdeling van de spanning tijdens het printproces in aanmerking worden genomen voor kwantificering van de bouwbaarheid. Ondertussen kan asymmetrisch knikbezwingen worden gereproduceerd zonder enige initiële geometrische imperfectie en bifurcatie lineaire knikanalyse te introduceren, die noodzakelijk zijn voor gepubliceerde op FEM gebaseerde modellen voor kwantificering van bouwbaarheid in 3DCP.

Om de impact van kruip op jonge leeftijd op bouwbaarheidsanalyse te onderzoeken, is een gespecialiseerde experimentele opstelling ontworpen om de kruip op jonge leeftijd van 3D-printbare mortel te karakteriseren. Een analytisch model gebaseerd op een dubbele machtsfunctie wordt gebruikt om de relatie tussen kruip- en laadduur en verouderingstijd vast te stellen. Een lokale krachtmethode

gebaseerd op het Boltzmann-superpositieprincipe wordt voorgesteld om het kruipgedrag op jonge leeftijd te simuleren. Vervolgens wordt dit simulatie-idee opgenomen in het 3D-printmodel om de impact van kruip op jonge leeftijd op de kwantificering van de bouwbaarheid te bestuderen.

Op basis van het onderzoekswerk wordt een nieuwe numerieke methode voor kwantificering van bouwbaarheid voorgesteld. Dit onderzoek geeft een diepgaand inzicht in het materiaal- en constructiegedrag van 3D-betonprinten in verse toestand. Op basis van dit werk kan verder onderzoek naar het structureel ontwerp en optimalisatie van afdrukparameters worden uitgevoerd. Een dergelijk numeriek model zal gunstig zijn voor de toepassing van 3DCP in de bouwsector, van de kwantificering van de printprestaties tot de optimalisatie van de printparameters.

ACKNOWLEDGMENTS

Doing a PhD is not as good as you expect or as bad as you fear. Finally, I survive and come to the moment of writing this section. It means I am approaching the end of this journey. At this very special moment, I would like to express my most sincere gratitude to my dear friends and colleagues who have helped and supported me during the past four years.

First of all, my special gratitude goes to China Scholarship Council and Femris for offering me an opportunity to do my PhD at the Microlab, Section of Materials and Environment, Department of Materials, Mechanics and Management & Design, Faculty of Civil Engineering and Geoscience, Delft University of Technology.

I would like to thank my promotor Prof.dr.ir Erik Schlangen. Thanks for giving me the position, and for supporting and encouraging me during this trip. It is a good fortune to become his student. Everything is still fresh in my memory as if things had just happened yesterday. In our first-time meeting, he told me 'You are always welcome to discuss'. I enjoyed all discussions we had and lots of pleasant 'five-minute' talks. His persistent support, patient guidance and professional attitude towards the research guide me and help me find the right research direction. His kindness and humor in daily life create a comfortable atmosphere for my PhD life. Most importantly, he not only gives me inspiration for my PhD project but also shows me how to become an independent researcher. Many thanks for his help, I cannot imagine what my PhD would be without his supervision.

My special thanks to my daily supervisor and copromotor Dr. Branko Šavija. How lucky I am to have such a nice supervision team during my PhD. As a daily supervisor, he is always high-efficiency and ready to help me. Every time, he responds to my questions and manuscript in a fast and highly efficient way, with detailed and constructive comments. When I feel lost or upset during my PhD process, he always encourages me and helps me to find the correct direction. His passion towards research and friendly attitude to me make me never feel isolated during my PhD journey. He not only teaches me how to think/write critically and logically but also shows me how to enjoy the research life. This thesis would not have been accomplished without his guidance. His interesting topics contributes many joyful coffee breaks that make everything become 'goed and promising'.

Besides my promotors, I would like to acknowledge the chairperson and all of my committee members: Prof. Hans Beunderman, Prof. Christian Louter, Prof. Jan Rots, Prof. Kim Van Tittelboom, Dr. Shunzhi Qian and Dr. Rob Wolfs for taking the time

to carefully review the draft of this work. Their insightful comments and constructive suggestions help me improve my thesis significantly.

I would like to take this moment to show my sincere gratitude to Dr. Zhiwei Qian for his continuous help in my PhD project and personal life in Netherlands. It is truly fortunate that I have met someone as kind as him. His constructive suggestions and guidance enable me to steer clear of several errors. Thanks for his support and enormous help in the past several years.

I would like to give my special thanks to my nice and lovely officemates: Albina Kostiuhenko, Bart Hendrix, Maiko van Leeuwen, Yask Kulshreshtha, Rowin Bol, Xiujiao Qiu and Marc Ottele. It's my fortune to share pleasant office time with all of you.

My special appreciation goes to my colleagues and friends: Prof. Klaas van Breugel, Dr. Guang Ye, Prof. Max Hendriks, Prof. Henk Jonkers, Dr. Oğuzhan Çopuroğlu, Dr. Mladena Luković, Dr. Mohammad Fotouhi, Dr. Dessi Koleva, Renée Mors, Hua Dong, Tianshi Lu, Jiayi Chen, Bei Wu, Xu Ma, Leyang Lyu, Hongzhi Zhang, Shi Xu, Wenjuan Lyu, Yading Xu, Shizhe Zhang (Kelly Mao), Jinbao Xie, Yu Zeng, Zhenming Li, Yidong Gan, Boyu Chen, Yu Chen, Hu Shi, Yu Zhang, Ali Ghaderiaram, Anne Linde van Overmeir, Luiz Miranda de Lima Junior, Zhiyuan Xu, Fernando Mendonca Filho, Bianca Fraga Silva, Irving Alfredo Flores Beltran, Emanuele Rossi, Xuhui Liang, Yun Chen, Zhi Wan (Jing Chen), Shan He (Zejia Zheng), Minfei Liang, Xuliang Hou (Ying Yang), Patrick Holthuizen, Claudia Romero Rodriguez, Marija Nedeljković, Kuba Pawlowicz, Stefan Chaves Figueiredo, Ameya Kamat, Guilherme da Silva Munhoz, Hao Huang, Zhipei Chen, Chen Liu, Yitao Huang, Beyazit Aydin, Shozab Mustafa, Zhenxu Qian, Yibing Zuo, Hao Cheng, Xi Li, Yong Zhang, Xingliang Yao, Dawei Gu, Marija Krstic and Çağlar Yalçinkaya. Thanks for the friendship, the coffee time, the parties and all the great time we shared together. Because of you all, I have got the most beautiful and precious memories at the TU Delft.

Many thanks to Arjan Thijssen, Ton Blom, Paul Vermeulen, and John van den berg for their professional help in all the lab work. Many thanks to Kees van Beek, he helped me design and conduct experimental tests and shared many research experiences when I was a rookie at Microlab. I also would like to acknowledge Iris Batterham, Jacqueline Bergenhenegouwen, Jaap Meijer, Iris Nederhof-van Woggelum, Sandra Schuchmann-Hagman and former secretary Claire de Bruin for their kind help on various daily issues.

Special thanks to Maiko van Leeuwen for his help in many experiments and the funniest jokes. As a friend, he always makes the enjoyable atmosphere of the lab, even in the difficult corona time. We have a lot of fun times together (BBQ activities, PSOR, and games). Because of him, I never feel isolated during my PhD journey. Thanks for arranging all the events. Of course, thanks for teaching me with Dutch.

I am also very thankful to all friends that I met in Netherlands. My gratitude goes to Fanxiang Xu, Yuan Wu, Rong Yu, Pei He, Xiuli Wang, Rui Yan, Yuxuan Feng,

Zhanchong Shi, Huan Wang, Zhaoying Ding, Yi Xia, Mengmeng Gao, Zheng Li, Lubin Huo, Fengqiao Zhang, Lichao Wu, Bo Li, Chi Jin, Bo Sun, Jincheng Yang, Weikang Feng, Xiaolin Liu, Xiaohui Liang, Li Wang, Haoyu Li, Chenjie Yu, Quanxin Jiang, Langzi Chang, Yang Jin, Bowen Li, Dengxiao Lang, Jian Zhang, Chunyan He, Biyue Wang, Lei Liu, Yuqian Tu, Yubao Zhou and Wenting Ma. Appreciate your help and support. All the lunches, dinners, parties and trips that we have spent together are memorable.

Many thanks also go to Ondrej Rokos, Ron Peerlings and Prof. Marc Geers from TU/E for their kind support and encouragement, and patiently waiting for me to start my new job.

Completion of this PhD research would not be possible without the enjoyable tennis time of all my dearest friends. I would like to thank my sports mates, Haicheng Liu, Chenlu Song, Rui Feng, Yingfu Xu, Yong Zhang, Minxing Xu, Xinxin Zhang, Zichao Li, Xiao Li, Ziqing Ma, Keji Pan and Zilong Zhao.

Sincere gratitude also goes to my 'bros and sisters' in Netherlands, Jin Chang, Yun Wan, 'Bai, Xiao', Yifan Fu, Ulaş, Shan Qu, Xinmin You, Qian Feng, Hao Yu, Xuan Li, Zhao Chen, and Tian Zhang. I feel so lucky to know all of you. Thanks for cheering me up when I was upset during this journey. Thanks for dragging me out of my nadir of darkness. Thanks for sharing so many constructive suggestions to me. Without all of your help, my life in the Netherlands would be difficult.

I owe lots of "thank you" to my friends in China, Ziyi Li, Guopeng Gong, Haibin Zhang, Kai Nie, Xianghui Liu, Hao Ye, Jia Wang, Jiuwen Bao, Yantai Zhang, Qiuyu Zhang, Xingsen Guo, Jinwei Ma, Hongtao Zhang, Kun Liu, Shuai Zhao, Jingting Zhao, Zhe Xu, Qingpeng Wang, Zhuangcheng Chang, Mengmeng Li, Ge Song, Wei Zhang and Ce Xing for always caring about me, taking care of me and supporting me along the way.

Finally, I want to express my gratitude to my girlfriend Lu Cheng, my father Kai Chang and my mother Aiqing Zhang, and my other family members for their unconditional and endless love, support, tolerance and encouragement.

Ze Chang

Delft, February 2023

LIST OF PUBLICATIONS

JOURNAL PUBLICATIONS

1. **Chang, Z.**, Zhang, H., Schlangen, E., & Šavija, B. (2020). *Lattice Fracture Model for Concrete Fracture Revisited: Calibration and Validation*. *Applied Sciences*, 10(14), 4822.
2. **Chang, Z.**, Xu, Y., Chen, Y., Gan, Y., Schlangen, E., & Šavija, B. (2021). *A discrete lattice model for assessment of buildability performance of 3D-printed concrete*. *Computer-Aided Civil and Infrastructure Engineering*, 36(5), 638-655.
3. **Chang, Z.**, Wan Z, Xu Y, Schlangen, E., & Šavija, B. (2022). *Convolutional neural network for predicting crack pattern and stress-crack width curve of air-void structure in 3D printed concrete*. *Engineering Fracture Mechanics*, 271: 108624.
4. **Chang, Z.**, Zhang H, Liang M, Schlangen, E., & Šavija, B. (2022). *Numerical simulation of elastic buckling in 3D concrete printing using the lattice model with geometric nonlinearity*. *Automation in Construction*, 142: 104485.
5. **Chang, Z.**, Liang M., Xu Y., Schlangen, E., & Šavija, B. (2022). *3D concrete printing: lattice modelling of structural failure considering damage and deformed geometry*. *Cement and Concrete Composites*. 104719.
6. **Chang, Z.**, Liang M., Xu Y., Wan Z., Schlangen, E., & Šavija, B. (2022). *Early-age creep of 3D printable mortar: experiments and analytical modelling*. *Cement and Concrete Composites*. (Accepted)
7. **Chang, Z.**, Liang M., He, S., Schlangen, E., & Šavija, B. (2022). *Lattice modelling of early-age creep of 3D printable mortar under incremental compressive loading*. (Under review)
8. **Chang, Z.**, Chen, Y., Schlangen, E., & Šavija, B. (2022). *A review of methods on buildability quantification of extrusion-based 3D concrete printing*. (Under review)
9. **Chang, Z.**, Liang M., Chen, Y., Schlangen, E., & Šavija, B. (2023). *Does early age creep influence buildability of 3D printed concrete? Insights from numerical simulations*. (Under review)
10. Chen, Y., **Chang, Z.**, He, S., Çopuroğlu, O., Šavija, B., & Schlangen, E. (2022). *Effect of curing methods during a long-time gap between two printing sessions on the interlayer bonding of 3D printed cementitious materials*. *Construction and Building Materials*, 332, 127394. (Correspondence)

11. Wan, Z., **Chang, Z.**, Xu, Y., Huang, Y., & Šavija, B. (2022). *Inverse Design of Digital Materials Using Corrected Generative Deep Neural Network and Generative Deep Convolutional Neural Network*. [Advanced Intelligent Systems](#), 2200333. **(Correspondence)**
12. Liang, M., Li, Z., He, S., **Chang, Z.**, Gan, Y., Schlangen, E., & Šavija, B. (2022). *Stress evolution in restrained GGBFS concrete due to autogenous deformation: bayesian optimization of aging creep*. [Construction and Building Materials](#), 324, 126690. **(Correspondence)**
13. Qiu, X., **Chang, Z.**, Chen, J., Schlangen, E., Ye G., Schutter De G., (2022). *ASR: Insights Into the Cracking Process via Lattice Fracture Simulation at Mesoscale Based on the Chemical Reactions at Microscale*. (Under review) **(Correspondence)**
14. Liang, M., **Chang, Z.**, Zhang Y., Chen H., He S., Schlangen, E., & Šavija, B., (2022). *Autogenous deformation induced- stress evolution in high-volume GGBFS concrete: Macro-scale behavior and micro-scale origin*. (Under review) **(Correspondence)**
15. Liang, M., **Chang, Z.**, Wan, Z., Gan, Y., Schlangen, E., & Šavija, B. (2022). *Interpretable Ensemble-Machine-Learning models for predicting creep behaviour of concrete*. [Cement and Concrete Composites](#), 125, 104295.
16. Liang M., Gan Y., **Chang Z.**, Wan Z., Schlangen, E., & Šavija, B. (2022). *Microstructure-informed deep convolutional neural network for predicting short-term creep modulus of cement paste*. [Cement and Concrete Research](#), 152, 106681.
17. Wan, Z., **Chang, Z.**, Xu, Y., Šavija, B. (2022). *Optimization of vascular structure of self-healing concrete using Deep neural network (DNN)*. [Construction and Building Materials](#), 364, 129955.
18. Xu, Y., Gan, Y., **Chang, Z.**, Wan, Z., Šavija, B., & Schlangen, E. (2022). *Towards Understanding Deformation and Fracture in Cementitious Lattice Materials: Insights from Multiscale Experiments and Simulations*. [Construction and Building Materials](#), 345: 128409.
19. Liang M., **Chang Z.**, He S., Chen Y., Gan Y., Schlangen, E., & Šavija, B. (2022). *Predicting Early-Age Stress Evolution in Restrained Concrete by Thermo-Chemo-Mechanical Model and Active Ensemble Learning*. [Computer-Aided Civil and Infrastructure Engineering](#), 37(14), 1809-1833.
20. Zhang, H., Xu, Y., Gan, Y., **Chang, Z.**, Schlangen, E., & Šavija, B. (2020). *Microstructure informed micromechanical modelling of hydrated cement paste: Techniques and challenges*. [Construction and Building Materials](#), 251, 118983.
21. Jiang, N., Zhang, H., **Chang, Z.**, Schlangen, E., Ge, Z., & Šavija, B. (2020). *Discrete lattice fracture modelling of hydrated cement paste under uniaxial compression at micro-scale*. [Construction and Building Materials](#), 263, 120153.

22. Chen, Y., Figueiredo, S. C., Li, Z., **Chang, Z.**, Jansen, K., Çopuroğlu, O., & Schlangen, E. (2020). *Improving printability of limestone-calcined clay-based cementitious materials by using viscosity-modifying admixture*. *Cement and Concrete Research*, 132, 106040.
23. Zhang, H., Xu, Y., Gan, Y., **Chang, Z.**, Schlangen, E., & Šavija, B. (2019). *Combined experimental and numerical study of uniaxial compression failure of hardened cement paste at micrometre length scale*. *Cement and Concrete Research*, 126, 105925.

CONFERENCE PROCEEDINGS

1. **Chang, Z.**, Zhang, H., Schlangen, E., & Šavija, B. (2019). *Lattice model for numerical analysis of fracture process of concrete material under various loading conditions*. In Proceedings of the 10th International Conference on Fracture Mechanics of Concrete and Concrete Structures.
2. **Chang, Z.**, Schlangen, E., & Šavija, B. (2020). *Extended lattice model to simulate the printing process of 3D printed cementitious materials*. In Second RILEM International Conference on Concrete and Digital Fabrication: Digital Concrete 2020 2 (pp. 814-823). Springer International Publishing.

CURRICULUM VITAE

ZE CHANG



03-10-1992 Born in Shandong, China

EDUCATION

Sep. 2011 – July. 2015	B.SC student
	Civil Engineering
	China University of Petroleum (East China), China
Sep. 2015 – July. 2018	M.SC student
	Structural Engineering
	Dalian University of Technology, China
Oct. 2018 – Present	PhD. candidate
	Civil Engineering and Geoscience
	Delft University of Technology, The Netherlands